MESOSCALE RESPONSE OF THE TROPICAL ATMOSPHERE TO PROPAGATING CONVECTION

by

Philippa Margaret Manning

Atmospheric Physics Group

Department of Physics

Imperial College

LONDON

A Thesis Submitted for the degree of Doctor of Philosophy

at the University of London

1983

Abstract

This thesis concerns the theoretical modelling of widespread unsaturated downdraughts ($\sim 10^5 km^2$) which occur in the wake of organised tropical storm systems. Tropospheric warming and drying are achieved particularly in the wake of tropical squall lines.

Several mechanisms have been put forward to explain the vigour of the post squall circulation. It has been suggested that the downdraught is driven by evaporation, however dynamically forced mechanisms are explored in this thesis. (Theoretical and observational studies indicate that the buoyant convection associated with the storm systems produces a net positive pressure deviation from hydrostatic values.

Using steady state theory it is possible to describe these phenomena (assuming no mixing occurs). The types of "decay mode" or "response" to a negative pressure gradient for various conditions of inflow shear and compressibility are examined. In addition an "interlocking" forcing and response model is developed which indicates that the convective updraught and mesoscale descent are the dynamically important features. A simple two-dimensional inflow/outflow picture of the three-dimensional flow can be developed if an energy closure condition is invoked.

Two or more cumulonimbi cannot be modelled numerically because of insufficient computing capacity. However observed changes in flow and thermodynamic properties at the rear of these systems can be interpreted using this theory. A large number of simpler models have been analysed in constructing the more complicated models. These aid

in understanding the interaction between kinetic and potential (buoyant) energies and work done by the pressure field. Solution of these theoretical cases involves solving systems of transcendental and second order differential eigenvalue equations.

Contents

Title page. 1

Abstract. 2

Contents. 4

List of figures. 8

List of tables. 11

Abreviations. 12

Chapter One: Observations and Modelling.

1.1 Introduction. 13

1.1.1 Transports by cumulonimbi in the tropical atmosphere. 13

1.1.2 The grouping of Cb into clusters and classification of type by dynamical regime. 16

1.1.3 Transformation of the environment by clusters. 18

1.1.3.1 Thermodynamic and dynamic transformations of the environment from budget and composite studies. 21

1.1.3.2 Subcloud/cloud layer transformation from budget studies. 24

1.1.3.3 Differences between squall and non-squall clusters. 26

1.1.3.4 Differences between squall clusters occurring over land and over sea. 27

1.2 Structure of squall clusters from observational studies. 28

1.2.1 Squall and anvil region distinguished in the windfield. 28

1.2.2 Downdraught structure deduced from thermodynamic changes. 35

1.2.3 Surface pressure changes. 38

1.2.4 Squall line structure. 40

1.2.5 Anvil structure. 41

1.2.6 Vertical velocities and mass fluxes. 42

1.2.7 Features important to mesoscale circulation dynamics. 43

1.3 Numerical modelling of mesoscale circulations. 44

1.3.1 Simulation of convective and mesoscale downdraughts associated with a line element. 45

1.3.2 The role of evaporation in mesoscale downdraught production. 45

1.3.3 Influence of water drag and precipitation presence on mesoscale downdraught production. 48

1.3.4 Mesoscale subsidence forced by the pressure field produced by a convective circulation. 49

1.4 Theoretical models of post-squall circulations. 51

1.4.1 Evaporation driven downdraughts. 52

1.4.2 Density currents as an organising mechanism. 54

1.4.3 Mesoscale circulations as responses to dynamic forcing. 54

Chapter Two: Convective Forcing Profiles.

2.1 Introduction and development of the general displacement equation for a three-dimensional convective updraught. 56

2.2 Models of convective updraughts and downdraughts with an undeviated streamline. 64

2.2.1 Summary of the results of MM. 64

2.2.2 Model with a shallow downdraught. 70

2.2.3 Model with a shallow downdraught of variable depth. 73

2.3 Models of convective updraughts with net deviation of all streamlines. 79

2.3.1 Model of a two-dimensional convective updraught with net deviation of all streamlines. 80

2.3.2 Model of a three-dimensional overturning updraught with net deviation of all streamlines. 83

2.3.3 The effect of shear and compressibility. 88

2.4 Summary. 100

Chapter Three: The Forced Mesosale Response "Type A".

3.1 Introduction and derivation of the general equations describing a forced circulation. 103

3.2.1 Summary of the results of TMM80 relating to forced flows. 108

3.2.2 Effects of compressibility on the forced flows described in TMM80. 120

3.2.3 Effects of shear on the forced flows described in TMM80. 127

3.2.4 Possible forced modes for easterly jet-type velocity profiles. 135

3.3 Forced flows in which net deviation of limiting streamlines occurs. 144

3.3.1 Variation of F_f with E. 146

3.3.2 Flows with no relative inflow at the rear, E=+1 and E=-3. 152

Chapter Four: The Forced Mesoscale Response "Type B".

4.1 Introduction. 160

4.1.1 A "Type B" prototype circulation. 161

4.2.1 The convective updraught circulation. 165

4.2.2 The forced downdraught circulation. 166

4.2.3 Closure of the system. 168

4.3 Solution with a neutrally buoyant downdraught. 170

4.4.1 Solutions of the full equation set. 171

4.4.2 Energy conversion within the udraught, downdraught and combined circulations. 172

4.4.3 Alternative closure schemes. 178

4.4.4 Variation of the net mass flux and F_f with E_f. 179

4.5 Dependence of propagation speed of updraught and downdraught

on inflow depth, shear and differential lapse rate ratio. 183

4.5.1 Inflow depth. 183

4.5.2 Shear. 184

4.5.3 Differential lapse rate ratio. 191

4.6 Outflow profiles of relative velocity, pressure and entropy perturbation and the role of the convective downdraught. 192

4.7 Summary. 195

Chapter Five: Concluding Remarks.

5.1 Summary. 197

5.2 Calculation of model parameters from data. 199

5.2.1 Calculation of $(B-\chi_f)$ from data. 200

5.2.2 Results of the comparison. 217

5.3 Suggestions for further research. 219

Appendix A. 222

Appendix B. 225

Acknowledgements. 227

References. 228

List of Figures.

1.2.1 Cross-section through squall-line after Gamache and Houze (1982).

1.2.2 Divergence over the squall cluster after Gamache and Houze (1982).

1.2.3 Relative wind profile sequence.

1.2.4 Cross-section through squall-line after Zipser (1977).

1.2.5 Composite surface pressure after Johnson and Nicholls (1983).

1.2.6 Composite 900mb relative humidity after Johnson and Nicholls (1983).

2.1.1 Type A convective circulation and forced response.

2.1.2 Type B convective circulation and forced response.

2.1.3 Schematic diagram of a generalised three-dimensional overturning convective updraught.

2.2.1 Convective circulation symmetric about undeviated middle-level streamline.

2.2.2 Outflow pressure profile.

2.2.3 Outflow profiles.

2.2.4 Schematic flow with shallow downdraught.

2.2.5 Schematic flow including forced middle-level flow.

2.2.6 Schematic diagram of variable depth flows with shallow downdraught.

2.2.7 Variation of updraught outflow depth with propagation speed after Tam (1979).

2.3.1 Schematic diagram of a two-dimensional updraught.

2.3.2 Variation of propagation speed with E.

2.3.3 Outflow profiles.

2.3.4 Outflow profiles.

2.3.5 $\delta p_1(r_1)$ versus r_1 for $1-r_1=r_0$.

2.3.6 $\delta p_1(r_1)$ versus r_1 for "thin"updraughts.

2.3.7 $\delta p_1(r_1)$ versus r_1 for "thick" updraughts.

2.3.8 Schematic diagram of three-dimensional convective updraught.

2.3.9 $\bar{U}_0$ versus r_0 for overturning updraughts.

2.3.10 Propagation speed versus inflow shear, D=0.

2.3.11 Propagation speed versus inflow shear, D=1.

2.3.12 Outflow profiles.

2.3.13 Schematic diagram of three-dimensional convective updraught.

2.3.14 r_1 versus propagation speed.

2.3.15 $\bar{U}_0$ versus du/dz, D=0.

2.3.16 $\bar{U}_0$ versus du/dz, D=1.

3.1.1 Type A circulation.

3.1.2 Schematic diagram of forced descent.

3.2.1 Schematic diagram of forced descent.

3.2.2 ϵ^2 versus E.

3.2.3 Outflow profiles.

3.2.4 Outflow profiles.

3.2.5 Outflow profiles.

3.2.6 Outflow profiles.

3.2.7 F versus D.

3.2.8 $\Delta KE/KE_0$ versus D.

3.2.9 $\langle\rho_0 v_0\rangle/\langle\rho_0\rangle$ versus dv_0/dz_0.

3.2.10 $\Delta KE/KE_0$ versus du_0/dz_0.

3.2.11 Outflow profiles.

3.2.12 Outflow profiles.

3.2.13 Variation of $\langle\rho_0 v_0\rangle/\langle\rho_0\rangle$ and $\Delta KE/KE_0$ with jet amplitude.

3.2.14 Outflow profiles.

3.2.15 Boundary curve (a versus F) for no return flow at rear.

3.2.16 Variation of $\langle \rho_o u_o \rangle / \langle \rho_o \rangle$ and $\Delta KE/KE_o$ with jet amplitude.

3.2.17 Outflow profiles.

3.2.18 Outflow profiles.

3.3.1 Schematic diagram of forced descent.

3.3.2 Schematic diagram of forced descent.

3.3.3 F_f versus E.

3.3.4 Schematic diagram of forced descent.

3.3.5 F_f versus E.

3.3.6 Schematic diagram of forced descent.

3.3.7 F_f versus E.

3.3.8 sin(x)/x versus x.

3.3.9 Permitted flow modes.

3.3.10 Permitted flow modes.

3.3.11 Permitted flow modes.

4.1.1 Prototype circulation.

4.1.2 Type B convective updraught and forced descent.

4.2.1 Schematic diagram of overturning updraughts.

4.2.2 Schematic diagram of forced descent.

4.4.1 (CAPE released)/KE_o versus E_f.

4.4.2 $\Delta KE/KE_o$ versus E_f.

4.4.3 (Rate of CAPE release)/(Inflow KE flux) versus E_f.

4.4.4 (Rate of KE production)/(Inflow KE flux) versus E_f.

4.4.5 $(1-r_1)/r_o$ versus E_f.

4.4.6 Mass fluxes versus E_f.

4.4.7 F_f versus E_f.

4.5.1 F_f versus r_o.

4.5.2 F_u versus Δc.

4.5.3 F_u versus $\sqrt{\frac{\gamma_u - \beta}{\beta - \gamma_f}}$.

4.5.4 Net mass fluxes versus Δc.

4.5.5 $\Delta KE/KE_o$ versus $\sqrt{\frac{\gamma_u - B}{B - \gamma_f}}$.

4.5.6 Net mass fluxes versus $\sqrt{\frac{\gamma_u - B}{B - \gamma_f}}$.

4.6.1 Outflow profiles.

4.6.2 Schematic diagram of flow including convective downdraught.

5.2.1 θ_e profiles.

5.2.2 θ_e profiles.

5.2.3 θ_e profiles.

5.2.4 θ_e profiles.

5.2.5 θ_e profiles.

5.2.6 θ_e profiles.

5.2.7 θ_e profiles.

5.2.8 θ profiles.

List of Tables.

2.2.1 α_d versus α_u.

2.2.2 $(u_1/c_d)_{bottom}$ versus α_u.

3.2.1 Properties of simple modes.

3.3.1 Summary of permitted modes.

5.2.1 VIMHEX squall line data.

5.2.2 Calculation details.

5.2.3 Parameters calculated.

Abbreviations.

BOMEX: Barbados Oceanographic and Meteorological Experiment.

CAPE: Convective Available Potential Energy.

COPT: Convection Profonde Tropicale.

ESSA: Environmental Sciences Services Administration.

GARP: Global Atmospheric Research Program.

GATE: GARP Atlantic Tropical Experiment.

ICSU/WMO: International Council of Scientific Unions/World Meteorological Organisation.

MG: Moncrieff and Green (1972).

MM: Moncrieff and Miller (1976).

TMM80: Thorpe et al (1980).

TMM82: Thorpe et al (1982).

VIMHEX: Venezuelan International Meteorological and Hydrological Experiment.

CHAPTER ONE

OBSERVATIONS AND MODELLING OF MESOSCALE CIRCULATIONS IN TROPICAL CLUSTERS.

1.1 Introduction.

1.1.1 Transports by Cumulonimbi in the Tropical Atmosphere.

The release of latent heat of condensation is a major source of kinetic energy within the tropics. Energy is exported to higher latitudes and available potential energy is generated which fuels large-scale systems in mid-latitudes (Riehl, 1969). The transfer of sensible and latent heat, principally from the sea surface, sustains the belt between latitudes 30°N and 30°S against heat loss by radiation and by moist warm air advection into extra-tropical regions. Riehl and Malkus (1958) performed a number of calculations showing that a recycling mass flux of the Hadley type was insufficient to produce the required energy transport from tropical regions and compensate for radiational cooling.

The mean temperature sounding in the tropics is approximately that obtained by parcel ascent of air with the average moisture and temperature of the surface layer. However the tropical atmosphere is by no means saturated - and on average is well below saturation. Moist static energy, $h = C_pT + Lq + gz$, as a function of height, shows a minimum in mid-troposphere; it is relatively dry apart from the near-surface and near-tropopause regions. Understanding how these profiles of temperature and humidity are maintained has advanced with

greater observational knowledge of tropical meteorology.

Non-precipitating cumuli are sufficient to distribute energy up to the level of the minimum in moist static energy. Above this level ducted "chimney" or "hot tower" ascent is required. However, even this "hot tower" mechanism, when constrained by the known mass recycling rate, does not transport enough heat vertically. Downdraughts are required to bring potentially colder air down to the surface so that the moist static energy of the air at low levels is increased by evaporation and heating. Riehl and Malkus originally suggested that convective downdraughts fulfilled this role but Kamburova and Ludlam (1966) showed that such near-saturated downdraughts could only be maintained when an intense rainfall rate and small size drops occurred in a weak downdraught. Later observations were to show that unsaturated downdraughts covered large areas in tropical clusters and were associated with light, stratiform precipitation.

A series of budget studies, including those by Gray (1973) and Yanai et al (1973), highlighted the importance of sub-synoptic disturbances in balancing the budgets of mass, water vapour and energy in the summer oceanic trade wind belt (5-25°N). The upward transport of water vapour in the lower levels of precipitating cloudy regions is achieved mainly by the sub-synoptic circulation. Gray estimates that a vertical "up-moist but down-dry" circulation of about 36Cmbd^{-1} was required at the subcloud level. Although the net mass transport by his "local" circulation is zero, at each level the upward transport of water vapour by cumulonimbi is greater than the downward transport between them. The tropical energy budget requires transports one or two orders of magnitude larger than the mean upward motions.

The latent heat released from cumulonimbi does not go directly into increasing the environmental temperature; residual cloud liquid particles around the cumulus, detrained or mixed out, tend to produce net cooling. Dry adiabatic sinking must occur at some other location, and on a generally larger scale to compensate the upward mass transport. Thus on average a warming of the environment is achieved.

In addition to transporting heat and moisture, deep convection also modifies the vertical distribution of horizontal momentum. Houze (1973) compared the vertical transports of angular momentum by convective cell-scale and meso-scale processes with the large scale and total required eddy fluxes. He found cumulus transports of angular momentum became comparable in magnitude to large scale fluxes in climatologically predictable regions and seasons, confirming the importance of these circulations in the transport of momentum.

Realistic parameterisations of heat, moisture and momentum due to convective processes are important in large scale numerical weather prediction. In particular we need to understand the impact of mesoscale organisation of convective processes. Such systems, as will be illustrated in the next section, dominate weather patterns in the tropics and are not uncommon in middle and high latitudes over oceans in winter. With the recent development of mesoscale meteorology, it is necessary to quantify the dynamics of mesoscale transport systems, so that transport processes can be incorporated in large scale models as flux laws. In particular it is preferable that cloud-scale fluxes of heat, momentum and moisture be in terms of properties of the large scale environment:- wind shear, stability and large scale fluxes.

1.1.2 The Grouping of Cumulonimbi into Clusters and Classification of Type by Dynamical Regime.

Daily satellite weather pictures became available over the tropical ocean in 1966 with the launch of the ESSA weather satellite. It quickly became apparent that convective cores, although ranging widely in size, spacing and lifetime, were frequently ordered into bands (Martin and Suomi, 1972); solitary cores and wave or spiral patterns were much less common. This concentration of convection was named a "cloud cluster"; a group of cumulonimbi joined in their mature and dissipating phases by a common cirrus shield between 100 and 1000km in horizontal dimension (ICSU/WMO). Satellite data studies (eg. by Williams and Gray, 1973; Martin and Suomi, 1972; Frank, 1970 and Aspliden et al, 1976) showed clusters occured in great numbers over the tropical oceans, providing a means of protected undilute ascent on a large scale as postulated by Riehl and Malkus.

The observational description of the "cloud cluster" became an objective of one of the GATE convection subprograms (Betts, 1974). Betts speculated that cluster transports may be controlled by the degree of organisation within the cluster. This in turn may depend on the synoptic conditions (wind shear, moisture availability etc). Hence any parameterisation of cumulonimbus transports within clusters must take into account the type of cluster occurring in a particular set of conditions. It was hoped that a large number of cluster case-studies could be made during the GATE to compute budgets typical of different classes of cluster.

A radar study of the distribution of precipitating echoes observed during the GATE by Houze and Cheng (1977) emphasised that although few

in number (8% of all echoes observed) the B/C scale (cloud cluster/mesoscale of area 10^3-$10^5 km^2$) accounted for 79% of the total echo area. By contrast the numerous C and D scale echoes (meso/cumulus scale of area 10^0-$10^3 km^2$) which were 92% of the total accounted for only 5% of the total area. The large B/C scale echoes tended to have a greater mean height and lasted longer. Higher intensity and multiple cores occurred most often in echoes exceeding an area of $500 km^2$. The larger echoes typically moved in the direction of the 850mb wind - unlike small echoes which moved more erratically.

Within mesoscale radar echo patterns Cheng and Houze (1979) examined the intensity and distribution of precipitation. They found that more than 40% of the total precipitation detected during the GATE fell in generally uniform, slowly varying regions of large radar echoes. This "mesoscale" rain falls mostly from large anvil clouds, is less intense, but covers a larger area and is more persistent than rain in actively convective portions of these systems. The convective precipitation fell from convective cores which occurred in larger echoes coexisting with the "mesoscale" rain areas - or from isolated smaller echoes with an area of less than $100 km^2$.

Maximum rainfall rates occurred for systems with cloud tops near 12km. A large number of tops were as high as 15-16km, produced by overshooting on occasions when the level of zero buoyancy rose to 14km. This study associated mesoscale rain and strong overshooting with synoptic scale ascent - suggesting that mesoscale system development may be predictable.

Betts (1974) also suggests that the classification of clusters would be aided by the development of analytic dynamical models in

which specific dynamic regimes are related to large scale parameters such as the Richardson number in Moncrieff and Green (1972), (hereafter MG). By this means the cluster type could be simply specified by the large scale conditions.

The cloud-scale dynamics of the most highly organised cluster, the "tropical squall line", has already been tackled by Moncrieff and Miller (1976), hereafter MM, in a model which treats only convective circulations. There is now a large body of evidence to suggest that unsaturated downdraughts on a larger horizontal scale play an important role in the thermodynamic transformation of the tropical atmosphere by tropical squall lines and other less well organised clusters.

This thesis will explore a number of analytic models which are suggested by the observations and numerical experiments described in this chapter.

1.1.3 The Transformation of the Environment by Clusters.

What information would we like from observations in order to test a numerical or analytic model?

In an ideal explicit numerical model of a squall line initiated with the pre-squall fields of velocity, humidity, temperature and other variables the dynamics of a squall line and its interaction with the large scale fields could in principle be simulated. However, this pre-supposes a closure scheme for the convection and large scale interaction, and a suitable parameterisation for convective processes in a model which has a horizontal grid spacing of order 10km.

Very little is known of the interaction mechanisms, but some

dynamical insight can be gained through the use of idealised analytic models. The large amplitude nature of squall line dynamics and environmental response suggests that a small amplitude or perturbation approach will not succeed. However, the quasi-steady nature of the squall line circulation allows a considerable amount of analysis to be performed.

A general large amplitude method was developed by Green and Pearce (1962), MG and MM, in which an equation for the displacement of parcels of air can be obtained. The transports and dynamical structure may then be elucidated. The analytic models to be presented in this thesis are based on solutions to these displacement equations, ie. the height of an outflow streamline as a function of the inflow height.

Moist static energy is often chosen as a tracer variable since it is conserved in moist processes. However as mentioned earlier, the tropical atmosphere shows a minimum in the vertical profile of moist static energy; it is not single-valued. The origin of air with a given moist static energy cannot be uniquely determined. In addition these profiles are usually quite noisy in undisturbed conditions and rather smooth in post-squall conditions. This is evidence that turbulent mixing has occurred - and the noisy pre-cluster profile may indicate considerably more than two possible levels of origin for air with a given moist static energy.

In assessing how well a model represents the dynamics of a circulation and its transport processes, we would like to know how energy is partitioned between heating, doing work against a pressure gradient and generating kinetic energy. Horizontal velocity can be

obtained observationally as a function of height but it is difficult to obtain reliable observations of pressure apart from at the surface. The heating is measured as a change in moist static energy. Unfortunately without knowing the level of origin of air it is not possible to work out this partitioning. Pre- and post- disturbance profiles of the horizontal components of the wind field can only be studied for general trends.

In modelling convective processes and thermodynamics in particular, updraught and downdraught lapse rates are required. The updraught lapse rate can be calculated with relatively little difficulty from dry and dew point temperature profiles for pre-disturbance conditions. The downdraught profile is much more difficult to determine because the process cannot be initially specified (as will be illustrated in section 1.4 on theoretical modelling) because descent usually occurs with a degree of subsaturation. It would be useful if more observational and diagnostic results were available for obtaining the downdraught depth, lapse rate and potential energy hence allowing a more suitable parameterisation of the evaporation process. Very little work has been done on this problem contrasting with the large amount of cloud physics research into condensation mechanisms.

Linked to the problem of unknown downdraught lapse rate is the unknown downdraught available potential energy. This bulk property may be important in predicting the propagation speed of the downdraught outflow.

Observational studies such as that undertaken by Gamache and Houze (1982) can produce fields of horizontal divergence. This enables the

one dimensional horizontal divergence field produced by the analytic model to be examined for consistency. Vertical velocity can only be reliably measured by aircraft flying through the system - and for reasons of safety this can only be achieved by special aircraft in disturbed parts of the cluster. Dual-Doppler radar can represent the trend in vertical velocity reasonably well by vertically integrating the horizontal divergence field. Absolute values cannot usually be determined.

Budget and composite studies have been available in greater numbers and for longer than individual case studies. They are useful because the smoothed profiles bring out the grosser features and overcome the problem of "noisy data" - although with the loss of finer detail.

Sections 1.1.3.1 to 1.1.3.4 will deal with budget descriptions of transformations effected by tropical clusters; differences between squall and non-squall clusters will be discussed and squall clusters occurring over land and ocean will be compared. Features of squall clusters will be dealt with in section 1.2. The results of some numerical modelling experiments will be reviewed in section 1.3 and theoretical models for forced downdraughts summarised in section 1.4.

1.1.3.1 Thermodynamic and Dynamic Transformations of the Environment from Budget and Composite Studies.

Both squall and non-squall clusters thermodynamically transform the environment in a similar manner, although to a different degree. For this reason observations of both types of cluster are considered together.

All clusters act to cool the atmosphere at low levels; below 800mb the dry static energy ($s=C_pT + gz$) falls (Fernandez, 1980; Miller and Betts, 1977 and Betts, 1976). Changes in dry static energy at upper levels seem to be more variable, but there is a tendency for warming between 700 and 800mb.

Moist static energy falls at low levels (below 700mb) and increases at upper levels (Fernandez, 1980; Miller and Betts, 1977; Mansfield, 1977; Betts et al, 1976 and Betts, 1976). Since it is a conserved property in moist displacement a change in value means air has been transported there from a different level. The fall in moist static energy at low levels indicates that descent of air from near the mid-level minimum has occurred. The increase at upper levels suggests either descent from high levels, which is unlikely, or ascent from the subcloud layer where the moist static energy is larger. The most likely origin is the subcloud layer since convective updraughts transport air from the subcloud layer to the level of the tropopause.

Changes in mixing ratio are consistent with trends seen in moist static energy (an increase near the surface) thought to be due to saturated downdraughts (Fernandez, 1980; Gray et al, 1975; Nitta, 1977; Miller and Betts, 1977 and Betts, 1976). The low level moistening is not seen in the profiles published in Betts et al (1976), or Mansfield (1977). There may be a problem of resolution in the case of Betts et al but the Mansfield curve shows no sign of increasing mixing ratio near the surface.

The layer between 700 and 800mb is frequently replaced by warmer drier air of lower moist static energy ie. a warm unsaturated downdraught produces a relatively stable layer. Near the surface a

cooling and moistening frequently occur suggesting a saturated downdraught mechanism; this suggests that two distinct types of downdraught exist in the rear of tropical squall clusters, namely warm dry descent overlying a layer of moist cool descent - "mesoscale" and "cloud" scale downdraughts respectively. This thesis is primarily concerned with the dynamics of the warm unsaturated downdraught which suppresses convection so effectively in the wake of a cluster.

The modification of the horizontal windfield is easily measured, although it is less easy to interpret the transport processes affecting these changes. Pre-squall profiles show relative inflow at the front in both squall and non-squall types of cluster. Most clusters show relative outflow at the rear at all levels. Venezuelan squall lines however are a notable exception, although it is not clear at what stage in the life of a cluster that relative inflow occurs.

Most clusters go through growing, mature (or conservative) and dissipating phases. The circulation of the mature phase is the primary concern of this thesis. Most composites taken include all three phases which makes a clear specification of inflow and outflow in the mature phase impossible.

Fernandez (1980) notes that the two-dimensional velocity profile indicates mass imbalance, implying the circulation must be three-dimensional. This is a feature which is brought out more strongly in individual case studies.

Cluster motion appears to show no directional preference relative to the mean wind. All clusters move much faster than the mean wind, and Fernandez (1980, 1982) finds the magnitude of the mid-level jet is a good predictor for cluster speed.

1.1.3.2 Subcloud/Cloud Layer Transformation from Budget Studies.

Several models of increasing complexity are used by Betts (1976) to describe composited Venezuelan cluster data. Essentially the subcloud layer ascends in updraughts and is replaced by air from immediately above, the descent being a result of the evaporation of precipitation in moist downdraughts. The calculated pressure depth of each of the two layers (assuming conservation of mean moist static energy as the air descends in downdraughts) correlates closely with the depth of the subcloud layer.

A net cooling and drying is observed which must result from two competing processes; evaporation of precipitation producing cooling, and descent of potentially warm air. A more detailed consideration of the moist static energy profile suggests that air found finally near the surface has descended from some distance above cloud base, while air found higher in the subcloud layer has not descended as far (ie. overturning has occurred).

A study of updraughts and downdraughts during the GATE revealed that such motions due to tropical convective cloud extend to near the ocean surface and exhibit a variety of characteristics (Emmitt, 1978). 81% of all updraughts and downdraughts were either warm/moist or cold/dry. (Cool/moist and warm/dry draughts were also observed.) Energy transports for cold dry downdraughts were as strong as those for warm moist updraughts, again emphasising the importance of sub-saturated forced descent. This forcing of the subcloud layer structure by downdraughts from the cloud layer is also stressed by Echternacht and Garstang (1976) in a study of changes in the structure of the tropical subcloud layer during BOMEX using a tethered balloon

system. In undisturbed conditions, cloud/subcloud layer coupling is restricted to regions between the top of the mixed layer and cloud base.

Barnes and Garstang (1982), in a study of the thermodynamic modification of the subcloud layer in GATE, relate the precipitation rate to the change in moist static energy in the subcloud layer. A mean precipitation rate of approximately $2mmh^{-1}$ divides situations in which specific humidity increases from those in which it decreases. (A temperature decrease always occurs.) In light rain the fall in temperature in the subcloud layer is almost entirely accounted for by evaporation, so the moist static energy does not change. In heavy precipitation the fall in moist static energy in the subcloud layer may be quite large (as much as $11kJkg^{-1}$ in previously undisturbed conditions). Where conditions were previously highly disturbed there may be as much as a 60% reduction in net energy transport for a precipitation rate between 2 and 20 mmh^{-1}.

A travelling convective system which can draw upon "fresh energy-rich air" in a deep layer will maximise the energy transfer in the surface layers. A stationary system is more likely to have to work in its own modified environment unless there is a large relative wind into the system.

A line arrangement of cumulonimbi is more efficient for the vertical transport of energy in the lower atmosphere than a similar area of disordered convective cells. For these reasons a tropical squall line is an ideal processor of air in terms of motion, size and organisation.

1.1.3.3 Differences Between Squall and Non-Squall Clusters.

In a comparison of squall and non-squall clusters occurring during VIMHEX it appears that the magnitude of the shear in both subcloud and cloud layers is greater for the non-squall cluster. Also the height of the mid-level jet is lower for the squall cluster than for the non-squall cluster (Fernandez, 1980).

Latent heat content and dry and moist static energies all show larger changes (following a similar trend) for squall clusters than non-squall clusters. Non-squall clusters show dry static energy increasing near 425mb although it is not clear how this change can be interpreted.

The non-squall clusters studied by Fernandez tended to show relative outflow at all levels to the rear whereas squall clusters had relative inflow at the rear between 950 and 675mb.

Six mesoscale precipitation features comprising a tropical cluster on 5 September 1974 during the GATE, with lifetimes varying between 8 and 24h, and whose horizontal dimensions varied between 190-580km, were studied by Leary and Houze (1979a). They developed a prototype for the life-cycle and structure of a mesoscale precipitation feature sufficiently general to describe both squall and non-squall structures. In essence a mesoscale precipitation feature develops from several isolated convective cells aligned perpendicular to the wind in a region of convergence. Such a configuration favours the development of new cells between and upwind of existing cells, where outflow from convective-scale downdraughts enhances low-level convergence. In this way the cumulonimbus cells propagate upwind relative to the surface flow. Slowly dissipating cells to the rear

lead to the development of a large area ($10^4 km^2$) of lighter, horizontally uniform precipitation.

1.1.3.4 Differences Between Squall Clusters Occurring over Land and Over Sea.

Fernandez (1982) also compares squall lines travelling over land (West Africa) with those travelling over the sea (the Eastern Tropical Atlantic). Although it may seem to be a simple comparison there are many pitfalls; for example Venezuelan squall lines have rather different characteristics from those in West Africa, with relative inflow at the rear in the former case but not in the latter. The properties which are changed by the surface composition must not be confused with those arrising from differences in the wind field.

In the cases examined by Fernandez (1982), three over West Africa and three over the Eastern Tropical Atlantic, on average the land squall lines lasted longer (40h cf. 10h), were of greater length (750km cf. 350km) and had greater buoyancy on lifting to 500mb ($\Delta T \sim 5.4K$ cf. $\sim 2.4K$). Their convective available potential energy (CAPE) was larger ($2093 Jkg^{-1}$ cf. $930 Jkg^{-1}$), had larger mixing ratio in the subcloud layer ($18.6 gkg^{-1}$ cf. $15.0 gkg^{-1}$) and had higher lifting condensation levels (LCL's). Both sets had the same average propagation speed however of $15 ms^{-1}$!

Over the land, greater drying occurred (ie. to 870mb cf. 950mb over the ocean), changes in moist static energy were larger, and the fall in latent heat content was greater. Easterly momentum increased over a much deeper layer for the squall lines travelling over land.

These differences are only ones of degree on the whole and are

probably the combined result of different moisture and wind profiles. In particular, the surface layer is important in the recovery of the boundary layer after the squall has passed. The sea surface transfers of heat and moisture tend to recover far more quickly than those over land (since the sun can only start reheating the surface during daytime when intervening cloud has cleared).

1.2 Structure of Squall Clusters from Observational Studies.

Composite studies reveal that the tropical cluster is an efficient transport mechanism in the tropical atmosphere, taking potentially warmer, moister subcloud layer air up to the high troposphere in cumulonimbus updraughts and replacing it by potentially cooler, near saturated air. Above this surface layer air has been forced to descend from the region of mid-tropospheric minimum in moist static energy, producing substantial warming and drying beneath a precipitating anvil cloud.

The following section summarises case studies of squall clusters including some of the finer detail of structure and behaviour.

1.2.1 Squall and Anvil Region Distinguished in the Windfield.

A three-dimensional view of the wind field in the vicinity of a squall cluster was obtained by compositing all observations over a period of nine hours during which features of dimensions in excess of 100km remained steady (Gamache and Houze, 1982). The front edge of the arc cloud which marks the forward edge of the advancing updraught was used as a reference. In this study two regions with quite different rain types were distinguished:- the squall line region

occupied by convective cumulonimbus towers producing high rainfall rates, $>14mmh^{-1}$, and behind the squall line, a region of light uniform stratiform rain beneath an anvil cloud, $<14mmh^{-1}$. The schematic cross-section, figure 1 in Gamache and Houze (1982), is reproduced in figure 1.2.1.

The surface wind relative to the system at the front of the squall line region was $12-15ms^{-1}$. Relative inflow at the front at all levels was also reported by Houze (1977) and Zipser (1977). Fortune (1980) could not resolve winds sufficiently to examine this but any relative inflow was very small. Within the squall line region the near surface flow decreased to zero, implying ascent. Behind the squall line flow was from front to back of the anvil with a brief reversal of direction behind the gust front. This represents the spreading convective downdraught flowing outwards at the surface. The squall line coincided with a line of convergence (corresponding to ascent in the cumulonimbus towers) while the anvil region was horizontally divergent.

At 800mb air still strongly entered the squall line region from the front and also weakly from the left end and left rear. The flow from the end and rear must be taking part in the convective circulation - ascending or descending. Feeding of the convective downdraught in large part from the sides is also reported in Houze (1977).

At 650mb there is inflow into the anvil from the rear of the system, with a cyclonic vortex in the anvil region and convergence. Air flowing into the back of the anvil region in middle levels (800-400mb) is also reported by Fortune (1980), Houze (1977) and

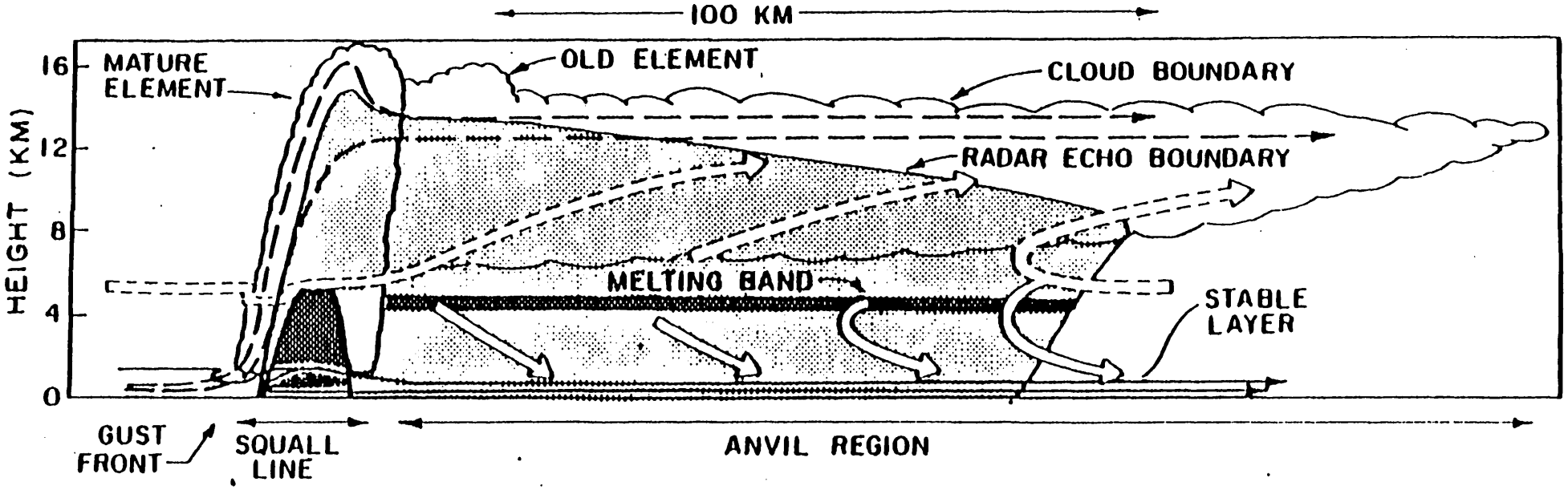


Figure 1.2.1. Schematic cross-section through squall system. Associated with the mature squall-line elements, dashed streamlines show convective-scale updraught, solid streamlines show downdraught circulation. Associated with the trailing anvil, wide solid arrows show mesoscale downdraught circulation, wide dashed arrows show mesoscale updraught circulation. Dark shading shows strong radar echo in the melting band and in the heavy precipitation zone of the mature squall line element. Lighter shading shows weaker radar echoes. Scalloped line indicates visible cloud boundary. (From Gamache and Houze, 1977)

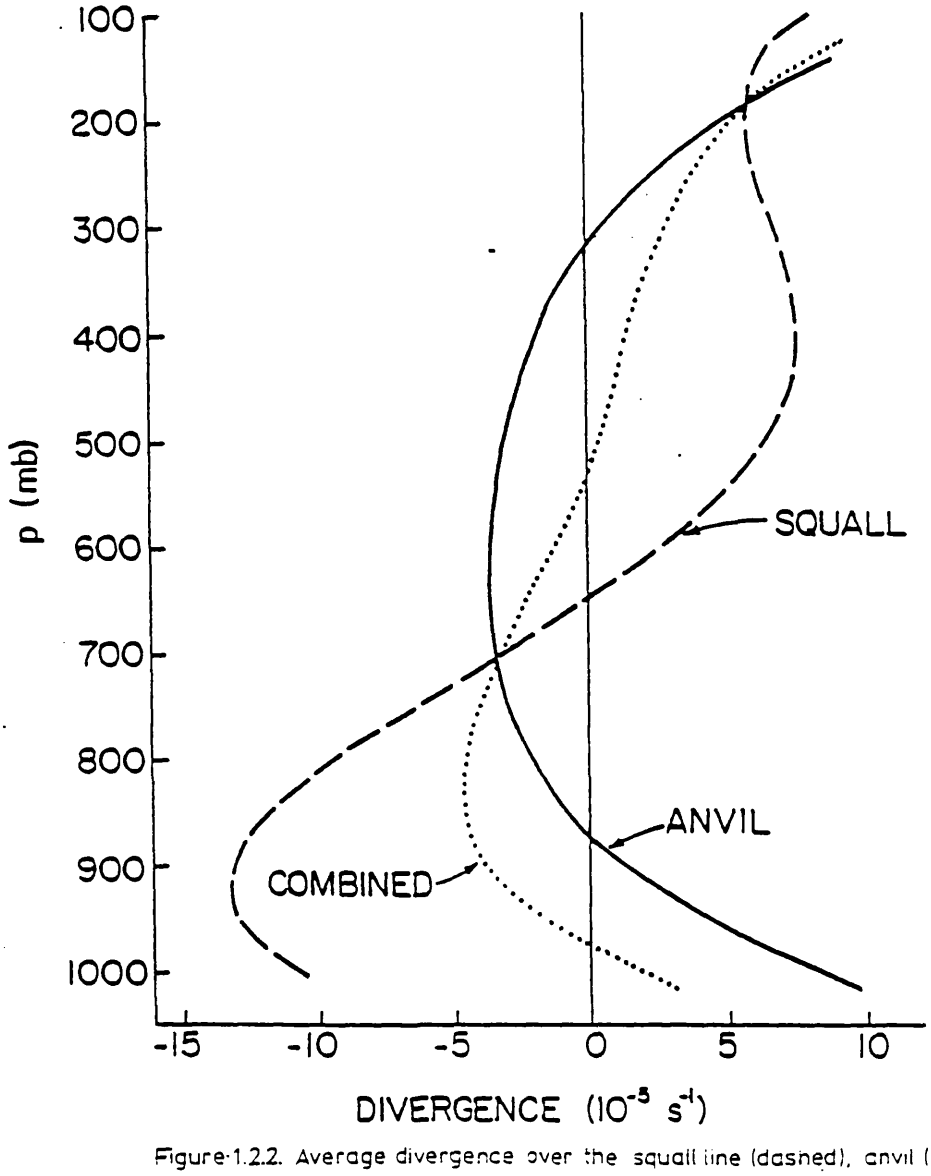


Figure 1.2.2. Average divergence over the squall line (dashed), anvil (solid) and combined (dotted) regions.

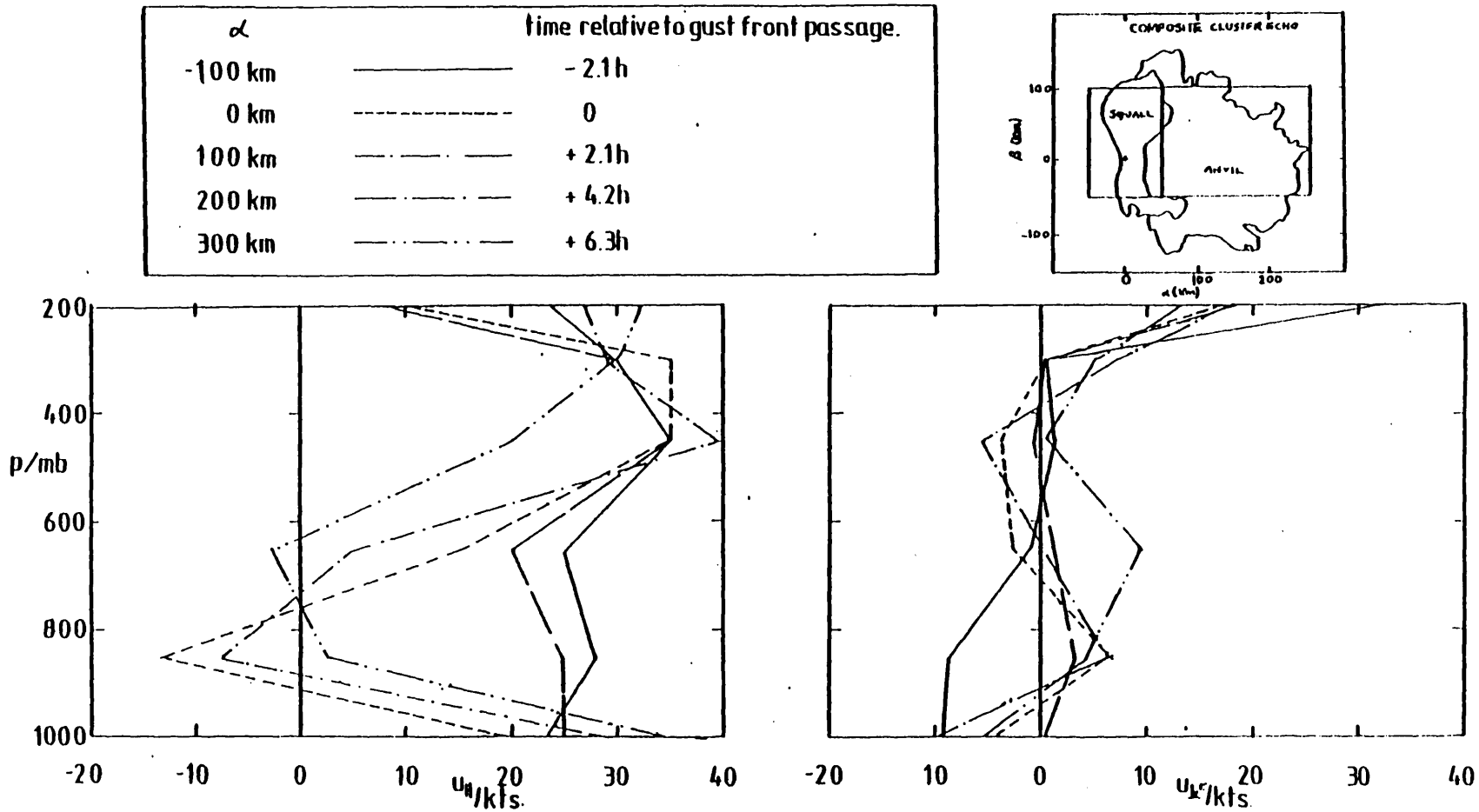


Figure 1.2.3 Relative wind profile sequence parallel and perpendicular to the direction of squall cluster motion for the 12 September 1974 during the GATE.

Zipser (1977). Flow from ahead of the squall line apparantly goes straight through to the anvil region and is decelerated - an observation consistent with ascent or descent at anvil base.

At 450 mb flow in the squall line region is diffluent indicating flow through the squall line is of fairly uniform speed and direction. There is divergence in the squall line region and convergence to the rear in the anvil region. At 300mb the flow is similar, becoming non-divergent in the anvil region (area average) and divergent in the squall and pre-squall regions.

At 200mb flow is from left front to right rear of the system, and diffluent especially in the anvil region with divergence increasing towards the rear.

The vertical profile of horizontal divergence calculated for squall line and anvil regions separately shows different behaviour in each case. Figure 12 from Gamache and Houze (1982) is reproduced in figure 1.2.2. The squall line region profile shows convergence up to 650mb and divergence above 600mb. These two regions correspond respectively to air entering convective updraughts and downdraughts (below the mid-tropospheric minimum in moist static energy at 650mb) and divergence and spreading in the convective updraught outflow which is strongest at 200mb, the tops of the deepest cells. The non-divergent flow at around 600-700mb corresponds to air which has flowed straight through to the anvil region between the cumulonimbus towers of the squall line.

The profile for the anvil region shows convergence in middle-levels (800-400mb) with strong divergence above and below. Other workers such as Martin and Sikdar (1979) who calculated

divergence over the entire cluster obtained a net divergence in the high troposphere (250mb) and diffluence near the surface - the latter being a result of divergence beneath the anvil and convergence beneath the squall line.

The profiles of vertical velocity calculated from the horizontal divergence (assuming w(1000mb)=0, w(100mb)=0 for the squall line region, w(150mb)=0 for the anvil region) show ascent everywhere within the squall line region. The anvil region however has descent below 600mb (peak value 9cms^{-1}) and ascent above (peak value 15cms^{-1}).

Profiles of vertical velocity calculated from the divergence of the horizontal velocity field must always be treated with some caution. Within the anvil region there are as few as three observations at 300mb and five at each of the 450 and 650mb levels. There appear to be sufficient observations at the surface and 850mb levels, 17 and 18 respectively within the anvil region, to suggest that the lower level descent has been clearly demonstrated. From the gridded data produced by Gamache and Houze for six pressure levels I extracted a time sequence of vertical profiles of horizontal velocity parallel to the direction of propagation. Sections at +50km, 0 and -50km "β" all showed the same trend at lower levels in the anvil region. The sequence at 0km "β" is shown in figure 1.2.3. The velocity profile between the surface and 850mb shows westerly acceleration of the low level flow from 100 to 300km behind the gust front. The acceleration at one level between successive profiles shows velocity increases of 5-10kts. Since these are extracted from gridded wind barbs which give velocity to 2.5kts and 5-10° an acceleration of air at low level towards the rear of the system seems to be occurring.

Ahead of the squall line weak descent occurs in the lower troposphere with stronger downward motion aloft. The downward motion at 350mb is believed to be a response to the intrusion of convective updraught air into the upper troposphere, ie. compensating subsidence in the pre-squall region.

1.2.2 Downdraught Structure deduced from Thermodynamic Changes.

In the 16 April 1968 Barbados squall line described in Zipser (1977) the changes in wet-bulb potential temperature (θ_w) corresponding to the differently transformed air masses were well marked. Figure 3 from Zipser's paper is reproduced here in figure 1.2.4. In the pre-squall air at the 150m level θ_w falls from 23.5°C to 21-22°C in the cool, near-saturated, heavy rain area, and then to 19-20°C between 25 and 40km behind the squall line in relatively warm dry air ($\Delta T \sim +4K$). This relatively warm dry air must originate above 750mb where air with θ_w in the range 19-20°C is usually found and must have descended in unsaturated downdraughts. Further behind the squall line there is an irregular alternation between air with θ_w in the ranges 19-20°C and 20-22°C - linked to heavier rain release from the anvil.

The lower part of the anvil region contains a well mixed layer between 150 and 400m ($\theta_w \sim 21.5°C$); above it is a strongly stable layer. Between 1000 and 2000m θ_w is $\sim$19°C. The lower and upper layers correspond to convective (saturated) and mesoscale (unsaturated) downdraughts respectively. In the moderate to heavy rain areas the relative humidity is less than 50% emphasising the unsaturated nature of the widespread downdraughts.

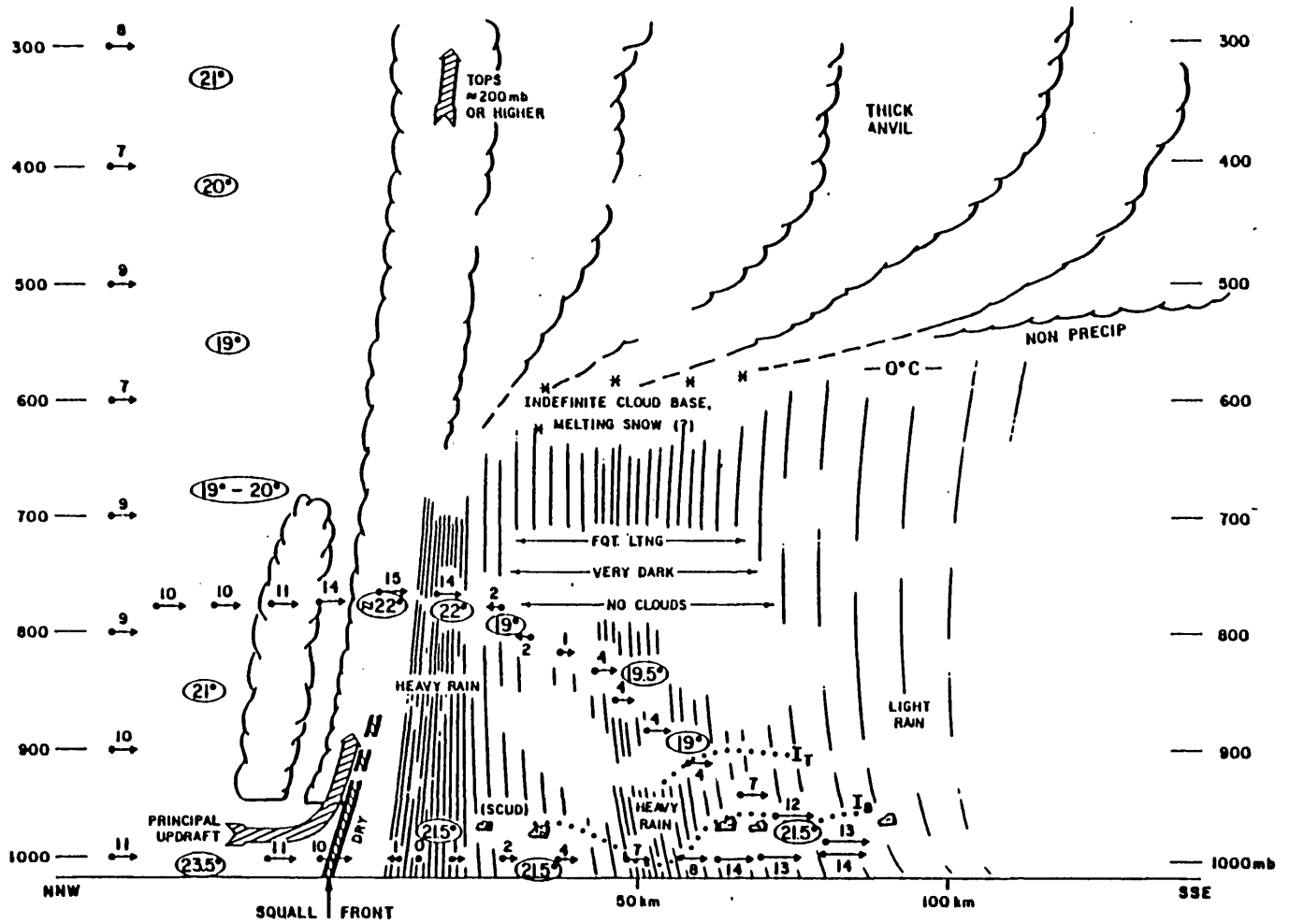


FIG. 11 Cross section through 18 August 1968 squall line near aircraft track indicated in Fig. 1. Flow relative to the squall measured by the aircraft (m s^{-1}) is indicated alongside aircraft track by horizontal arrows. Circled numbers are θ_w in °C. Relative winds and θ_w from the composite pre-squall sounding (Fig. 2b) are shown along the left-hand margin. The dotted lines mark estimated locations of stable layer base (l_B) and top (l_T).

Cool near-saturated air found by surface measurements indicated that warm, dry air did not penetrate to the surface without mixing. The percentage of unsaturated air was greater with altitude and with the age of the system.

Soundings taken over the water showed a mixed layer varying between 50 and 500m in depth. Over land no mixed layer was detected - since the heating from below had not restarted.

Wet-bulb potential temperature and latent heat content were both observed to decrease below 800mb in Houze (1977) corresponding to low level outflow whilst both increased above 500mb in the upper level outflow. Houze estimated that a section 200km long was characterised by downdraughts extending from mid to lower troposphere. Fortune (1980) similarly found air of low wet-bulb potential temperature (328K) above the surface - which is more usually found in the 600-800mb layer. In Zipser (1969) air with an equivalent potential temperature (θ_e) of 330K must have descended from between 500 and 700mb to a level of about 850mb in unsaturated downdraughts. This evidence of descent again coincides with steady rain from middle level clouds. Updraught outflow air above 500mb had θ_e in the range 338-343K indicating mixing had occurred with lower θ_e environmental air since within the pre-squall subcloud layer θ_e was ~350K.

A massive downdraught, similar to that described by Zipser (1969), occurs in Martin and Sikdar (1979). The surface layer between 25 and 50mb deep was relatively colder and moister than the layer between 700 and 950mb. Above this was a deeper layer of warmer drier air which had been transported downward in unsaturated downdraughts from the exceptionally dry layer between 700 and 800mb.

The thermodynamic changes strongly indicate descent is occurring in near-saturated convective downdraughts under the squall line and in unsaturated mesoscale downdraughts beneath the anvil cloud from the mid-tropospheric minimum in moist static energy.

1.2.3 Surface Pressure Changes.

The surface pressure frequently rises with the onset of rain, a consequence of the large depth of cold saturated air and perhaps the nonhydrostatic effect of deceleration. Zipser (1977) reports pressure rises of between 0.1 and 2.5mb. Houze (1977) reported a 1mb rise in pressure. The pressure may fall later (-0.3 to -3.7mb was reported in Zipser, 1977). The meso-low is believed to be associated with warm dry air at low levels and occurs between 3 and 5h after the squall corresponding to 150 to 250km.

Johnson and Nicholls (1983) composited all available surface and subcloud layer data with respect to the gust front of the 12 September 1974 GATE squall-line for which Gamache and Houze (1982) produced composited wind fields in a similar fashion. The composite surface pressure and 900mb relative humidity fields (figures 9 and 11 from Johnson and Nicholls, 1983) are reproduced in figures 1.2.5 and 1.2.6. The pressure rises by 2mb with the arrival of the squall line and falls again over the same space scale of 50km by 2mb. The surface pressure then continues to fall by another 2mb over a horizontal length scale of 300-400km extending nearly 200km behind the radar reflectivity contour (corresponding to the rainfall zone). The minimum relative humidity (50%) at 900mb coincides with the minimum surface pressure suggesting a much larger scale for the "mesoscale" response than that of the rain area.

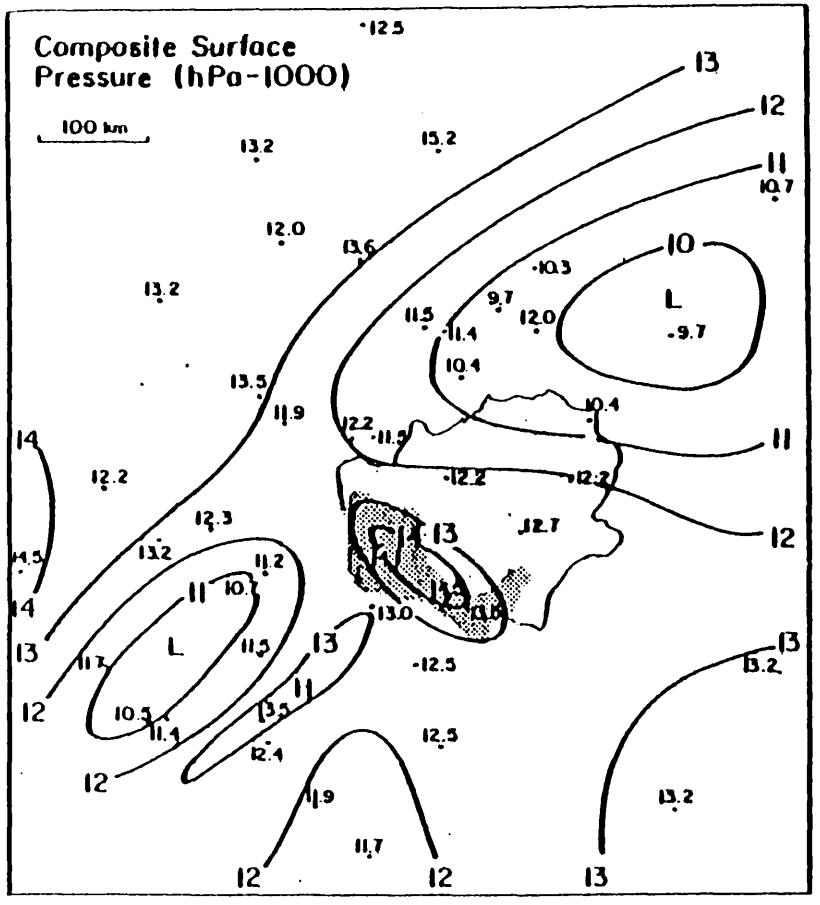


FIG.12.5. Composite surface pressure (minus 1000 hPa). Semi-diurnal pressure oscillation has been removed.

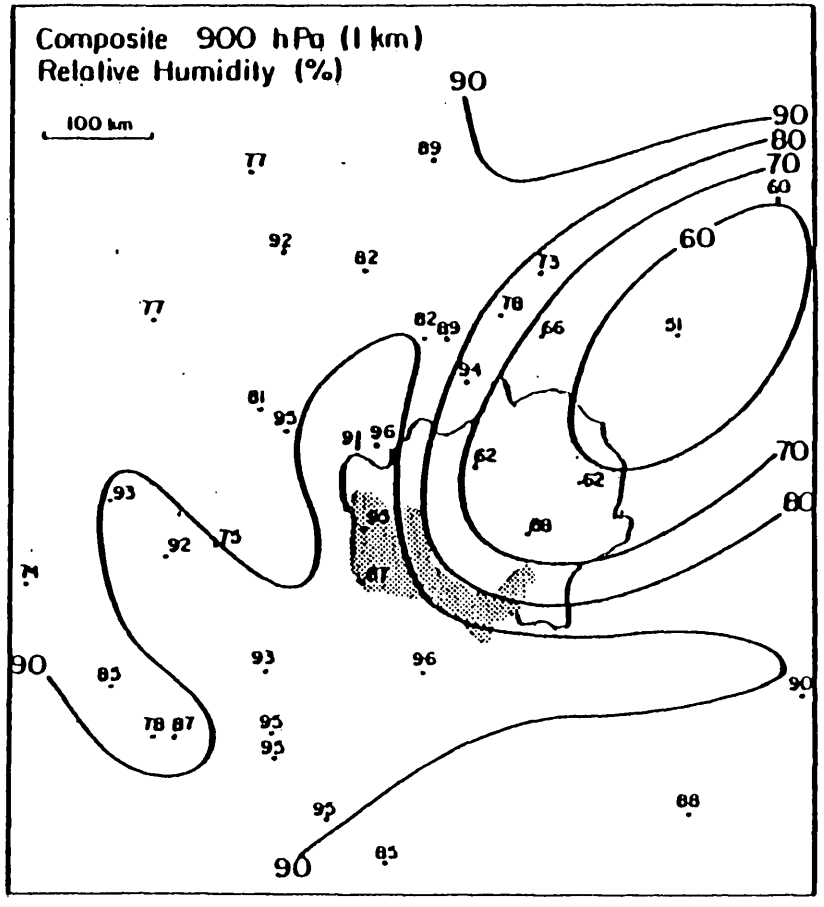


FIG.12.6. Composite 900 hPa (~1 km) relative humidity (%).

1.2.4 Squall Line Structure.

The convective squall line contains cumulonimbus in various stages of growth. Houze (1977) reports that 21 convective cells or line elements were tracked for the particularly vigorous 4-5 September 1974 squall line which passed through the GATE area. New line elements formed at or ahead of the leading edge of the arc cloud; old line elements dissipated at the rear, their remnants becoming part of the anvil cloud from which light rain fell. Line elements became elongated along the length of the arc cloud, a typical dimension being 65X30km^2 in this case. The curvature of the forward edge of intense echo of the line element corresponds to the convective downdraught of the cell and is much greater than that of the arc cloud. This would suggest that the convective downdraught is not a candidate for explaining the high degree of organisation in the squall system, although the downdraught is important for causing low-level convergence which is important in initiating new cells.

Line elements were fed strongly at low level from ahead. Houze suggests that the updraught slopes backwards in the vertical as it rises over the convective downdraught. Flow into the convective downdraughts, as previously mentioned, was predominantly from the sides.

Most of the abrupt changes in surface measurements of dry and wet-bulb temperature and pressure were the result of line elements passing over measuring instruments so that use of surface pressure tendency, for example, in testing a model should be made with caution.

Such changes may not be representative of the mesoscale forcing.

1.2.5 Anvil Structure.

The first few hundred kilometres behind a squall line are occupied by an anvil cloud. Cloud base is usually at around 650-600mb (Gamache and Houze 1982, Zipser, 1977). Just behind the convective cells the anvil may be 6-10km thick tapering to transparant cirrus at perhaps 350km (Zipser, 1977). Rain extends for approximately 100km behind the squall line. Below the anvil base there is very little low cloud.

In five cases of anvil precipitation associated with intense convective cells, Leary and Houze (1979b) detected a radar bright band below the level of the 0°C isotherm. This was also reported in Houze (1977). Above the bright band the anvil is composed of ice crystals whose reflectivity increases lower down as they grow and aggregation occurs in the saturated anvil. Reflectivity increases more sharply as the ice crystals melt and then decreases as the raindrop fall speed increases compared with ice crystal fall speed. Reflectivity falls further below the bright band as raindrops evaporate as they fall into unsaturated air.

The narrowness of the bright band and its horizontal uniformity confirms the absence of convective updraughts and downdraughts which would either have prevented the fall of ice particles to the 0°C isotherm or spread the melting over a broader layer. The absence of hail (which only forms in strong updraughts) further emphasises the lack of convection. Leary and Houze suggest that the hexagonal graupel present above the melting layer, which would produce the observed reflectivity profile, implies a high density of supercooled

cloud liquid water aloft. Freezing would thus generate heat, producing mesoscale uplift in this region.

Leary and Houze estimated that approximately 25% of the liquid water between 0.5 and 2.5km was lost to evaporation beneath the melting layer producing low level cooling rates of several degrees per hour and thus contributing to the maintenance of a mesoscale downdraught.

1.2.6 Vertical Velocities and Mass Fluxes.

The importance of the mesoscale downdraught is recognised when its mass flux was found to be six times that of a large intense mid-latitude thunderstorm in Martin and Sikdar (1979). Fortune (1980) estimated that the mass transported by all downdraughts within a squall line was 1/10 to 1/3 that of the mass entering the anvil from convective updraughts. This transport would have to be incorporated into any cumulus parameterisation scheme hoping to calculate momentum and moisture transports.

Descent beneath the raining anvil is generally accepted to occur. A number of workers give estimates for its magnitude:- $10cms^{-1}$ at 500m over a 150km diameter (Zipser, 1977), $6cms^{-1}$ at 900mb and $10cms^{-1}$ at 800mb by Zipser (1969), a peak value of $6cms^{-1}$ below 600mb (Gamache and Houze, 1982).

Althought the existence of ascent in the anvil has been suggested by a number of studies, the only published calculation of vertical velocity within the anvil has been made in Gamache and Houze (1982) where a peak upward value of $15cms^{-1}$ at 350mb was diagnosed. However since the profile of vertical velocity is calculated from the

horizontal divergence field constrained by w=0 at 1000mb and at 150mb some caution in using absolute values must be employed.

1.2.7 Features Important to Mesoscale Circulation Dynamics.

In subsequent chapters the dynamics of the forced post squall circulation will be explored through a series of analytic models. In extracting information from observations it is difficult to avoid giving undue emphasis to features which are easily measured eg. surface pressure rise coinciding with the arrival of the convective downdraught and the concurrent heavy rainfall.

The main mesoscale features are the convective updraught - which eventually forms the anvil cloud, and the mesoscale unsaturated downdraught. The convective downdraught is often difficult to distinguish in observations and is ill-defined in terms of origin and displacement of air. In subsequent analysis little attention will be paid to it, since it does not appear to be compatible with a description of the mesoscale circulations. Consequently, the positive pressure rise at the ground will not become a required property of the analytic models.

All models will have relative inflow into the moving system at the front; this is consistent with observations that the squall cluster propagates relative to the flow at all levels. Relative inflow at the back of the anvil region will not be permitted, but its implications will be discussed since this is a commonly occuring feature in many squall lines.

Mixing of environmental air into the updraught air occurs to a sufficient extent to increase the depth of the anvil outflow

considerably over the depth predicted for undilute ascent as has been noted by Riehl (1969).

It is beyond the scope of the models developed to incorporate outflows modified by mixing. However the results produced by these models suggest that important dynamical properties have been retained.

1.3 Numerical Modelling of Mesoscale Circulations - A Summary.

In a numerical model it is possible to assess the importance of a mechanism on the dynamics of a particular circulation. For example the evaporation of rain water is "switched off" in Brown (1979) to determine whether it is possible to produce a substantial widespread downdraught beneath a precipitating anvil without evaporation. In Schlesinger (1973) water drag and buoyancy generation by pressure perturbation are among a number of possibilities explored. Results relevant to mesoscale circulations in and beneath precipitating stratiform rain from these two papers will form the principal material for discussion in this section.

In section 1.5.1 evidence from Miller and Betts (1977) is used to confirm that two types of downdraught can be simulated in a numerical model for a squall-type circulation.

In Fritsch and Chappell (1980a,b) the production of mesoscale high and low pressure regions which had been suggested earlier in Hoxit et al (1976) was investigated.

1.3.1 Simulation of Convective and Mesoscale Downdraughts Associated with a Line Element.

The existence of two distinct types of downdraught associated with a squall cluster has been reported in a number of studies including Houze (1977) and Zipser (1977).

In Miller and Betts (1977) trajectories were constructed for air originating at a number of levels in a model simulation of a tropical squall line element which was first described in MM. Updraught outflow of air originating near 950mb occurred between about 200 and 500mb. Air entering the system between 650 and 850mb descended in cell rain areas with vertical velocities between -1 and -6ms^{-1}. It descended with negative buoyancy to the lowest 50-100mb. Air finaly leaving above this convective outflow layer however descended much more slowly ($w \sim -1/2$ to $-1ms^{-1}$), warming adiabatically and must have been "sucked down".

Miller and Betts described these two types of downdraughts as "system" and "cell" downdraughts distinguishing them by their very different descent rates. The anvil in this simulation was not as extensive as those reported in the GATE area by Houze (1977) or Barbados by Zipser (1977). However the simulation clearly illustrated two types of descent. It remained to be demonstrated whether the principle mechanism in both cases was cooling caused by evaporation of precipitation.

1.3.2 The Role of Evaporation in Mesoscale Downdraught Production.

The role of evaporation in mesoscale downdraught production and maintenance is explored in Brown (1979). A three-dimensional

hydrostatic primitive equation model is used with horizontal grid spacing of 25km and vertical grid spacing of 50mb. Potential temperature and geopotential height are the only two quantities permitted to vary in the y-direction so that energy is conserved. The cumulus parameterisation used ignores momentum transport and radiative processes. An ensemble of one-dimensional, updraught only, entraining plumes detrains at a level centred about the level of neutral buoyancy for parcel ascent from 975mb. The upward mass flux within clouds is defined to be a constant (β) times the large scale upward flux at 900mb. $\beta > 1$ implies compensating subsidence in the environment.

Convection transports mass from low to high levels, with condensation increasing the potential temperature and decreasing the water vapour mixing ratio. Detrained water is isobarically mixed into the environment, evaporating completely and instantaneously if the environment is not saturated. Initial conditions assume a large scale simple wave disturbance with a wavelength of 1000km is present. The initial conditions and free parameters were chosen to maximise the evaporation of precipitation.

In runs denoted by S1 and S2 the effect of evaporation is assessed by keeping all conditions the same except that no evaporation of precipitation is allowed in S2. S1 and S2 are indistinguishable for the first 1.5h of simulation - when precipitation from the anvil becomes appreciable. Highest convective cloud top during this period is between 450 and 500mb. In S1 after 3h the temperature at 875mb is dropping, a meso-high develops at low levels where convergence weakens. Upward motion decreases at 900mb and after 4-5h of simulation time a large scale downdraught is replacing the strong ascent which existed after 3h. The large scale has become saturated

within 30 minutes. Net warming then occurs within the anvil and a large scale updraught develops in middle and upper troposphere. The maximum level at which cloud exists is now the anvil top at 300mb. The original disturbance weakens greatly in response to the evaporation of anvil rain. An evaporation driven downdraught still exists 9h into the simulation; downward transport of air was evident in the equivalent potential temperature field.

In S2 where no evaporation of precipitation occurs there is much stronger anvil ascent after 6h. Thus it was demonstrated that evaporation of precipitation on the large scale limits the growth of strong upward motion within the anvil but increases precipitation from the anvil. Brown estimated that the large scale ascent in the case with no evaporation was twice that where evaporation occurred. He concluded that the strength of the meso-scale downdraught in S1 was representative of those of Zipser (1977) and Houze (1977), although weaker. The downdraught in S1 had a peak strength of $10cms^{-1}$ over a 50-100km diameter area.

The mesoscale downdraught produces a weak gust-front at the surface, resembling a convective downdraught ploughing up potentially warm boundary layer air. A number of workers have explored the possibility of a density current as organising mechanism for the squall cluster. This point will be mentioned further in section 1.6 on theoretical models.

Warming of 0.5-1K was produced in a layer between 850 and 950mb and the mixing ratio (q) was nearly 20% lower. It is difficult to compare this figure with observations because of their great variability:- +3K at 900mb in the Barbados squall line described in

Zipser (1977) and virtually no change in the GATE squall line described in Houze (1977).

1.3.3 The Influence of Water Drag and Presence of Precipitation on Mesoscale Downdraught Development.

A number of other influences are explored in Schlesinger (1973) in a two-dimensional model of deep moist convection. The grid spacing was 3.2km and 700m in the vertical. As in previous simulations mentioned in this chapter no frozen water was treated. The control experiment produced a quasi-steady updraught in a cloud core.

In experiment M2-A the consequences of eliminating water drag on downdraught development were explored for an initially conditionally and convectively unstable atmosphere in which a weak convective circulation was present. In the absence of water drag the evaporation of precipitation is still sufficient to initiate and maintain an intense downdraught. Updraught velocities are greater than in the control experiment with drag; the area of significant rainfall is larger and the anvil is more extensive. He concluded that water drag is not essential for initiating a downdraught and in fact acts as a brake on updraught velocity.

When precipitation is suppressed (although liquid water can still exert drag) in experiment M2-D, it appears that insufficient downdraught development occurs to produce convergence and secondary cloud development (as in the control run - M2). Precipitation is essential in redistributing liquid water so that a high concentration at low levels can produce evaporation, cooling and negative buoyancy.

A deeper layer of dry air at middle levels (run M2-E) produces the

interesting result that a more intense and prolonged storm is simulated. Downdraught intensity is not decreased by increased middle level dryness as might be thought. Decreasing the depth of middle level dry air (run M2-F) produced a shorter lived - but similar intensity storm.

1.3.4 Mesoscale Subsidence Forced by the Pressure Field Produced by a COnvective Circulation.

An alternative proposal was that the system downdraught may be forced by the dynamical fields produced by the convection. In Fritsch and Chappell (1980a,b) a numerical simulation is used to explore the following hypothesis:- that where mesoscale subsidence forced by a deep convective complex which is initially in mass balance exists, compressional warming aloft would eventually produce a positive pressure increase aloft. The raised pressure would cause acceleration away from the "high" at upper levels. Pressure would then fall at low levels with the loss of mass from the column, producing low level acceleration.

This hypothesis was developed for mid-latitude squall lines and "mespscale convective complexes" in which inflow and outflow both occur at the front of the system. In a tropical squall line where outflow is from the back, a fall in surface pressure towards the rear of the anvil is occasionally observed, (Zipser, 1977, Johnson and Nicholls, 1983), perhaps produced by this type of mechanism - which would enhance the flow of air away from the squall line at low levels.

In Fritsch and Chappell (1980b) the warm sector of an extra-tropical cyclone is modelled to simulate an idealised

squall-line environment. A cumulus parameterisation scheme is used in a three-dimensional model with a horizontal grid spacing of 20km and a vertical spacing of 50mb.

Initial convection produces warming between 1 and 12.5km in the vertical. Cooling in the boundary layer is produced by moist downdraughts and in the anvil at a height of about 13.6km. Changes aloft are rapidly advected away. Surface changes persist for longer and the pressure begins to rise as a response to the cold moist (but relatively dry and consequently heavier) air reaching the surface.

The pressure field is relatively unperturbed 2km above the surface although a well-organised squall line exists. In the gust front peak wind speeds double, as a response to the expanding surface meso-high, increasing the low level convergence and upward motion at 900mb and 15-30 minutes after the convective outbreak a meso-low forms below the region of upper level warming. Strong vertical circulations develop; subsidence of $10cms^{-1}$ at 800mb and ascent of $0.5ms^{-1}$ at 300mb compared with vertical velocities of $1cms^{-1}$ previously are occuring. There is significant warming in a layer 200-400mb deep - although in this mid-latitude simulation it did not penetrate below 500mb so new convection was not suppressed.

In this model cloud-compensating subsidence is confined to the same grid element in which it was generated. However it is important to note that subsidence beneath a squall anvil may extend 100km downwind from the generating region.

Two types of downdraught have been distinguished and it is possible that long-lived mesoscale circulations operate in a positive feedback cycle creating pressure perturbations which maintain the

circulation.

Evaporation of precipitation decreases the intensity of a storm, decreasing the strength of the updraught and thereby making it longer lived. Anvil vertical velocity is suppressed, so that a larger liquid water condensation occurs producing more precipitation. This then falls into the air below with evaporation contributing to the development of a mesoscale downdraught in an unknown degree. Water drag is eliminated as essential to downdraught development. Precipitation is essential in producing a concentrated cooling at low-levels for convective downdraught development. A deeper layer of drier middle level air appears to produce a longer lived and more intense storm - perhaps because the moist high energy air fuel is being "rationed" in some sense. However this last result comes from a two-dimensional simulation on which Schlesinger comments that vertical velocity may be over-estimated.

1.4 Theoretical Models of Post-Squall Circulations.

Three types of theoretical model for maintaining the post-squall mesoscale circulation are described in this section. Two of these models describe the forced lower troposphere downdraught while the third model suggests a forcing mechanism for both anvil (updraught) circulation and the lower level downdraught. The types of model are:- downdraughts "dragged down" by a density current of convective origin, downdraughts driven by evaporation of precipitation, and the relaxation of the post-squall air mass in a circulation which responds to the pressure and momentum imbalances produced by the convective updraughts and downdraughts.

1.4.1 Evaporation Driven Downdraughts.

A number of papers discuss the evaporation of rainfall producing downdraughts on the convective- or meso- scale depending on rainfall rate, drop size and draught intensity. Kamburova and Ludlam (1966) examined downdraughts originating at 500mb and descending to 800mb. For simplicity, evaporation into air of low wet-bulb potential temperature from the middle troposphere is assumed to produce an approximately steady downdraught. The downdraught is horizontally uniform containing rain of a specified intensity and uniform drop size. The temperature at the surface of the evaporating drops is assumed to be equal to the wet-bulb potential temperature. The air assumes a near-saturated adiabatic profile only in intense rainfall with small drop size in very weak downdraughts (average w of $2ms^{-1}$). In moderate intensity rain ($50mmh^{-1}$) the temperature profile approximates to the dry adiabatic process - regardless of drop size, and the initial relative humidity falls by nearly 20%. In general, small drop sizes evaporate most efficiently. The environmental lapse rate and rainfall intensity govern the strength of the downdraught produced. Lapse rates close to the dry adiabatic from ground to mid-troposphere produce strong downdraughts. High intensity rainfall enhances evaporation and produces negative buoyancy.

Weak downdraughts (of less than $1ms^{-1}$) such as those beneath anvils are produced in moderate rainfall and conditions in which the lapse rate is close to dry adiabatic.

Ryan and Carstens (1978) used a similar model to that of Kamburova and Ludlam to examine observations behind squall lines during VIMHEX. A Marshall-Palmer distribution of rain drop sizes was used (instead of

the single drop size mentioned previously). An estimate of vertical velocity and rainfall rate had to be made since data were not available. Predicted and observed profiles of humidity and potential temperature agreed quite well - however the predictions could not be made uniquely.

Betts and Silva Dias (1979) produced another model based upon Kamburova and Ludlam (1966) in an attempt to find a simple description of the downdraught process. The model was applied to VIMHEX and GATE data. The microphysical parameters were combined into a "pressure scale for evaporation", Π_e. It was hoped to relate the magnitude of Π_e to the properties of the inflow air since Π_e increases with downdraught speed and mean drop size and decreases with an increasing rainfall rate. Two theoretical cases were considered. The first assumed the temperature path of downdraught air paralled a moist adiabat; with Π_e constant the downdraught approaches a constant relative humidity and constant pressure difference to the lifting condensation level equal to Π_e. The larger Π_e, in this case, the more unsaturated the downdraught became in its descent.

In the second case treated, the downdraught temperature path is assumed to parallel the environment (so that downdraught buoyancy is constant). The downdraught moves towards saturation when the environment is more stable than moist adiabatic, and away from saturation when the environment is less stable than the moist adiabatic.

It was unfortunately found that vertically averaged values of Π_e from tropical data were not correlated with inflow properties and Betts and Silva Dias suggested it may not be simple to predict from

large scale variables, however they appear to follow the pressure difference to the LCL of the outflow quite closely.

1.4.2 Density Currents as an Organising Mechanism.

In the model simulation of MM it was noted that a "density current" produced by downdraught outflows persisted in a "remarkably steady state". It was suggested that the squall line convective element speed was matched to that of the spreading density current to maintain the organisation of the circulation. In Miller and Betts (1977) trajectories constructed for this simulation emphasised the convective downdraught outflow underlying the "system downdraught" outflow. It was suggested that the cold outflow from the density current flowing downstream might accelerate the overlying air and produce descent from middle to low level. Charba (1974) found the lower cold structure of a mid-latitude squall line was well described by a "gravity current".

In one of the analytic models examined in chapter four it is found that the convective downdraught cannot take part in the circulation described - however this does not rule it out in the immediate post squall region as one of the factors in initiating descent.

1.4.3 Mesoscale Circulations as Responses to Dynamic forcing.

The three-dimensional convective analytic model of a squall line in MM will be described in detail in chapter two. A budget of momentum integrated in the vertical through the inflow and outflow along the direction of propagation of the system shows that there is momentum imbalance in two-dimensions. This is true for

three-dimensional circulations and the hypothesis that this imbalance in the two-dimensional momentum field provides a dynamic forcing for the post squall mesoscale circulation will be explored. The equations setting out a simple forced response are presented in Thorpe et al (1980), hereafter TMM80, and are discussed and developed in chapter three.

All three processes mentioned probably occur to some degree. A forced circulation requires evaporation of rainfall to cool it, otherwise the adiabatic warming would be unrealistically large. The convective downdraught may be an important initiating forcing mechanism, but the analytic models developed in chapters three and four show that it is dynamically unimportant for the mesoscale region behind a squall line.

CHAPTER TWO

CONVECTIVE FORCING PROFILES.

2.1 Introduction and Development of the General Displacement Equation for a Three-dimensional Convective Updraught.

Various convective mechanisms are examined in this chapter. Updraughts and downdraughts of different geometries, with sheared or unsheared inflows, and compressible or incompressible structures are studied. The convective updraught and downdraught circulation described in Moncrieff and Miller (1976), hereafter MM, which is a special case of the work described here is used as a starting point for suitable forcing mechanisms for a mesoscale response. The results of MM and extensions by Tam (1979) to include updraughts which become shallower or deeper on ascent are summarised. The consequences of including a shallow convective downdraught are considered for the forcing mechanisms. These types of forcing mechanism give rise to a type "A" or "sequential" mesoscale circulation. Forcing and response occur on separate time and space scales illustrated in figure 2.1.1 below. The mesoscale responses occurring in such circulations are described in chapter three.

A second type "B" or "simultaneous" forcing is considered where convective updraught and mesoscale response are interlocking and inherently three-dimensional. This type "B" circulation is sketched in figure 2.1.2 below. A model of the convective updraught is developed in which net deviation of all streamlines occurs. (The two-dimensional updraught is also included for comparison. In order

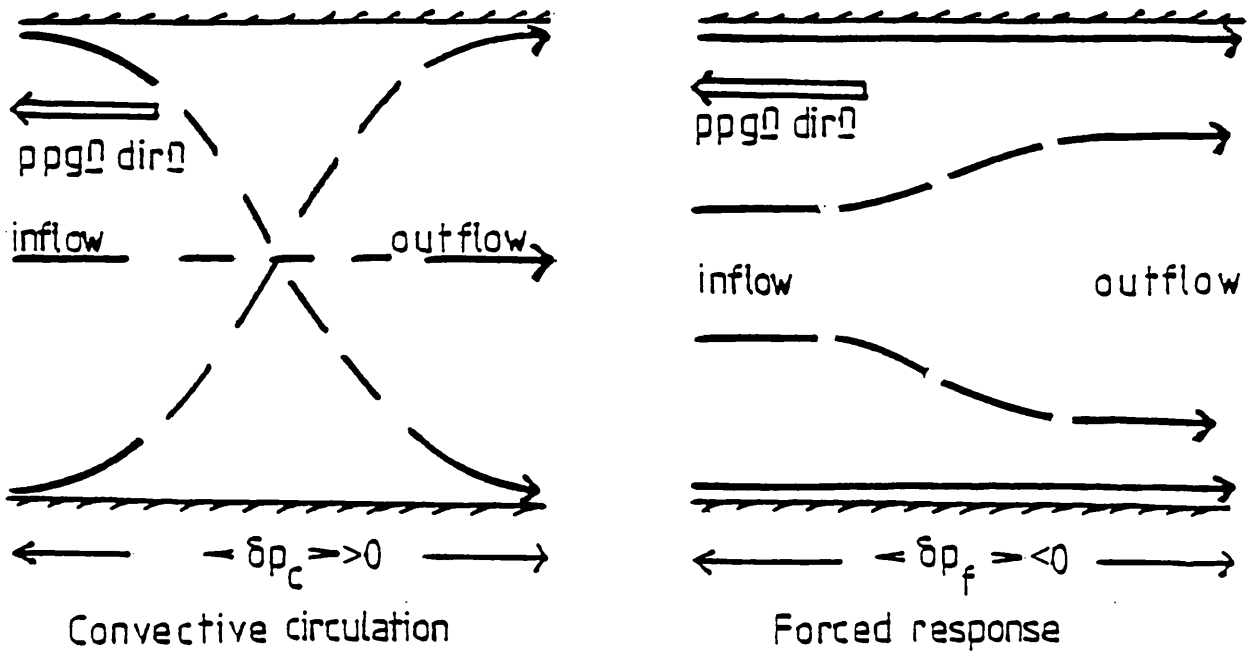


Figure 2.1.1

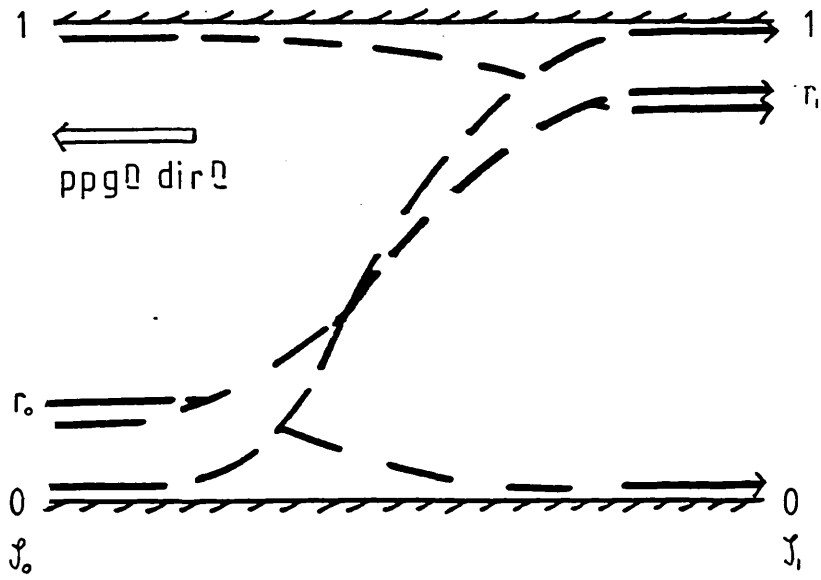


Figure 2.1.2

to make the circulation structure physically consistent extra constraints have to be considered. For instance, in the full circulation including forced response detailed in chapter four, there must be pressure continuity on outflow between the lower surface of the updraught and the upper surface of the forced downdraught.

The basic equation set used is the Boussinesq approximation for an inviscid fluid of varying mean density (as in MM). These are:-

$$\frac{D\underline{v}}{Dt} + f\underline{k}\wedge\underline{v} + \underline{\nabla}\left(\frac{\delta p}{\rho}\right) - g\delta\phi\,\underline{k} = 0 \quad , \tag{2.1}$$

$$\underline{\nabla}.\left(\rho\underline{v}\right) = 0 \quad , \tag{2.2}$$

$$\frac{D}{Dt}(\delta\phi) + wB = \frac{Q}{C_p} \quad . \tag{2.3}$$

Q is an entropy source; δp and $\delta\phi$ are deviations of pressure and log-potential temperature from a mean state, with static stability $B=(\partial \ln\theta/\partial z)$. The Boussinesq approximation is accurate to second order in the deviation quantities. Advective time scales are much shorter than inertial ones ($D/Dt>>f$), so the explicit effects of the earth's rotation may be ignored. Since the time taken for a parcel of air to pass through the squall line is a few tens of minutes, significantly shorter than the squall line's lifetime, the flow may be supposed stationary relative to axes moving at the propagation speed of the convective system. The following conservative quantity developed in MG for a three-dimensional steady flow is used:-

$$\frac{1}{2}\underline{v}^2 + \frac{\delta p}{\rho} - \int_{z_0}^{z} g\delta\phi_p\, dz = C_1(\psi) \tag{2.4}$$

is a function of streamline only where $\delta\phi_p = \phi - \phi_0(z)$. ϕ is the log potential temperature of a parcel of air travelling along a particular streamline; $\phi_0(z)$ is the undisturbed log potential temperature. The outflow level of a streamline entering at a level z_0 is denoted by $z_1(z_0)$ as x tends to infinity. All variables subscripted $(\,)_0$ denote inflow values; $(\,)_1$ denotes an outflow value. The flow is shown

schematically in figure 2.1.3. Hence at large distances from the squall line:-

$$\frac{1}{2}V_1^2 + \frac{\delta p}{\rho}(x=\infty, z=z_1) - \int_{z_0}^{z_1} g\delta\phi_p\, dz = \frac{1}{2}V_0^2 + \frac{\delta p}{\rho}(x=-\infty, z=z_0). \quad (2.5)$$

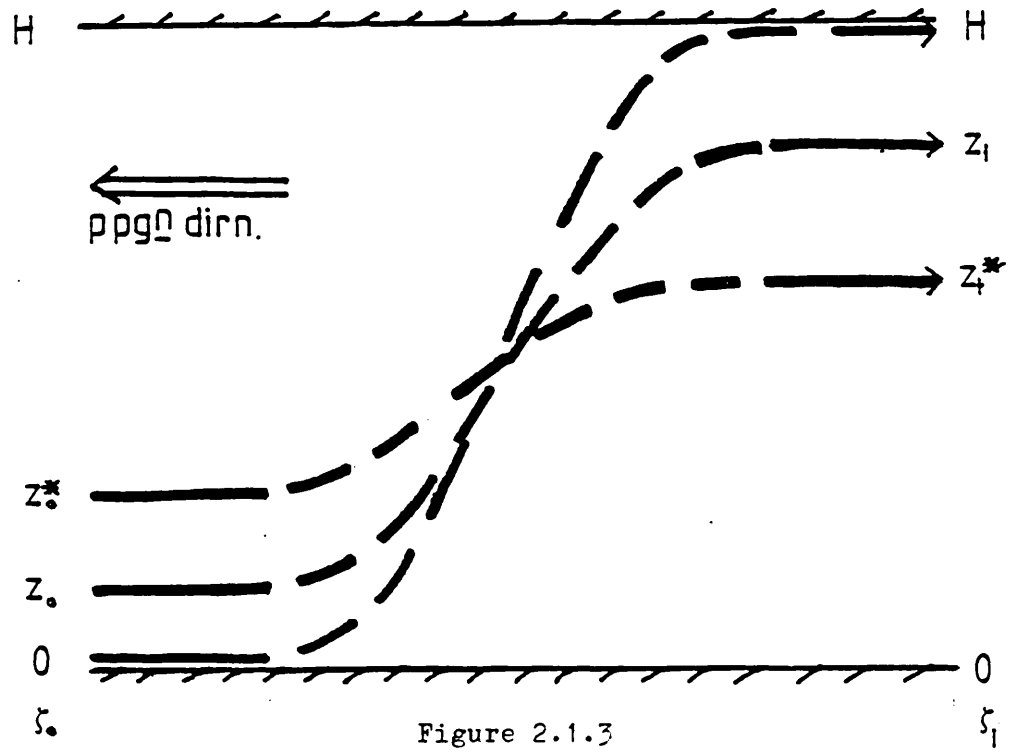


Figure 2.1.3

The remote flow is assumed to be hydrostatic so:-

$$\frac{\partial}{\partial z}\left(\frac{\delta p}{\rho}\right) = g\delta\phi. \quad (2.6)$$

Integrating $$\frac{\delta p}{\rho}(x=\infty, z=z_1) = \Delta + \int_{z_0^*}^{z_1^*} g\delta\phi_p\, dz + \int_{z_1^*}^{z_1} g\delta\phi_1\, dz_1. \quad (2.7)$$

(i) (ii) (iii)

The terms on the right hand side represent:-

(i) the dynamical pressure change along the reference streamline, $z_0 = z_0^*$ to $z_1 = z_1^*$, (obtained with (ii) from 2.5)

(ii) the pressure change due to heating along a streamline since the

reference streamline suffers a net deviation,

(iii) the difference in pressure deviation between the outflow reference level, z_1^*, and the outflow streamline of interest, z_1.

The departure from hydrostatic pressure for the reference streamline on outflow is $\Delta + \int_{z^*}^{z_1^*} g\delta\phi_p dz$. Substituting for $\frac{\delta p}{p}(x=\infty, z=z_1)$ in 2.5 using 2.7 and taking the inflow to be hydrostatic so that $\frac{\delta p}{p}(x=-\infty, z=z_0)=0$ gives

$$\frac{1}{2}\underset{\sim}{V}_1^2 + \Delta + \int_{z_0^*}^{z_1^*} g\delta\phi_p dz + \int_{z_1^*}^{z_1} g\delta\phi_1 dz_1 - \int_{z_0}^{z_1} g\delta\phi_p dz = \frac{1}{2}\underset{\sim}{V}_0^2. \qquad (2.8)$$

Since solutions which depend on bulk parameters rather than on detailed vertical structure are required, the pseudo moist-adiabatic lapse rate, γ, and environmental static stability, B, are assumed constant with height. More importantly these simplifications allow analytic solutions to be obtained and can be relaxed only at the expense of requiring purely numerical solutions of the displacement equations to be developed from 2.8. $\delta\phi_p$ and $\delta\phi_1$ may be simply expressed:-

$$\delta\phi_p = (\gamma - B)(z - z_0) \qquad (2.9)$$

$$\delta\phi_1 = (\gamma - B)(z_1 - z_0). \qquad (2.10)$$

On substitution of 2.9 and 2.10 in 2.8 and with some manipulation this gives:-

$$\frac{1}{2}\underset{\sim}{V}_1^2 + \Delta + g(\gamma - B)\int_{z_0^*}^{z_0} (z_1 - z_0) dz_0 = \frac{1}{2}\underset{\sim}{V}_0^2. \qquad (2.11)$$

Note, when $z_0 = z_0^*$, $\Delta = \frac{1}{2}\underline{v}_0^2 - \frac{1}{2}\underline{v}_1^2$, the dynamical pressure change for the reference streamline. If the outflow and inflow are both in the x-z plane, the mass continuity equation 2.2 becomes

$$\rho_0 u_0 dz_0 = -\rho_1 u_1 dz_1 \tag{2.12}$$

where the inflow profile $\underline{v}_0 = u_0\underline{i}$, and outflow profile, $\underline{v}_1 = u_1\underline{i}$. Representing the density scale height by H_0, the surface density by ρ_s then

$$\rho = \rho_s \exp(-z/H_0). \tag{2.13}$$

We define c to be the inflow speed for the reference streamline, and write $\Delta = \frac{1}{2}c^2E$. Making the transformations $z/H = \zeta$, $H/H_0 = D$, $1/F^2 = g(\gamma - B)H^2/c^2$, 2.11 becomes, using 2.12 and 2.13:-

$$\left(\frac{d\zeta_0}{d\zeta_1}\right)^2 = \left\{1 - \left(\frac{c}{u_0}\right)^2\left[E + \frac{2}{F^2}\int_{\zeta_0^*}^{\zeta_0}(\zeta_1 - \zeta_0)\,d\zeta_0\right]\right\}\exp\left[-2(\zeta_1 - \zeta_0)D\right]. \tag{2.14}$$

This is the general compressible, non-uniform shear displacement equation for a three-dimensional convective updraught. In MM, Tam (1979) and this thesis the lowest streamline is assumed to reach the top boundary producing the condition

$$\zeta_0(\zeta_1 = 1) = 0. \tag{2.15}$$

The pressure change at the top boundary is unconstrained and so a rigid lid is effectively imposed. This is not a necessary constraint and a free surface at the top boundary is an alternative. The

reference level for the pressure on inflow, $\mathcal{J}_o^*$, is defined to be r_o, and on outflow, $\mathcal{J}^*=r_1$, so that the second boundary condition is

$$\mathcal{J}_o\left(\mathcal{J}_1 = r_1\right) = r_o. \tag{2.16}$$

The only analytically tractable form of 2.14 so far discovered occurs for the incompressible, constant inflow case, D=0, $du_o/dz_o=0$. For this case 2.14 may be differentiated with respect to $\mathcal{J}_1$ to obtain

$$\frac{d^2\mathcal{J}_o}{d\mathcal{J}_1^2} = -\frac{1}{F^2}\left(\mathcal{J}_1-\mathcal{J}_o\right). \tag{2.17}$$

The solution to 2.17 with the boundary conditions 2.15, and 2.16, which must also satisfy 2.14 ,is

$$\mathcal{J}_o = \mathcal{J}_1 - \frac{1}{\sinh\frac{1-r_1}{F}}\left[\sinh\frac{\mathcal{J}_1-r_1}{F} + (r_1-r_o)\sinh\frac{1-\mathcal{J}_1}{F}\right] \tag{2.18}$$

where $$F\left(1\pm\sqrt{1-E}\right)\sinh\frac{1-r_1}{F} = 1-(r_1-r_o)\cosh\frac{1-r_1}{F}. \tag{2.19}$$

Solutions which represent an overturning circulation, $d\mathcal{L}_o/d\mathcal{J}_1\leqslant 0$ for $r_1\leqslant\mathcal{J}_1\leqslant 1$, correspond to the positive square root. The negative root corresponds to a two dimensional solution, $d\mathcal{L}_o/d\mathcal{J}_1\geqslant 0$ for $1\leqslant\mathcal{J}_1\leqslant r_1$, which will be briefly described in section 2.3.1. The two-dimensional solution is extensively explored in Thorpe et al (1982), hereafter TMM82.

The outflow relative velocity profile is obtained from 2.12, 2.18 and 2.19,

$$\frac{u_1}{c} = \frac{1}{F\sinh\frac{1-r_1}{F}}\left[\cosh\frac{\rho_1-r_1}{F} - (r_1-r_0)\cosh\frac{1-\rho_1}{F}\right] - 1 . \quad (2.20)$$

The log potential temperature deviation profile is given by 2.10 and 2.18,

$$\frac{\delta\phi_1}{(\gamma-B)H} = \frac{1}{\sinh\frac{1-r_1}{F}}\left[\sinh\frac{\rho_1-r_1}{F} + (r_1-r_0)\sinh\frac{1-\rho_1}{F}\right] . \quad (2.21)$$

The outflow pressure perturbation profile is obtained using 2.7, 2.9, 2.10 and 2.18 and simplified using 2.20,

$$\frac{\delta p_1}{\frac{1}{2}\rho_s c^2} = E + \left(\frac{r_1-r_0}{F}\right)^2 + 2\left(\frac{u_1}{c} - \sqrt{1-E}\right) . \quad (2.22)$$

These equations are nondimensionalised by making the following substitutions:-

$$\frac{u_1}{\left(g(\gamma-B)H^2\right)^{1/2}} \longrightarrow u_1 , \quad (2.23)$$

$$\frac{\delta p_1/\rho_s}{\frac{1}{2}g(\gamma-B)H^2} \longrightarrow \delta p_1 , \quad (2.24)$$

$$\frac{\delta\phi_1}{(\gamma-B)H} \longrightarrow \delta\phi_1 . \quad (2.25)$$

In non-dimensional form 2.20, 2.21 and 2.22 become

$$u_1 = F\left\{\frac{1}{\sinh\frac{1-r_1}{F}}\left[\cosh\frac{\mathcal{J}_1-r_1}{F}-(r_1-r_0)\cosh\frac{1-\mathcal{J}_1}{F}\right]-1\right\}, \quad (2.26)$$

$$\delta\phi_1 = \frac{1}{\sinh\frac{1-r_1}{F}}\left[\sinh\frac{\mathcal{J}_1-r_1}{F}+(r_1-r_0)\cosh\frac{1-\mathcal{J}_1}{F}\right], \quad (2.27)$$

$$\delta p_1 = F^2\left[E+\left(\frac{r_1-r_0}{F}\right)^2+2\left(\frac{u_1}{F}-\sqrt{1-E}\right)\right]. \quad (2.28)$$

The properties of this equation set and of the general equation 2.14 with the boundary conditions 2.15 and 2.16 will be discussed in relation to the results of MM and Tam (1979).

2.2 Models of Convective Updraughts and Downdraughts with an Undeviated Streamline.

2.2.1 Summary of the Results of MM.

The convective updraught described in MM has an undeviated middle-level stream-line. In the notation developed in section 2.1 this corresponds to $r_i=r_o=0.5$. As illustrated below in figure 2.2.1 the downdraught configuration is obtained by rotating the updraught about the axis $\mathcal{J}=0.5$.

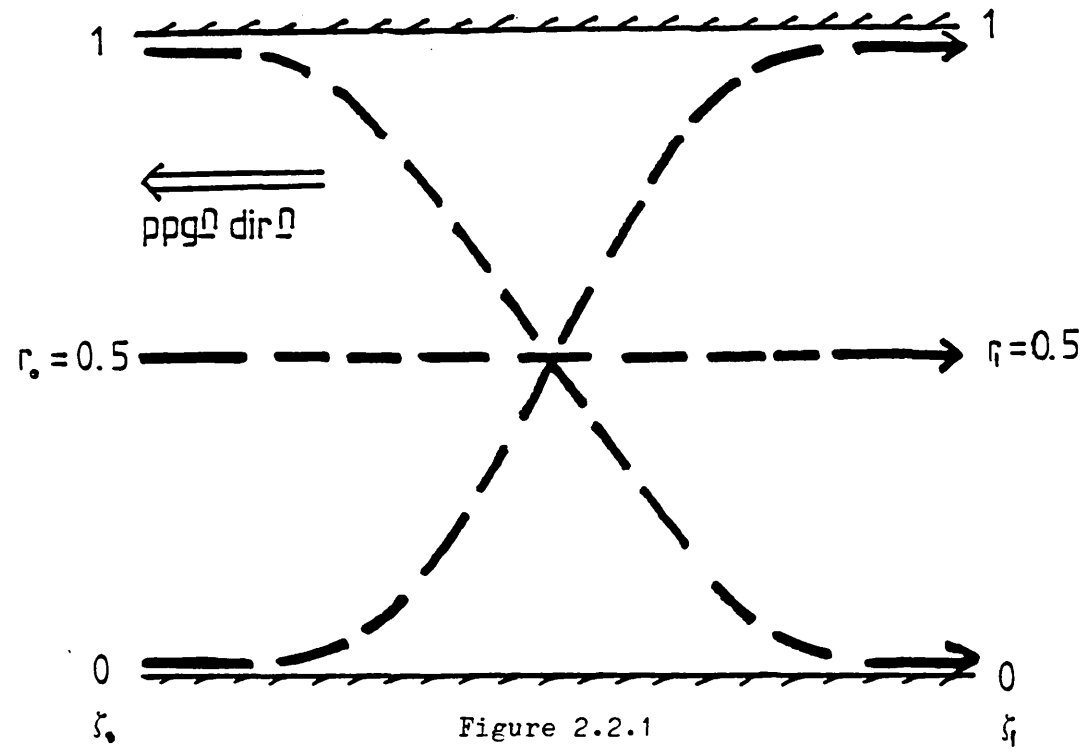


Figure 2.2.1

The eigenvalue equation 2.19, with the boundary condition $r_o = r_1 = 0.5$ now becomes,

$$F\left(1+\sqrt{1-E}\right)\sinh\frac{1}{2F} = 1. \qquad (2.29)$$

The solution for the incompressible unsheared case is found where the maximum fractional increase in the kinetic energy of the updraught occurs as in MM and this solution corresponds to E=1. The expressions for relative velocity, pressure perturbation and entropy perturbation on outflow from 2.26, 2.27 and 2.28 are given below.

$$u_1 = F\left(\cosh\frac{\zeta_1-r_1}{F} - 1\right), \qquad (2.30)$$

$$\delta\phi_1 = F\sinh\frac{\zeta_1-r_1}{F}, \qquad (2.31)$$

$$\delta p_1 = F^2 (1 + 2u_1 / F). \qquad (2.32)$$

For this case the dynamical pressure change and the total pressure change at $\gamma_1 = r_1$ are equal for the reference streamline since it shows no net deviation. Figure 2.2.2 shows the total pressure deviation and the dynamical pressure change as a function of height within the outflow. The updraught convective available potential energy (UCAPE) is the "CAPE" defined in MM as

$$\int_{bottom}^{top} g \delta\phi_p \, dz .$$

Taking UCAPE to be 1000Jkg^{-1}, a value typical of Venezuelan and GATE squall lines (Fernandez, 1980, 1982), the total pressure change varies between 0.5mb (0.05UCAPE) at mid-level for the undeviated streamline and 4.2mb (0.42UCAPE) at the highest outflow level. The convective downdraught (assumed to undergo pseudo-saturated descent) has an identical but inverted pressure perturbation profile. Outflow profiles of relative velocity, pressure perturbation and entropy perturbation are shown in figure 2.2.3.

The total pressure change is composed of the dynamical part and the change produced by warming. The dynamical pressure change varies between 0.5mb (0.05UCAPE) at mid-level and -5.9mb (-0.59UCAPE) for the uppermost streamline. This pressure fall of nearly 6mb reflects the large acceleration of the air which leaves at high level. The pressure change through heating is very large at this level, more than 10mb. This is because the thermal contribution to the pressure change is proportional to the square of the vertical displacement, and because (Υ-E) is independent of height.

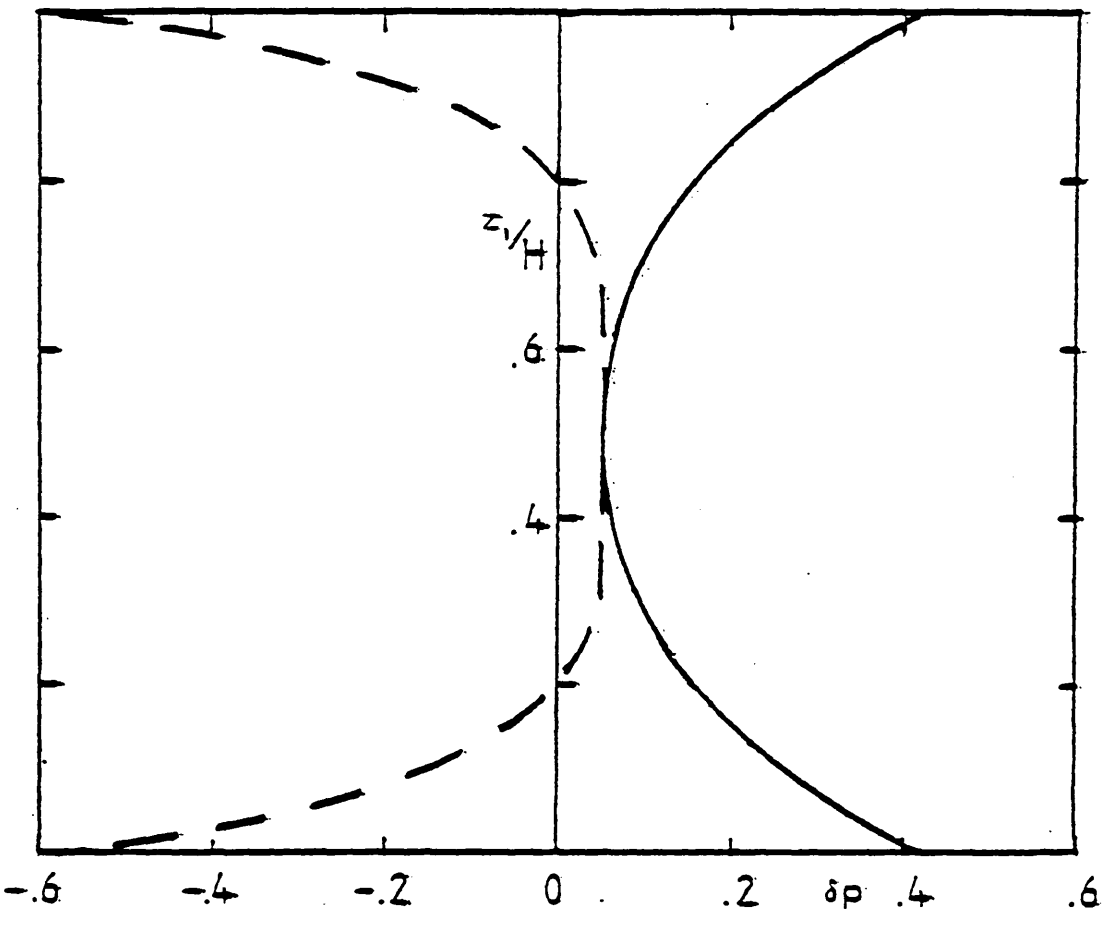


Figure 2.2.2. Outflow profiles of δp_{total} (solid line) and $\delta p_{dynamic}$ (broken line). $D=0$, $E=1$ and $r_0 = r_1 = 0.5$.

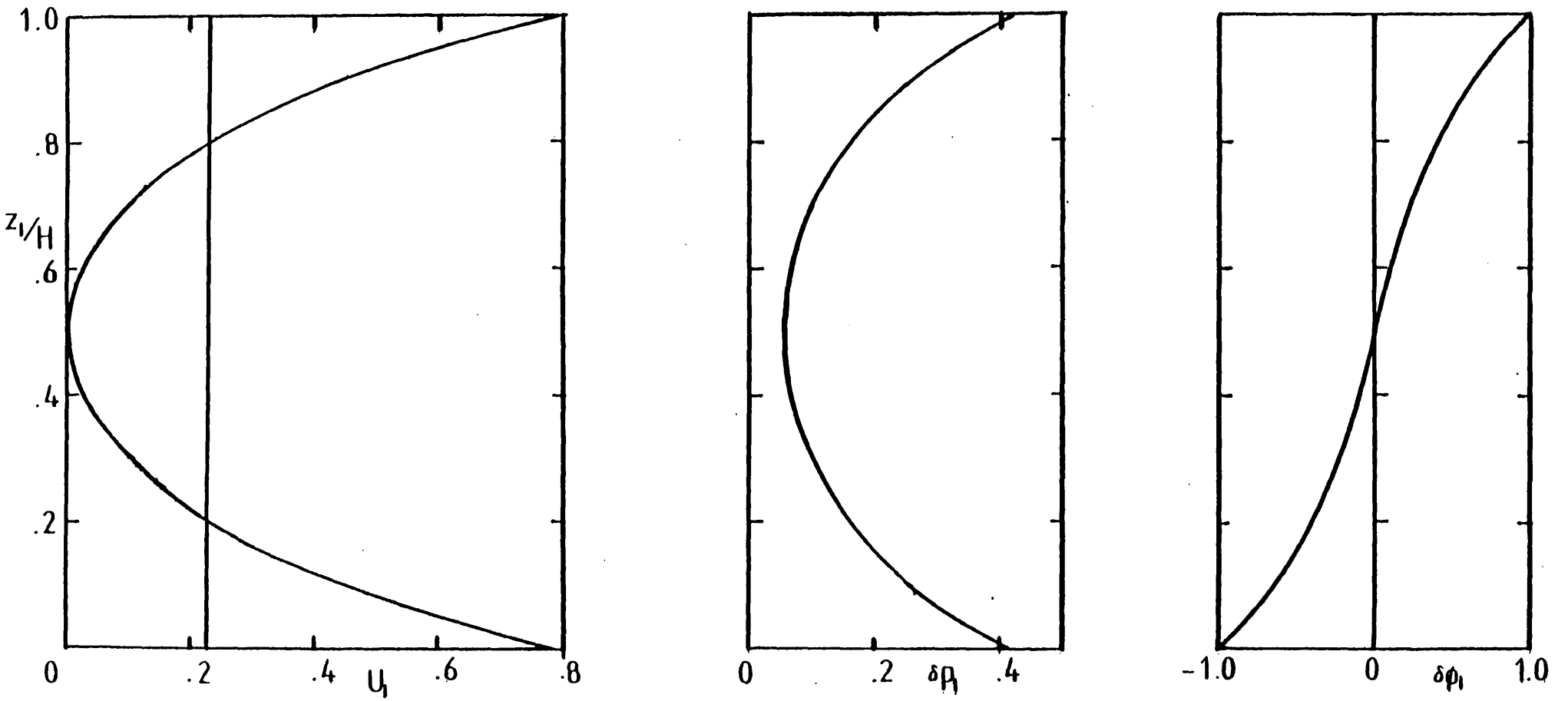


Figure 2.2.3 Outflow profiles of relative velocity, pressure perturbation and log(θ) perturbation (heavy lines). Inflow profile of relative velocity is also shown (lighter lines). D=0, E=1, $r_* = r_1 = 0.5$.

In considering narrow updraughts in section 2.3 this large pressure rise due to the large net displacement of the lowest streamline on outflow (see figure 2.2.2) will be important when we attempt to match the presure changes at the boundaries between different types of flow. For constant lapse rates, it is reasonably obvious that a way to reduce the total pressure change is to accelerate the air so that the dynamical component of the pressure change at the boundary is negative.

The outflow profiles for unsheared incompressible flow (figure 2.2.3) show the following features, which provide the forcing profiles for a subsequent circulation. The flow is accelerated at upper and lower levels, above $\mathfrak{f}_1=0.8$ and below $\mathfrak{f}_1=0.2$ while the mid-level flow is decelerated with a stagnation point at the mid-level in the outflow. The upper level flow is accelerated from $u_0=F$ to $u_1=F(\mathrm{ch}(1/2F)-1)$ in nondimensional units. When F=0.230 (the solution found by MM) the maximum outflow velocity is 0.794. The velocity is increased by nearly 250%. This corresponds to an acceleration from $10.3\mathrm{ms}^{-1}$ to $37.3\mathrm{ms}^{-1}$, a velocity change of $26\mathrm{ms}^{-1}$. In practice such a severely sheared profile with mid-level stagnation of the outflow cannot be used to force a mesoscale response as is shown in chapter three; a modified, smaller amplitude, cosine-type profile is used to represent the velocity perturbation.

The pressure perturbation is everywhere positive with larger positive deviation at lowest and highest outflow levels. The mean pressure change, given by

$$\int_0^1 \delta_R \, d\sigma_1 = 3F^2$$

is approximately 1.6mb if UCAPE=1000Jkg^{-1}.

The change in log potential temperature ($\delta\phi_1$) shows that heating occurs in the updraught outflow, increasing at a greater than linear rate with height. The downdraught shows a matching decrease in $\delta\phi_1$ below the mid-level. The maximum heating or cooling is given by $|\sigma_1-\sigma_2|=1$, $\delta\phi_1=1$. For example, a difference in lapse rates of 10^{-6}m^{-1} with a disturbance height of 10km would give $\delta\theta/\theta \sim 10^{-2}$, $\delta\theta \sim 3$K ($\theta \sim 300$K).

The forcing effect of a positive pressure perturbation with a westerly minimum in the velocity profile will be explored in chapter three.

2.2.2 Model with a Shallow Downdraught.

In this section a more realistic model of the convective downdraught is developed. The observational evidence presented in chapter one does not support a downdraught model which extends through the entire depth of the troposphere. Betts' (1976) results indicate that the convective downdraught air originates immediately above the subcloud air and probably occupies a pressure depth equal to that of the subcloud layer. The updraught air originates in the subcloud layer. The circulation shown in figure 2.2.4 with a shallow downdraught and a streamline which is undeflected in the vertical is examined first.

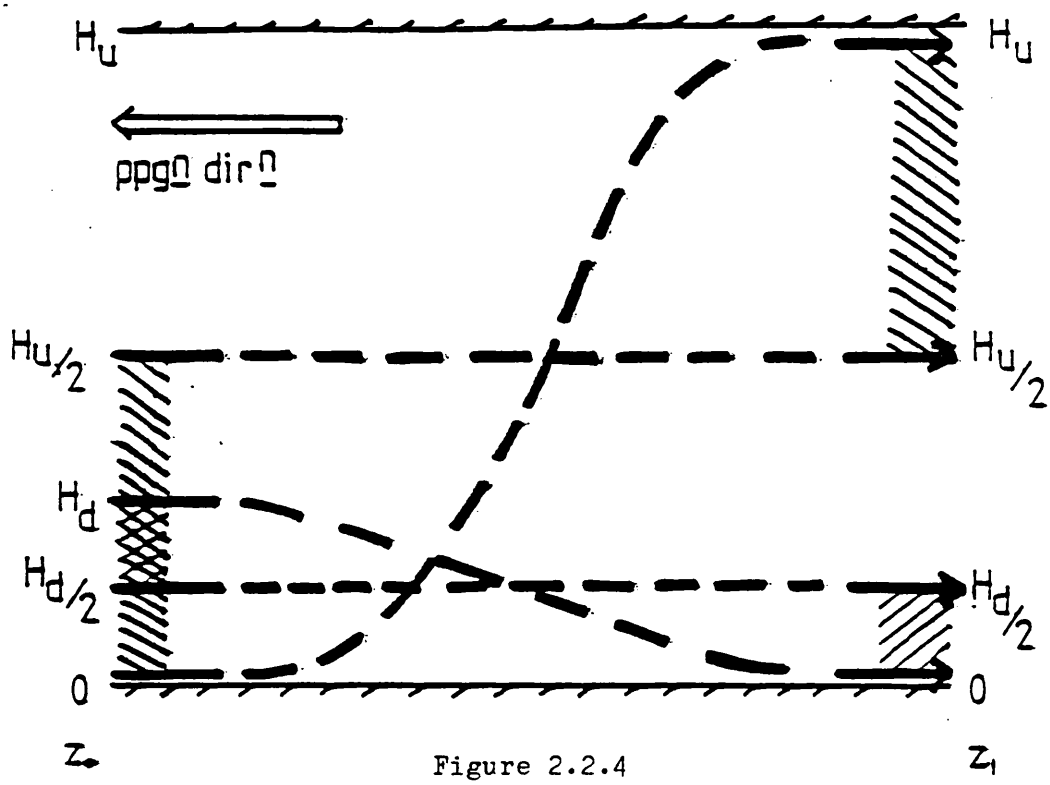


Figure 2.2.4

In figure 2.2.4 there is no relative inflow above the updraught and the downdraught inflow - or between updraught and downdraught on outflow. Assuming pressure continuity between the lowest level of the updraught and the highest level of the downdraught on outflow some useful deductions may be made. Updraught and downdraught circulations individually fulfil the requirements of mass continuity. However a further refinement of this model would be to specify widths in the transverse (y-direction), for updraught, downdraught and intermediate flows, so that a more rigorous treatment of air with a common level of origin could be made although such a refinement will not be attempted here. Precisely the same eigenvalue equation 2.29 as in MM applies because there is a streamline which has zero vertical displacement. The depth of the downdraught is now H_d and $F_d = c_d/\sqrt{g(\gamma - B)_d H_d^2}$ where the subscript "d" now indicates a downdraught variable. For the updraught $F_u = c_u/\sqrt{g(\gamma - B)_u H_u^2}$.

If both updraught and downdraught transform CAPE into mean flow

kinetic energy with maximum efficiency so that $E_u=E_d=1$, 2.29 becomes $F\sinh(1/2F)=1$. Then $F_u=F_d=0.23$ and $c_u/(UCAPE)^{1/2}=c_d/(DCAPE)^{1/2}$ where UCAPE and DCAPE are the updraught and downdraught CAPE respectively. ($UCAPE=g(\gamma-B)_u H_u^2/2$, $DCAPE=g(\gamma-B)_d H_d^2/2$.)

If the pressure change at $\zeta_1=H_u/2$ is equal to that at $\zeta_1=H_d/2$ then from 2.22 $\frac{1}{2}\rho_s c_u^2=\frac{1}{2}\rho_s c_d^2$. So $c_u=c_d$, UCAPE=DCAPE and $(\gamma-B)_u H_u^2=(\gamma-B)_d H_d^2$. If the descent in the convective downdraught follows the saturated adiabat, then $(\gamma-B)_u=(\gamma-B)_d$ and the height scales of updraught and downdraught (H_u and H_d) must be equal. This is the model developed in MM.

If $(\gamma-B)_u\neq(\gamma-B)_d$ then $(\gamma-B)_u/(\gamma-B)_d=(H_d/H_u)^2$ and H_d/H_u is known to be less than 1 from observations. If H_d corresponds to a layer 300mb deep and H_u to a layer 900mb deep, equating layers of equal mass to those of equal depth in this incompressible model, then $H_d/H_u=1/3$ and $(\gamma-B)_u/(\gamma-B)_d=1/9$. This implies a massive amount of evaporation into the convective downdraught producing substantial cooling.

A second interpretation is possible:- If we assume $(\gamma-B)_u=(\gamma-B)_d$ and $H_d/H_u=1/3$, retain the criterion of maximum mechanical efficiency for updraught and downdraught and examine the consequences for the difference in pressure change between $\zeta_1=H_u/2$ and $\zeta_1=H_d/2$ then

$$UCAPE/DCAPE=(H_u/H_d)^2=9$$

$$F_u=F_d=0.23$$

$$\tfrac{1}{2}\rho_s c_u^2 \Big/ \tfrac{1}{2}\rho_s c_d^2 = (F_u/F_d)^2 (UCAPE/DCAPE) = 9.$$

According to 2.22 applied above to this special case, a pressure gradient must exist across the intervening air - a positive deviation which increases with height. In addition the updraught must propagate at three times the speed of the downdraught which suggests that no

"steady state" is obtainable. Consider what must happen to air originally above the inflow to the convective updraught and downdraught and below $\mathcal{J}_o = H_u$, illustrated in figure 2.2.5 below. Suppose it leaves at the rear of the circulation between $H_u/2$ and $H_d/2$. Air which is forced to descend and whose pressure rises must be decelerated as is shown in chapter three. Therefore air descending to near $\mathcal{J}_1 = H_u/2$ and $\mathcal{J}_1 = H_d/2$ must be decelerated. Mass continuity however requires that some of the air in the middle of the layer must be accelerated. This large middle-level acceleration is never found observationally and indeed the middle-level flow is always decelerated.

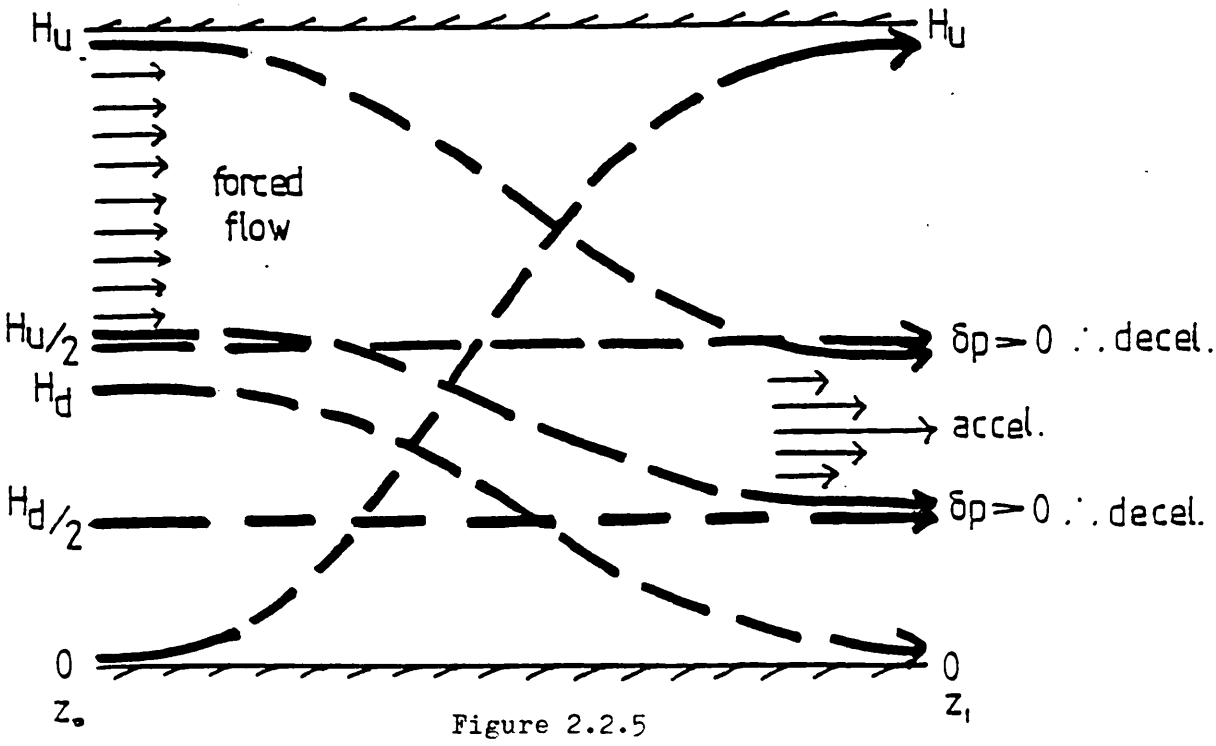


Figure 2.2.5

2.2.3 Model with a Shallow Downdraught:- Extended to allow Outflow to become Deeper or Shallower than Inflow.

Changing the level of the undeviated streamline so that inflow and outflow depths are unequal is the next stage of complexity for the

model suggested in section 2.2.2. A flow of the type sketched in figure 2.2.6 below is considered.

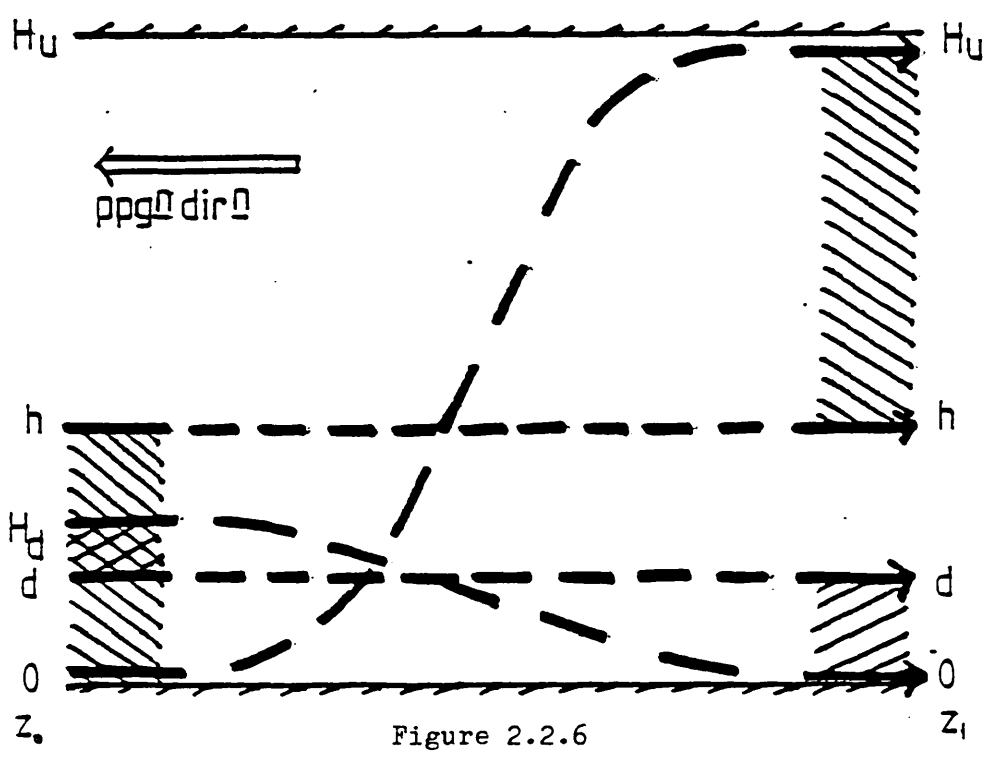


Figure 2.2.6

The equations describing the updraught are set out below. From 2.18 and 2.19

$$z_0 = z_1 - (1+\sqrt{1-E_u})\, F_u H_u \sinh \frac{z_1-h}{F_u H_u} \qquad (2.33)$$

where $$(1+\sqrt{1-E_u})\, F_u \sinh \frac{H_u-h}{F_u H_u} = 1 \qquad \text{for } h \leq z_1 \leq H_u. \qquad (2.34)$$

Similarly for the convective downdraught

$$z_0 = z_1 - (1+\sqrt{1-E_d})\, F_d H_d \sinh \frac{z_1-d}{F_d H_d} \qquad (2.35)$$

where $$\frac{(1+\sqrt{1-E_d})F_d \sinh \frac{d}{F_d H_d}}{} = 1 \qquad \text{for } 0 \leq f \leq d. \quad (2.36)$$

The results for the case E=1 for the updraught are documented in Tam (1979). From figure 2.4.2 of Tam, reproduced in figure 2.2.7, we see F increases as α increases (where $\alpha=(H_u-h)/H_u$), F tending to zero as α tends to zero (no outflow) and F tending to infinity as α tends to 1. Since c_u is proportional to F_u, a deepening updraught with $\alpha>0.5$ will produce a larger pressure change along the lowest outflow streamline than a narrowing updraught.

An updraught and downdraught can be associated as in the previous section by constancy of pressure between $z_1=h$ and $z_1=d$. As before, this implies $c_u=c_d$ for the case $E_u=E_d=1$. F_u can be calculated from 2.34 for a range of values of α as in Tam (1979). Then, since $c_u=c_d$,

$$F_d/F_u=\sqrt{\text{UCAPE/DCAPE}}\,.$$

F_d is calculated for a range of values of $(\text{UCAPE/DCAPE})^{1/2}$. d/H_d is found by solving 2.36, which is of the same form as 2.34. The results are shown in table 2.2.1. For example if $\alpha_u=0.6$, $F_u=0.326$ and UCAPE/DCAPE=2 then $d/H_d=0.699$. Both updraught and downdraught become deeper on outflow. The outflow relative velocity profile is obtained from 2.12 and 2.33 or 2.35. For UCAPE=1000Jkg^{-1} a propagation speed of 14.6ms^{-1} for the system would be predicted. For this configuration:-

$$u_1(H_u)=0.326\text{x}2.23\text{x}(2\text{UCAPE})^{1/2}=32.5\text{ms}^{-1}$$

$$u_1(0)=0.326\text{x}1.39\text{x}(2\text{UCAPE})^{1/2}=20.3\text{ms}^{-1}$$

To reduce these velocities further (they are rather large indicating velocity changes of 18ms^{-1} and 6ms^{-1}) both $(H_u-h)/H_u$ and d/H_d must be

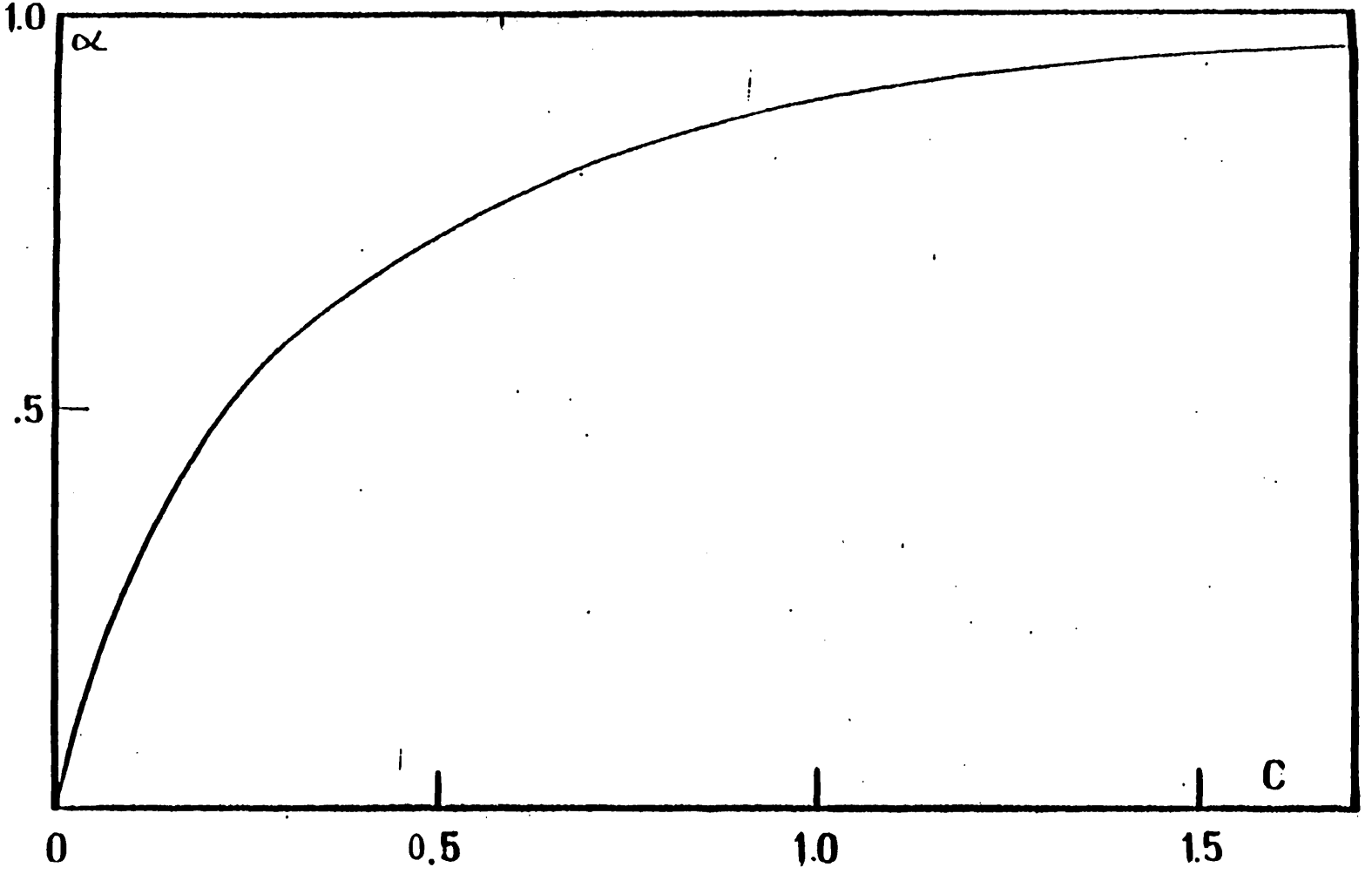


Figure 2.2.7. Variation of updraught outflow depth, α, with propagation speed, c(=F), Tam (1979).

α_u	F_u	α_d for F_d/F_u equal to:			
		$\sqrt{10}$	$\sqrt{5}$	$\sqrt{2}$	$\sqrt{1}$
0.0	0.0	0.0	0.0	0.0	0.0
0.1	0.022	0.234	0.182	0.130	0.1
0.2	0.056	0.431	0.347	0.256	0.2
0.3	0.100	0.591	0.493	0.375	0.3
0.4	0.157	0.720	0.621	0.491	0.4
0.5	0.230	0.817	0.730	0.599	0.5
0.6	0.326	0.887	0.818	0.699	0.6
0.7	0.464	0.953	0.888	0.793	0.7
0.8	0.678	0.967	0.939	0.874	0.8
0.9	1.125	0.987	0.975	0.944	0.9
1.0		1.0	1.0	1.0	1.0

Table 2.2.1

α_u	$(u_1/d)_{top}$	$(u_1/d)_{bottom}$ for F_d/F_u equal to:			
		$\sqrt{10}$	$\sqrt{5}$	$\sqrt{2}$	$\sqrt{1}$
0.0	∞	∞	∞	∞	∞
0.1	46.11	13.46	19.23	31.64	46.11
0.2	16.80	4.75	7.02	11.69	16.80
0.3	9.07	2.32	3.59	6.12	9.07
0.4	5.43	1.25	2.02	3.62	5.43
0.5	3.45	0.70	1.19	2.23	3.45
0.6	2.23	0.39	0.70	1.39	2.23
0.7	1.37	0.22	0.39	0.82	1.37
0.8	0.78	0.10	0.20	0.45	0.78
0.9	0.34	0.04	0.08	0.18	0.34
1.0	0.0	0.0	0.0	0.0	0.0

Table 2.2.2

increased - see table 2.2.2. Alternatively the ratio UCAPE/DCAPE would need to be increased. The calculation of this ratio from observations is not straightforward and will be discussed in chapter five. However it is an important bulk parameter which would shed some light upon which of these downdraught models resemble the atmosphere most closely.

The pressure change on outflow for the updraught may be obtained by integrating 2.7, using 2.9 and 2.10 for $\delta\phi_p$ and $\delta\phi_1$, and 2.33 for $z_1 - z_0$.

$$\frac{\delta p_1}{\rho_s} = \frac{1}{2} c_u^2 E_u + \epsilon_u c_u^2 \left(\cosh \frac{z_0 - h}{F_u H_u} - 1 \right)$$

where $\epsilon_u = 1 + (1 - E_u)^{1/2}$. Similarly for the downdraught:-

$$\frac{\delta p_1}{\rho_s} = \frac{1}{2} c_d^2 E_d + \epsilon_d c_d^2 \left(\cosh \frac{z_1 - d}{F_d H_d} - 1 \right).$$

The mean pressure change within the updraught where $\alpha_u = (H_u - h)/H_u$ is

$$\frac{1}{2} c_u^2 E_u + \epsilon_u c_u^2 \left(\frac{F_u}{\alpha_u} \sinh \frac{\alpha_u}{F_u} - 1 \right),$$

and for the downdraught the mean pressure change is obtained by replacing all "u" subscripts by "d" where $\alpha_d = d/H_d$.

For the same value of α_u used in the velocity calculation the maximum and mean pressure perturbations for updraught and downdraught may be calculated in units of "UCAPE".

For the updraught $\delta p_{max} = 0.58$. $\delta p_{mean} = 0.25$.

For the downdraught $\delta p_{max} = 0.40$. $\delta p_{mean} = 0.20$.

Comparing with NM where $\delta p_{max} = 0.42$ and $\delta p_{mean} = 0.16$ we see that

updraughts and downdraughts which become deeper on outflow experience larger pressure perturbations. However there is now an unsymmetric pressure perturbation pattern on outflow with a larger mean pressure rise in the updraught outflow compared with the downdraught outflow.

The model with a shallow downdraught developed in this section requires both updraught and downdraught to become deeper on outflow, when the updraught inflow depth h is less than $0.5H_u$. For this flow $c_u h - c_d(H_d - d) > 0$ since $c_u = c_d$ and $h > H_d - d$. Therefore there is a net upward mass flux on the convective scale. This must be balanced by a net downward mass flux on the mesoscale or large scale.

The shallow downdraught models in section 2.2.2 and this section, 2.2.3, both require inflow to updraught and downdraught from the same level. The "interlocking" model developed in chapter four includes a convective updraught with net deviation of all streamlines. Updraught and downdraught air flows come from different levels. The updraught model for this system is explored in section 2.3.

2.3 Models of Convective Updraughts with Net Deviation of All Streamlines.

There are two quite different cases to consider. First, when each streamline "jumps" vertically maintaining its relative position so there is no overturning of the flow; second, where the air overturns and the air from the lowest level flows out at the highest level.

2.3.1 Model of a Two-Dimensional Convective Updraught with Net Deviation of All Streamlines.

This two-dimensional model of a convective updraught is included for completeness in describing convective updraughts. Such a circulation is suggested as a component of two-dimensional mid-latitude squall lines in TMM82, and indeed in recent observational models of certain case studies of West African squall clusters (J.Testud, personal communication). The circulation is shown schematically in figure 2.3.1 below.

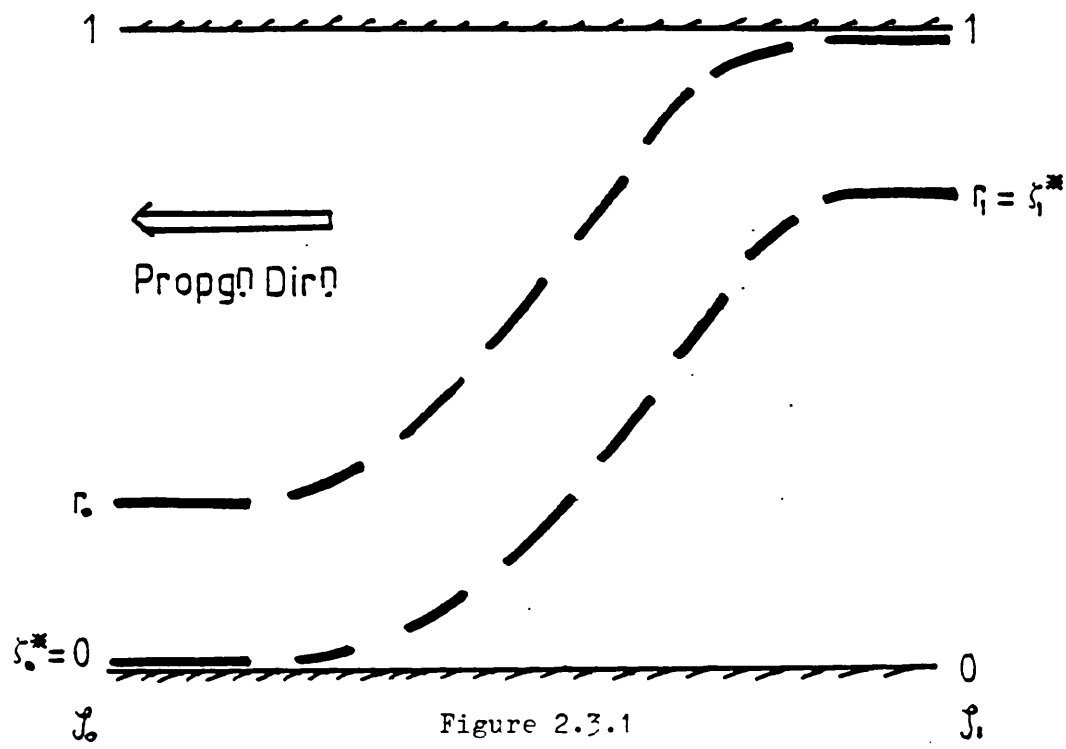


Figure 2.3.1

The derivation of the displacement equation describing the two-dimensional updraught follows that for the three-dimensional updraught 2.14.

If the outflow and inflow are both in the x-z plane the mass continuity equation (2.2) for a two-dimensional circulation becomes

$$\rho_0 u_0 \, dz_0 = \rho_1 u_1 \, dz_1 \tag{2.37}$$

The inflow reference level, ζ_0^*, for flow leaving at $\zeta_1^* = r_1$ is 0. The boundary conditions for the limitimg streamlines are now

$$\zeta_0(\zeta_1 = 1) = r_0 , \tag{2.38}$$

$$\zeta_0(\zeta_1 = r_1) = 0 . \tag{2.39}$$

The displacement equation 2.40 set out below together with the two boundary conditions, 2.38 and 2.39, describe a two-dimensional convectively driven circulation where all inflow is at the front and all outflow is to the rear.

$$\left(\frac{d\zeta_0}{d\zeta_1}\right)^2 = 1 - E - \frac{2}{F^2}\int_0^{\zeta_0} (\zeta_1 - \zeta_0)\, d\zeta_0 . \tag{2.40}$$

The unsheared, incompressible solutions with D=0 and $u_0 = c$ are considered. For this case 2.40 may be differentiated with respect to ζ_1 to obtain

$$\frac{d^2\zeta_0}{d\zeta_1^2} = -\frac{1}{F^2}(\zeta_1 - \zeta_0) \tag{2.41}$$

The solution to 2.41 with the boundary conditions 2.38 and 2.39 must also satisfy 2.40. Hence we have

$$\zeta_0 = \zeta_1 - \frac{1}{\sinh \frac{1-r_1}{F}} \left[(1-r_0) \sinh \frac{\zeta_1 - r_1}{F} + r_1 \sinh \frac{1-\zeta_1}{F} \right] \tag{2.42}$$

where $$F\left(1-\sqrt{1-E}\right)\sinh\frac{1-r_1}{F} = 1-r_0-r_1\cosh\frac{1-r_1}{F}\,. \qquad (2.43)$$

Solutions taking the positive square root have relative inflow at the rear which is not described by these equations and are now discarded.

The y-component of vorticity η for a two-dimensional steady flow is additionally constrained in the following way. From TMM80

$$\frac{D}{Dt}\left[\frac{\eta}{\rho}+\frac{g(\gamma-B)(z-z_0)}{\rho_0 u_0}\right]=0.$$

If the inflow is initially unsheared then

$$\frac{\eta_1}{\rho_1} = -\frac{g(\gamma-B)(z_1-z_0)}{\rho_0 u_0}$$

or $$\frac{\partial u_1}{\partial z_1} = -\frac{g(\gamma-B)(z_1-z_0)}{\rho_0 u_0}\,\rho_1\,.$$

In a convective updraught in which log potential temperature increases on ascent relative to the environment, the outflow must become negatively sheared. This implies that a solution which stagnates at any point on outflow must have relative inflow at the rear. Solutions with E=1 are not possible for a two dimensional updraught if we insist that there must be no relative inflow at the rear. Rewriting 2.43

$$E = 1-\left(1-\frac{1-r_0-r_1\cosh\frac{1-r_1}{F}}{F\sinh\frac{1-r_1}{F}}\right)^2$$

we see that E can only be positive when the updraught outflow depth is greater than the inflow depth (ie. $1-r_0>r_1$ or $1-r_1>r_0$). The

variation of F with E is shown in figure 2.3.2 for r_o=0.2 with r_1 taking the values 0.7, 0.8 and 0.9. Positive values of E only occur for updraughts which become deeper on outflow.

Outflow profiles of relative velocity, pressure perturbation and entropy perturbation are shown in figures 2.3.3 and 2.3.4 for E=+0.5 and E=-0.5. In the former case only profiles for updraughts whose depths increase are shown. In both figures an initially unsheared velocity profile becomes negatively sheared on outflow. The pressure perturbation is positive and increases with height. Log potential temperature increases for air throughout the updraught.

2.3.2 Model of a Three-Dimensional Overturning Convective Updraught with Net Deviation of All Streamlines.

The general equations describing this flow were developed in section 2.1. The inflow reference level, ζ_o^*, for air leaving at $\zeta_1^*=r_1$ is r_o. As in MM the case of maximum efficiency of conversion of CAPE to mean flow kinetic energy is considered. The flow leaving at $\zeta_1=r_1$ is brought to rest with E=1. This is the first three-dimensional circulation described in which the reference streamline, from $\zeta_o^*=r_o$ to $\zeta_1^*=r_1$, experiences a net deviation, as in figure 2.1.2.

When there is no net change in the depth of the flow, $1-r_1=r_o$, it can be seen from figure 2.3.5 that $\delta p(r_1)$ increases as r_1 increases. Both total pressure deviation (δp_{total}) and dynamical pressure change (δp_{dynam}) are plotted as a function of r_1. The difference between the two curves is the contribution from heating which increases as r_1 increases. The net displacement of air leaving at height r_1 is r_1-r_o and increases with r_1. The dynamical pressure

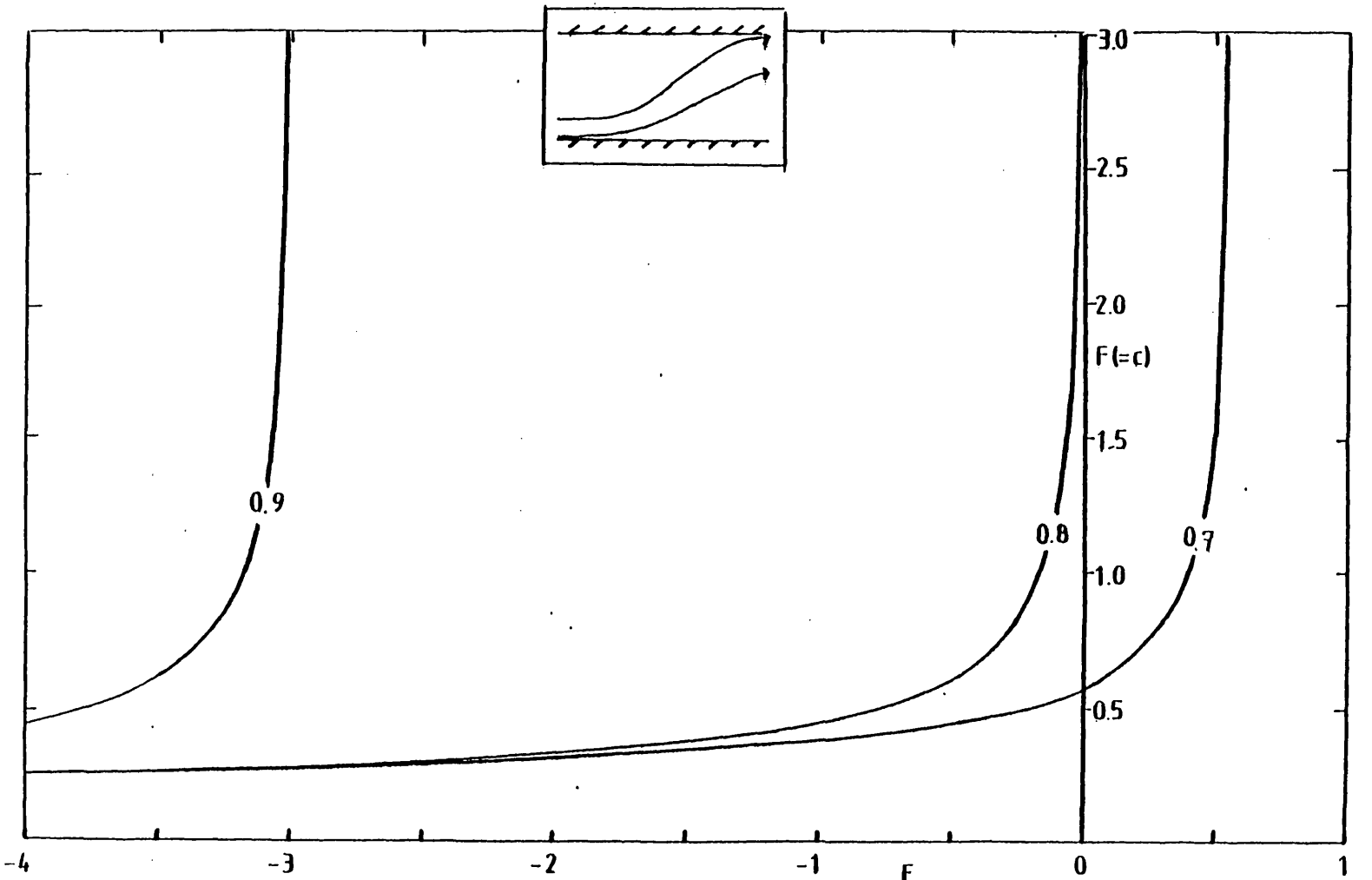
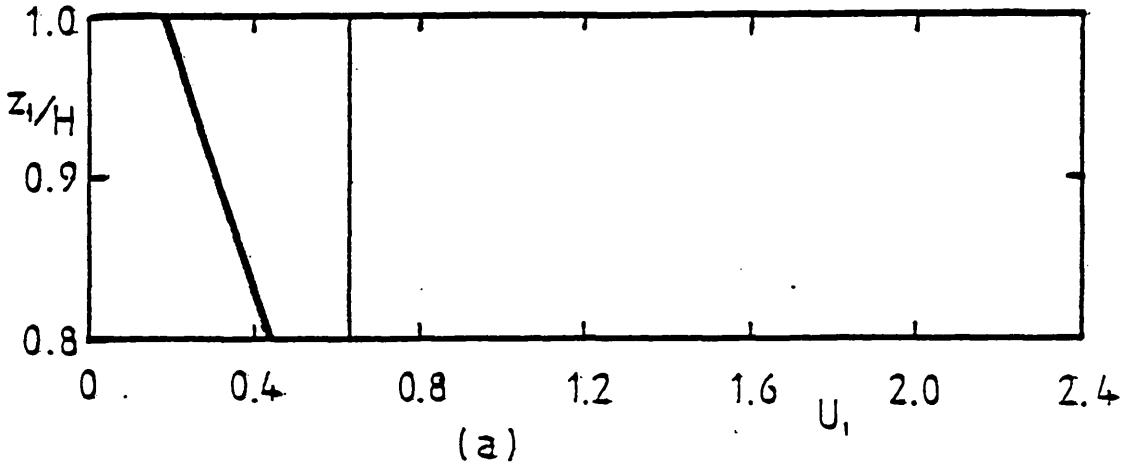
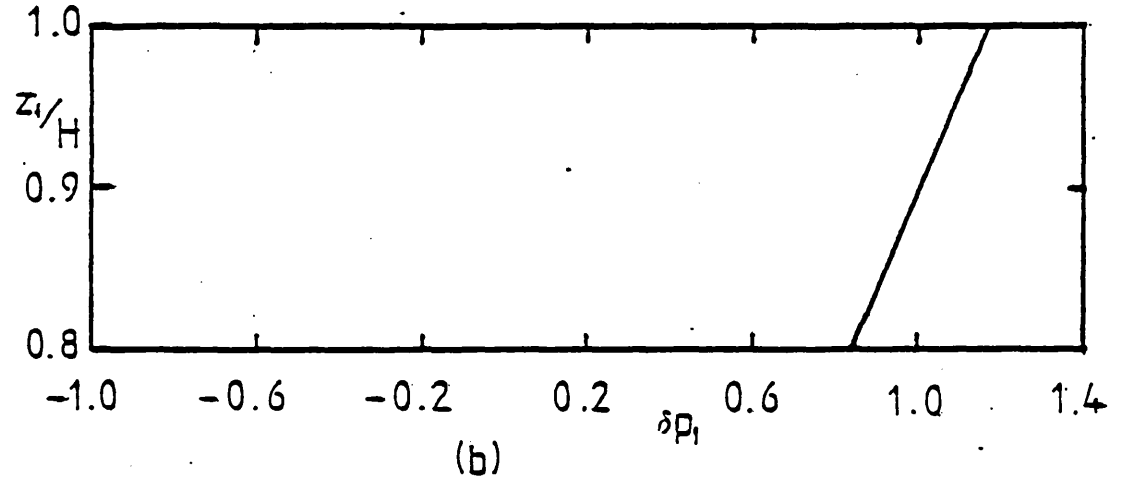


Figure 2.3.2 Variation of propagation speed with E for two-dimensional convective updraughts with inflow depth $r_i = 0.2$. Outflow depth $r_j = 0.7, 0.8, 0.9$





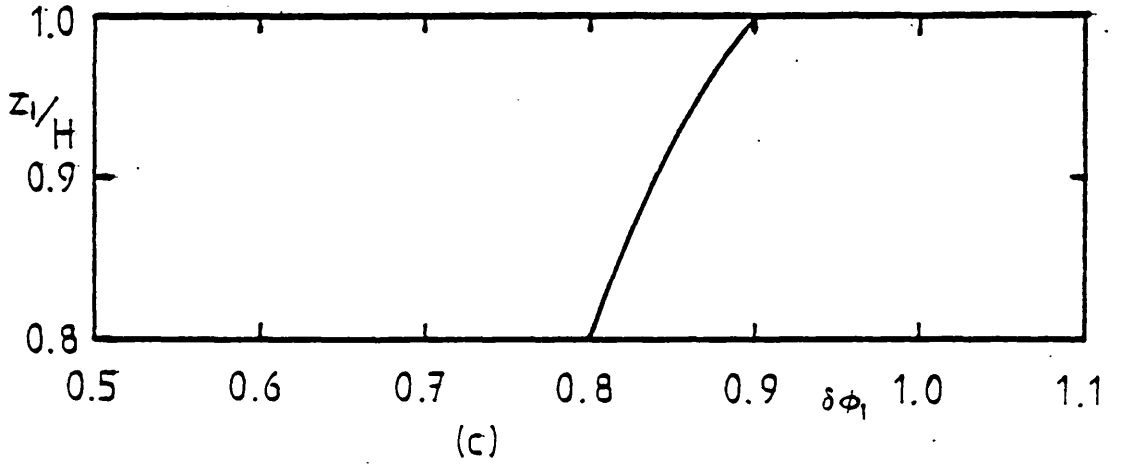
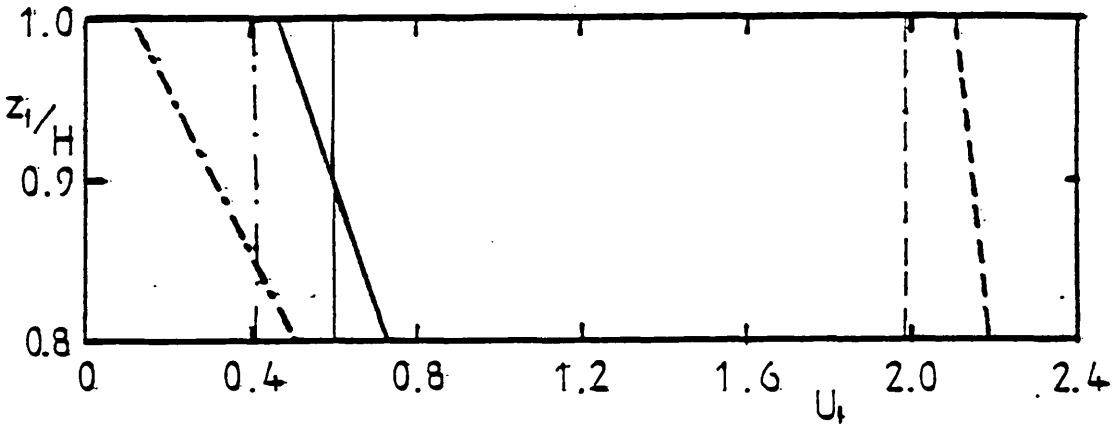
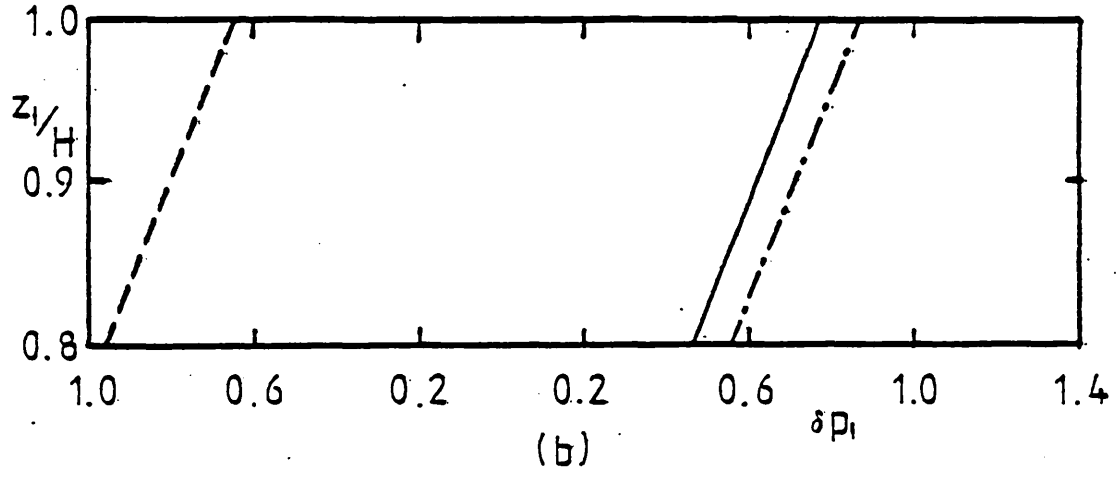


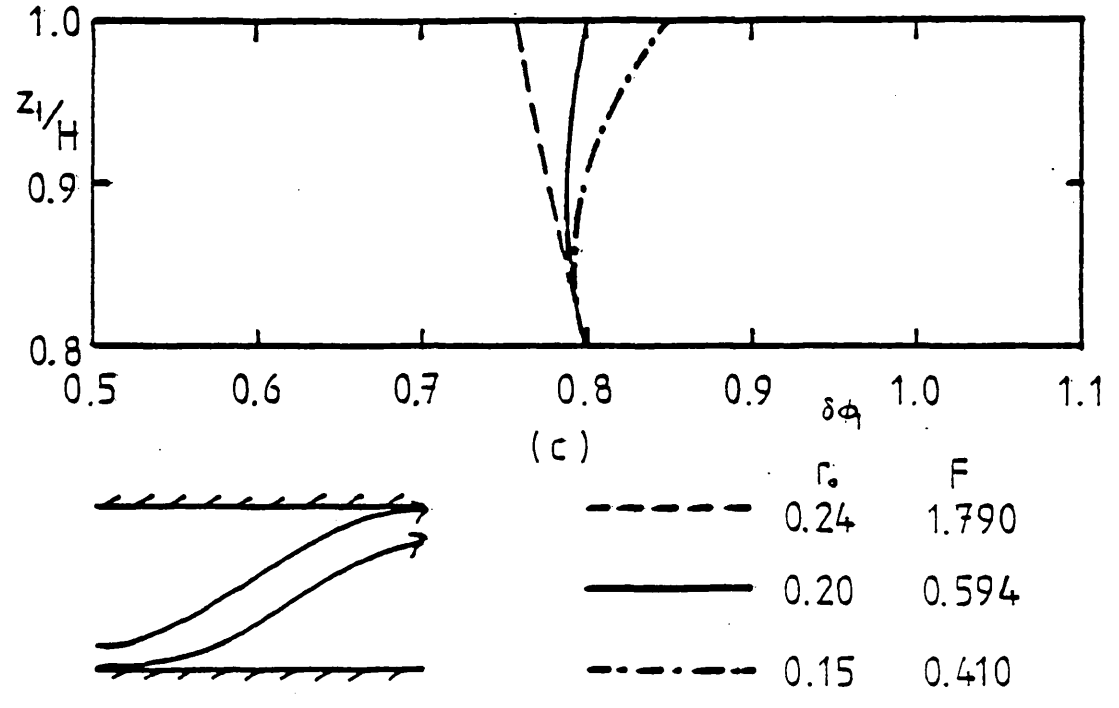
Figure 2.3.3. Outflow profiles of (a) relative outflow velocity, (b) pressure perturbation and (c) log(θ) perturbation. Inflow speed, $F = 0.632$, $r_* = 0.1$, $r_1 = 0.8$, $E = +0.5$.



(a)



(b)



(c)

r_o	F
0.24	1.790
0.20	0.594
0.15	0.410

Figure 2.3.4. As figure 2.3.3 except $E = -0.5$ and r_o takes the values 0.24, 0.20 and 0.15

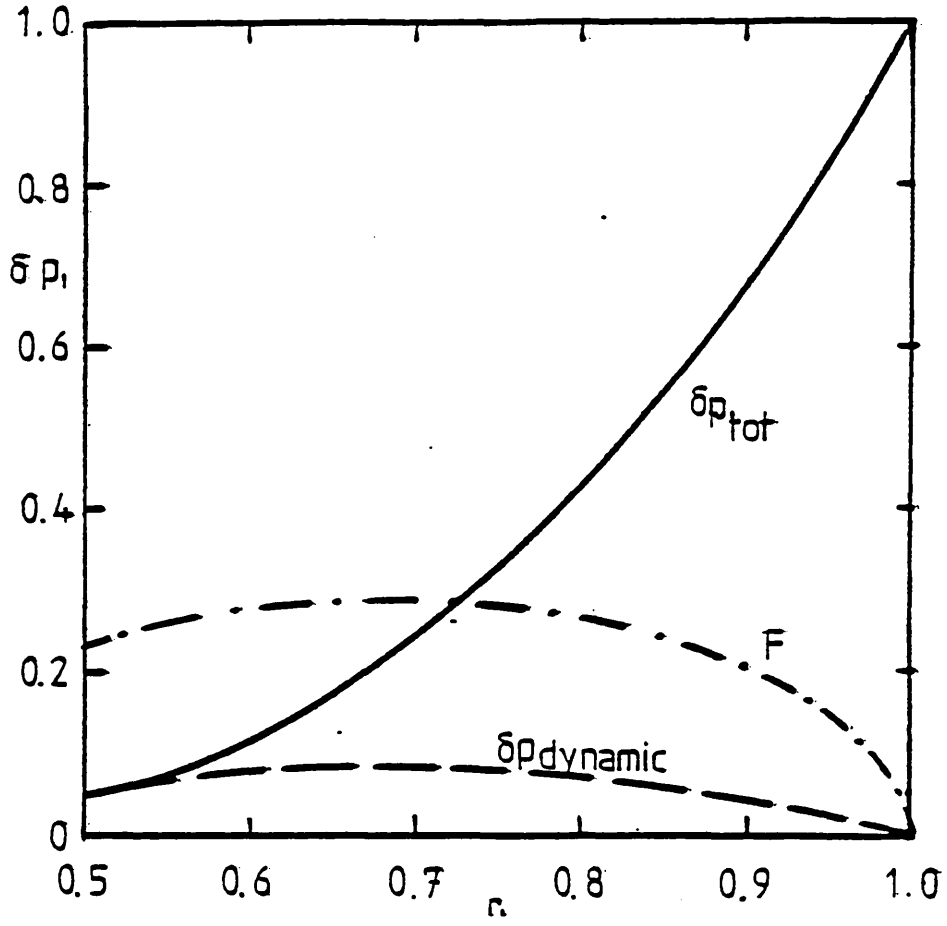


Figure 2.35. δp_{total} and $\delta p_{dynamic}$ at $r_1 = r_1$ as r_1 varies for constant depth three-dimensional updraugts ($r_2 = 1 - r_1$). $E = 1$. The variation of F (propagtion speed) with r_1 is also shown.

change has a maximum for r_1 between 0.65 and 0.7 and falls to zero as r_1 tends to 1. This follows the behaviour of F which peaks similarly and falls to zero as r_1 tends to 1. It appears that as the flow becomes increasingly narrower, a greater percentage of CAPE released goes into the pressure perturbation rather than into mean flow kinetic energy.

The effect of changing the outflow depth with respect to the inflow depth is shown in figures 2.3.6 and 2.3.7 for two different values of r_1. For a relatively "thick" updraught with r_o=0.45 the pressure changes are of the same order as those for $r_o=r_1=0.5$. As the updraught outflow becomes narrower the total pressure change along the reference streamline increases. (This contrasts with the case of no net deviation of the reference streamline described in section 2.2.3.)

For the "thinner" updraught, r_o=0.2, the pressure changes are an order of magnitude larger. This large pressure perturbation where the updraught is narrower is clearly going to be important at the interface between a convective flow and a forced flow, treated in chapter four. There is a maximum sustainable pressure change for a forced flow as will be shown in chapter three.

2.3.3 The Effect of Shear and Compressibility.

The general displacement equation 2.14 with the boundary conditions 2.15 and 2.16 describe a three-dimensional convective updraught of variable depth with compressibility and a sheared inflow. Initially, updraughts with constant depth are considered ie. $1-r_1=r_o$. Such a configuration is illustrated in figure 2.3.8 below. The numerical method for solving these equations is described in appendix A.

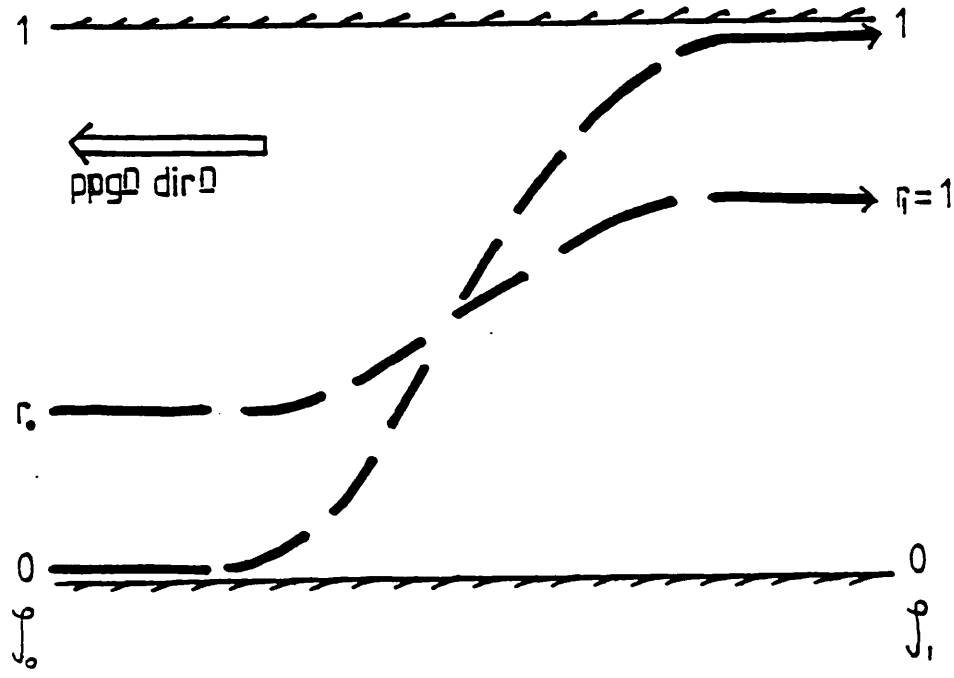


Figure 2.3.8

When the inflow velocity is sheared a definition of propagation speed must be made for the system. Here the propagation speed is defined as the mean inflow speed in the relative frame (weighted by the density for the compressible case). The propagation speed is normalised by $(2UCAPE)^{1/2}$ while the inflow shear is normalised by $(g(\gamma-B))^{1/2}$.

Figure 2.3.9 shows the variation of the propagation speed with inflow depth for incompressible (D=0) and compressible flows (D=1). Here and in all compressible cases the density scale height and the height scale of the disturbance are equal for tropical cumulonimbi. In general the compressible solutions have much lower propagation speeds than the incompressible solutions.

The variation of propagation speed with a negative vertical shear of the horizontal velocity is shown in figure 2.3.10 for D=0 and in figure 2.3.11 for D=1. The easterly jet profile commonly found in the

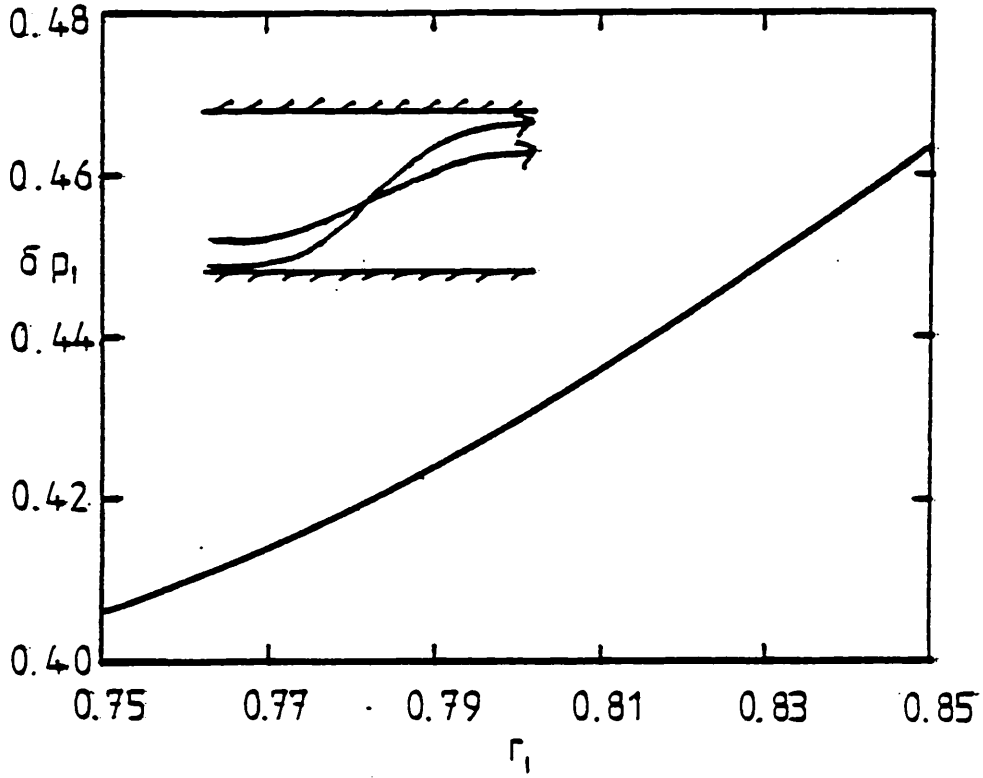


Figure 2.3.6. Variation of $\delta p(r_1)$ with r_1 for "thin" updraughts of constant inflow depth, r_0=0.2. E=1.

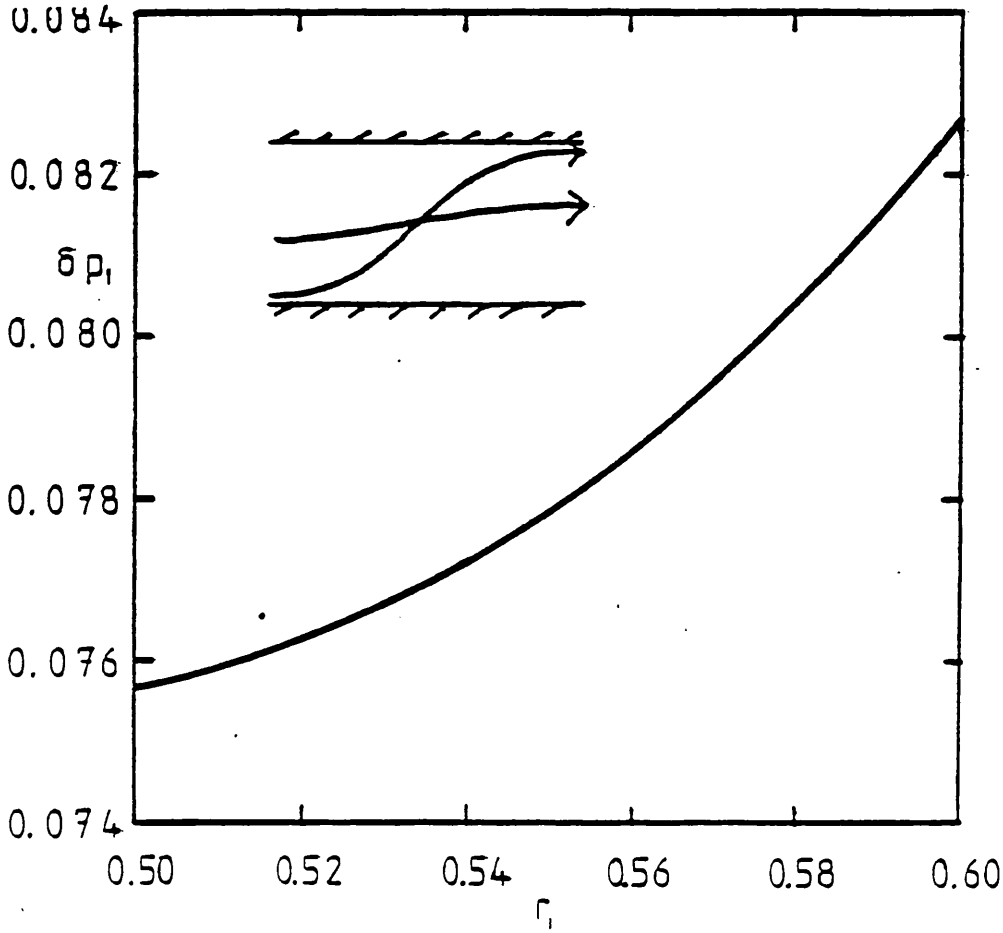


Figure 2.3.7. As figure 2.3.6 except for "thick" updraughts with r_0=0.45.

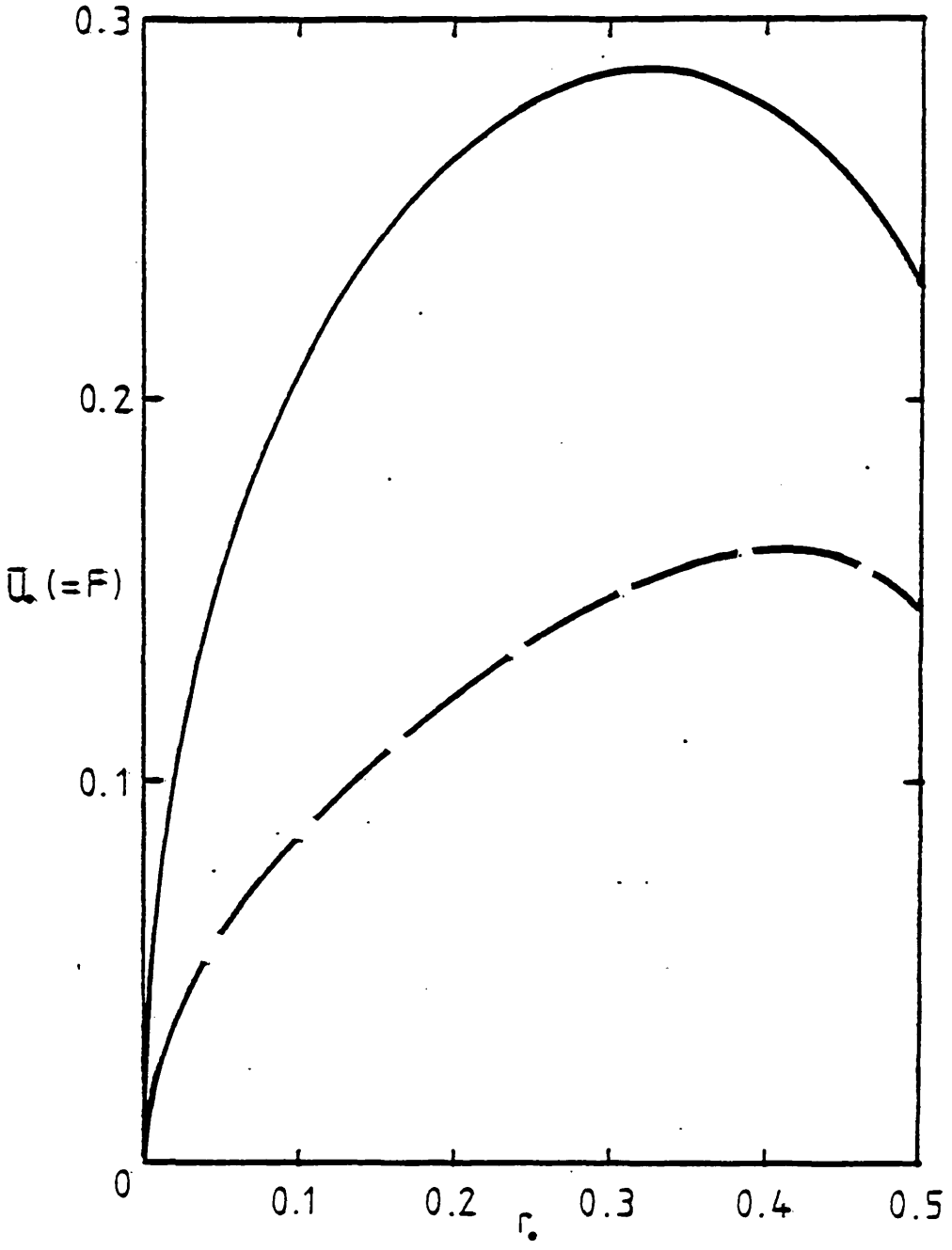


Figure 2.3.9. Variation of propagation speed with inflow depth, r_*, for constant depth overturning convective updraughts ($1-r_l=\dot{r}_*$). D=0 (solid line) and D=1 (broken line). E=1.

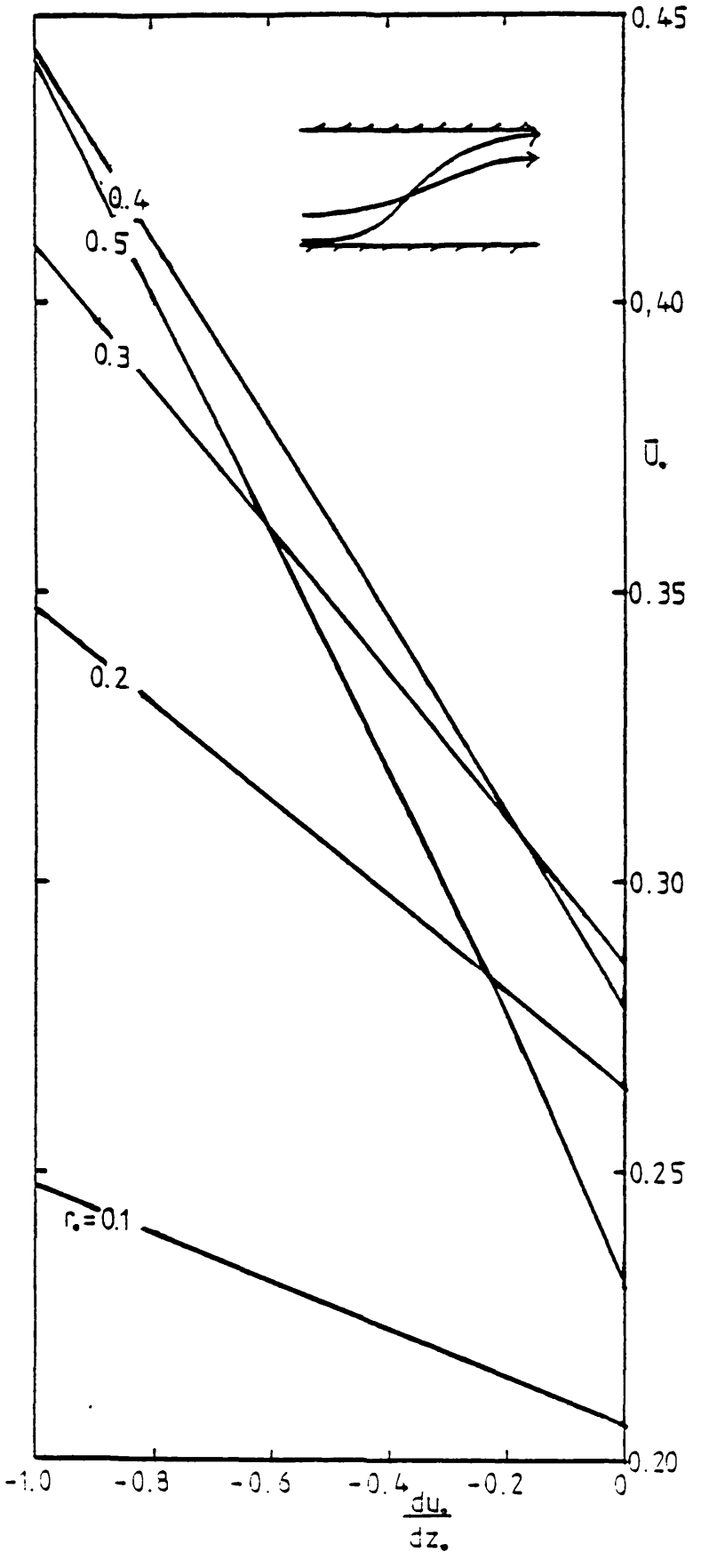


Figure 2.3.10. Variation of propagation speed (defined to be the mean relative inflow speed) with uniform inflow shear. D=0, E=1 and $1-r_i=r_*$

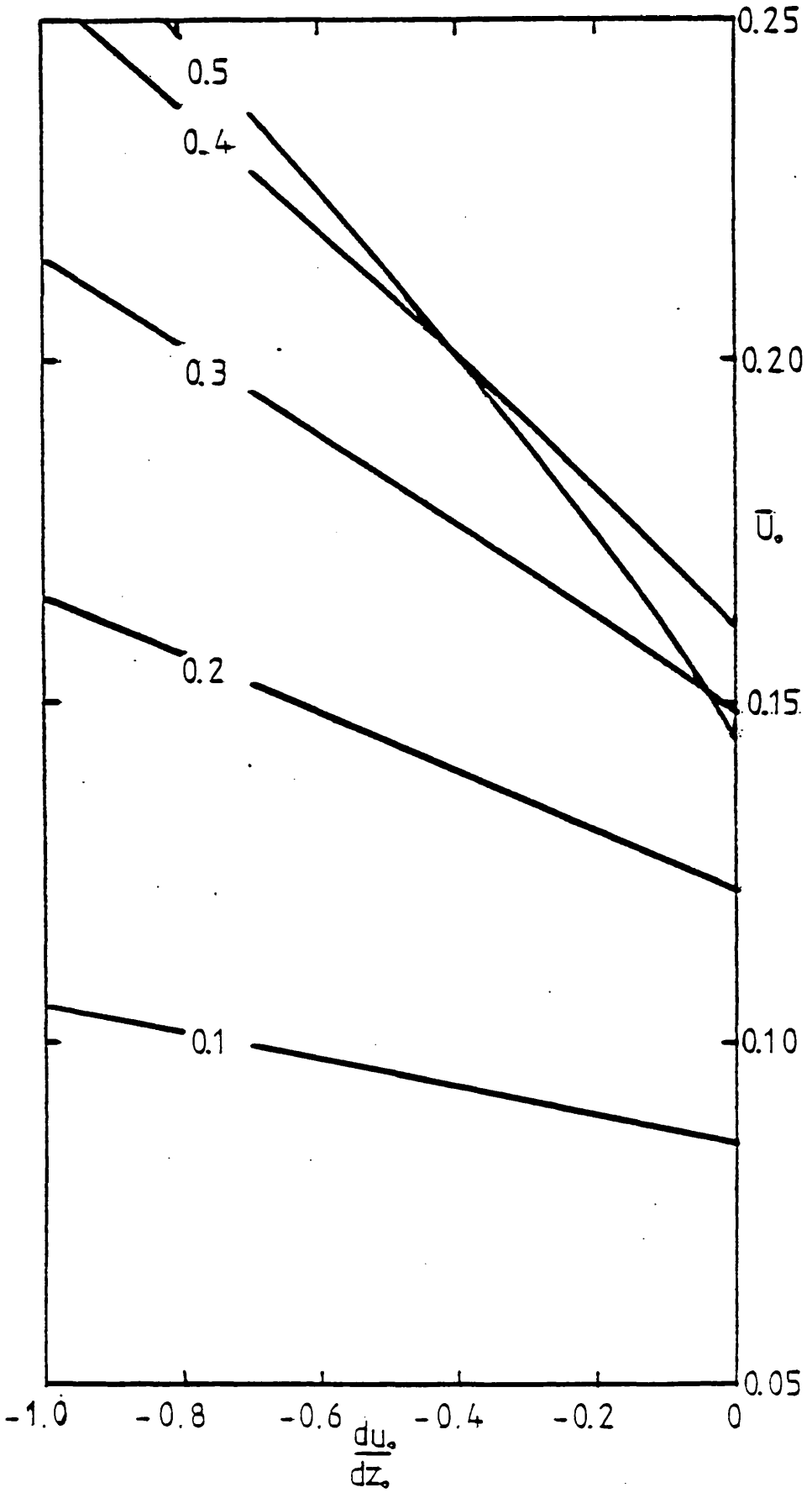


Figure 2.3.11. As for figure 2.3.10 except for D=1.

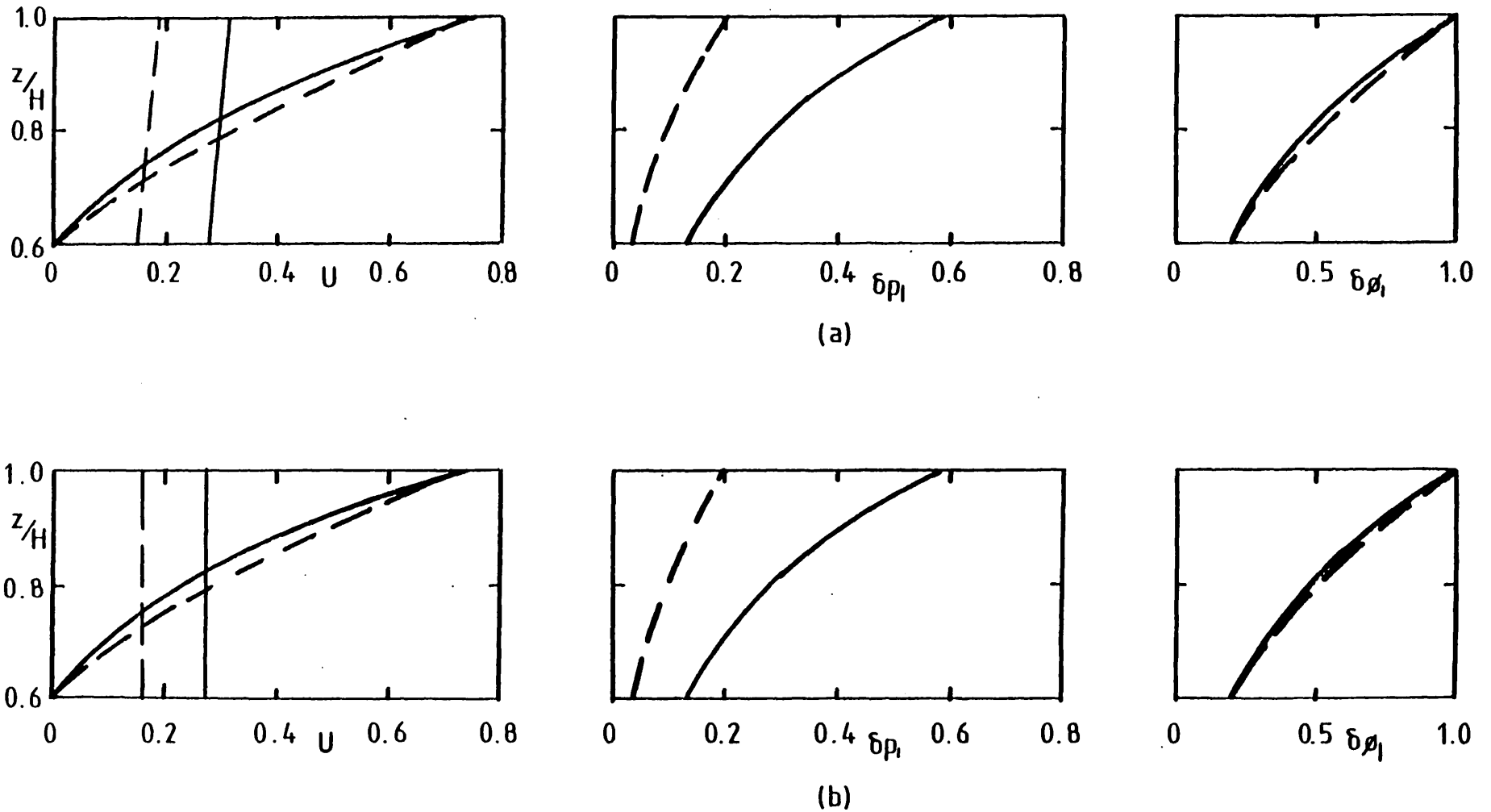


Figure 2.3.12. Outflow profiles of relative velocity, pressure and log(θ) perturbation for a three-dimensional convective updraught. Inflow relative velocity with (a) shear = -0.1 and (b) shear = 0 are shown y thinner lines r_c=0.4, r_t=0.6, E=1. The compressible case is shown by broken lines.

tropics has negative shear in the boundary layer. The variation of propagation speed with shear is linear for inflow depths between 0.1 and 0.3 for $-1 \leqslant du_o/dz_p \leqslant 0$. For larger inflow depths the propagation speed increases less than linearly with increasing negative shear.

Outflow profiles of relative velocity, pressure perturbation and entropy perturbation were calculated for unsheared and sheared inflow profiles ($du_o/dz_p = 0$ and -0.1) for incompressible and compressible flows for a variety of inflow depths. The method of calculation of u_1, δp_1 and $\delta\phi_1$ is given in appendix A. Results are essentially similar for different inflow depths ($0.1 \leqslant r_o \leqslant 0.5$). The case with $r_o = 0.4$ is shown in figure 2.3.12.

Outflow velocity is generally larger in the middle-layers for compressible solutions compared with incompressible solutions. Since the density is lower on outflow, the flow must be faster. The pressure perturbation for the reference streamline is lower - because the propagation speed is lower in the compressible cases, and because the pressure change is scaled by the exponential factor $\exp(-\gamma_1 D)$. Entropy increases are larger in the compressible case for air leaving in the middle of the outflow layer. This is a consequence of larger net vertical displacements of air parcels.

Thin updraughts whose depths change on ascent are now considered ie. $1-r_1 \neq r_o$, to assess the relative importance of the change of depth to the propagation speed. Such an updraught is sketched in figure 2.3.13 below.

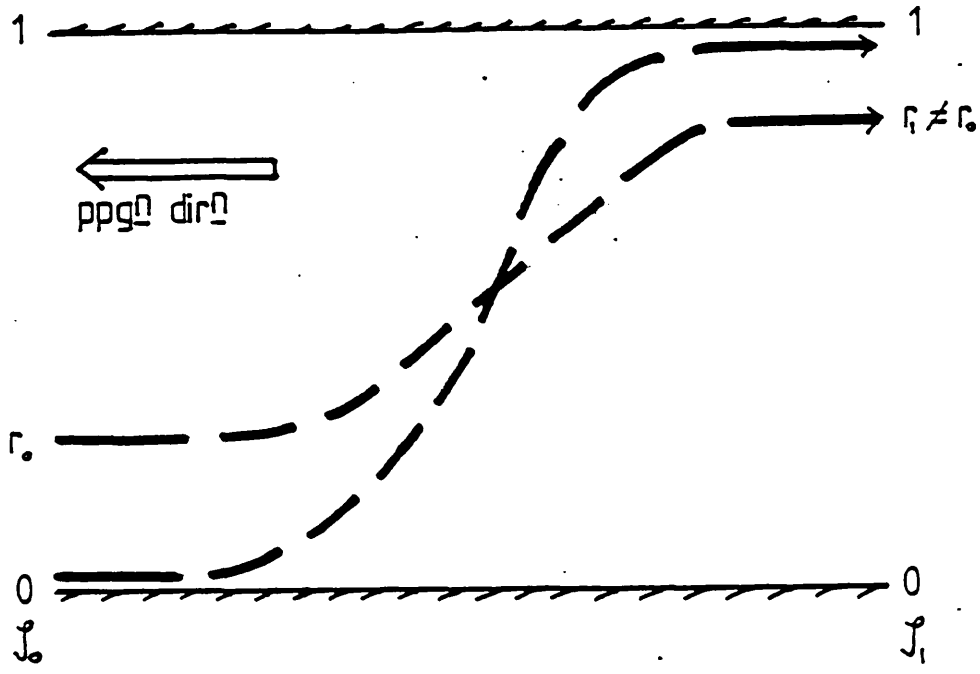


Figure 2.3.13

The same procedure for solving the general displacement equation 2.14 with the boundary conditions 2.15 and 2.16 was followed as in the first part of this section.

The variation of propagation speed with r_1 for constant inflow depth, r_o, is shown in figure 2.3.14. A 10% change in r_1 (for r_o=0.2) produces a 38% change in propagation speed for $r_o \sim 1-r_1$.

Figure 2.3.15 shows the variation of propagation speed with shear for an updraught with depth r_o=0.2 on inflow. This variation is plotted for a narrower outflow depth (r_1=0.9), an equal outflow depth (r_1=0.8) and a broader outflow depth (r_1=0.7). As the outflow depth increases the propagation speed increases for a given shear. Compressible results with D=1 show a similar trend in figure 2.3.16. A 10% change in shear for du_o/dz_o=-0.5, r_o=0.2 and r_1=0.8, produces a 3% change in propagation speed. The variation of propagation speed with shear is seen to be relatively unimportant compared with outflow

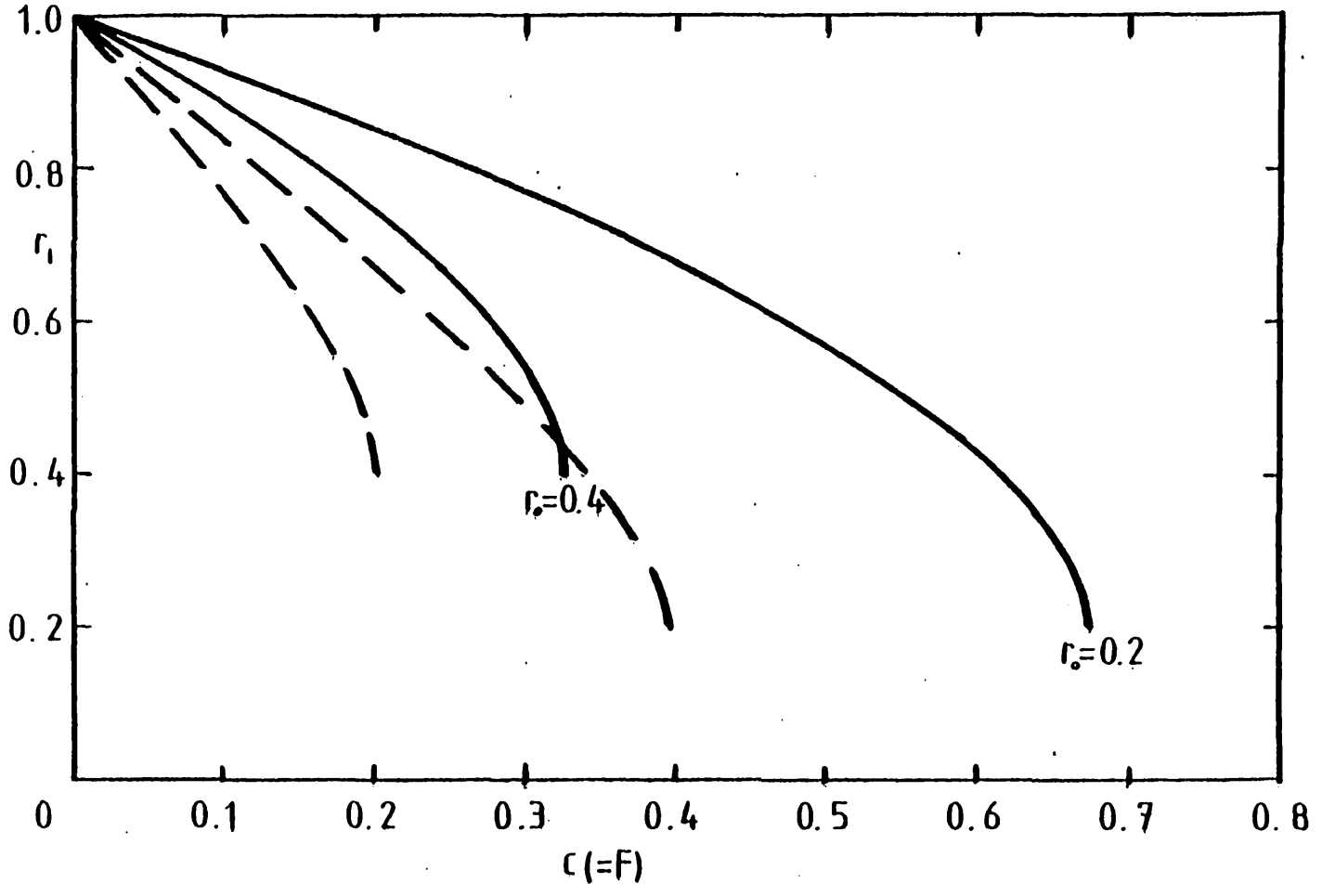


Figure 2.3.14. Variation of outflow depth (r_1) with propagation speed for variable depth updraughts. Incompressible (D=0, solid line) and compressible (D=1, broken line) results are shown for inflow depths r_0=0.2 and 0.4. E=1.

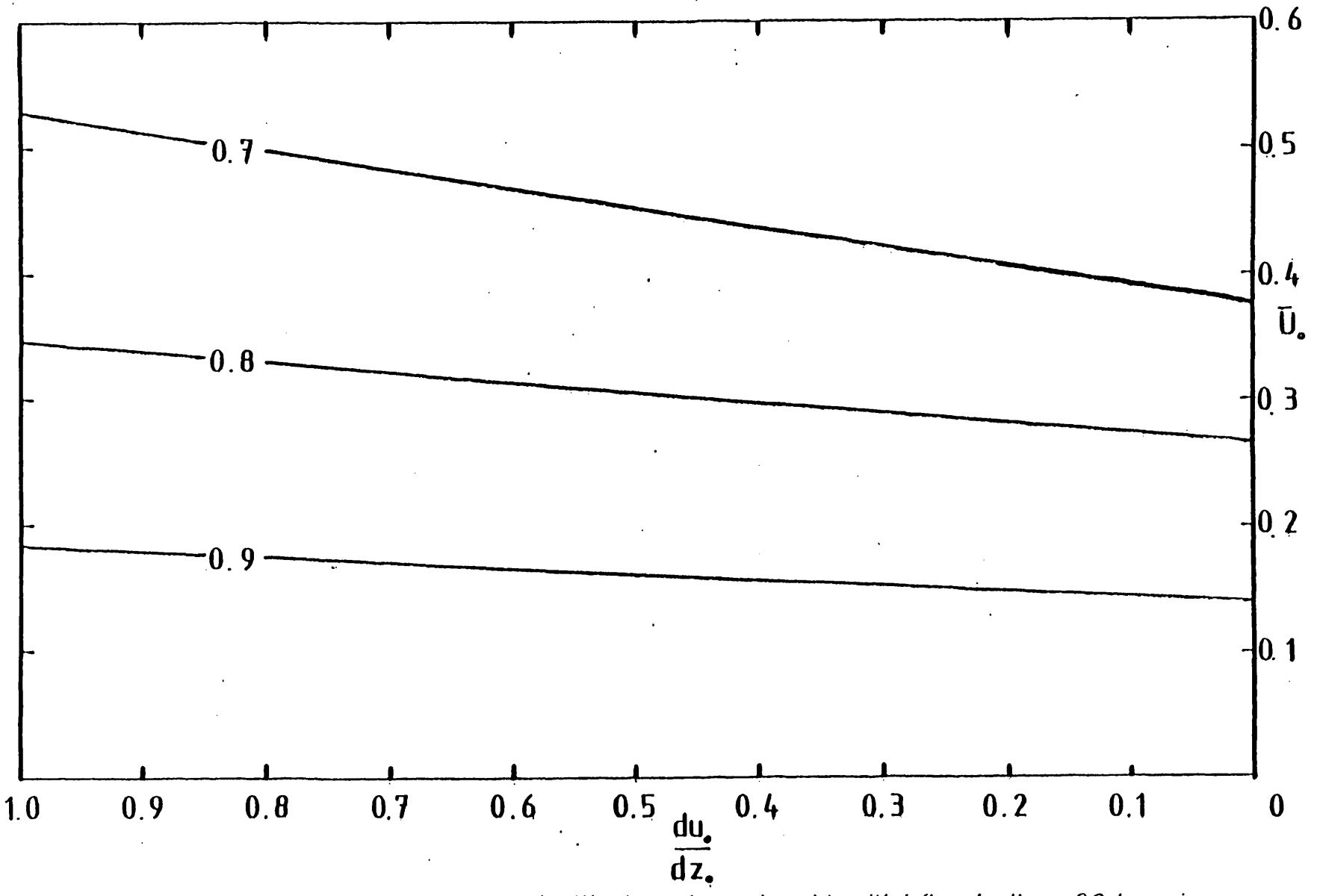


Figure 2.3.15. Variation of propagation speed with shear for updraughts with inflow depth r_o =0.2 becoming thinner (r_i =0.9), remaing constant depth (r_i =0.8) or thicker (r_i =0.7) on outflow. D=0, E=1.

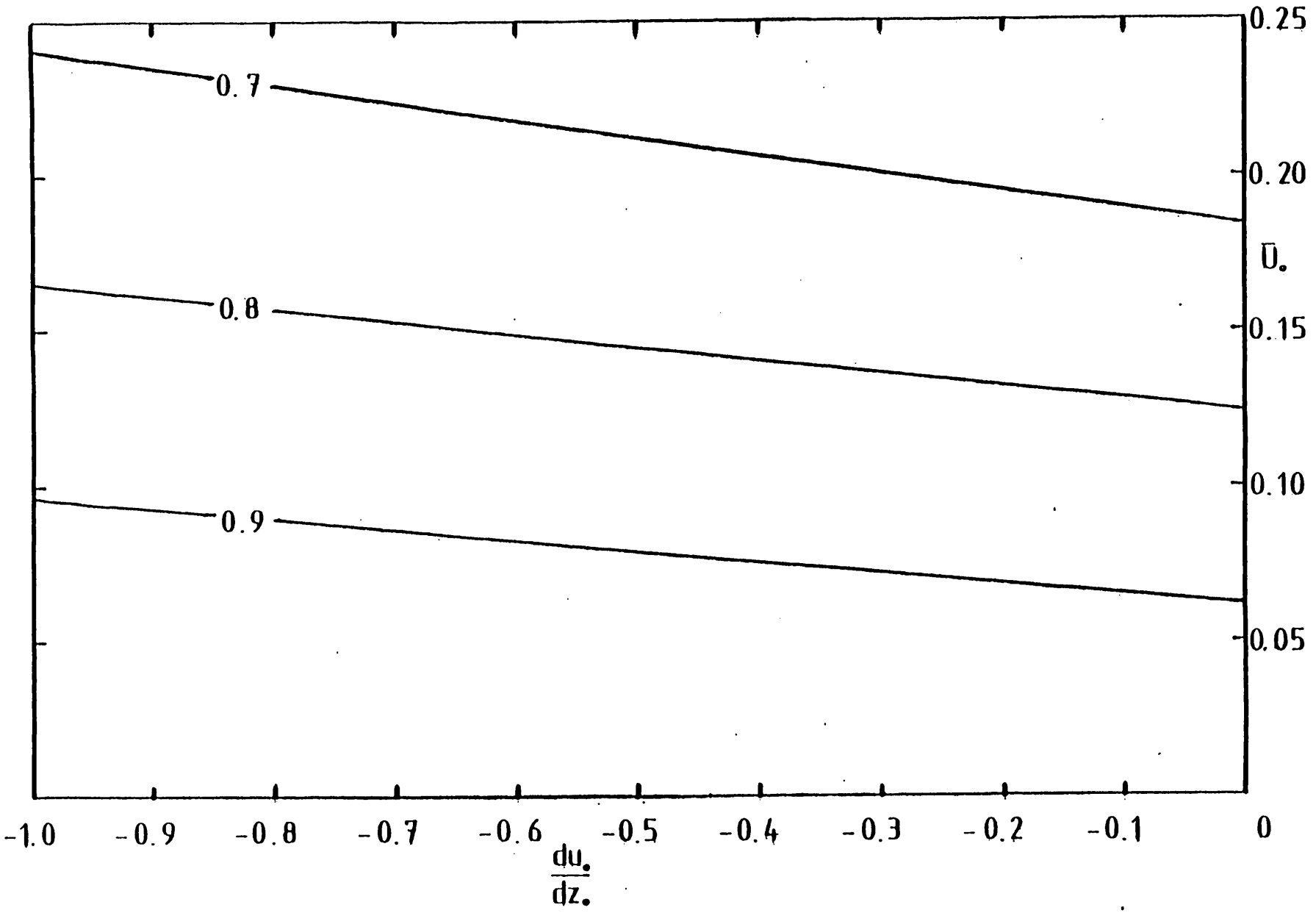


Figure 2.3.16. As figure 2.3.15 except D=1.

depth.

The variation of propagation speed with outflow depth will not be quantified here. As we will see in chapter four the depth of the convective updraught outflow is controlled by the forced flow and by the pressure perturbation at the interface between the two layers on outflow. The outflow depth is not known at the outset.

2.4 Summary.

The properties of the model of a convective updraught developed in MM have been documented and the partitioning of outflow pressure perturbation has been explored. The magnitude of the vertically averaged mean pressure change was estimated to be +1.6mb for UCAPE=1000Jkg^{-1}. The outflow relative velocity profile stagnates at the mid-level and is increased by nearly 250% at the top of the outflow. Profiles with positive pressure perturbation and relative velocity with a mid-level easterly jet and increasing westerly flow at upper and lower levels will be used as forcing mechanisms to a mesoscale circulation in chapter three.

Various modifications to the basic flow are considered in trying to produce less severely sheared (more realistic) profiles. A shallow downdraught travelling with the same speed as the updraught requires the evaporation of large amounts of precipitation. For saturated descent to occur, retaining the criterion of "maximum mechanical efficiency" for updraught and downdraught, a vertical pressure gradient must exist across the intervening outflow air. However mid-level acceleration of air would be required, since this flow is bounded by positive pressure perturbations, which is not found

observationally. In chapter four the forced flow has a positive pressure perturbation at the level $\zeta_1 = r_1$ falling to an (unconstrained) negative value at the surface. The trend is similar but the change in sign of the surface pressure perturbation implies a different type of velocity profile with middle level deceleration and lower level acceleration. The more complex model developed in section 2.2.3 with variable depth suggests the positive pressure perturbation is unsymmetric and increasing with height. Changing the level of the undeviated streamline reduces the maximum outflow velocity for updraughts and downdraughts which become thicker on outflow. In both this model and the preceding shallow downdraught model there is a net upward vertical mass transfer which requires compensating subsidence to occur either on the mesoscale or on the synoptic scale at some other location.

The "thin" updraughts developed in section 2.3 are believed to be more realistic since there is no longer an "undeviated" streamline. The two-dimensional model described in section 2.3.1 becomes increasingly negatively sheared on outflow. A few examples of such two-dimensional updraughts have been noted observationally including an apparantly two-dimensional updraught depicted in Chong et al (1983) in a West African Squall line. The three-dimensional updraught produces a larger positive pressure perturbation on outflow when the inflow layer is thinner. Compressibility is seen to decrease the propagation speed of the three-dimensional updraught by as much as 50%. Changing the depth of outflow relative to the inflow appears to be more important than introducing shear.

Of these properties summarised, the effects of non-uniform inflow shear and constant inflow pressure perturbation will be explored in

chapter three. A vertical gradient of pressure perturbation and warming at low and high levels are predicted by the models developed. However observations do not presently exist to confirm whether these conditions occur in the immediate post-squall region.

CHAPTER THREE

THE FORCED MESOSCALE RESPONSE TYPE "A"

3.1 Introduction and Derivation of the General Equations Describing a Forced Circulation.

This chapter and chapter four are concerned with the mesoscale forcing in the rear of the convection at the front of a squall cluster; in particular the response to the cloud induced pressure gradients. The philosophy is that the convective part of the squall line provides a very distinctive pressure field in the outflow of the squall, of order 10km behind the squall front. This pressure field is out of balance with the large scale environment and clearly some adjustment must take place. There are two main adjustment mechanisms on quite distinctive time and space scales, namely, geostrophic adjustment on a large space and time scale and gravity wave adjustment. The squall line is special in the sense that it introduces a pressure disturbance into the atmosphere which is propagating relative to the wind in the whole troposphere and it is thus likely that the adjustment mechanism is quite distinctive. This is probably the basic reason why the mesoscale ascent and descent is so clearly different from that appearing in mid-latitudes where the pressure perturbation does not propagate relative to the wind everywhere. In this chapter the effect of a propagating pressure field, produced by the squall line convective dynamics is examined to see what types of response can exist in a steady frame of reference

moving at the speed of the squall line.

Outflows from the three-dimensional squall line models were documented in chapter two. These can be used in two different ways in modelling the interacting flows involving convective and forced (mesoscale) circulations. In this chapter the type "A" or "wake" model is described. This type "A" flow is illustrated below in figure 3.1.1.

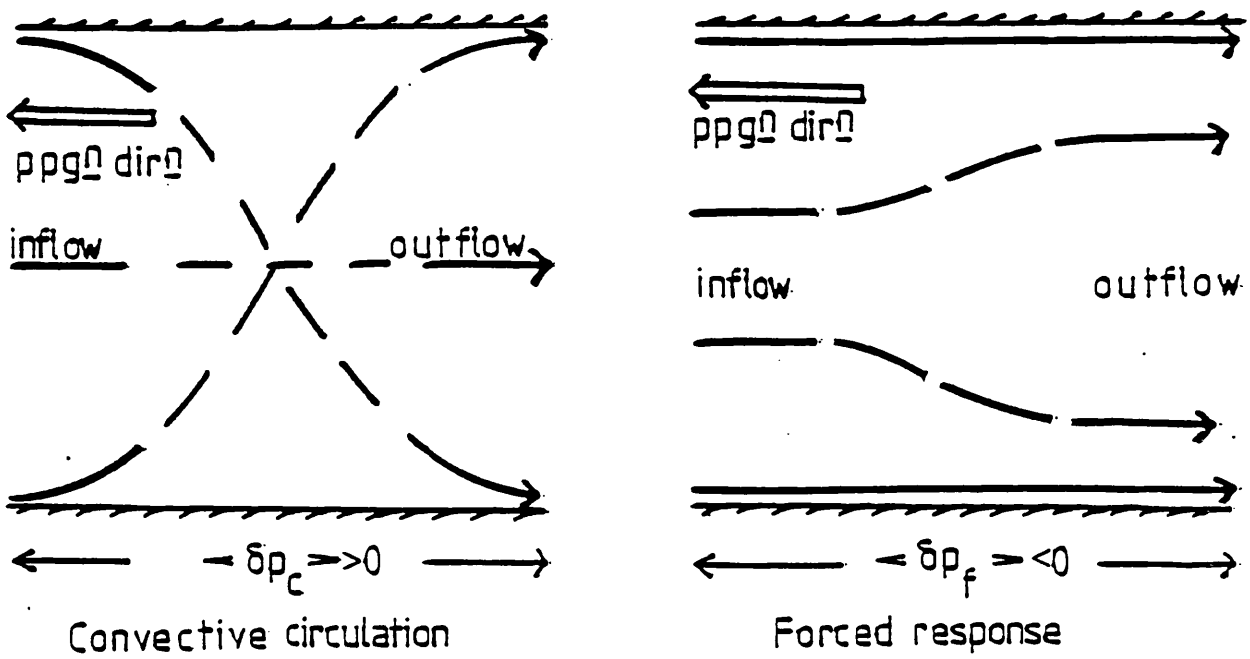


Figure 3.1.1

Outflow from a squall line model defines the inflow to the dynamical response model. The forcing profiles of pressure perturbation and relative velocity drive a subsequent mesoscale response.

A type "B" or "interlocking" model is explored in chapter four to describe the high level mass injection by convective updraughts accompanied by a positive pressure deviation for this air. The environmental air is envisaged to be simultaneously forced down by this mass injection and the positive pressure perturbation on outflow

between updraught and downdraught decelerates the air at middle levels. This approach was illustrated in figure 2.1.2 of the previous chapter.

The three-dimensional convective circulations described in chapter two produce a net momentum flux in the x-direction which is not balanced by the x-component of the horizontal pressure gradient on the scale of the squall line elements. From the x-momentum and the mass continuity equations, integrating from $x=-\infty$ to $x=+\infty$ and vertically from z=0 to z=H:-

$$\int_0^H \left[\rho u^2 + p\right]_{-\infty}^{+\infty} dz + \frac{\partial}{\partial y}\int_0^H \int_{-\infty}^{+\infty} \rho uv\, dx\, dz + \left[\int_{-\infty}^{+\infty} \rho uw\, dx\right]_0^H = 0$$

When the flow is bounded by rigid lids the last term is zero since w(0)=w(H)=0. In both two and three-dimensional systems net x-momentum flux generation in the x-direction cannot be balanced by a net transverse flux generation. Thus both two and three-dimensional flows must conserve the quantity $\int_0^H \left[\rho u^2 + p\right] dz$.

Three-dimensional flows such as that described in MM76 generate x-momentum flux if the inflow and outflow basic states about which pressure perturbations are calculated are assumed to be the same. If $p_h(x,z)$ represents the hydrostatic pressure and departures are represented by $\delta p(z)$ then we must have:-

$$\int_0^H \left(\rho_1 u_1^2 + p_h(+\infty, z_1) + \delta p(z_1)\right) dz_1 = \int_0^H \left(\rho_0 u_0^2 + p_h(-\infty, z_0) + \delta p(z_0)\right) dz_0$$

Since in the squall line model $\int_0^H \left(\rho_1 u_1^2 + \delta p(z_1)\right) dz_1 > \int_0^H \left(\rho_0 u_0^2 + \delta p(z_0)\right) dz_0$

it follows that, $\int_0^H p_h(+\infty, z_1)\, dz_1 < \int_0^H p_h(-\infty, z_0)\, dz_0$, ie. there must be an external pressure field producing a net pressure decrease across the convective system. This may be formalised in the model as a pressure

change along the rigid upper boundary doing work on the fluid. In the real atmosphere the upper fluid boundary (the tropopause) may be distorted such that H=H(x) and w(H)≠0 at all points on the upper boundary. In this way the term $\left[\int_{-\infty}^{+\infty} \rho u w \, dz\right]_0^{H(x)}$ may contribute to the x-momentum flux generation,

ie. $$\int_0^{H(+\infty)} (\rho u_1^2 + \delta p(z_1)) dz_1 - \int_0^{H(-\infty)} (\rho_0 u_0^2 + \delta p(z_0)) dz_0$$

$$= -\left[\int_0^{H(+\infty)} p_h(z_1) dz_1 - \int_0^{H(-\infty)} p_h(z_0) dz_0\right] - \int_{-\infty}^{+\infty} \rho u w \, dx \Big|_{H(x)}$$

The momentum flux term dependent on the upper boundary configuration may show net descent if the hydrostatic base state pressure fall is insufficient to balance the x-momentum flux increase generated. Much remains to be understood in this problem which this analytic treatment cannot hope to explore. Numerical simulations could be usefully employed in this context.

In chapter two we have seen that a mean positive pressure deviation is generated in the x-direction; it is suggested that such an imbalance in the two-dimensional momentum field could be responsible for a forced two-dimensional circulation of the type described as a "jump" solution in TMM80. In section 3.2.1 the results of TMM80 for forced flows are summarised and extended to include non-uniform inflow velocity and compressibility. In particular, jet-like velocity profiles of the type obtained as outflow in MM with certain modifications are used as inflow profiles to the forced circulation. Finally, the forced downdraught model is extended so that all streamlines experience a net vertical displacement in

preparation for the "interlocking" type "B" model described in chapter four.

Derivation of the equations describing the forced response procedes in the same manner as in chapter two for the convective circulation up to 2.14. However, it should be noted that the appropriate form of the mass continuity equation for a two-dimensional circulation is given by 3.1 below.

$$\rho_0 u_0 dz_0 = \rho_1 u_1 dz_1 \qquad (3.1)$$

The archetype of the forced response may conveniently be described by examining the simple two-dimensional circulation schematically represented in figure 3.1.2 below. The extension to multiple layers is easily obtained once the simple model has been formulated as will be shown later.

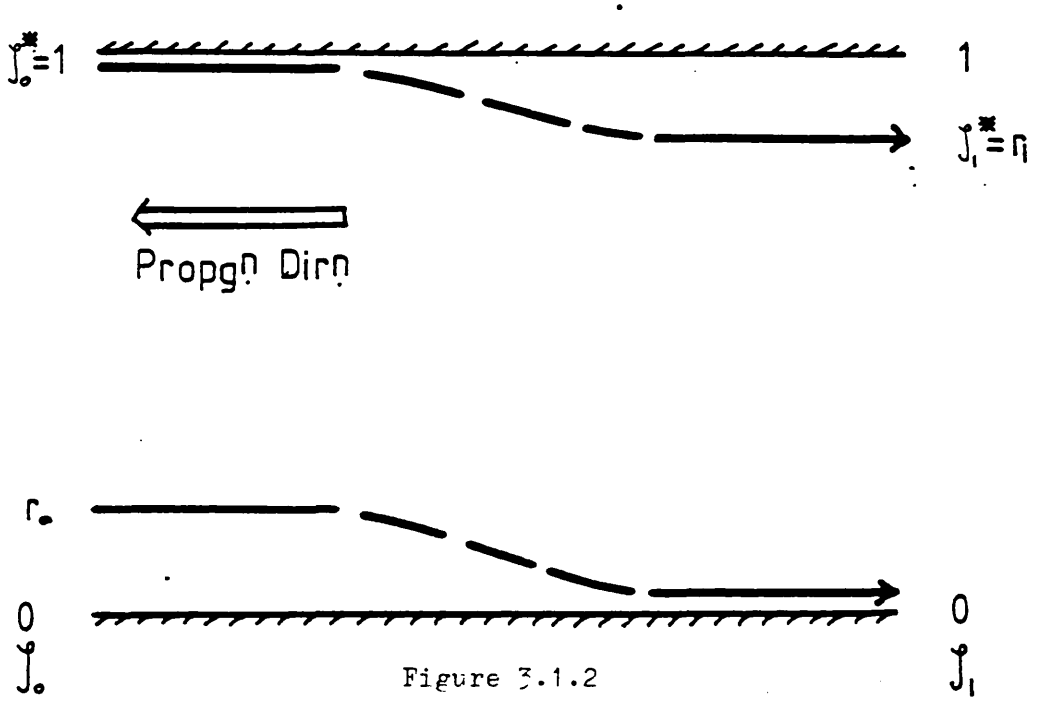


Figure 3.1.2

In this case the top streamline is assumed to descend from the

upper boundary, $\mathcal{J}_0=1$, to leave at $\mathcal{J}_1=r_1$ while the lowest streamline descends from $\mathcal{J}_0=r_0$ to $\mathcal{J}_1=0$. These boundary conditions are expressed formally below:-

$$\mathcal{J}_0(\mathcal{J}_1 = r_1) = 1 \tag{3.2}$$

$$\mathcal{J}_0(\mathcal{J}_1 = 0) = r_0 \tag{3.3}$$

γ is now the downdraught lapse rate of potential temperature for air taking part in the forced circulation so that $\gamma<B$, and in the dry adiabatic case $\gamma=0$. Hence $F^2=c^2/(g(\gamma-B)H^2)$ is negative and will be replaced by $-F_f^2=c^2/(g(\gamma-B)H^2)$. The reference level for pressure changes is the streamline leaving at $\mathcal{J}_1^*=r_1$. Hence $\mathcal{J}_0^*=1$. 2.14 then becomes:-

$$\left(\frac{d\mathcal{J}_0}{d\mathcal{J}_1}\right)^2 = \left[1-\left(\frac{c}{u_0}\right)^2\left(E-\frac{2}{F_f^2}\int_1^{\mathcal{J}_0}(\mathcal{J}_1-\mathcal{J}_0)\,d\mathcal{J}_0\right)\right]\exp\left[-2(\mathcal{J}_1-\mathcal{J}_0)D\right]. \tag{3.4}$$

3.4 and the boundary conditions 3.2 and 3.3 form the general equation set for compressible, sheared, two-dimensional forced circulations.

3.2.1 Summary of the Results of TMM80 Relating to Forced Flows.

An unsheared incompressible flow is considered in TMM80. The flow is depicted below in figure 3.2.1. For this circulation $u_0=c$ and 3.4 becomes:-

$$\left(\frac{d\mathcal{J}_0}{d\mathcal{J}_1}\right)^2 = 1 - E + \frac{2}{F_f^2}\int_1^{\mathcal{J}_0}(\mathcal{J}_1-\mathcal{J}_0)\,d\mathcal{J}_0. \tag{3.5}$$

The boundary conditions, from 3.2 and 3.3, are:-

$$\mathcal{J}_0(\mathcal{J}_1=1) = 1 \tag{3.6}$$

$$\mathcal{J}_0(\mathcal{J}_1=0) = 0. \tag{3.7}$$

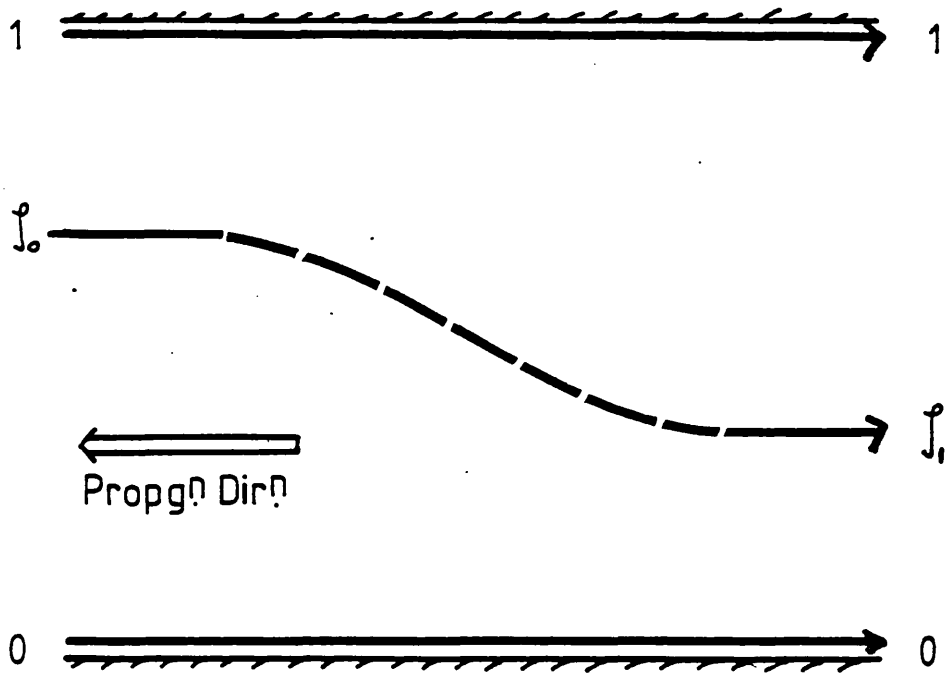


Figure 3.2.1

Differentiation of 3.5 with respect to $\mathcal{J}$ yields a linear equation but this powerful linearisation for a finite amplitude system can only be employed if the inflow is unsheared because only in this case can $d\mathcal{J}_0/d\mathcal{J}_1$ ($\neq 0$ by definition) be cancelled in the differential equation.

$$\frac{d^2\mathcal{J}_0}{d\mathcal{J}_1^2} = \frac{1}{Ff^2}\left(\mathcal{J}_1-\mathcal{J}_0\right) \tag{3.8}$$

The solution to the simple equation 3.8 with boundary conditions 3.6 and 3.7 must also satisfy the non-linear equation 3.5 giving amplitude constraints and yielding:-

$$\mathcal{J}_0 = \mathcal{J}_1 - F_f \cos\frac{1}{F_f}\left(1 \pm \sqrt{1-E}\right) \sin\frac{\mathcal{J}_1}{F_f} \tag{3.9}$$

$$\text{where } \sin(1/F_f)=0 \tag{3.10}$$

$$\text{so } 1/F_f = n\pi \quad (n=1,2,3,\ldots).$$

For no return flow to exist at the rear we require that $u_1/u_0 \geq 0$ for all values of $\mathcal{J}_1$ in the range $0 \leq \mathcal{J}_1 \leq 1$. From 3.9 use of the continuity equation 3.1 leads to the following expression for u_1/u_0:-

$$\frac{u_1}{u_0} = 1 - \cos\frac{1}{F_f}\left(1 \pm \sqrt{1-E}\right) \cos\frac{\mathcal{J}_1}{F_f} \,. \tag{3.11}$$

The integer n determines the permitted number of descent and ascent regions. When n is odd ($\cos(1/F_f)=-1$) and $\cos(\mathcal{J}_1/F_f)$ takes the value (-1), we see that the negative root is required to avoid relative inflow occurring at the rear, while if $\cos(\mathcal{J}_1/F_f)$ takes the value (+1), then the condition $u_1/u_0 \geq 0$ implies $1+(1-(1-E)^{1/2}) \geq 0$ or $E \geq -3$. When n is even ($\cos(1/F_f)=+1$), the negative root is again required with the condition $E \geq -3$. The upper limit for E is 1, otherwise the solutions to 3.11 would not be physically meaningful.

Unlike the solution to the eigenvalue equation (2.29) for the three-dimensional convective circulation described in MM, F_f may take an infinite number of values (one for each positive value of n), physically representing vertical modes, and F_f is independent of E. Even with n specified, the solution to 3.8 is not uniquely determined and a closure must be invoked such as specifying the dynamical pressure change (proportional to E) along the reference streamline. Solutions which maximise the increase in mean flow kinetic energy are

considered as in MM, a condition which effectively maximises the mechanical efficiency of the circulation. Since potential energy is being created by the system the net work done by the pressure field is therefore maximised. In the next section the relationship between the mean flow kinetic energy and work done by the pressure field is demonstrated. The net increase of kinetic energy is given by 3.12 below, and for convenience this is normalised with respect to the inflow kinetic energy.

$$\frac{\int_0^H \frac{1}{2}\rho_1 u_1^2 dz_1 - \int_0^H \frac{1}{2}\rho_0 u_0^2 dz_0}{\int_0^H \frac{1}{2}\rho_0 u_0^2 dz_0} = \frac{1}{2}\epsilon^2 \qquad (3.12)$$

where $\epsilon = 1-(1-E)^{1/2}$. The relationship between ϵ^2 and E is shown in figure 3.2.2. ϵ^2, and the net kinetic energy production, are a maximum for $E = \pm 1$ corresponding to E=1 and E=-3. The double maximum in the kinetic energy curve may be interpreted by considering the form of the flow.

Expressions for pressure perturbation and entropy perturbation on outflow are obtained as follows. The pressure perturbation is given by 2.7, when $z_0^* = z_1^* = H$. Using 2.9 and 2.10 for $\delta\phi_p$ and $\delta\phi_1$. $J_1 - J_0$ is given by 3.9 hence:-

$$\frac{\delta p_1}{\rho_s} = \frac{1}{2}c^2 E + \epsilon c^2 \cos\frac{1}{F_f}\left(\cos\frac{J_1}{F_f} - \cos\frac{1}{F_f}\right).$$

This may be simplified using 3.11 to give:-

$$\frac{\delta p_1}{\rho_s} = \frac{1}{2}c^2 E + c^2\left(\sqrt{1-E} - \frac{u_1}{c}\right). \qquad (3.13)$$

$\delta\phi_1$ is given by 2.10 using 3.9:-

$$\delta\phi_1 = -(B-\gamma)HF_f \epsilon \cos\frac{1}{F_f} \sin\frac{f_1}{F_f} \tag{3.14}$$

u_1, $\delta p_1/\rho_s$ and $\delta\phi_1$ are now conveniently normalised by the quantities $(g(B-\gamma)H^2)^{1/2}$, $g(B-\gamma)H^2/2$ and $(B-\gamma)H$. These normalised expressions for u_1, δp_1 and $\delta\phi_1$ are:-

$$u_1 = F_f\left(1-\epsilon\cos\frac{1}{F_f}\cos\frac{f_1}{F_f}\right) \tag{3.15}$$

$$\delta p_1 = F_f^2\left[E + 2\left(\sqrt{1-E} - \frac{u_1}{F_f}\right)\right] \tag{3.16}$$

$$\delta\phi_1 = -F_f\epsilon\cos\frac{1}{F_f}\sin\frac{f_1}{F_f} \quad . \tag{3.17}$$

The n=1 and n=2 type solutions for E=+1 and E=-3 are shown in figures 3.2.3-3.2.6. The E=+1, n=1 type solution corresponds to forced descent. Descent with warming ($\delta\phi_1>0$) occurs at all levels with maximum net vertical displacement at $f_1=0.5$. The E=-3, n=1 type mode corresponds to forced ascent with cooling at all levels. The solution with E=0, having no forced pressure change across it has neither ascent nor descent occuring at any level, as can be seen from 3.6 and is not an eigensolution but represents the undisturbed flow. In effect E=0 marks a dividing line between ascent (E<0) and descent (E>0) regimes. It is important to note that unless the flow has a pressure gradient forcing across it (E<0 or E>0), no steady circulation can be maintained. In the descent outflow, low level air is accelerated and high level air is decelerated while the reverse is true of the ascending outflow.

For both ascent and descent, the mean outflow pressure

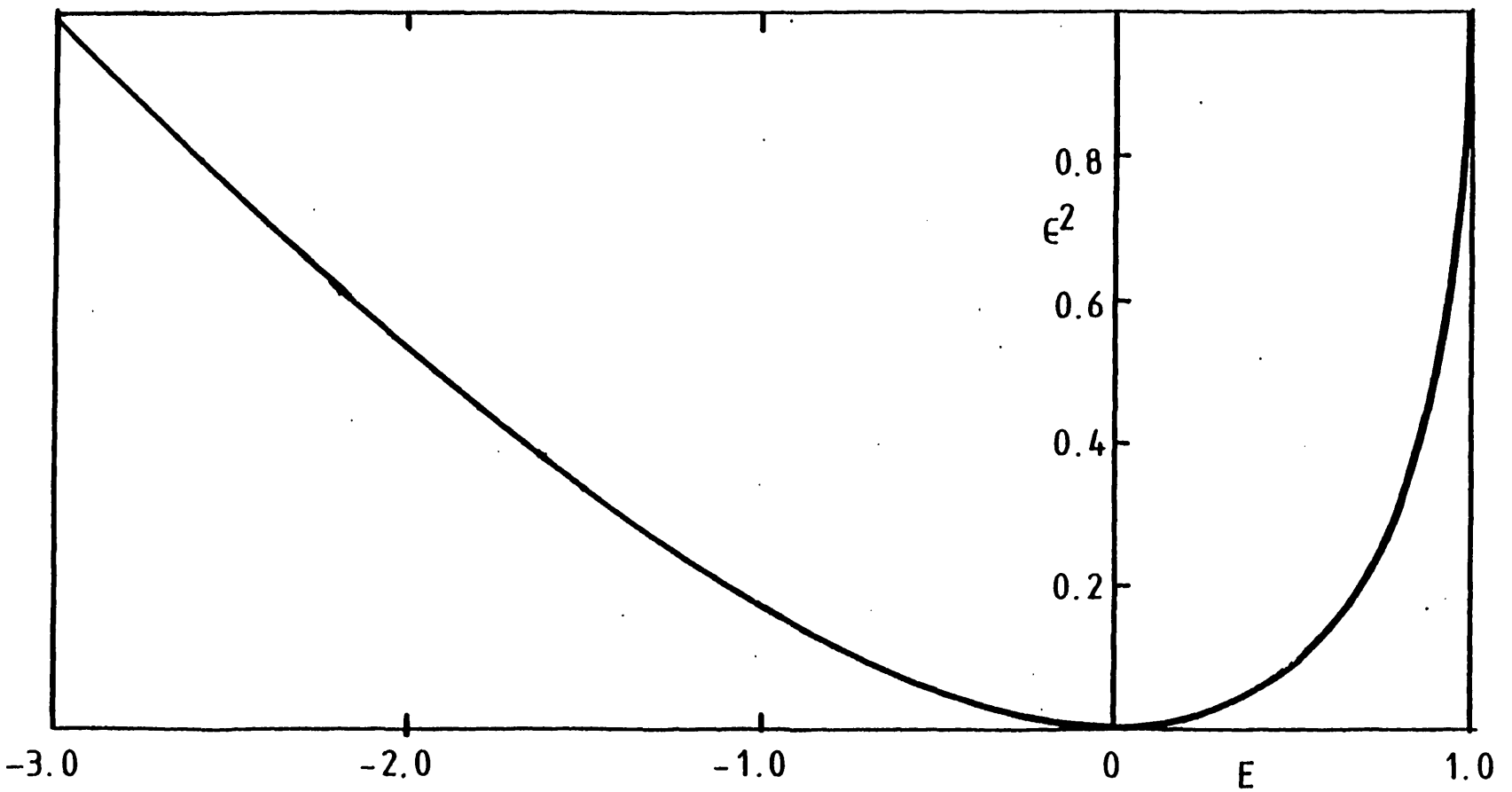


Figure 3.2.2. Variation of ϵ^2 with E where $\epsilon=1-\sqrt{(1-E)}$.

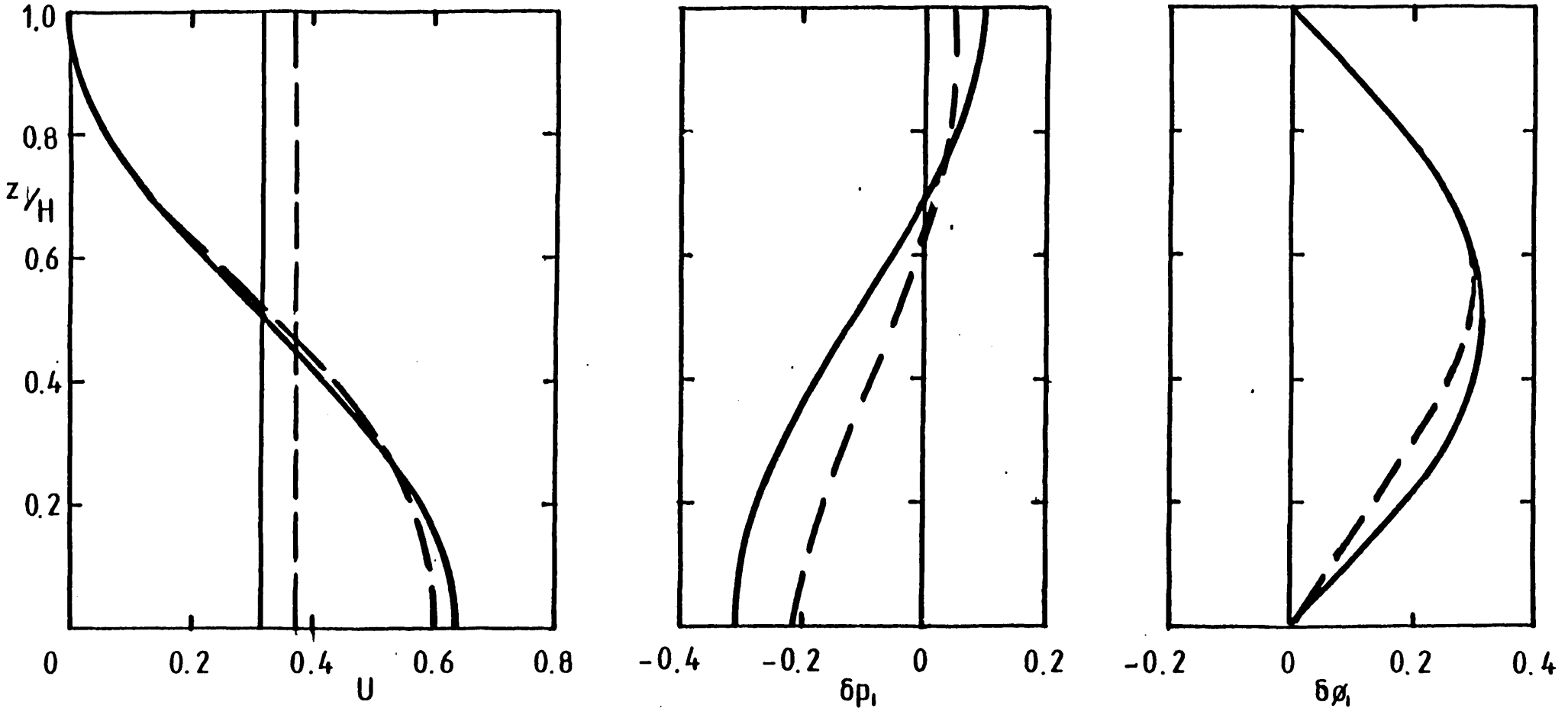
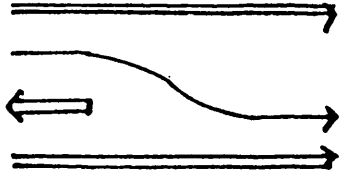


Figure.3.2.3. Outflow profiles of relative velocity, pressure and entropy perturbation (broad lines) for an n=1 descent mode. Compressible profiles (D=1) are in broken lines. The inflow relative velocity is given by thin lines.



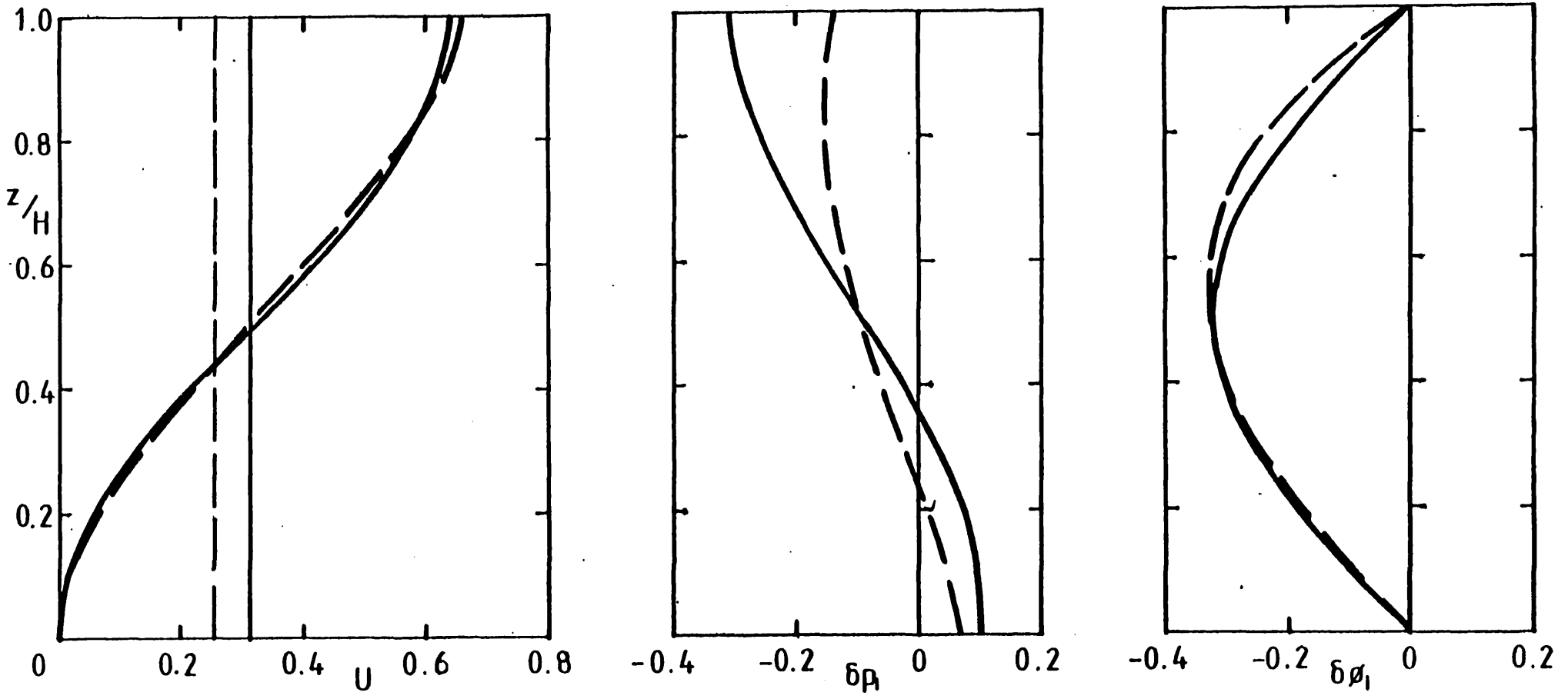
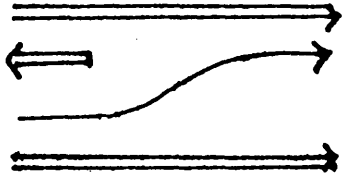


Figure 3.2.4. As figure 3.2.3 except for an n=1 ascent mode.



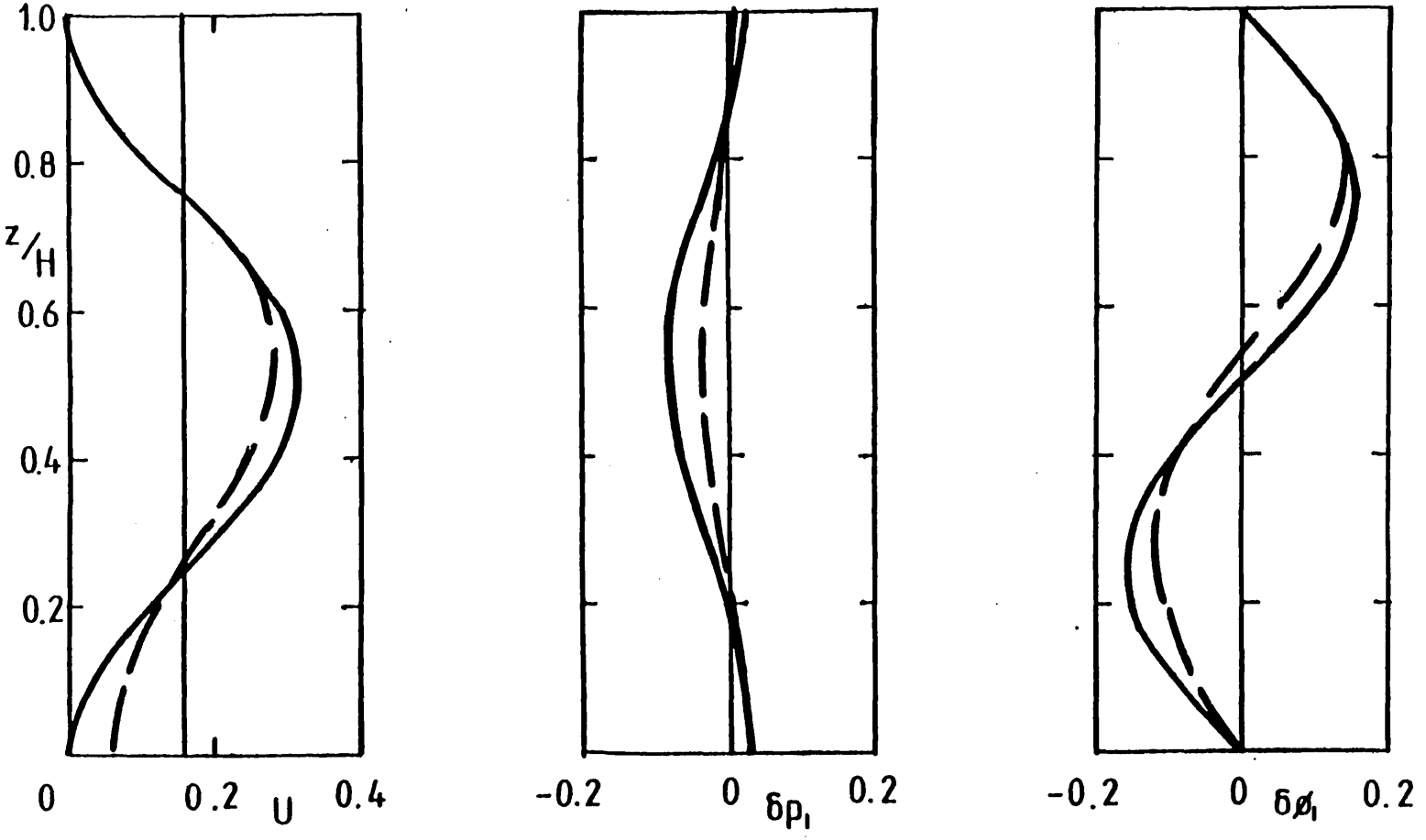
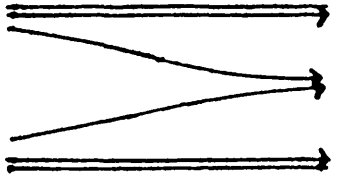


Figure 3.2.5. As figure 3.2.3 except for an n=2 mode with upper level descent and lower level ascent.



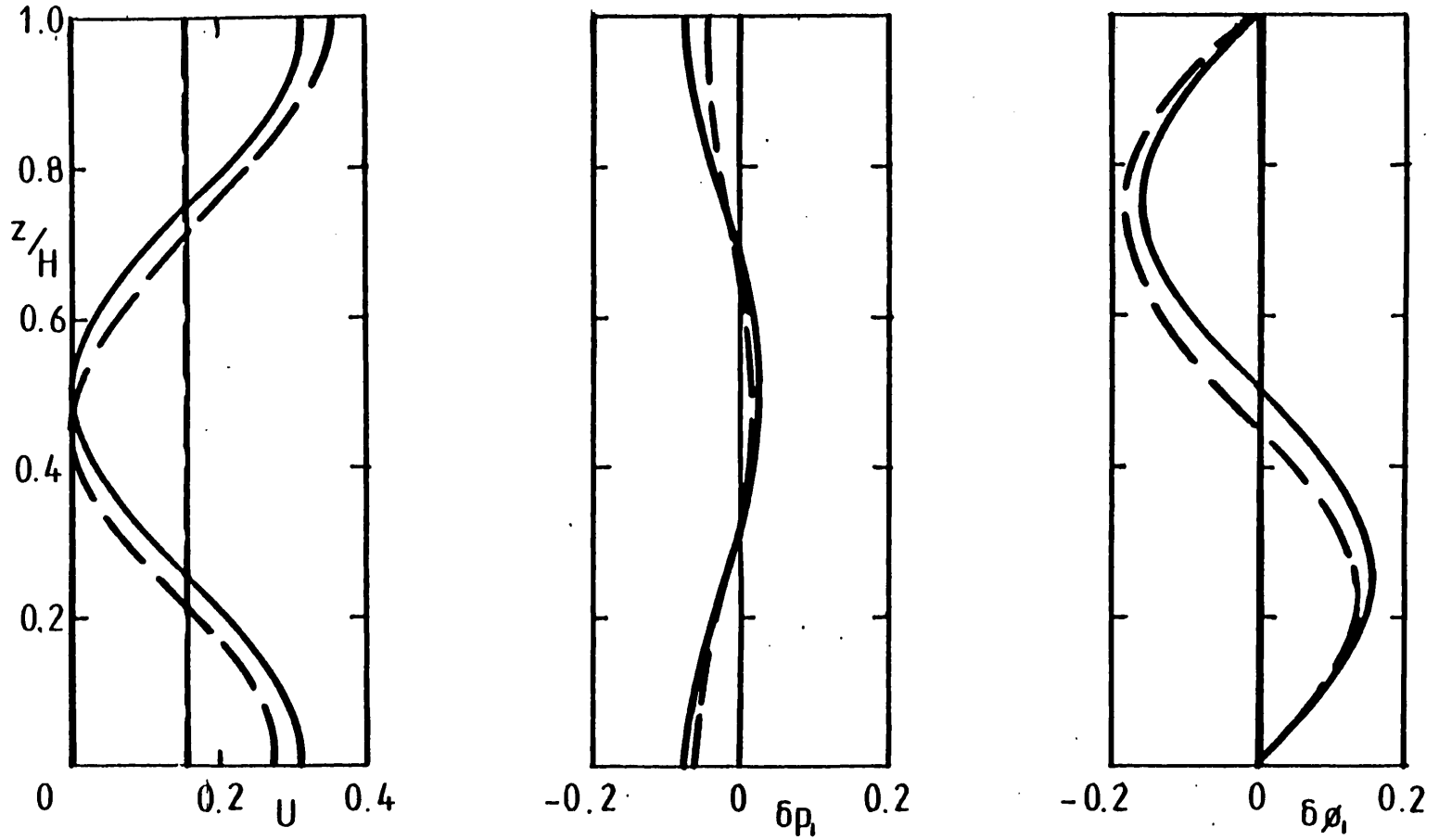
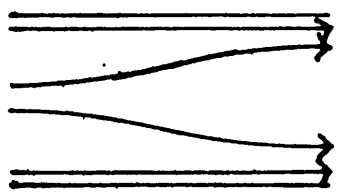


Figure 3.2.6. As figure 3.2.3 except for an n=2 mode with upper level ascent and lower level descent.



perturbation is negative (the mean pressure change from 3.13 is $-1/2c^2\epsilon^2$ or $-F_f^2\epsilon^2$ in dimensionless units), which is obtained by integrating 3.13 with respect to ζ_1. However, in the case of the ascent there is a negative vertical gradient of perturbation pressure (see figure 3.2.4); a positive vertical gradient of perturbation pressure occurs in the case of the descent (figure 3.2.3); thus both the sign of the mean pressure change and the vertical gradient are important in determining the nature of the forced flow. In the model including a shallow downdraught in section 2.2.3 of the previous chapter, the vertical gradient of outflow pressure perturbation increased with height. If this type of forcing occurs we would expect a maximum fall in pressure at upper levels in the response. This corresponds to the type of forcing occurring when ascent is produced. However, although the pressure perturbation forcing produced by the convective circulation is positive with a small positive vertical gradient, no observational measurements of pressure perturbation have been found to confirm or disprove such a pressure distribution. The mean pressure difference between updraught and downdraught was approximately 15% of the mean pressure change for the example given in section 2.2.3.

Higher modes (n=2,3....) are simply related to the n=1 modes and can be obtained by vertically stacking alternately ascending and descending layers. u_1, δp_1 and $\delta\phi_1$ are scaled by F_f, F_f^2, and F_f respectively. The vertical co-ordinate is scaled by 1/n.

The n=2 type solutions show both ascent and descent for each value of E chosen. The upper part of the outflow profiles for the E=+1, n=2 mode shown in figure 3.2.5 resemble the flow shown for the E=+1, n=1 mode with descent occurring for $0.5<\zeta_1<1$. The lower part of the

outflow profiles for the E=+1, n=2 mode resembles the flow shown for the E=-3, n=1 mode with ascent occurring for $0<\mathcal{J}_1<0.5$. The propagation speed is half that of the n=1 type modes. Pressure changes scale as the square of the propagation speed, and so are 1/4 of the magnitude. Vertical displacements are halved compared with the n=1 mode since $(\mathcal{J}_1-\mathcal{J}_0)\propto F_f$ from 3.9.

The n=2 type mode, E=-3, has upper level ascent and lower level descent shown in figure 3.2.6. All modes show a mean fall in pressure across the flow. The outflow pressure perturbation profiles for n-even modes are symmetric about the mid-level whereas n-odd modes have pressure changes of opposite sign at the upper and lower boundaries.

Suppose the mean pressure change across the forced part of the flow is equal and opposite to that across the convective part of the flow. We now ask in a simplistic way:- "what would be the consequences for the propagation speeds of the squall line and the "response"?". Then, where FCAPE = $g(B-\delta)H^2/2$, using the results of section 2.2.1

$$3F^2\,UCAPE=-(-F_f^2\,FCAPE)$$

$$UCAPE/FCAPE=1/(3n^2\pi^2(0.23^2))$$

ie. only discrete values of the ratio UCAPE/FCAPE are allowed. However, the speeds of propagation of the two parts of the flow relative to the mean wind speed would be very different:-

$$c_{convective}-c_{forced}=c_{convective}\,(1-(F_f/F)(FCAPE/UCAPE)^{1/2})=-0.732c_{convective}.$$

The convective part of the circulation would travel more slowly than the forced part.

An alternative and more physically reasonable approach assumes that the two parts of the circulation travel with the same speed so that

$$F(UCAPE)^{1/2}=F_f(FCAPE)^{1/2}.$$

Then the ratio of the mean pressure change across the convective flow to that across the forced flow would be:-

$$\frac{\langle \delta p \text{ forced} \rangle}{\langle \delta p \text{ convective} \rangle} = -\frac{1}{3}.$$

So in this case the mesoscale response to the rear of the squall lines cannot fully achieve adjustment to the ambient pressure field, and some adjustment would be necessary on the large scale. The ratio UCAPE/FCAPE would still be constrained ie.

$$UCAPE/FCAPE=F_f^2/F^2=1/(n^2\pi^2(0.23^2)).$$

3.2.2 The Effect of Compressibility on the Forced Flows Described in TMM80.

In considering the effects of shear and compressibility on these forced flows we would like to express the dependence of the flow behaviour on the quantity being varied and its effect on the mean pressure change across the circulation. In addition we would like some information about the transformation of energy between different forms, ie. kinetic, potential (or buoyancy) energy and work done by the pressure field. We now consider the magnitude of terms in the integrated x-momentum equation developed in section 3.1 for the two-dimensional problem ie.

$$\int_0^H \left[p + \rho u^2 \right]_{-\infty}^{+\infty} dz = 0$$

Rearranging:- $$- \frac{\langle \delta p_1 \rangle}{\langle \rho_0 u_0^2 \rangle} = \frac{\langle \rho_1 u_1^2 \rangle - \langle \rho_0 u_0^2 \rangle}{\langle \rho_0 u_0^2 \rangle} \qquad (3.18)$$

or the fractional change in kinetic energy per unit volume, $\Delta KE/KE_0$, which also preserves the sign of the mean pressure change. Maximising this quantity with respect to E also maximises the mechanical efficiency of the circulation.

Unfortunately it is not possible to impose a mean pressure change across the flow and then determine the inflow conditions necessary to maintain a steady circulation. Instead, the change in velocity (or kinetic energy) along one streamline must be specified (E fixed) and for a particular inflow shear the mean pressure change on outflow may be calculated.

The method of solution of the displacement equation 3.4 with boundary conditions 3.6 and 3.7 is essentially similar to the scheme employed in chapter two for the displacement equation 2.14 and its respective boundary conditions. The method of solution of 2.14 together with the calculation of outflow profiles of relative velocity, pressure and entropy deviation is set out in appendix A. D is increased in small steps from zero with correspondingly small increases in F_f which start from the incompressible mode solutions. For each value of D, $\Delta KE/KE_0$ is maximised with respect to F subject to the condition that no relative inflow occurs at the rear.

The variation of propagation speed with D is shown in figure 3.2.7

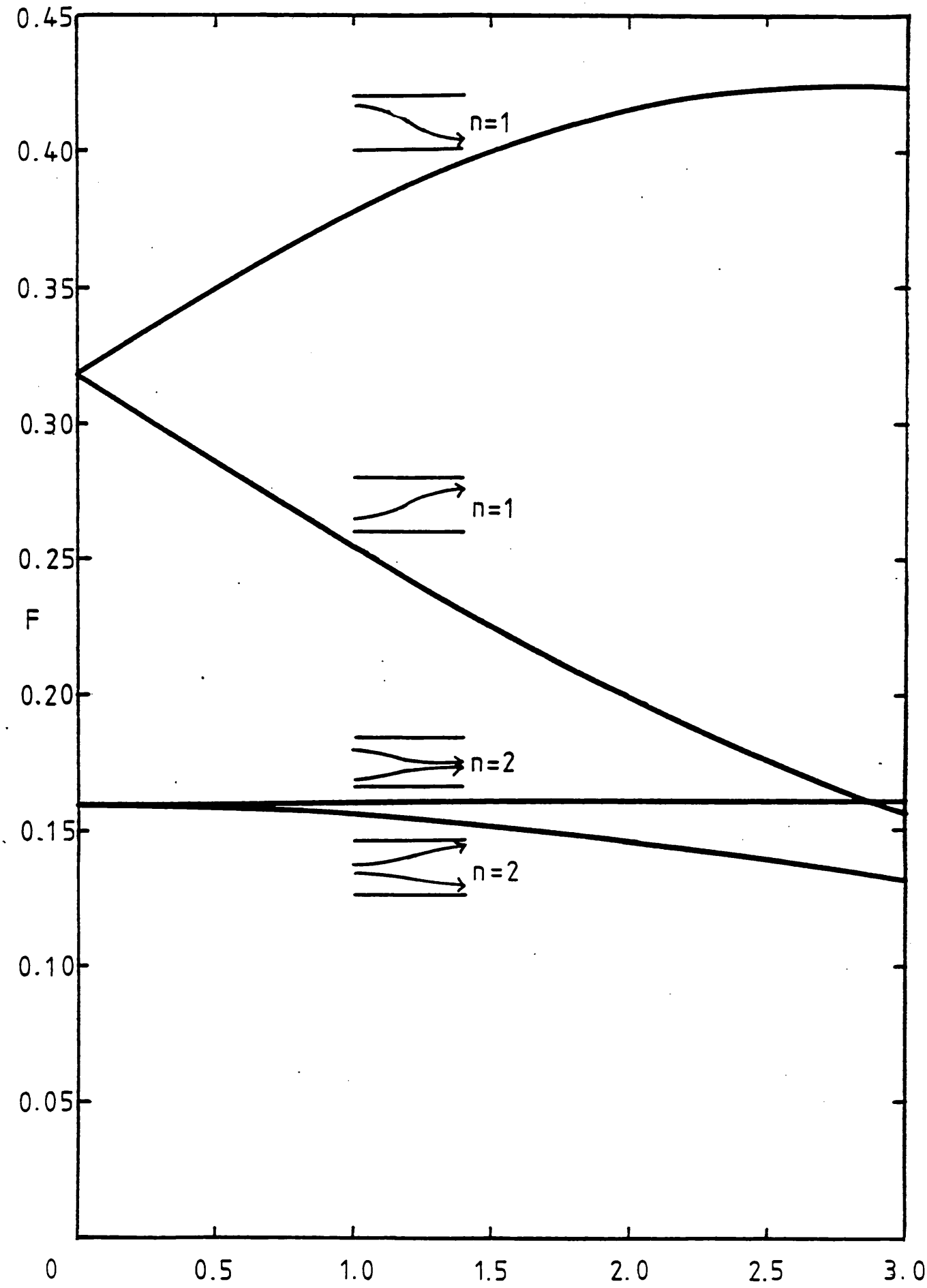


Figure 3.2.7. Variation of propagation speed (F) with compressibility (D) for n=1 and n=2 modes for maximum mechanical efficiency.

for n=1 ascent and descent modes. The incompressible solution is given by D=0. D=1 corresponds to a density scale height equal to that of the disturbance height, which value will be used in future calculations. The ascent and descent regime propagation speeds behave in very different ways as D is increased. The descent mode tends to propagate more quickly; the propagation speed increases by 18% when D=1 over the incompressible value. The ascent mode propagation speed falls by 20% over the same range of D.

For the n=2 type modes which contain both descending and ascending layers, the changes in propagation speed are much smaller (see figure 3.2.7). When there is upper level descent, the propagation speed increases by less than 1% as D increases from 0 to 1. When there is upper level ascent the propagation speed falls by less than 2%. These changes can be ignored for all practical purposes for the n=2 type modes.

The n=1 and n=2 mode outflow profiles with D=1 are shown in figures 3.2.3-3.2.6 for comparison with the incompressible results. The relative outflow velocity profiles for the n=1 compressible modes are essentially similar to the incompressible profiles (see figures 3.2.3 and 3.2.4) although the propagation speeds are substantially different (table 3.2.1). The n=1 compressible descending mode shows slight acceleration at mid-levels and deceleration at upper and lower levels compared with the incompressible outflow relative velocity. Changes are in the opposite sense for the n=1 ascending mode. Outflow pressure and entropy perturbation profiles show greater differences. For the descending mode (figure 3.2.3) the layer over which the pressure perturbation falls is shallower (0.62H cf. 0.69H) and the mean pressure fall is now approximately halved (-0.05 cf. -0.10, see

table 3.2.1). The mean pressure fall is not reduced by as much for the ascent mode (-0.07 cf. -0.10). Entropy changes are larger for the ascent mode when compressibility is introduced indicating larger mean vertical displacements of air. By contrast the descending mode shows lower entropy changes corresponding to smaller downward displacements.

The relative outflow velocity profiles for the two n=2 modes are modified in slightly different ways compared with the incompressible profiles. The mode with upper level ascent (figure 3.2.6) shows upper level acceleration and lower level deceleration relative to the incompressible case, corresponding to the density variation introduced as a consequence of mass conservation. The pressure perturbation profile is similar to the incompressible case but is of smaller amplitude (table 3.2.1). The level dividing updraught from downdraught has dropped to $\mathcal{Y}_1$=0.45 on outflow so that the updraught layer is deeper. The n=2 mode with upper level descent and lower level ascent (figure 3.2.5) shows deceleration at mid-level with low and high-level acceleration relative to the incompressible outflow relative velocity profile. The low level ascent layer has a depth of 0.55H and is deeper than in the incompressible case (0.5H).

$\Delta KE/KE_o$ is plotted against D in figure 3.2.8 for the n=1 and n=2 modes. The effect of compressibility on $\Delta KE/KE_o$ for the n=1 ascent and descent circulations is quite different. $\Delta KE/KE_o$ increases by 58% for the ascending mode for D=1 over the incompressible value, whereas for the descending mode $\Delta KE/KE_o$ falls by 42% over the same range of D. The n=2 mode combining upper level ascent with lower level descent shows little variation of kinetic energy generation with D (table 3.2.1). However the n=2 mode with upper level descent and lower level

n	D	Upper level flow type	u_0	$\langle \delta p \rangle / \rho_s$	$\Delta KE/KE_0$
1	0	ascent	0.318	-0.101	0.50
1	1	ascent	0.254	-0.065	0.79
1	0	descent	0.318	-0.101	0.50
1	1	descent	0.378	-0.053	0.29
2	0	ascent	0.159	-0.025	0.50
2	1	ascent	0.156	-0.015	0.50
2	0	descent	0.159	-0.025	0.50
2	1	descent	0.160	-0.009	0.29

Table 3.2.1

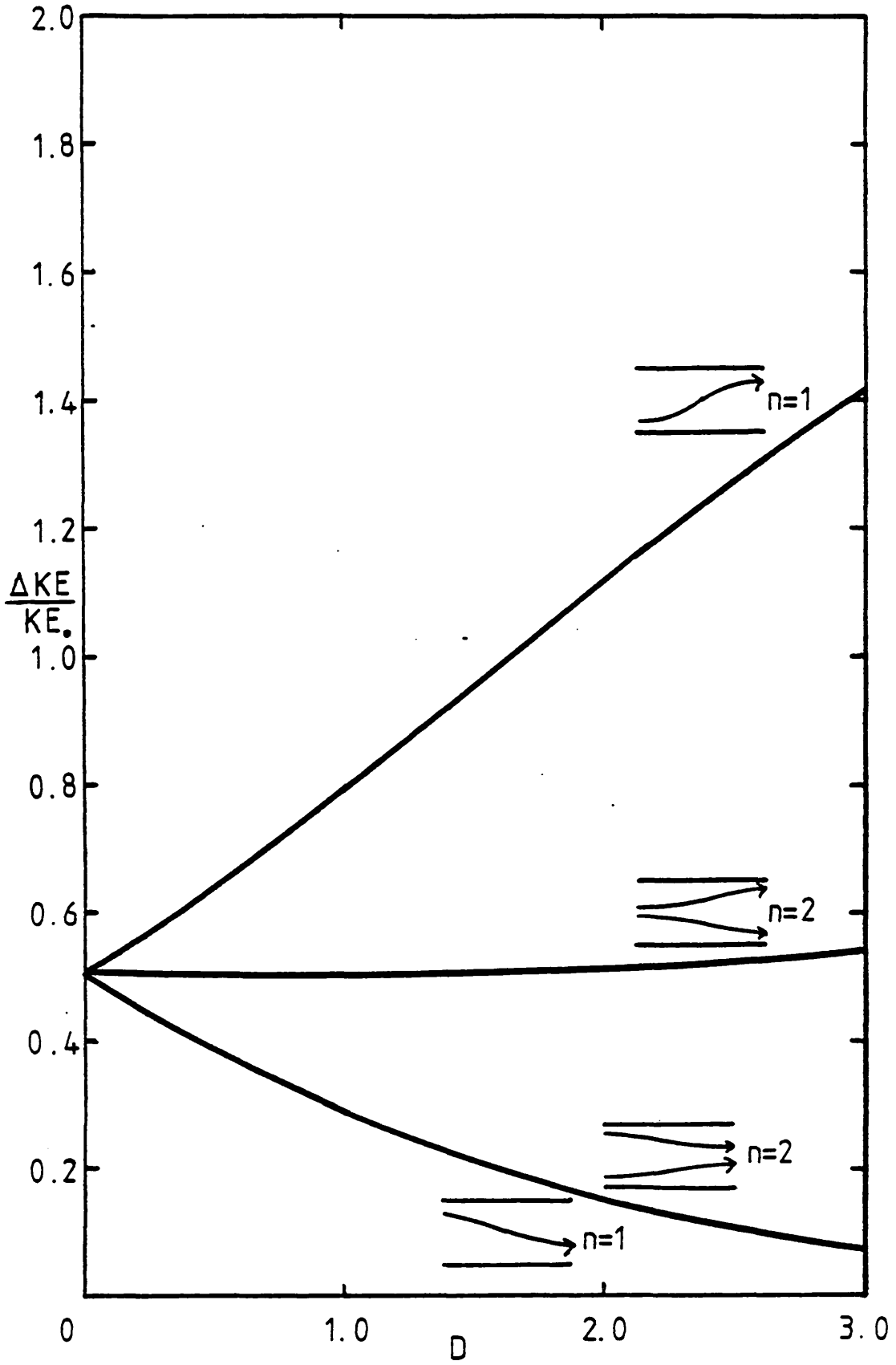


Figure 3.2.8. Variation of $\Delta KE / KE_{\bullet}$ with compressibility for n=1 and n=2 modes The curve for the n=1 descent mode coincides with that for the n=2, upper level descent, lower level ascent, mode. For each value of D the maximumum mechanical efficiency solution is shown.

ascent shows the same variation of $\Delta KE/KE_o$ with D as the n=1 descent mode. For the n=2 mode with upper level ascent the mass distribution must cause the effect of compressibility on ascent and descent modes separately to cancel. Table 3.2.1 summarises the differences which compressibility makes to propagation speed, mean pressure perturbation and to $\Delta KE/KE_o$ for n=1 and n=2 modes.

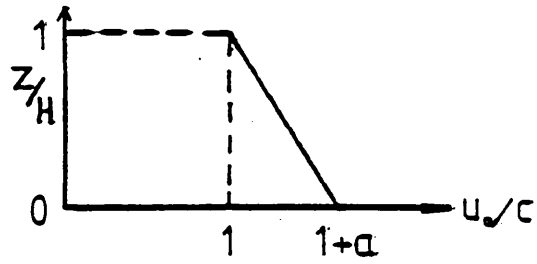
$\langle \delta p_1 \rangle$ is a quantity calculated by integrating twice with respect to height. Errors are estimated to be of the order of 10^{-3} in $\langle \delta p_1 \rangle$. When D=0, $F_f = 1/\pi$ or $1/2\pi$ the error in the ratio calculated is of the order of $|\text{error}(\delta p_1)|/2F_f^2$ or between 10^{-2} and 10^{-3}. Where D=3 and F_f is much larger the error is smaller. From 2.5 we see that the mean fall in pressure (or the work done by the pressure field) effects an increase in the mean flow kinetic energy and the generation of negative buoyancy which increases the CAPE of the air; work done by the pressure field thereby increases both kinetic and potential energies in the response region in the rear of the squall cluster.

3.2.3 The Effect of Shear on the Forced Flows Described in TMM80.

The forced regimes considered in TMM80 were simple in that the inflow shear was zero; this was necessary to allow analytic solutions to be obtained and hence the basic dynamical properties to be determined. The introduction of a non-zero inflow shear complicates the displacement equation considerably, to the extent that it is then not possible to obtain a linear second-order counterpart. No analytic solutions have been obtained even in the case of constant shear. Since the outflow from the "cloud-scale" part of the squall cluster is usually quite strongly sheared (normally with a jet-like profile) it is instructive to consider the case of non-zero shear on the forced

regime. In this section simple types of shear profile are considered, with quite interesting results. In particular since the unsheared (TMM80) downdraught solution produces negative shear, it is valuable to question how negative and positive inflow shear interact with the internally baroclinically generated vorticity.

A uniform shear is introduced into the flow such that $u_o(1)=c$ and $u_o/c=1+a(1-z_o)$. Then $du_o/dz_o=-acH$ or $-aF_f$ in normalised units of $(g(B-\gamma))^{1/2}$. Such an inflow profile is shown below:-



As in the previous section, when the effect of compressibility was examined, E is varied to maximise the increase in the mean flow knetic energy (the maximum mechanical efficiency). The propagation speed of the forced flow is defined to be the mean inflow speed ($<\rho_o u_o>/<\rho_o>$) as for the convective flows described in chapter two.

The effect of uniform shear on the propagation speed of the n=1 descent mode is shown in figure 3.2.9. Negative shear increases the descent mode propagation speed whereas positive shear leads to a decrease. For the incompressible case (D=0) the ascent mode propagation speed shows the same variation with shear but in the opposite sense, ie. negative shear causes a descent mode to propagate faster but an ascent mode to travel more slowly. When compressibility is also introduced (D=1) the descent mode tends to propagate faster for all shears than the incompressible case (approximately 20% over the range $-0.5\leqslant du_o/dz_o\leqslant 0$). The ascent mode travels 20% more slowly over the range $0\leqslant du_o/dz_o\leqslant 0.5$ when compressibility is introduced. Note

that the ascent mode (D=1) propagation speed is plotted with the sign of the shear reversed in figure 3.2.9 to facilitate comparison with the descent circulation. (This procedure is also followed for the variation of $\Delta KE/KE_o$ with shear in figure 3.2.10.)

The effect of shear on the increase of mean flow kinetic energy, $\Delta KE/KE_o$, is shown in figure 3.2.10. Positive shear enhances the net kinetic energy increase of the flow for a descent mode while negative shear reduces the net kinetic energy increase relative to the unsheared case. For an ascent mode, the opposite tendency is shown. Compressibility reduces the net kinetic energy increase of ascent modes and increases that of descent modes as was found in section 3.2.2. In all these maximum mechanical efficiency cases described, $\Delta KE/KE_o$ remains positive so that the pressure field is always doing work to create kinetic and potential energy.

Outflow profiles of relative velocity, pressure and entropy perturbation for $du_o/dz_o=-0.3$ are shown in figure 3.2.11 for the n=1 descent mode. Also plotted for the incompressible case are the outflow profiles for an initially unsheared flow. In both unsheared and sheared cases the flow becomes more negatively sheared. However, the changes in outflow relative velocity are of smaller magnitude when the inflow is negatively sheared. Changes in the magnitude of $\delta\phi_1$ are correspondingly smaller.

These changes may be interpreted by using the conserved quantity $C_s(\psi)$ for a two-dimensional flow given in Moncrieff, 1981. The following equation expresses the relationship between the shear of the flow (the y-component of vorticity, $\eta=\partial u/\partial z$) and the buoyancy generation:-

$$\frac{\eta_1}{\rho_1} = \frac{\eta_0}{\rho_0} - \frac{g(\gamma-B)(z_1-z_0)}{\rho_0 u_0} \quad . \tag{3.19}$$

Air which is forced to descend ($(\gamma-B)(z_1-z_0)>0$) generates negative vorticity. If the same descent were to occur for the sheared as for the unsheared flow, η_1 would be larger for the sheared case and would generate return flow at the rear of the circulation. To comply with the condition of no relative inflow at the rear, smaller vertical displacements occur producing a reduced negative vorticity compared with the unsheared case. The no return flow condition actually accounts for the decrease in $\Delta KE/KE_0$ for a descending mode in negative shear since the redistribution of momentum is limited.

The effect of positive shear ($du_0/dz_0=0.1$) on a descent mode is shown in figure 3.2.12. From equation 3.19 we see that the forced descent ($(\gamma-B)(z_1-z_0)>0$), generating negative vorticity, is partially cancelled by the inflow positive vorticity ($\eta_0>0$) which would lead to a smaller negative outflow shear than in the unsheared inflow case. However, the condition for maximum mechanical efficiency requires the outflow negative shear to be maximised - creating a greater vertical redistribution of momentum and consequently larger net vertical displacements, and increased kinetic energy of the mean flow.

The effect of negative shear on ascent is equivalent to the effect of positive shear on descent and similarly for positive shear on ascent and negative shear on descent in the incompressible case.

This examination of the effect of uniform shear on the n=1 ascent modes has shown that the condition of maximum mechanical efficiency can produce changes which would not be anticipated by a simple

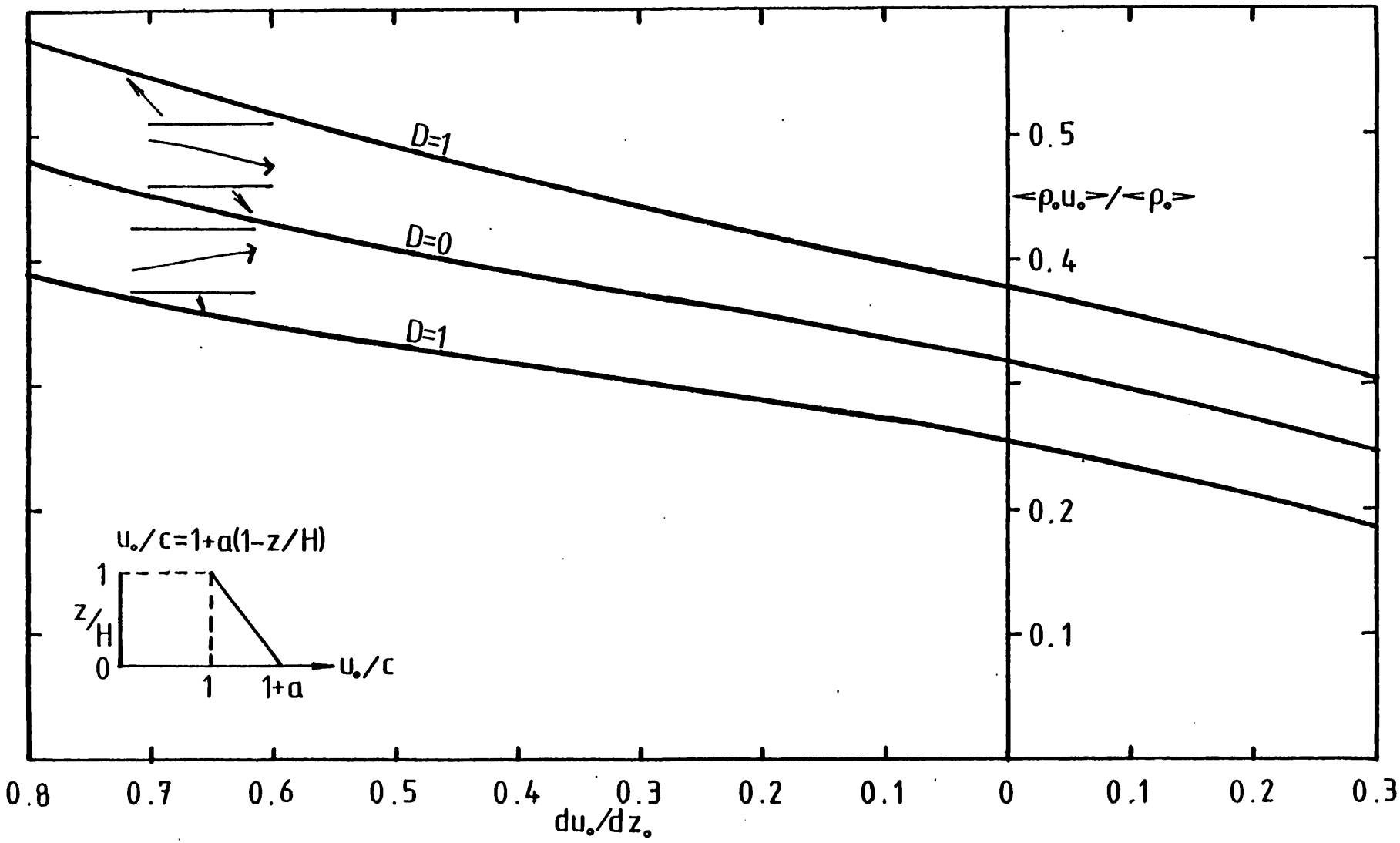


Figure 3.2.9. Variation of propagation speed with inflow shear for n=1 ascent and descent modes. The ascent mode for the incompressible flow follows the curve for the descent mode with the sign of the shear reversed. The D=1 ascent case is plotted with the sign of the shear reversed.

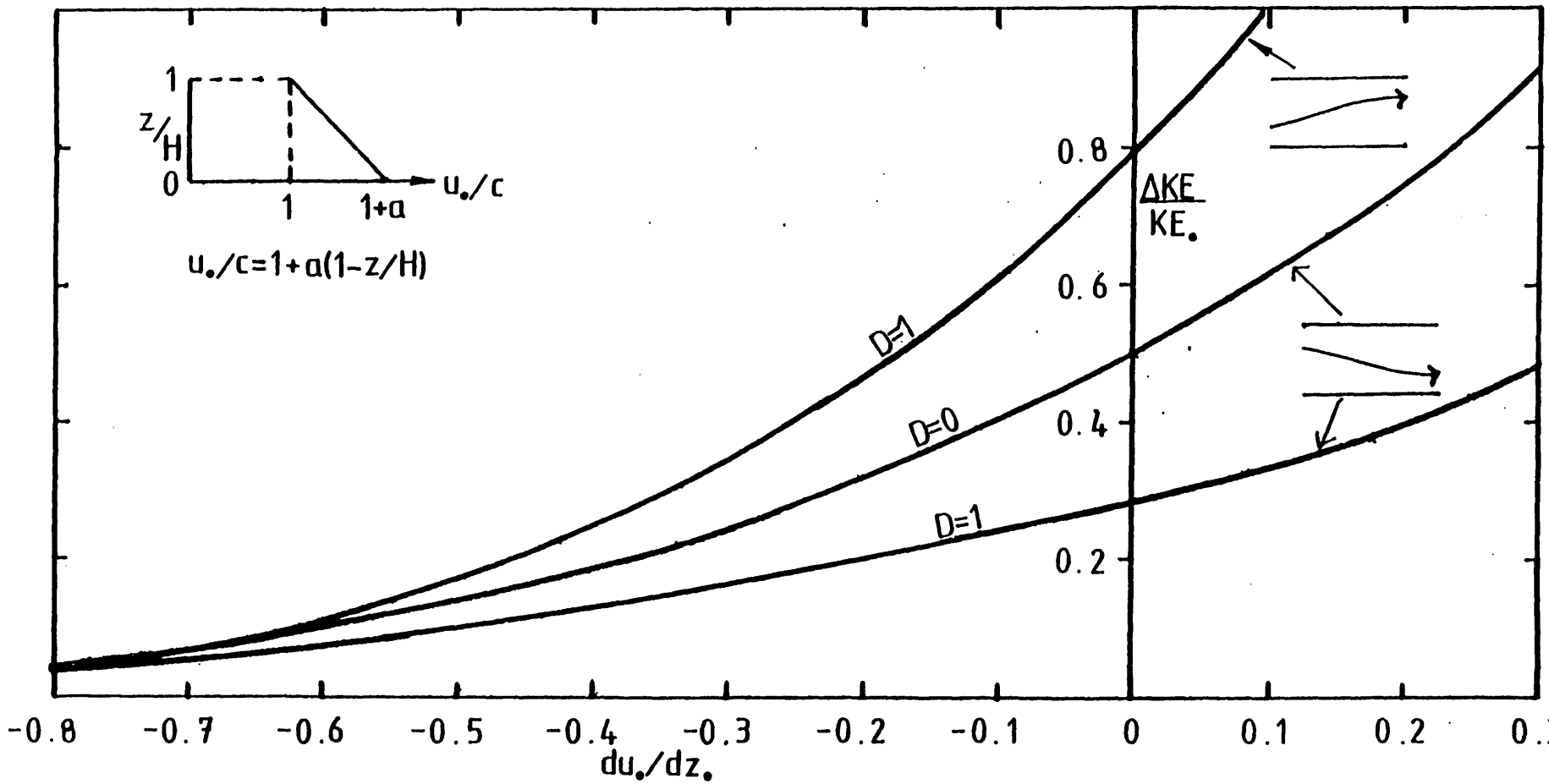


Figure 3.2.10. Variation of $\Delta KE/KE_*$ with shear for n=1 descent and ascent modes. See caption to figure 3.2.9 for explanation.

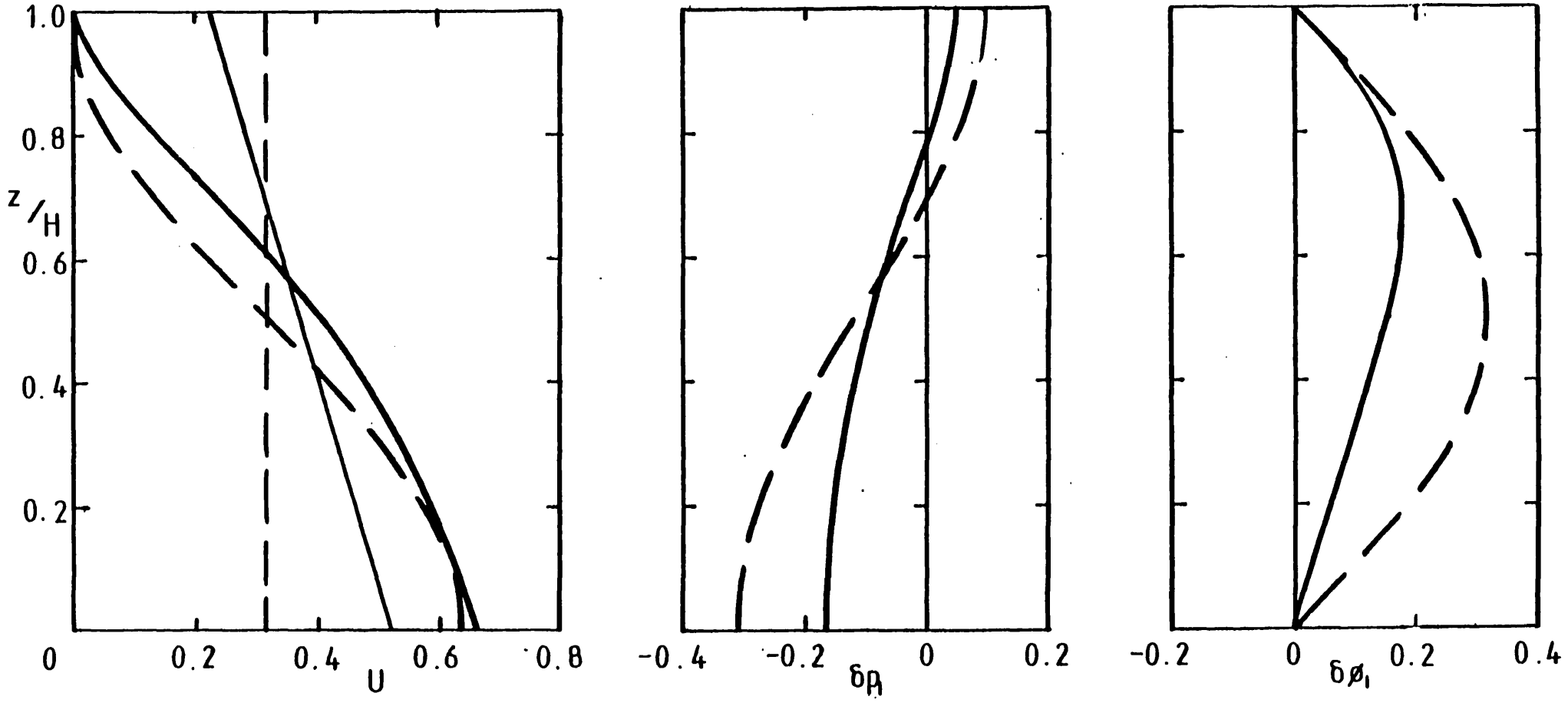
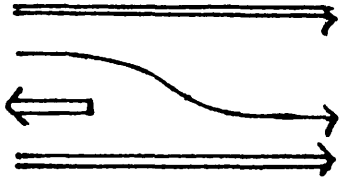


Figure 3.2.11. Outflow profiles of relative velocity, pressure and entropy perturbation (broad lines) for an n=1 mode which is initially negatively sheared (solid lines) and unsheared (broken lines). Inflow relative profiles are given by thin lines.



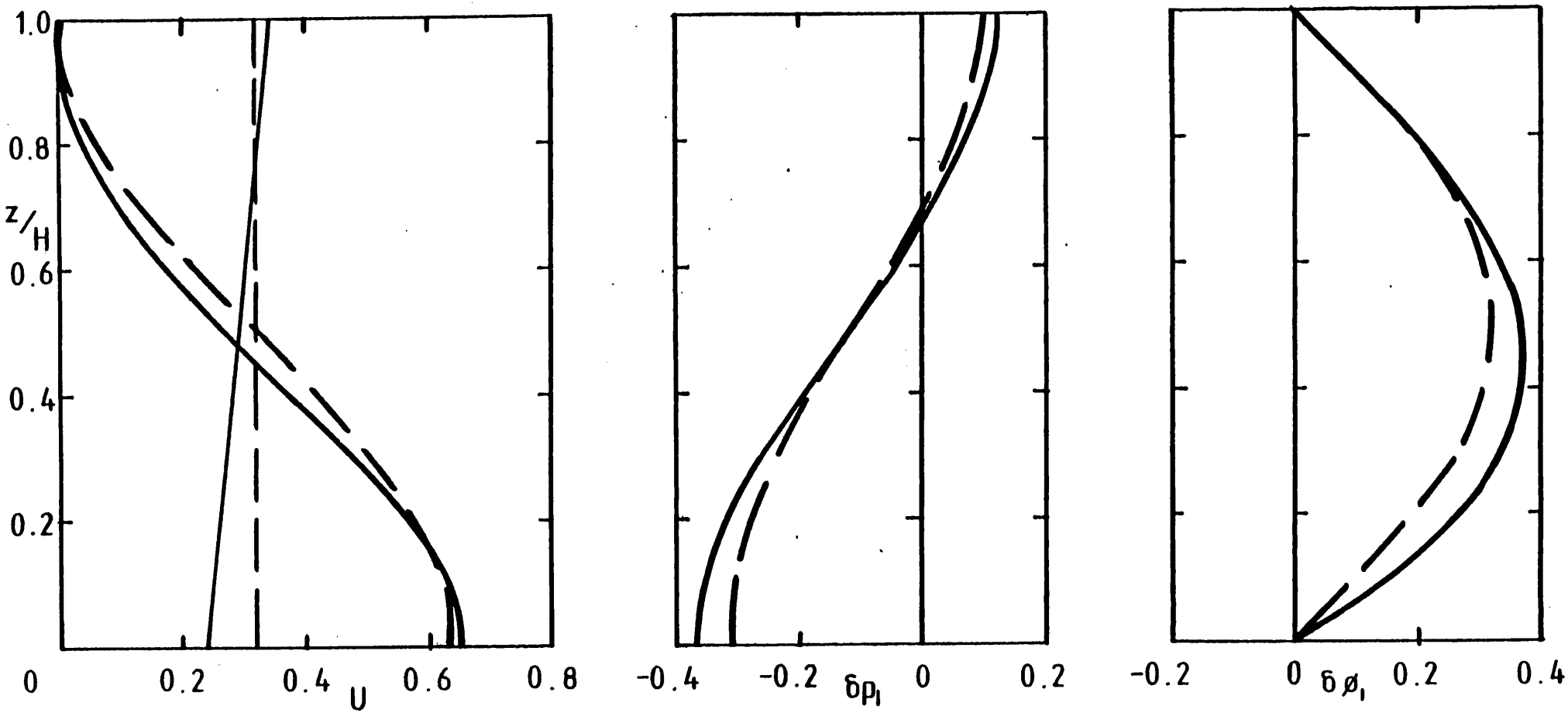
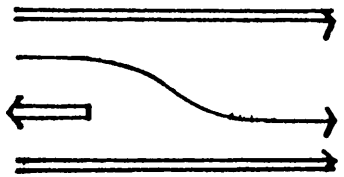


Figure 3.2.12. As figure 3.2.11 except for an initially positively sheared flow.



examination of the vorticity equation, 3.19. The condition of no return flow at the rear has decreased the negative shear of the outflow compared with the unsheared case, whereas the oppcsite outcome would have been anticipated from 3.19. By insisting on maximum mechanical efficiency for a descending circulation which is initially positively sheared a similarly unexpected result has been produced.

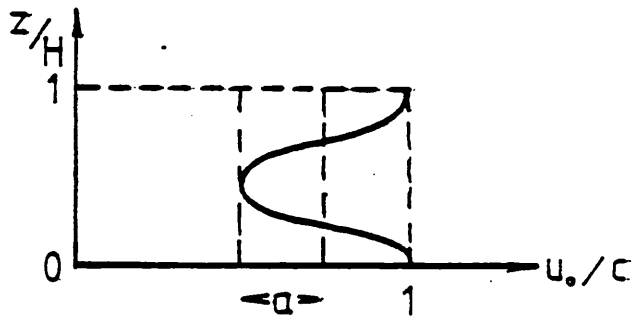
An easterly sheared jet profile, typical of squall cluster regions (Fernandez, 1980 and 1982), is studied in the next section. It is expected that a circulation in which the upper level is initially positively sheared and ascends and the lower level is initially negatively sheared and descends may occur. For the incompressible case both parts of the circulation travel with the same propagation speed. However the results of this section would suggest that for a compressible circulation the descending part will propagate faster than the ascending part. In addition to these difficulties the requirement of no relative inflow at the rear may restrict the jet amplitude (since upper and lower level acceleration require mid-level deceleration because mass continuity must be maintained).

3.2.4 Possible Forced Modes for Easterly Jet Type Velocity Profiles.

In order to quantify the above statements about the importance of the sign of the vertical shear, inflow profiles of the following type were considered:-

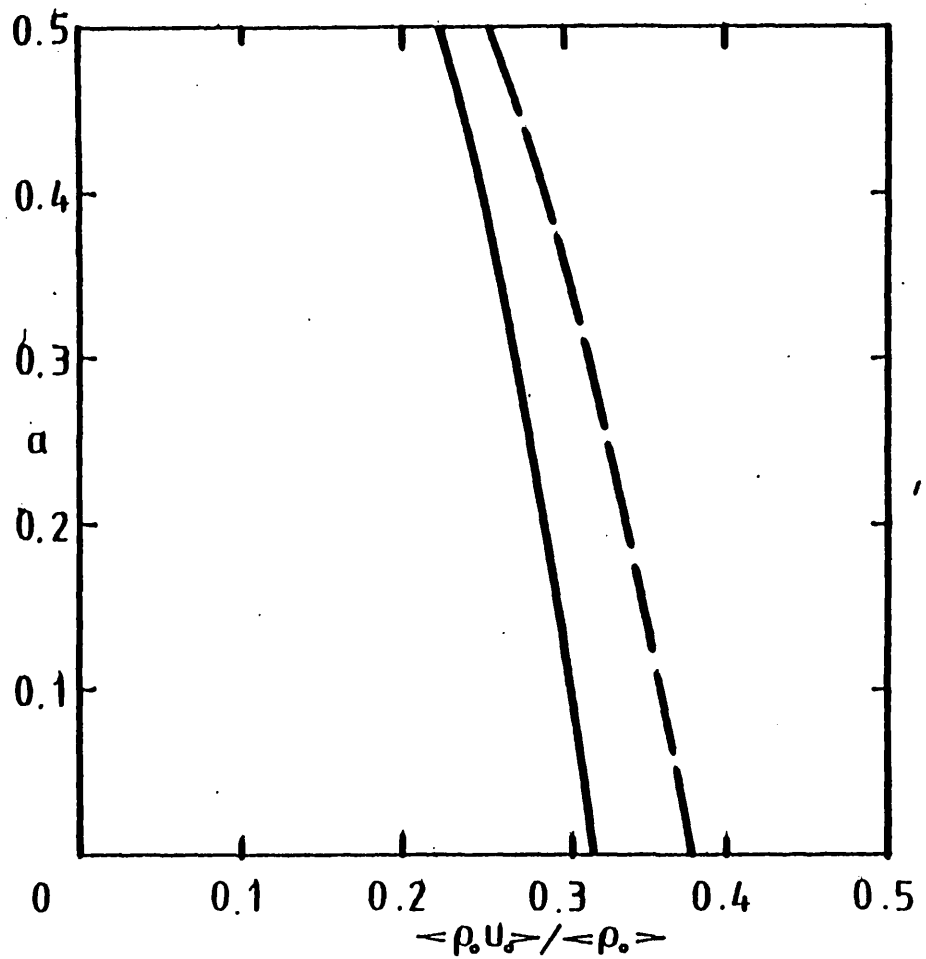
$$u_o/c=(1-a)+a\cos(2\pi\hat{p})$$

Such an inflow profile is shown below:-

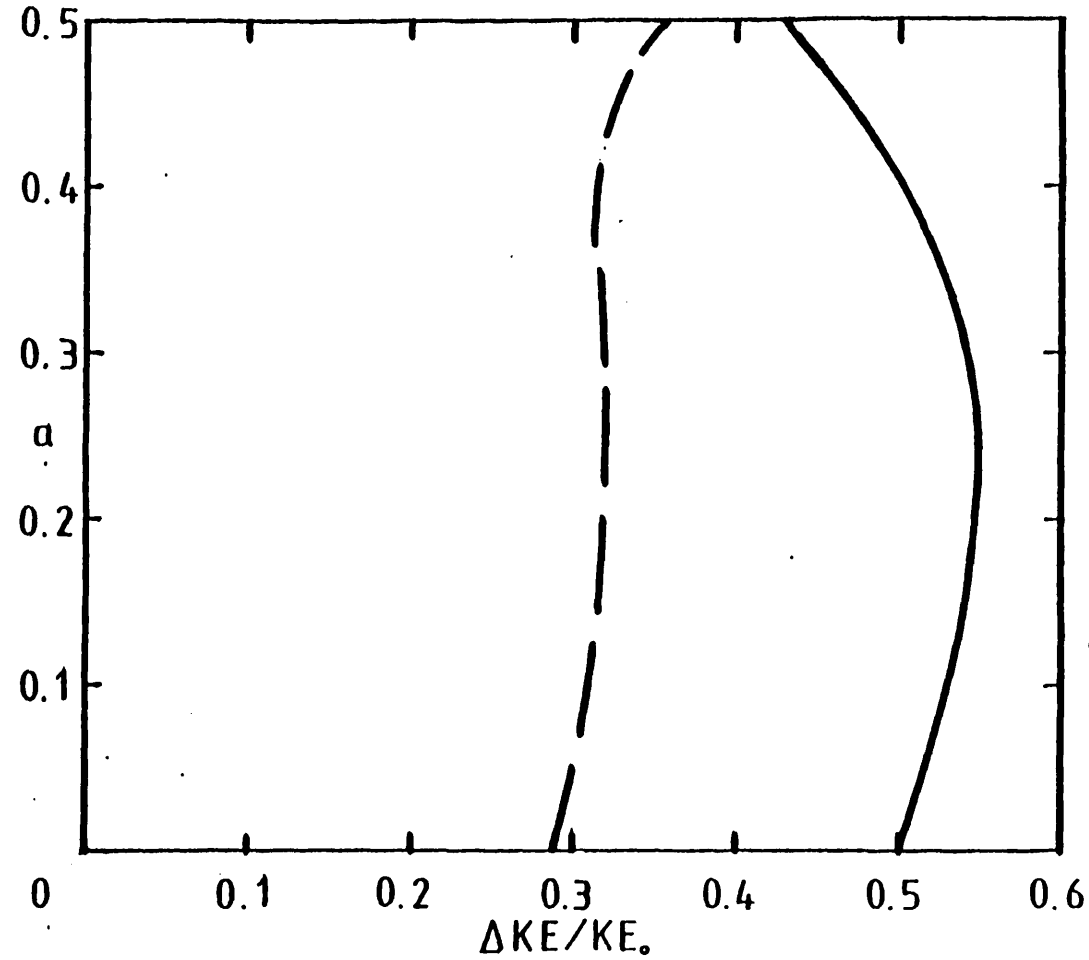


The amplitude of the jet is 2ac ($2aF_f$ in normalised units). Solutions with acceleration of the low level flow are considered. For the n=1 type mode, low level acceleration occurs for E=+1 and for the n=2 type mode, E=-3, as was demonstrated in section 3.2.1 for the unsheared case.

The n=1 type descent mode may occur for E=+1 when $0 \leq a < 0.5$ and there is no relative inflow at the rear. Figures 3.2.13a and b show the variation of the propagation speed and the mean fractional change of kinetic energy per unit volume with jet amplitude. The propagation speed decreases as the jet amplitude increases. Mean flow kinetic energy density is increased compared to the value obtained for the unsheared flow when $a<0.4$ for the incompressible flow - and for all a in the compressible case. However, the outflow profiles of relative velocity, pressure and entropy changes displayed in figure 3.2.14 for a=0.45 show a massive amount of descent has occurred. Air finally leaving at $\mathcal{J}_1 = 0.3$ has descended approximately 0.5H. A large relative deceleration occurs at upper levels in the wind profile as a function of height, and the mid-level and low level profile shows that the velocity increases. The mean pressure change for the incompressible flow is -0.071 and -0.041 for the compressible flow. The absolute value of the pressure change can only be calculated if a value can be assigned to FCAPE. This will be discussed in chapter five.



(a)



(b)

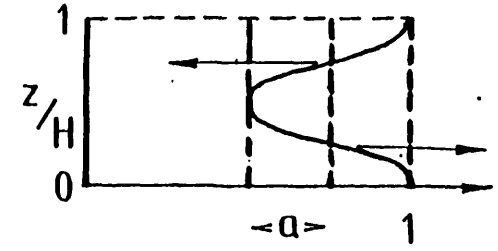


Figure 3.2.13. Variation of (a) propagation speed and (b) $\Delta KE/KE_0$ with jet amplitude, 2a, for an n=1 descent mode D=0 (solid lines), D=1 (broken lines).

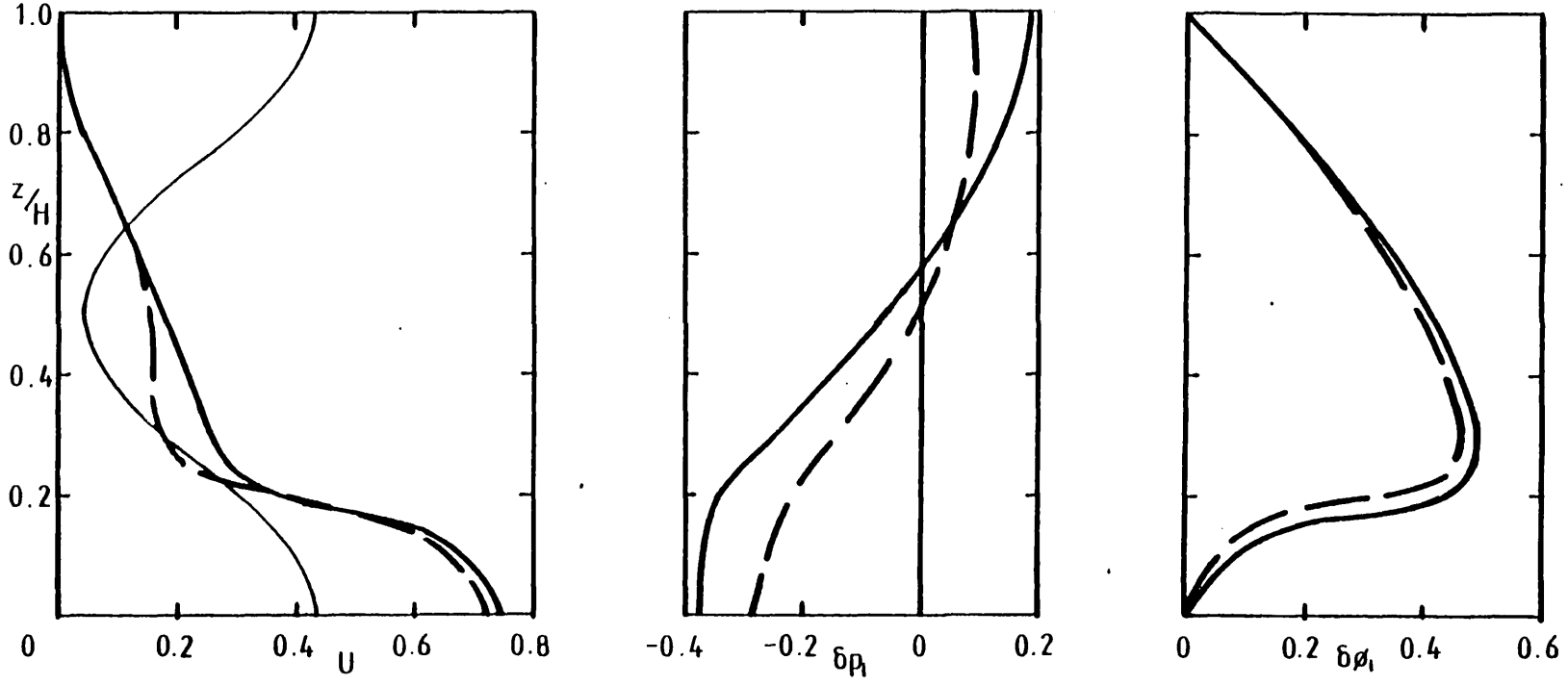


Figure 3.2.14. Outflow profiles of relative velocity, pressure and entropy perturbation (broad lines) for an n=1 descent mode which has a jet-type velocity profile initially (thin line). D=1 compressible case (broken lines).

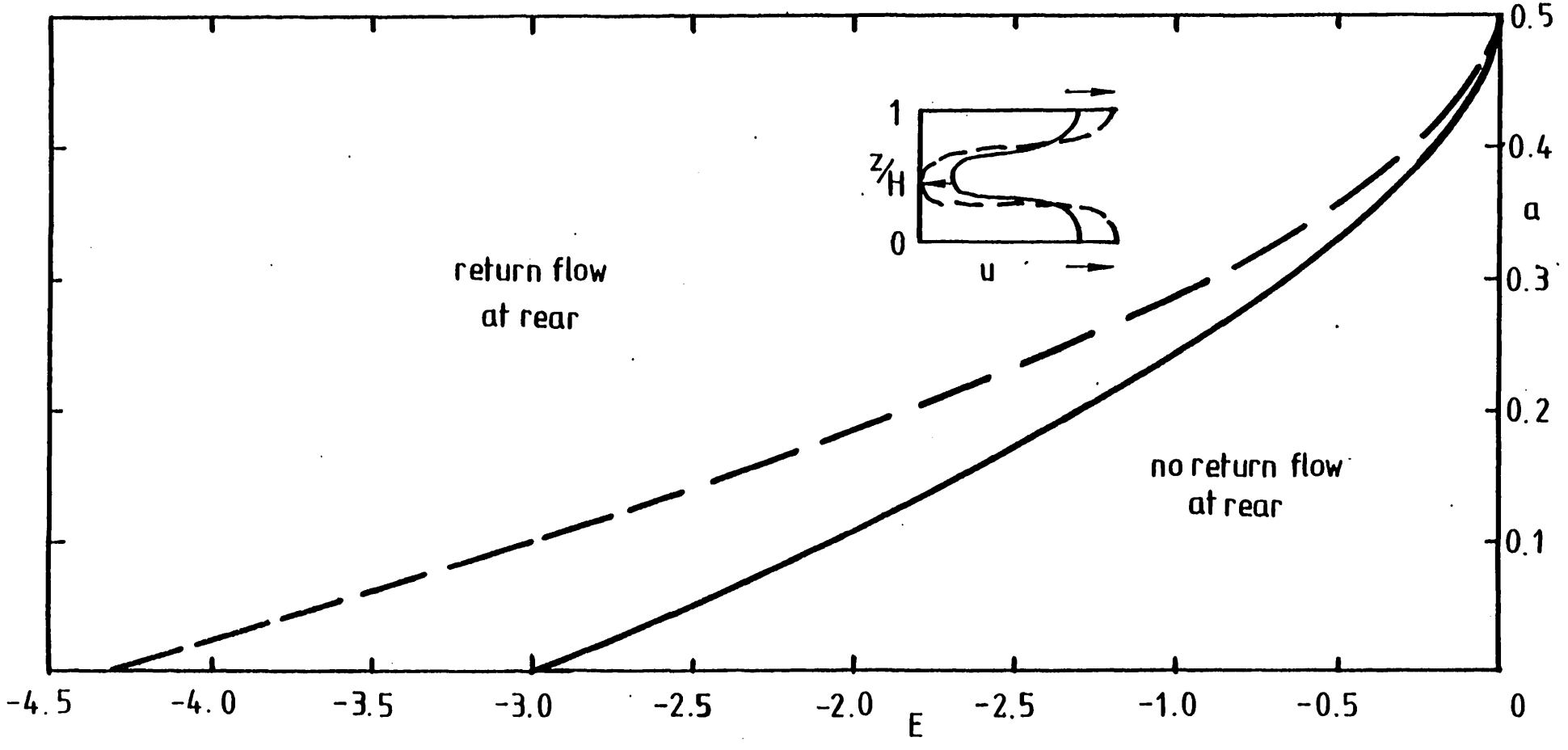
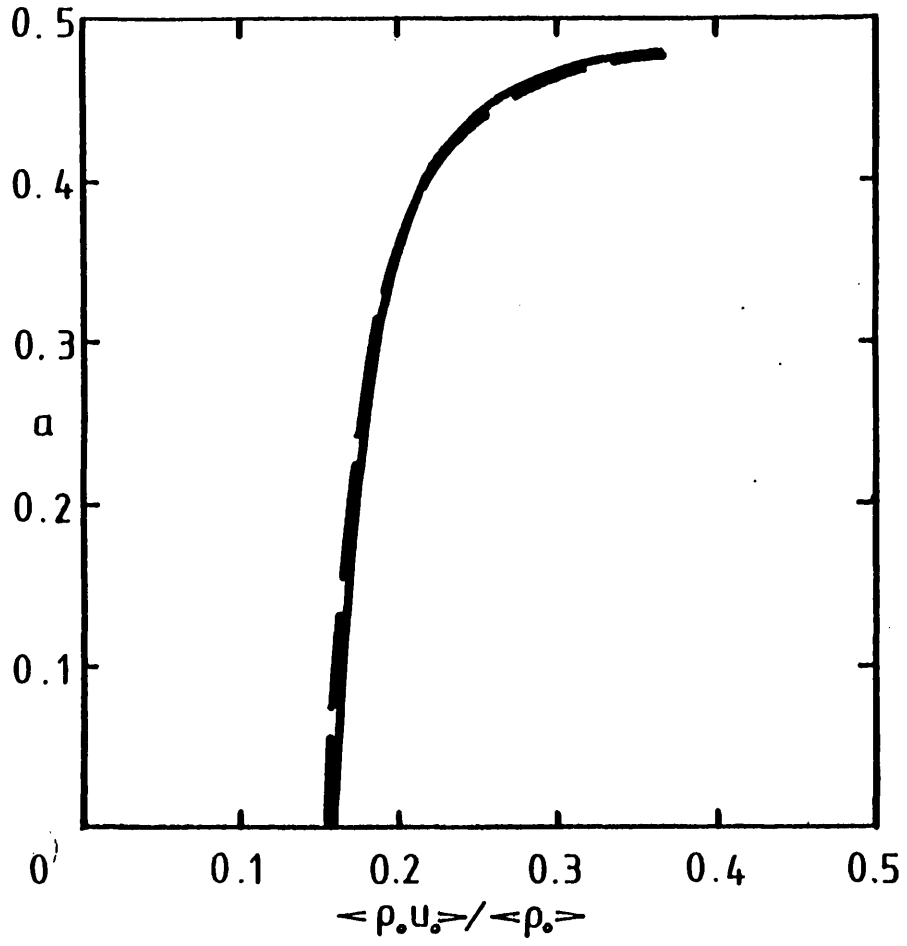
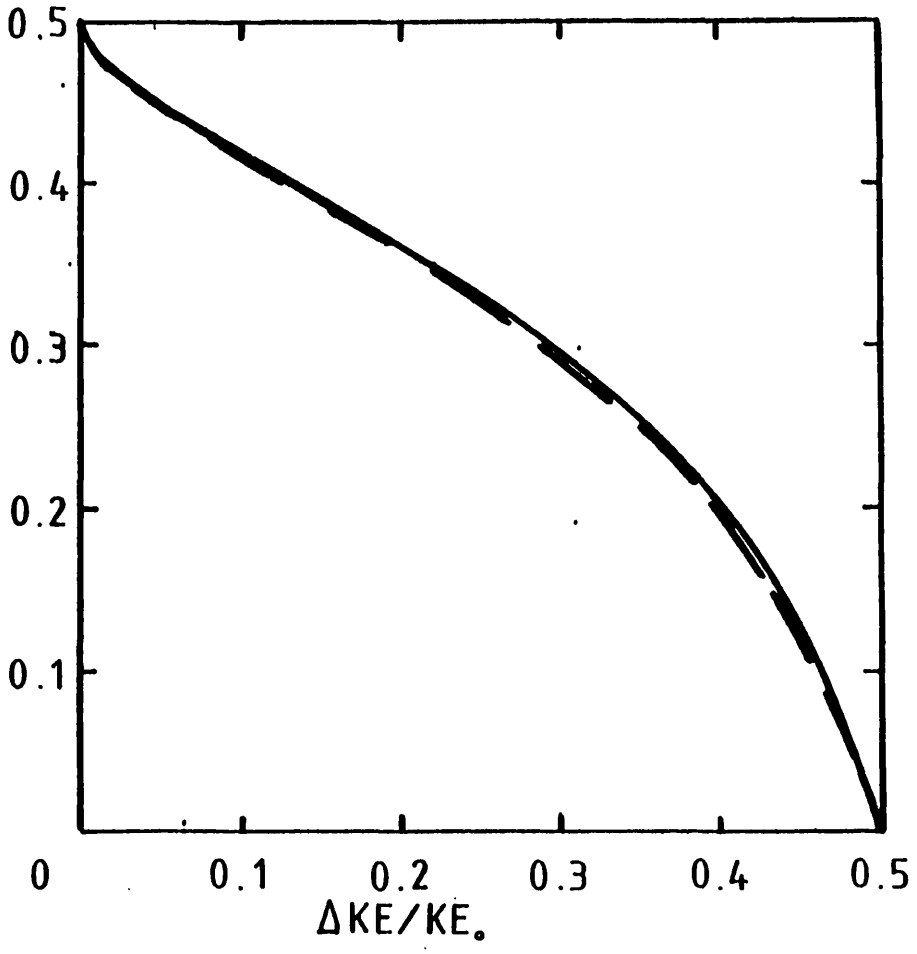


Figure 3.2.15. Boundary curve for no relative inflow at the rear for n=2 mode circulations with upper level ascent, lower level descent for E against a.



(a)



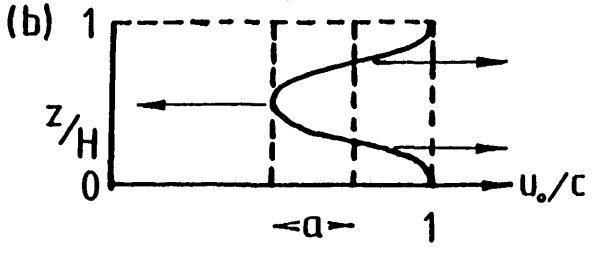


Figure 3.2.16. As figure 3.2.13 except for an n=2 mode with upper level ascent, lower level descent.

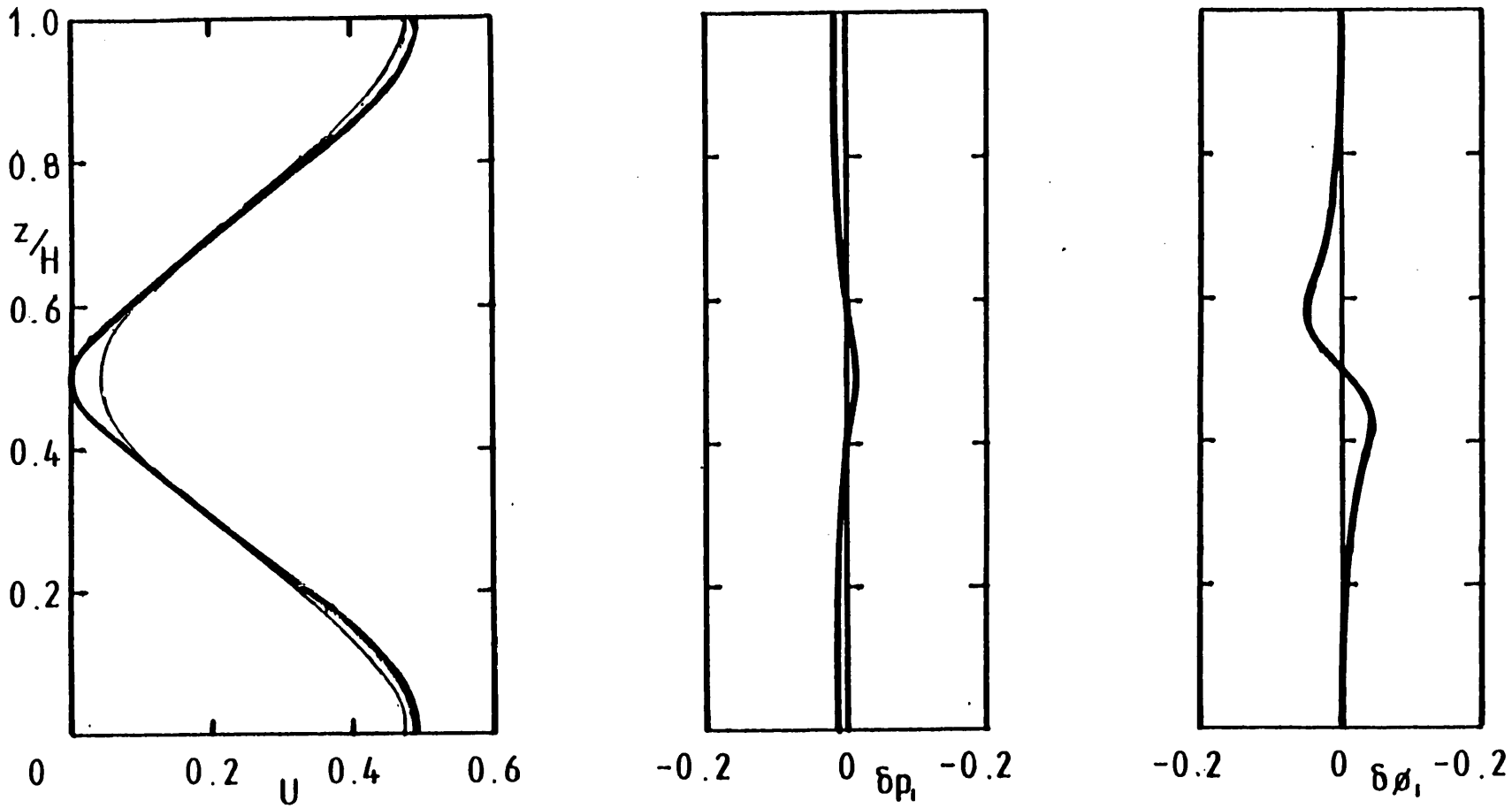


Figure 3.2.17 As figure 3.2.14 except for an n=2 mode with upper level ascent, lower lower level descent. $a = 0.45, E = -0.06$.

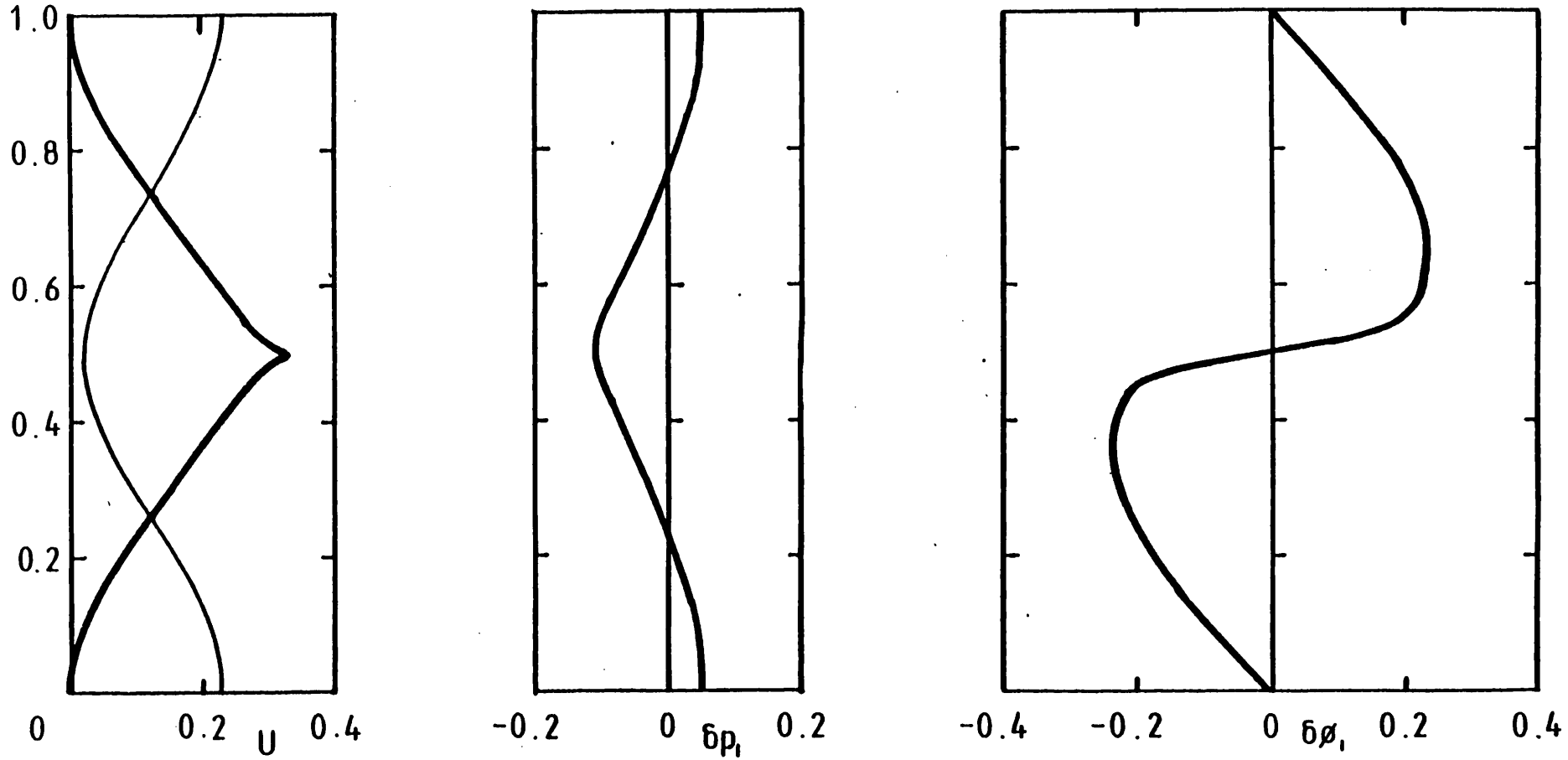


Figure 3.2.18. As figure 3.2.14 except for an n=2 mode with upper level descent, lower level ascent. $a = 0.45$, $E = 1$.

The distribution of solutions for n=2 type modes as a function of E and a is shown in figure 3.2.15. The boundary curve represents the maximum efficiency solutions for a given jet amplitude. As the amplitude of the jet increases E tends to zero, ie. a forced flow of a symmetric type cannot occur when the jet amplitude is large. The extreme case (a=0.5) can only occur when E=0 (ie. no forcing at all). Compressibility does not significantly extend the range of parameter space in which solutions occur. Figures 3.2.16a and b show the variation of propagation speed and $\Delta KE/KE_o$ with a. As a tends to 0.5, the propagation speed tends to zero, corresponding to a case with no forcing. The generation of mean flow kinetic energy also tends to zero as a tends to 0.5.

Outflow relative velocity, pressure and entropy perturbation profiles with a=0.45 are shown for E=-0.06 in figure 3.2.17. It is no surprise, that for E small and negative, the changes to the velocity, pressure and entropy perturbation profiles are all small. There is a slight acceleration of the upper and low level flow and a very small deceleration of the middle level flow. Upper level ascent with cooling and lower level descent with warming occur. It would be possible to have large amplitude changes if the inflow at mid-levels were larger. However, observations suggest that the flow close to the rear of the squall line is nearly stagnant (Gamache and Houze, 1982).

The profiles with E=+1 show a very large mid-level acceleration (eg. figure 3.2.18). There is upper level descent and lower level ascent. However, the regime with low level cooling and upper level warming is exactly opposite to the observed changes in the rear of squall clusters and so, in the present context, can be discounted as being physically unreasonable.

In summary, it is unlikely that an n=2 type forcing of a jet profile occurs with both upper level and lower level acceleration. A more likely occurrence is the n=1 type forcing with upper level deceleration and lower level acceleration, and descent with warming at all levels.

3.3 Forced Flows in which Net Deviation of Limiting Streamlines Occurs.

This section deals with forced flows which must interact with a convective flow in the manner described as type "B", and which are useful in identifying the qualitative effects of inflow to the rear of the mesoscale response region. Net descent of the lower streamline may occur because of a net mass flux from the pre-squall subcloud layer, through convective updraughts, to the level of the anvil outflow. This injection of boundary layer air into upper levels may also cause descent of the air previously occupying that layer in a forced circulation.

In this section it is shown that many of the higher order solutions listed in section 3.2.1 are not possible unless relative inflow at the rear occurs for flows in which the limiting streamlines experience a net vertical displacement. Such a flow is illustrated in figure 3.3.1 below.

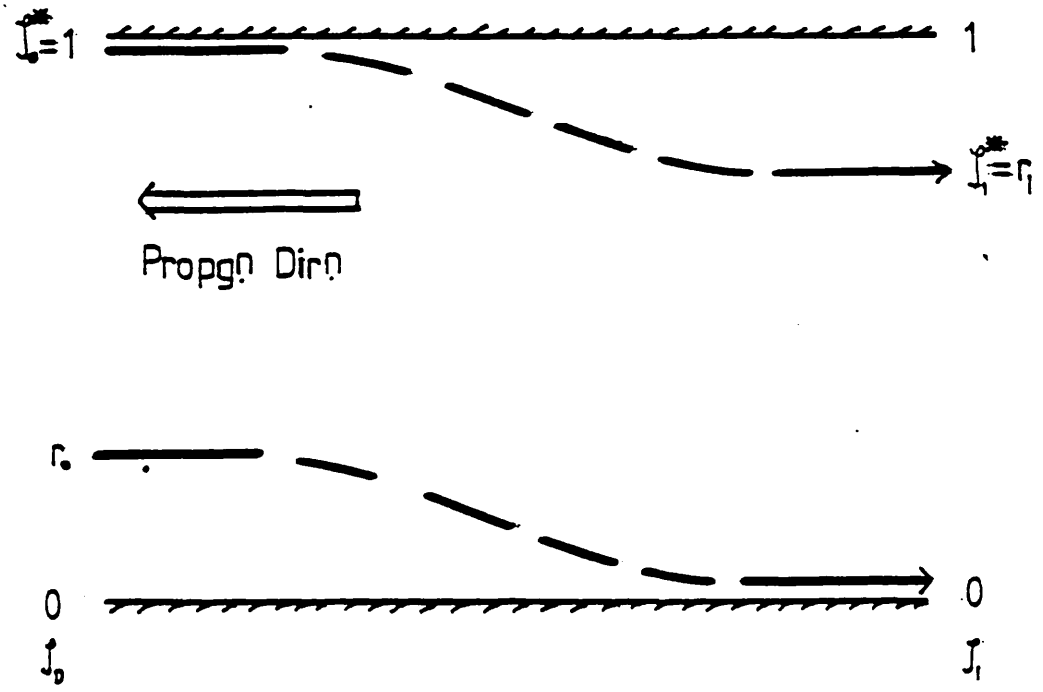


Figure 3.3.1

The displacement equation 3.5 for an incompressible unsheared flow together with the boundary conditions 3.2 and 3.3 are now solved. Differentiating 3.5 as before with respect to $\mathcal{J}_1$ we obtain equation 3.8. The solution to this equation and boundary conditions 3.2 and 3.3 which must also satisfy equation 3.5 is

$$\mathcal{J}_0 = \mathcal{J}_1 + \frac{1}{\sin \frac{\pi}{F_f}} \left[(1-r_1) \sin \frac{\mathcal{J}_1}{F_f} + r_0 \sin \frac{r_1 - \mathcal{J}_1}{F_f} \right] \qquad (3.20)$$

where
$$F_f \left(1 \pm \sqrt{1-E} \right) \sin \frac{\pi}{F_f} = r_0 - (1-r_1) \cos \frac{\pi}{F_f} . \qquad (3.21)$$

Since we require $d\mathcal{J}_0/d\mathcal{J}_1 \geq 0$ for $0 \leq \mathcal{J}_1 \leq r_1$ the positive square root is neglected. Solutions taking the positive square root always have $d\mathcal{J}_0/d\mathcal{J}_1 \leq 0$ for $\mathcal{J}_1 = r_1$, the equality operating only when E=0, which implies relative inflow at the rear must occur. By taking the limit

of the case $1-r_1=r_o=\delta$ to be very small, equations 3.20 and 3.21 can be reduced to equation 3.9 with $1/F_f=n\pi$, which is the result found in TMM80.

3.3.1 Variation of F with E.

Previously the unsheared incompressible solutions produced in TMM80 showed no dependence of F_f on E. When net deviation of one or both streamlines occurs F_f becomes dependent on $\dot{E}$. Three cases are considered. Firstly, net vertical deviation of the lowest streamline; secondly, net vertical deviation of the uppermost streamline; finally, equal net vertical displacement of both lowest and highest streamlines. Net displacements of C.05 are considered as examples below.

(i) For $r_o=0.05$ and $r_1=1$ the flow is shown schematically in figure 3.3.2 below.

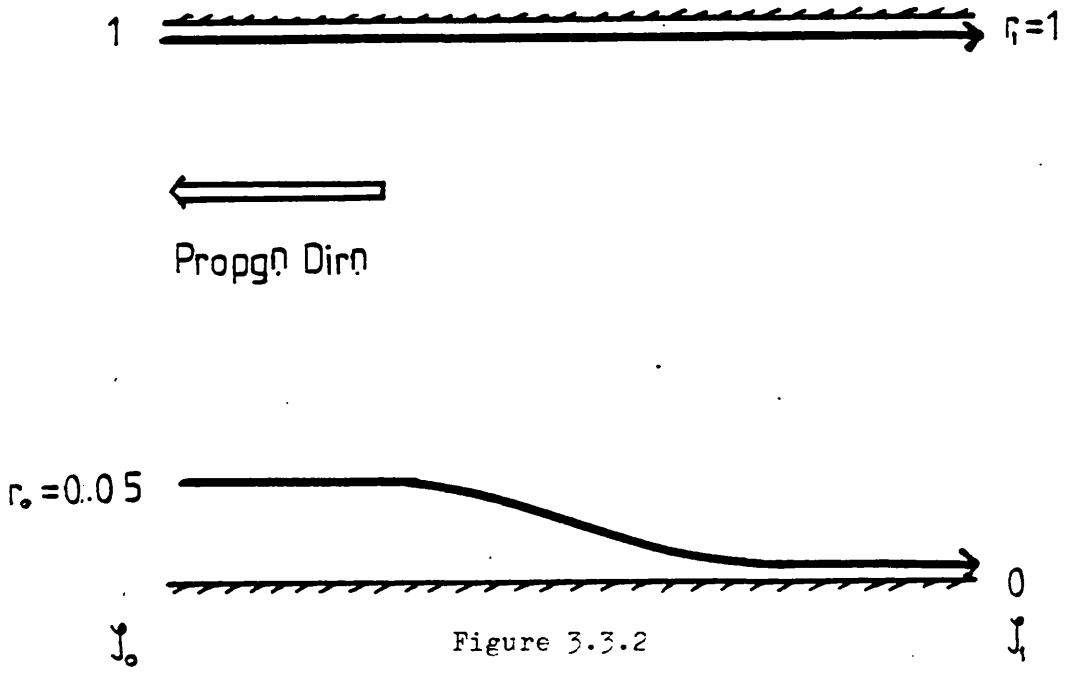


Figure 3.3.2

3.21 becomes $$\sin\frac{1}{F_f} = \frac{r_o}{F_f(1-\sqrt{1-E})}, \qquad (3.22)$$

The variation of F_f with E when $r_o=0.05$ is shown in figure 3.3.3. (Also shown is the variation of F_f with E for $r_o=0$). When E is positive eigensolutions (F_f) cannot exist when $1-(1-E)^{1/2} \geq 0.05$. When E is negative the minimum value of $\sin(1/F_f)/(1/F_f)$ is -0.22. Hence when $r_o=0.05$ there can be no eigensolutions to 3.22 for $-0.506 \leq E \leq 0.098$. For higher order modes (larger $1/F_f$) the range in which no eigensolutions occur is larger since the maximum value of $r_o/(1-(1-E)^{1/2})$ is limited by the maxima and minima of the function $\sin(1/F_f)/(1/F_f)$, ie. $1-(1+r_o/0.22)^2 \leq E \leq 1-(1-r_o)^2$.

(ii) For $r_o=0$, $r_1=0.95$ the flow is shown schematically in figure 3.3.4 below.

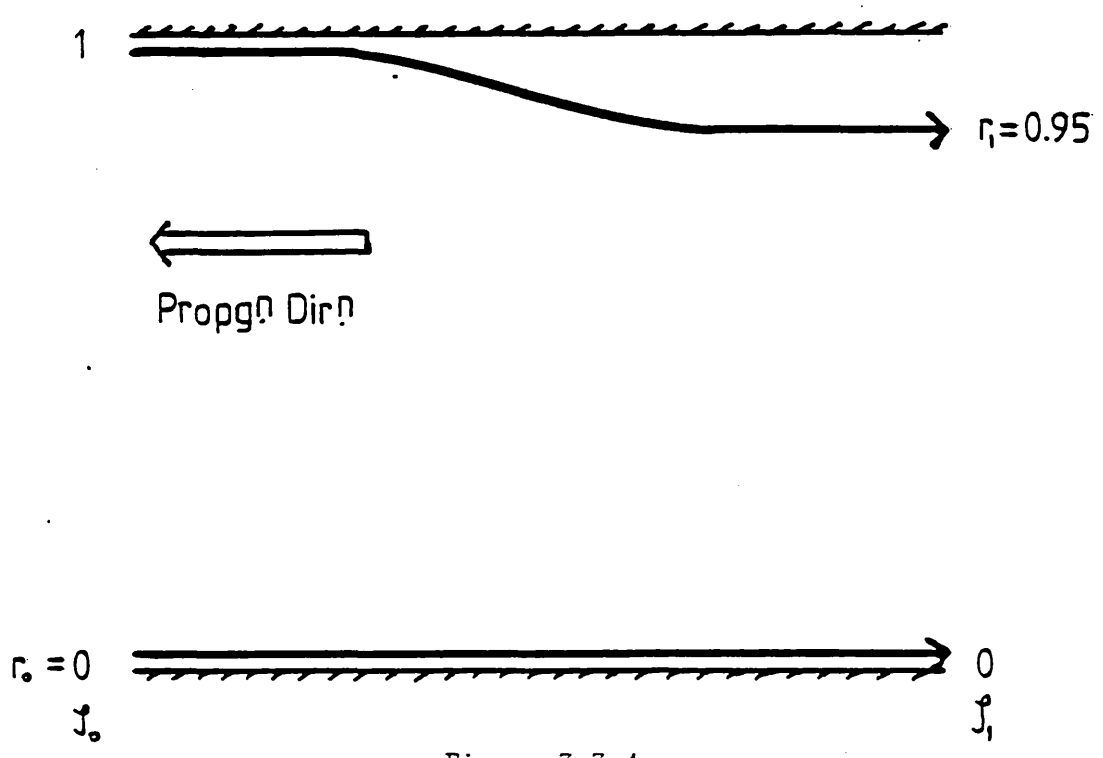


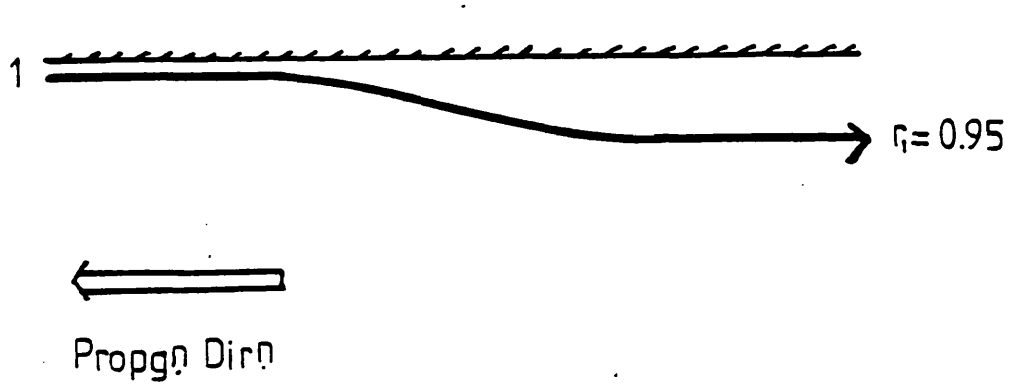
Figure 3.3.4

Equation 3.21 becomes :-

$$\tan \frac{\Gamma}{F_f} = -\frac{(1-\Gamma)}{F_f(1-\sqrt{1-E})} . \qquad (3.23)$$

The variation of F_f with E is shown in figure 3.3.5. Solutions to the eigenvalue equation 3.23 occur for all values of E, however there are small breaks in the ranges of possible solutions near $1/F_f = n\pi$ as in case (i) above.

(iii) For $r_o=0.05$, $r_1=0.95$ the flow is sketched in figure 3.3.6 below.



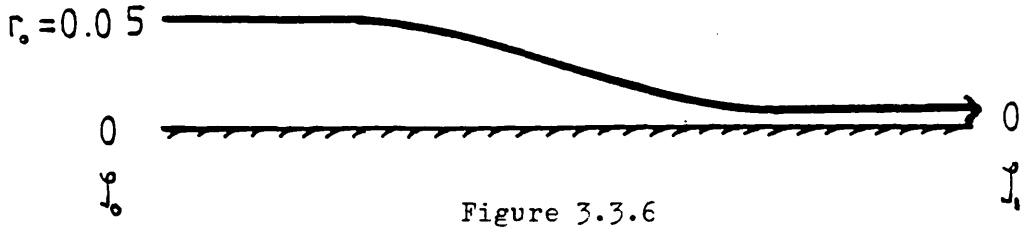


Figure 3.3.6

The range of possible solutions for the flow displayed in figure 3.3.6 is a combination of those shown in figures 3.3.3 and 3.3.5. The eigenvalue equation 3.21 becomes:-

$$\cot \frac{\Gamma}{2F_f} = \frac{1-\Gamma}{F_f(1-\sqrt{1-E})} . \qquad (3.24)$$

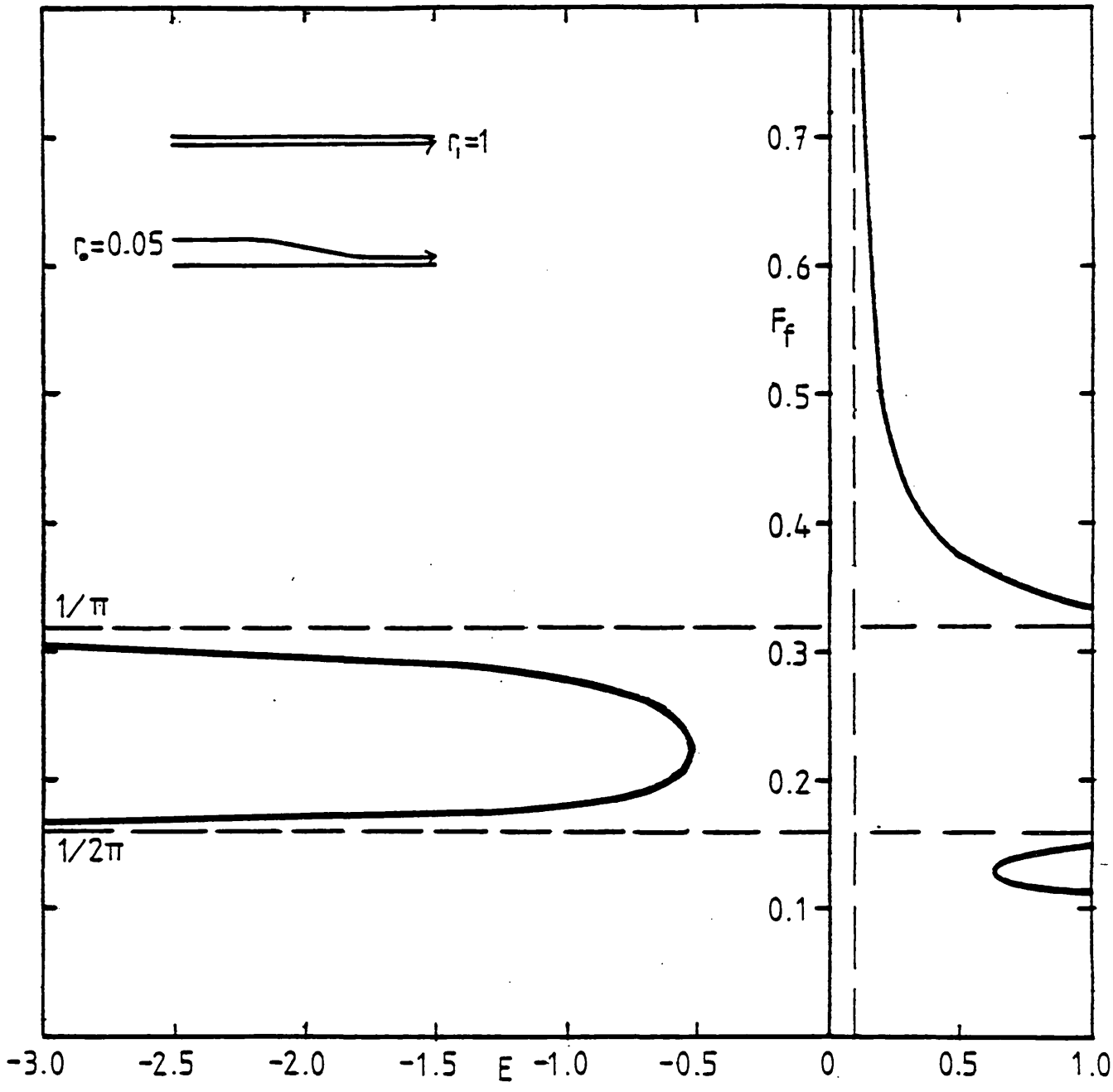


Figure 3.3.3. Variation of F_f with E, r_e=0.05, r_i=1.0.

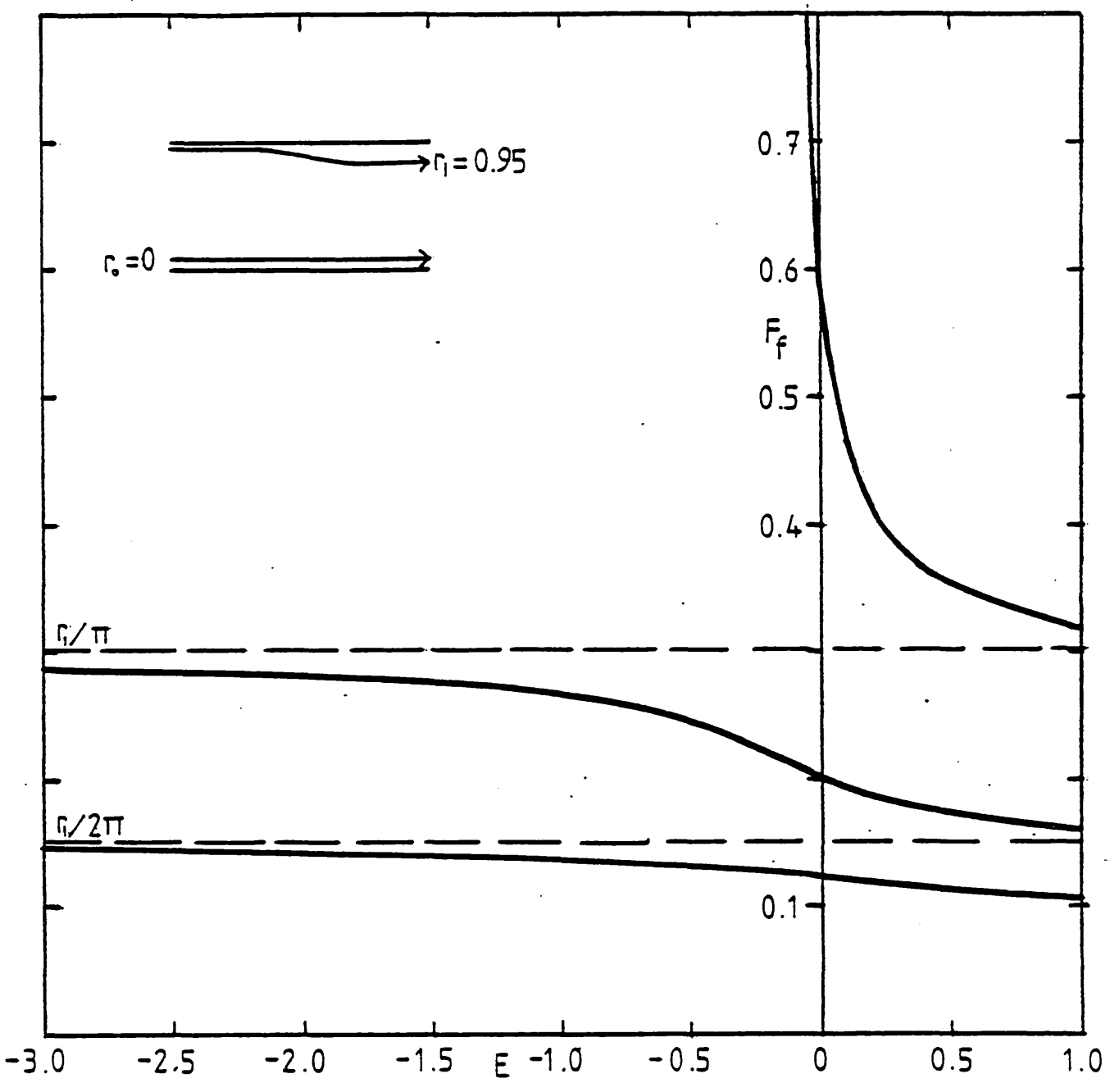


Figure 3.3.5. Variation of F_f with E, $r_0 = 0$, $r_1 = 0.95$.

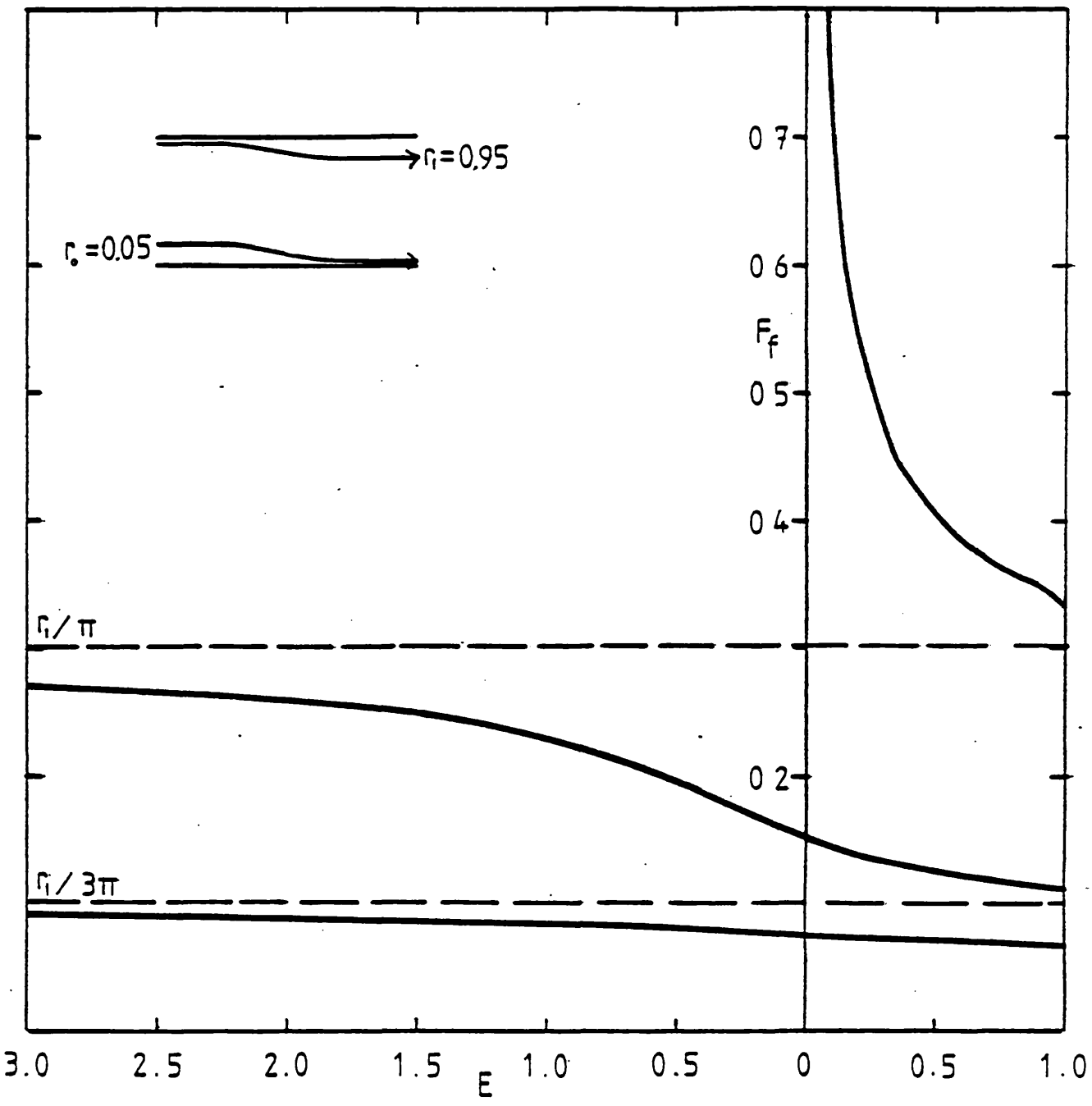


Figure 3.3.7. Variation of F_f with E, $r_0 = 0.05$, $r_1 = 0.95$.

The variation of F_f with E is shown in figure 3.3.7.

3.3.2 Flows with No Relative Inflow at the Rear for E=+1 and E=-3.

In general, it is not possible to state which solutions of the transcendental equation 3.21 have relative inflow at the rear. However, considering the cases which previously corresponded to maximum increases in mean flow kinetic energy in section 3.2.1, ie. E=+1 and E=-3 some insight can be gained. We require that there be no relative inflow at the rear, ie. $u_1 \geq 0$. From the continuity equation 3.1 and 3.20 the expression for relative outflow velocity is given by:-

$$\frac{u_1}{c} = 1 + \frac{1}{F_f \sin\frac{\pi}{F_f}}\left[(1-r_1)\cos\frac{\phi_1}{F_f} - r_o \cos\frac{\pi-\phi_1}{F_f}\right]. \qquad (3.25)$$

(i)(a) When $r_1 = 1$, 3.25 using 3.22 reduces to:-

$$\frac{u_1}{c} = 1 - \epsilon \cos\frac{1-\phi_1}{F_f} \qquad (3.26)$$

where $\epsilon = 1-(1-E)^{1/2}$. Since the maximum value of ϵ is +1 no relative inflow occurs for any r_o. When E=1, $\epsilon = 1$ and 3.22 becomes:-

$$\sin\frac{1}{F_f} = \frac{r_o}{F_f}, \qquad (3.27)$$

Since we require both F_f and r_o to be positive and $0 \leq r_o \leq 1$ the solutions must lie in the ranges $0 \leq 1/F_f \leq \pi$, $2\pi \leq 1/F_f \leq 3\pi$, ... or $2n\pi \leq 1/F_f \leq (2n+1)\pi$, where n=0,1,2... From the sketch of y=sin(x)/x in figure 3.3.8 below we see that as $1/F_f$ increases (F_f decreases) fewer solutions become

available. For $r_o > 0.13$ only one solution is possible.

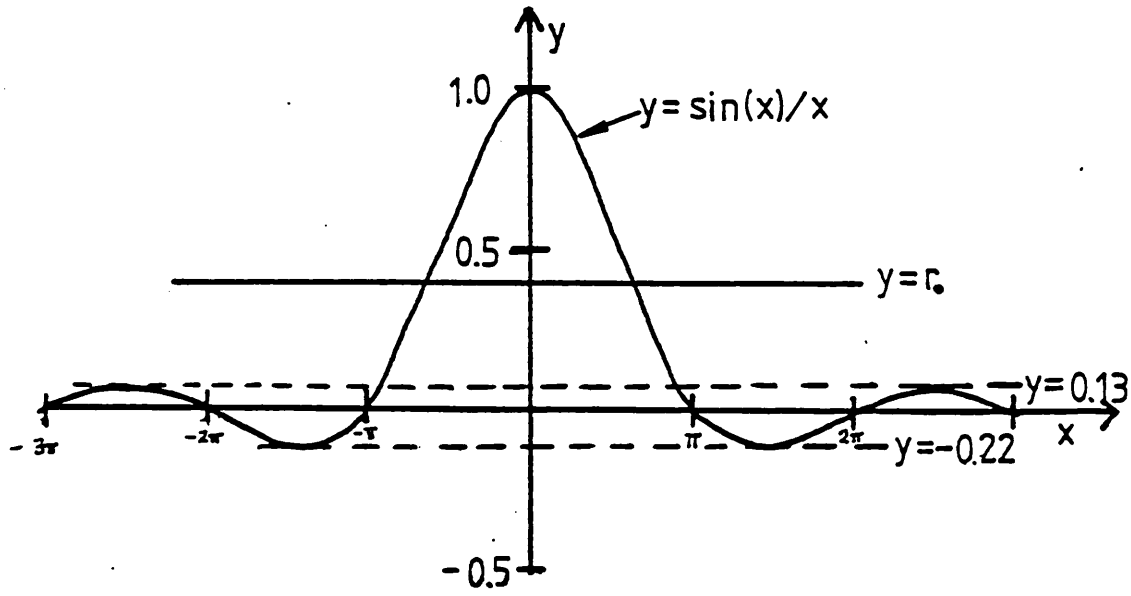


Figure 3.3.8

The type of solution obtained can be seen by studying the equation for the entropy change on outflow. From 2.10 using 3.20:-

$$\delta\phi_1 = (B-\gamma)H \frac{1}{\sin\frac{\pi}{F_f}} \left[(1-r_1)\sin\frac{\vartheta_1}{F_f} + r_o \sin\frac{\pi-\vartheta_1}{F_f} \right]. \qquad (3.28)$$

When $r_1 = 1$, 3.28 becomes:-

$$\delta\phi_1 = (B-\gamma)\, H\, r_o \quad \sin\frac{1-\vartheta_1}{F_f} \Big/ \sin\frac{1}{F_f} \,. \qquad (3.29)$$

When $0 \leq 1/F_f \leq \pi$, $\frac{\delta\phi}{\vartheta_1} > 0$ for all ϑ_1, ie. descent with warming occcurs at all levels. When $2\pi \leq 1/F_f \leq 3\pi$ two or three distinct layers are defined. The top layer warms, the middle layer cools and the lowest layer (present if $1/F_f > 2\pi$) warms. Similarly, it can be shown that all higher mode solutions must have "n odd" in the sense that there are an odd

number of layers alternately showing ascent and descent. Warming with descent always occurs in the highest and lowest layers for $r_o > 0$.

(i)(b) When E=-3, 3.26 becomes:-

$$\frac{u_1}{c} = 1 + \cos\frac{1-\rho_1}{F_f} \tag{3.30}$$

where from 3.22 $$\sin\frac{1}{F_f} = -\frac{r_o}{F_f} . \tag{3.31}$$

Following similar reasoning to that used in the E=+1 case, allowed values of $1/F_f$ must lie in the ranges $(2n-1)\pi \leq 1/F_f \leq 2n\pi$ where n=1,2... The maximum value of r_o, from figure 3.3.8 is given by the amplitude of the first negative peak so that $r_o \leq 0.22$. From 3.29 we see that these solutions correspond to "n even" modes with low level warming and descent, upper level cooling and ascent. Examples of flow regimes for both E=+1 and E=-3 are shown in figure 3.3.9.

(ii)(a) When $r_o=0$, 3.25 using 3.23 reduces to:-

$$\frac{u_1}{c} = 1 - \epsilon\cos\frac{\rho_1}{F_f} \Big/ \cos\frac{\pi}{F_f} . \tag{3.32}$$

When E=+1, ϵ =+1 and 3.23 becomes:-

$$\tan\frac{\pi}{F_f} = -\frac{(1-\pi)}{F_f} . \tag{3.33}$$

Solutions to 3.33 with $0 \leq \pi_1 \leq 1$ occur for $\pi/F_f=0$, $\pi/2 \leq \pi/F_f \leq \pi$, $3\pi/2 \leq \pi/F_f \leq 2\pi$.... However from 3.32 $u_1 \leq C$ when $\pi/F_f > 3\pi/2$ so allowed solutions with no relative inflow at the rear occur only when $\pi/2 \leq \pi/F_f \leq \pi$ non-trivially. From 3.28 entropy changes are given by:-

$$\delta\phi_1 = (B-\gamma)H(1-r_1)\sin\frac{\eta_1}{F_f} \Big/ \sin\frac{r}{F_f} \quad . \tag{3.34}$$

These solutions correspond to $\delta\phi_1 \geq 0$ for all η_1 and describe a flow with descent at all levels, as shown in figure 3.3.10.

(ii)(b) When E=-3, ϵ =-1, and from 3.32 $u_1/c>0$ when $\cos(\eta_1/F_f)/\cos(r/F_f)>-1$. 3.23 becomes:-

$$\tan\frac{r}{F_f} = \frac{1-r}{F_f} \quad . \tag{3.35}$$

Solutions to 3.35 when $0\leq r_1\leq 1$ occur for $0\leq r_1/F_f\leq\pi/2$, $\pi\leq r_1/F_f\leq 3\pi/2$.... When $r_1/F_f>\pi$ we see from 3.32 that relative inflow occurs at the rear. However, 3.35 has non-trivial solutions for $0\leq r_1/F_f\leq\pi/2$ only when $(1-r_1)/r_1\geq 1$ or $r_1\leq 0.5$. From 3.34 we see that this mode corresponds to acceleration of the flow at all levels with warming and descent. Examples of flow regimes for both E=+1 and E=-3 are shown in figure 3.3.10.

(iii)(a) Finally we consider the case $r_o=1-r_1=\delta$. Equation 3.25 becomes, using 3.24

$$\frac{u_1}{c} = 1-\epsilon\sin\frac{2\eta_1-r}{F_f} \Big/ \sin\frac{r}{2F_f} \quad . \tag{3.36}$$

When E=+1, ϵ =+1 and 3.24 becomes:-

$$\cot\frac{r}{2F_f} = \frac{1-r}{F_f} \quad . \tag{3.37}$$

Solutions lie in the ranges $0\leq r_1/2F_f\leq\pi/2$, $\pi\leq r_1/2F_f\leq 3\pi/2$... For no relative inflow at the rear we require $u_1/c\geq 0$ ie.

$\sin((2\xi-r_1)/2F_f)/\sin(r_1/2F_f)\leq 1$. When $0\leq r_1/2F_f\leq\pi/2$ this condition is satisfied. However, in all other ranges, relative inflow occurs at the rear. 3.28 becomes:-

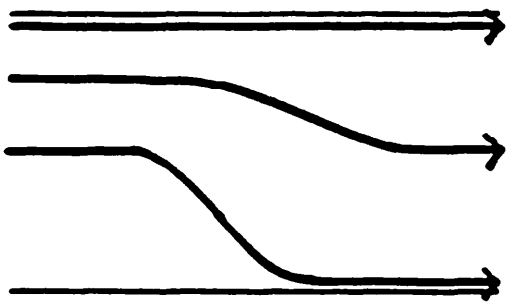
$$\delta\phi_1 = (B-\gamma)\,\delta H \cos\frac{2\xi_1-r_1}{F_f} \Big/ \cos\frac{r_1}{2F_f}. \qquad (3.38)$$

The permissable solutions, from 3.38, are n=1 type modes with warming and descent throughout the depth of the circulation.

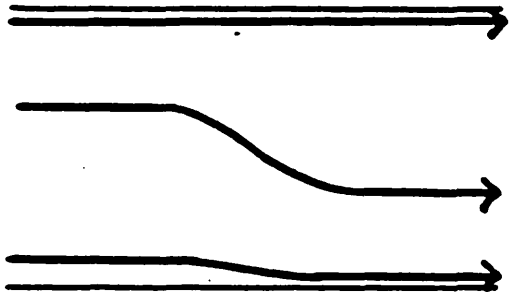
(iii)(b) When E=-3, ϵ =-1, solutions for $r_1/2F_f$ occur in the ranges $\pi/2\leq r_1/2F_f\leq\pi$, $3\pi/2\leq r_1/2F_f\leq 2\pi$... The requirement for no relative inflow to occur at the rear, $\sin((2\xi-r_1)/2F_f)/\sin(r_1/2F_f)\geq -1$ from 3.36, cannot be satisfied in any of the possible ranges. An example of the type of flow expected is shown in figure 3.3.11 for E=+1.

We see that net deviation of limiting streamlines and the requirement of no relative inflow at the rear effectively limits the number of possible solutions for the cases examined. These three cases ((i), (ii), (iii)) are summarised in table 3.3.1.

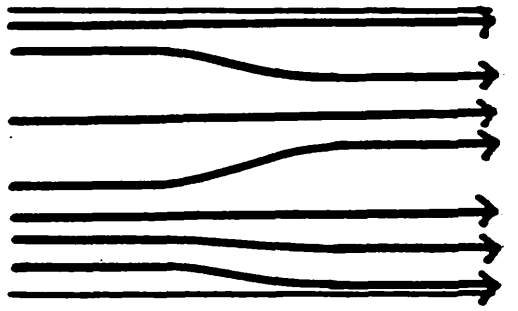
The many solutions available for various r_2 and r_1 are best explored in the light of the requirements of the circulations in chapter four. In general the outflow relative velocity profile must be checked for each solution to detect relative inflow at the rear, and the value of E giving rise to the maximum mechanical efficiency solution must be found.



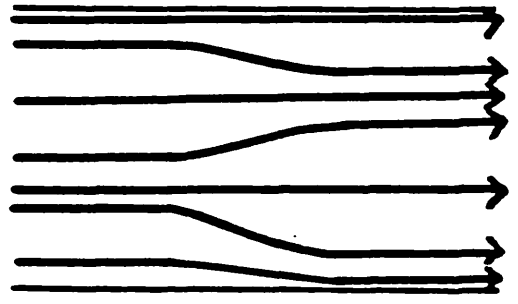
$1/F_f \backsim \pi/2$, $n=1$, $r_o \backsim 0.5$.



$1/F_f \backsim \pi-\delta$, $n=1$, $r_o \backsim 0.1$.

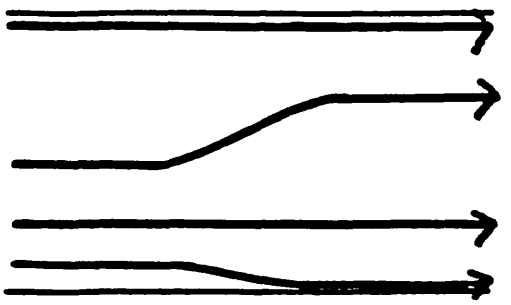


$1/F_f \backsim 2\pi+\delta$, $n=3$, $r_o \leq 0.13$.

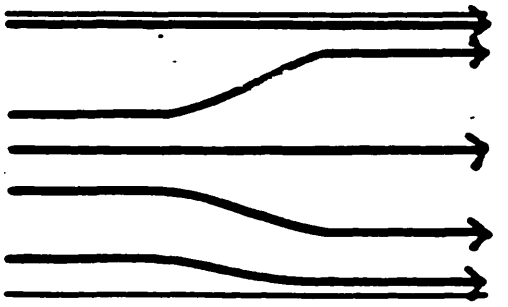


$1/F_f \backsim 3\pi-\delta$, $n=3$, $r_o \leq 0.13$.

E=+1



$1/F_f \backsim \pi+\delta$, $n=2$, $r_o \leq 0.22$.



$1/F_f \backsim 2\pi-\delta$, $n=2$, $r_o \leq 0.22$.

E=-3

Figure 3.3.9. Permitted flow modes, $r_i=1$.

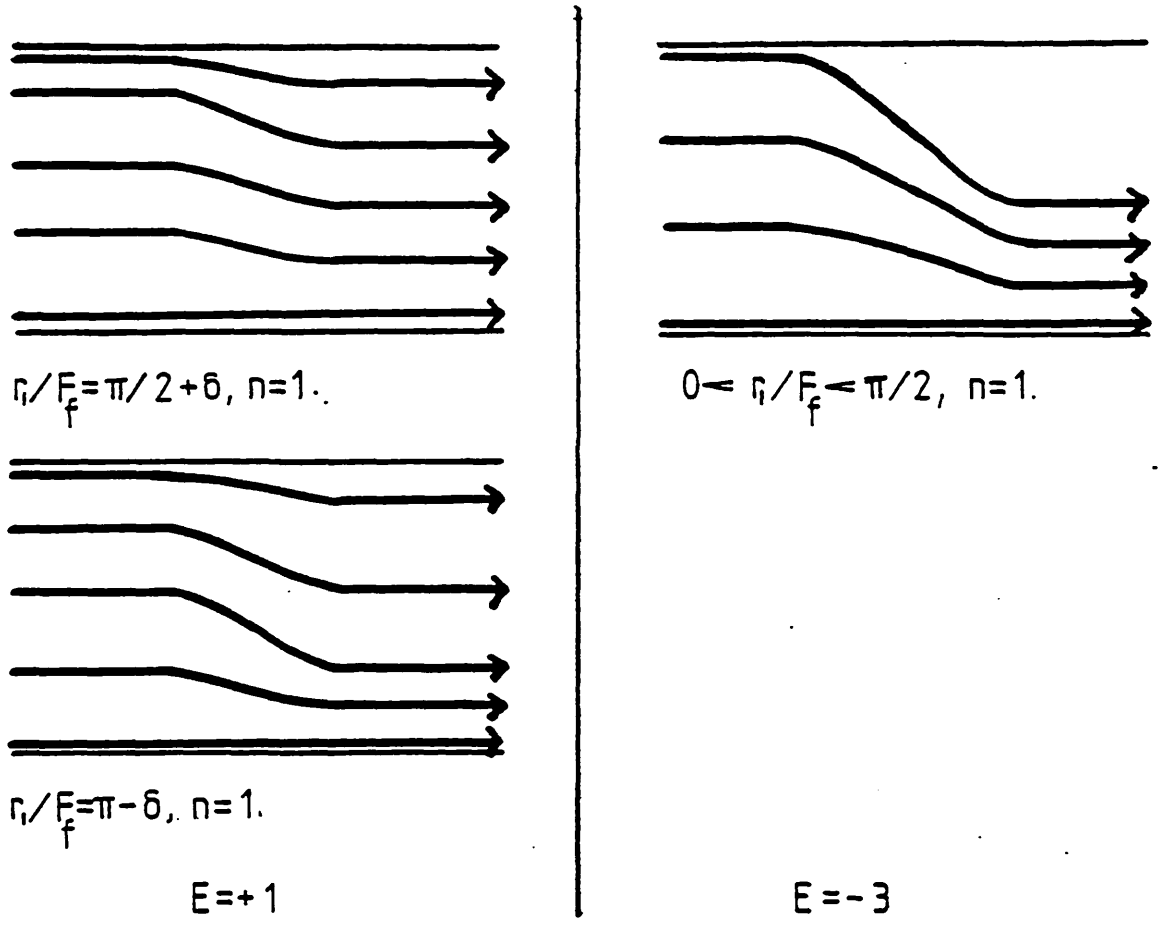


Figure 3.3.10. Permitted flow modes, $r_o = 0$.

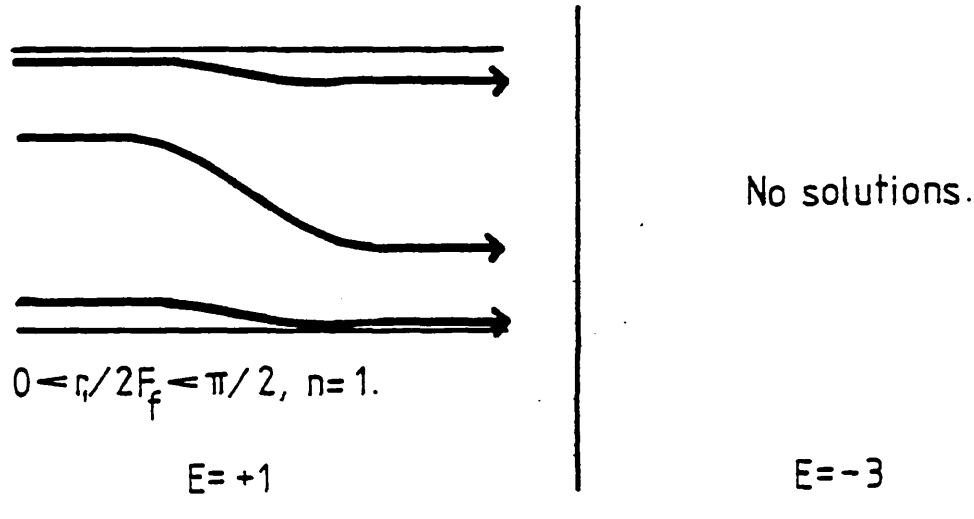


Figure 3.3.11. Permitted flow modes, $r_o = 1 - r_i \neq 0$.

r_0	r_1	E=+1	E=-3
$0 \leq r_0 \leq 1$	$r_1=1$	"n-odd" modes only allowed with upper and lower level descent and warming:- n=1, $0 \leq r_0 \leq 1$; n=3, $0 \leq r_0 \leq 0.13$; n=5, etc	"n-even" modes only allowed with upper and lower level ascent and cooling:- n=2, $0 \leq r_0 \leq 0.22$; n=4, etc
$r_0=0$	$0 \leq r_1 \leq 1$	"n=1" mode only allowed with warming and descent at all levels.	"n=1" mode only allowed with warming and descent at all levels; $(1-r_1) \leq 0.5$.
$r_0=1-r_1$, $0 \leq r_0 \leq 1$.		"n=1" mode only allowed with warming and descent at all levels.	No solutions.

Table 3.3.1

CHAPTER FOUR

THE FORCED MESOSCALE RESPONSE

TYPE "B"

4.1 Introduction.

In chapter three the convective forcing and the mesoscale response were described as two consecutive events (type "A"). In this chapter the forcing and response occur simultaneously in a steady frame of reference (type "B").

The dry, forced subsidence of air beneath the precipitating squall line anvil has been emphasised in Zipser (1977) and Houze (1977). The air taking part in this circulation must either have followed a path around a line element or have found itself behind a newly-growing line element.

The convective updraught transports air from the subcloud layer to upper levels, Betts (1976). Since it is initially negatively sheared and becomes positively sheared on outflow, this updraught air must overturn. A two-dimensional updraught which does not overturn, as described in TMM82, must obey a vorticity constraint which would require the shear on outflow to become more negative when heating occurs in the updraught. The squall line updraught must consequently be described by a three-dimensional overturning circulation.

The convective downdraught is by contrast a feature which is quite difficult to detect in terms of level of origin of air and direction and amount of descent, Houze (1977).

4.1.1 A Type "B" Prototype Circulation.

A simple model which encompasses a forced downdraught is sketched schematically in figure 4.1.1 below.

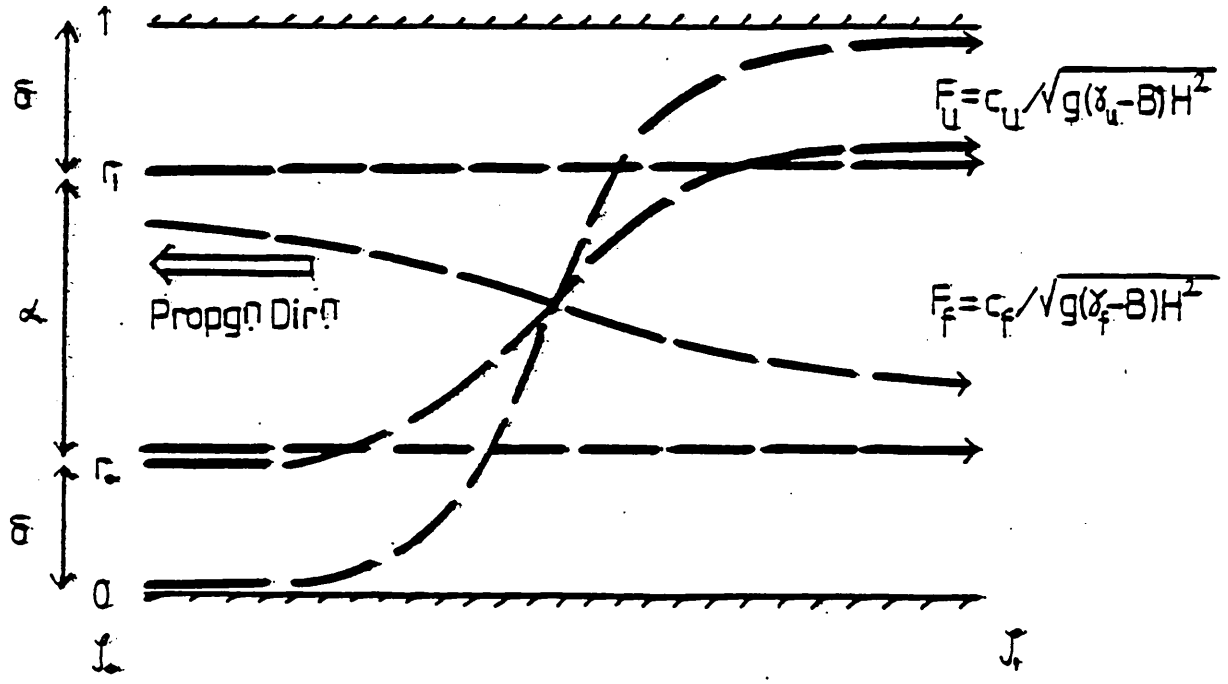


Figure 4.1.1

The convective updraught is described in section 2.3.2. For the forced flow the theory is described in section 3.2.1 and is the circulation depicted in TMM80. The subscript "u" refers to convective updraught and "f" to forced downdraught variables. In the circulation shown in figure 4.1.1, the convective updraught maintains a constant depth ($r_0 = 1 - r_1 = \delta$). The forced downdraught layer of depth αH is above the convective updraught inflow and below the convective updraught outflow. Pressure continuity at $\eta_1 = r_1$ from 2.22 and 3.13 gives:-

$$\frac{1}{2}c_u^2\left[E_u + \left(\frac{r_1 - r_0}{F_u}\right)^2\right] = \frac{1}{2}c_f^2 E_f . \qquad (4.1)$$

The eigenvalue equation for a convective flow 2.19 gives:-

$$\left(1+\sqrt{1-E_u}\right)F_u \sinh\frac{\delta}{F_u} = 1-\alpha\cosh\frac{\delta}{F_u} \qquad (4.2)$$

and from section 3.2.1 $1/F_f=\pi$ for an n=1 mode descent solution. F_f and F_u are defined in figure 4.1.1 where $\alpha=r_1-r_o$. Assuming no shear on inflow ($c_u=c_f$) and writing $1-r_1=\delta$, $\alpha=1-2\delta$, 4.1 becomes:-

$$E_f = E_u + \left(\frac{1-2\delta}{F_u}\right)^2 . \qquad (4.3)$$

We cannot impose maximum mechanical efficiency ($E_u=E_f=1.$) on both updraught and downdraught. If $E_f=1$ then E_u must be less than one from 4.3 for non-trivial values of F_u. Consider the case of maximum generation of kinetic energy for the forced flow ($E_f=1$). Substituting for E_u in 4.2 we have:-

$$F_u = \left(1-(1-2\delta)\cosh\frac{\delta}{F_u}\right) \Big/ \sinh\frac{\delta}{F_u} - (1-2\delta).$$

This equation in F_u is in a suitable form for solution by an iterative technique when δ is specified. The details are given in Appendix B. E_u can be obtained from 4.3. From 3.9 the maximum forced vertical displacement is $\alpha F_f H$. From the expressions for F_u and F_f, given in figure 4.1.1, the maximum warming ($\Delta\theta_{max}$) may be calculated, taking H=1Ckm and UCAPE=1000Jkg^{-1}.

$$\delta\phi_{1\,max} = (B-\gamma_f)F_f(r_1-r_o)\,H$$

$$\Delta\theta_{max} \simeq 300\,\delta\phi_{1\,max}$$

α	δ	F_u	Δz/km	$\Delta\theta$/K	E_u
0.1	0.45	0.3278	0.3183	20.25	0.907
0.2	0.40	0.4082	0.6366	15.70	0.760
0.3	0.35	0.4836	0.9549	14.69	0.615
0.4	0.30	0.5572	1.2732	14.63	0.485
0.5	0.25	0.6303	1.5915	14.98	0.371
0.6	0.20	0.7035	1.9099	15.55	0.273
0.7	0.15	0.7770	2.2282	16.26	0.188
0.8	0.10	0.8509	2.5465	17.06	0.116
0.9	0.05	0.9252	2.8648	17.93	0.538

Table 4.1.1

For this "prototype" case the predicted warming is very large (14-20K), see table 4.1.1, being a minimum when the updraught is neither very "thin" nor very "thick", ie. $1-r_1 \sim 0.3$. The propagation speed is high ranging from 0.328 when $1-r_1 = 0.45$ to 0.925 when $1-r_1 = 0.05$ in normalised units or 14.7 to 41.4ms^{-1}.

The circulations to be examined in the bulk of this chapter will allow the updraught to become shallower or deeper on outflow. More reasonable potential temperature changes of a few degrees are then produced.

The simplest model in which inflow and outflow circulations are specified at all inflow and outflow levels, which encompasses a forced downward circulation and a three dimensional overturning updraught, is sketched below in figure 4.1.2. A further development including a convective downdraught is discussed in section 4.6.

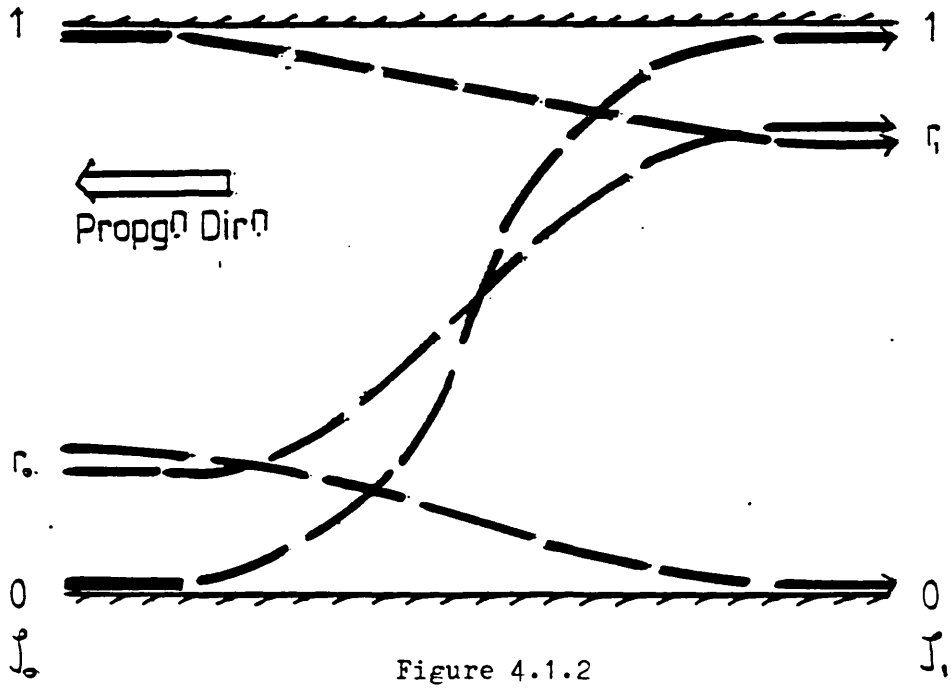


Figure 4.1.2

All air initially in the layer $r_0 \leq \zeta_0 \leq 1$ descends to leave between the surface and $\zeta_1 = r_1$. The convective updraught ascends from the subcloud layer $0 \leq \zeta_0 \leq r_0$ leaving above the forced flow. In reality this transformation is considered as a set of discrete cells travelling through the environmental air. Only the remote flow (the asymptotic solution) can be described with the equations developed here. The flow is certainly non-hydrostatic within the updraught and may be unsteady as new cells form and decay during the lifetime of a squall cluster. However air parcels travel through the system in times which are typically tens of minutes, much shorter than either a line element lifetime or the duration of the steady phase. In this circumstance the displacement equation describes the modification of the thermodynamic properties of the inflow air quite adequately.

4.2.1 The Convective Updraught Circulation.

The equations describing the updraught circulation were derived in chapter two and are restated below. The flow is taken to be incompressible with constant relative inflow velocity c_u, see figure 4.2.1.

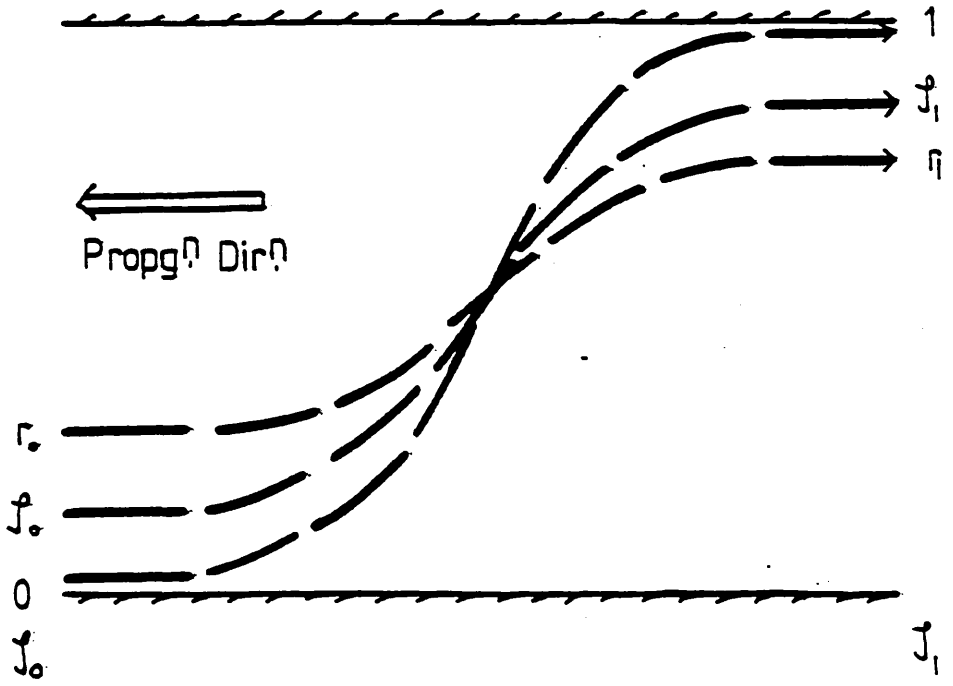


Figure 4.2.1

The subscript "u" now refers to updraught variables. The solution to the displacement equation 2.14, subject to the boundary conditions 2.15 and 2.16, is

$$f_o = f_1 - \frac{1}{\sinh \frac{1-r_1}{F_f}} \left[\sinh \frac{f_1-r_1}{F_u} + (r_1-r_o) \sinh \frac{1-f_1}{F_u} \right] \qquad (4.4)$$

where $$\left(1+\sqrt{1-E_u}\right) F_u \sinh \frac{1-r_1}{F_u} = 1 - (r_1-r_o) \cosh \frac{1-r_1}{F_u} \qquad (4.5)$$

and $$E_u = 1 - \left[u_1(r_1) / c_u \right]^2 \qquad (4.6)$$

$$F_u = c_u / \sqrt{g(\gamma_u - B)H^2}. \qquad (4.7)$$

The equations for outflow relative velocity, entropy perturbation and pressure perturbation, 2.20, 2.21 and 2.22, are

$$\frac{u_1}{c_u} = \frac{1}{F_u \sinh \frac{1-r_1}{F_u}} \left[\cosh \frac{s_1 - r_1}{F_u} - (r_1 - r_0) \cosh \frac{1-s_1}{F_u} \right] - 1 \qquad (4.8)$$

$$\frac{\delta\phi_1}{(\gamma_u - B)H} = \frac{1}{\sinh \frac{1-r_1}{F_u}} \left[\sinh \frac{s_1 - r_1}{F_u} + (r_1 - r_0) \sinh \frac{1-s_1}{F_u} \right] \qquad (4.9)$$

$$\frac{\delta p_1}{\frac{1}{2}\rho_s c_u^2} = E_u + \left(\frac{r_1 - r_0}{F_u} \right)^2 + 2 \left(\frac{u_1}{c} - \sqrt{1 - E_u} \right). \qquad (4.10)$$

4.2.2 The Forced Downdraught Circulation.

The equations describing this circulation were derived in chapter three and are summarised below. The limiting streamlines are shown in figure 4.2.2.

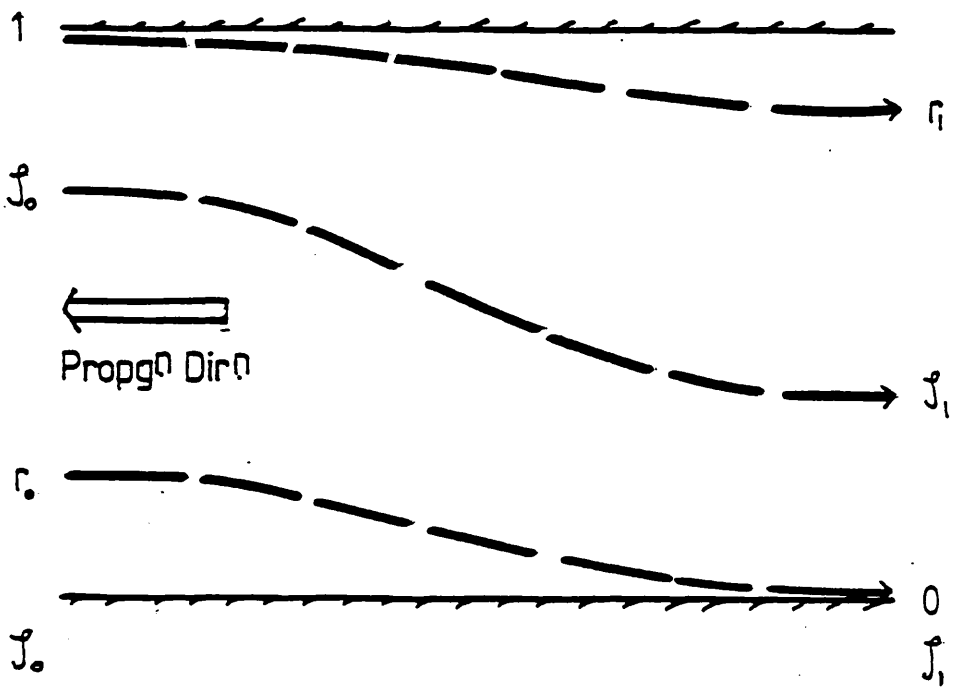


Figure 4.2.2

Variables subscripted "f" now refer to the forced downdraught circulation. The solution to the displacement equation 3.4, with boundary conditions 3.2 and 3.3, for an incompressible unsheared inflow, is

$$f_0 = f_1 + \frac{1}{\sin \frac{\pi}{F_f}} \left[(1-r_1) \sin \frac{f_1}{F_f} + r_0 \sin \frac{r_1 - f_1}{F_f} \right] \qquad (4.11)$$

where $$(1 - \sqrt{1-E_f}) F_f \sin \frac{r_1}{F_f} = r_0 - (1-r_1) \cos \frac{r_1}{F_f} \qquad (4.12)$$

$$E_f = 1 - \left[u_1(r_1) / c_f \right]^2 \qquad (4.13)$$

$$F_f = c_f / \sqrt{g(B-\gamma_f)H^2}. \qquad (4.14)$$

The equations for the relative outflow velocity and entropy perturbation, 3.25, and 3.28, are given below. The presure perturbation on outflow is obtained from 2.7, where $\delta\phi_p$ and $\delta\phi_1$ are given by 2.9 and 2.10, $\Delta = \frac{1}{2}c_f^2 E_f$ and $(\mathfrak{J}_1 - \mathfrak{J}_0)$ is given by 3.20. The expression is simplified using 3.21 and 4.15 to give 4.17.

$$\frac{u_1}{c_f} = 1 + \frac{1}{F_f \sin\frac{\Gamma_1}{F_f}}\left[(1-r_1)\cos\frac{\mathfrak{J}_1}{F_f} - r_1\cos\frac{r_1-\mathfrak{J}_1}{F_f}\right] \qquad (4.15)$$

$$\frac{\delta\phi_1}{(B-\gamma_f)H} = \frac{1}{\sin\frac{\Gamma_1}{F_f}}\left[(1-r_1)\sin\frac{\mathfrak{J}_1}{F_f} + r_0\sin\frac{r_1-\mathfrak{J}_1}{F_f}\right] \qquad (4.16)$$

$$\frac{\delta p_1}{\frac{1}{2}\rho_s c_f^2} = E_f - \left(\frac{1-r_1}{F_f}\right)^2 - 2\left(\frac{u_1}{c_f} - \sqrt{1-E_f}\right). \qquad (4.17)$$

4.2.3 Closure of the Equation System.

At $\mathfrak{J}_1 = r_1$ (see figure 4.1.2) the outflow pressure must be continuous otherwise a discontinuity in the pressure would result in infinite accelerations. The layer $r_1 \leq \mathfrak{J}_1 \leq 1$ is assumed to consist of updraught outflow air, and the entire region below must be occupied by air which has descended in the forced downdraught. There is no variation of displacement in the y-direction in outflow or inflow, so in this sense the outflow is two-dimensional. So continuity of pressure using 4.10 and 4.17 at $\mathfrak{J}_1 = r_1$ gives the condition,

$$\frac{1}{2}c_u^2\left[E_u+\left(\frac{r_1-r_0}{F_u}\right)^2\right]=\frac{1}{2}c_f^2\left[E_f-\left(\frac{1-r_1}{F_f}\right)^2\right], \qquad (4.18)$$

Substituting for c_u and c_f using 4.7 and 4.14,

$$E_u+\left(\frac{r_1-r_0}{F_u}\right)^2=\left(\frac{F_f}{F_u}\right)^2\frac{\left[E_f-\left(\frac{1-r_1}{F_f}\right)^2\right]}{\frac{\gamma_u-B}{B-\gamma_f}}, \qquad (4.19)$$

The parameter r_o is assumed to be the scaled height of the subcloud layer. This was found to be the depth of the inflow layer to Venezuelan clusters described in Betts (1976). In this incompressible formulation any comparison with data must use the pressure depth of the inflow in mb scaled by the pressure depth of the disturbance in mb so that mass intervals are equal.

B is the environmental lapse rate of $\log\theta$ (assumed constant) and γ is the pseudo-moist adiabatic parcel lapse rate of $\log\theta$. γ_f is the parcel lapse rate in forced descent but is not easily determined, since its value depends on the proportion of condensate in the updraught which evaporates into the forced circulation. Neutrally buoyant descent with $B=\gamma_f$ is examined in the isentropic case in section 4.3. A more complicated formulation with detailed calculation of mixing ratios, evaporation and rainfall rates is not justified for the idealised model used. Increasing evaporation into the forced downdraught corresponds to increasing γ_f and $\sqrt{\frac{\gamma_u-B}{B-\gamma_f}}$ thus reducing the potential warming of the downdraught air. The equation set is solved for a variety of values of $\sqrt{\frac{\gamma_u-B}{B-\gamma_f}}$ and by comparison with observations a reasonable value is suggested.

The inflow shear is represented as two layers of air moving at

different speeds. $\Delta c = c_f - c_u$, the difference between mean inflow speed above and below cloud base, or

$$\frac{\Delta c}{\sqrt{2UCAPE}} = \frac{F_f}{\sqrt{\frac{\gamma_u - B}{B - \gamma_f}}} - F_u \,. \qquad (4.20)$$

The system is finally closed by maximising the increase in mean flow kinetic energy as in MM. This is achieved by solving equations 4.5, 4.12, 4.19 and 4.20 simultaneously for F_u, F_f, E_u and r_1 while varying E_f. This variation is also examined in section 4.4.2 for updraught and downdraught individually.

4.3 Solution with a Neutrally Buoyant Downdraught.

A neutrally buoyant downdraught ($\gamma_f = B$) simplifies the general problem and presents an interesting result. The forced downdraught becomes deeper on descent, suggesting that the forced flow controls the circulation pattern. Consider 4.12 and 4.14 as $(B - \gamma_f)$ tends to zero. Since $F_f \propto c_f/(B-\gamma_f)^{1/2}$, F_f must tend to infinity as $(B - \gamma_f)$ tends to zero.

Then $$\lim_{F_f \to \infty} \left(F_f \sin \frac{\pi}{F_f} \right) = \pi$$

$$\lim_{F_f \to \infty} \left(\cos \frac{\pi}{F_f} \right) = 1$$

and equation 4.12 becomes $(1-r_o)/r_1 = (1-F_f)^{1/2}$. Substituting in 4.18 for $(1-E_f)$ when $c_u = c_f$ and re-arranging

$$1-E_u = \left(\frac{1-r_0}{r_1}\right)^2 + \left(\frac{r_1-r_0}{F_u}\right)^2 . \qquad (4.21)$$

Consider equation 4.5 for $(1-r_1)/F_u<1$. Substituting for $(1-E_u)^{1/2}$ using 4.21 and re-arranging gives

$$\frac{1}{F_u^2} = \frac{1}{(r_1-r_0)^2}\left[\left(\frac{r_0}{1-r_1}\right)^2 - \left(\frac{1-r_0}{r_1}\right)^2\right] .$$

If $r_0>1-r_1$, $1/F_u^2>0$,

$r_0<1-r_1$, $1/F_u^2<0$,

ie. there are no real solutions for F_u if $r_0<1-r_1$. No solutions with a freely convecting updraught occur if the forced flow becomes thinner on outflow.

4.4.1 Solutions of the Full Equation Set.

The most satisfactory method of solution found is to fix E_f and rewrite equations 4.5, 4.12, 4.19 eliminating F_f from 4.12 and 4.19 using 4.20 in the form

$$r_1 = F_1(r_1, F_u, E_u) \qquad (4.22)$$

$$F_u = F_2(r_1, F_u, E_u) \qquad (4.23)$$

$$E_u = F_3(r_1, F_u, E_u) \qquad (4.24)$$

These three equations 4.22, 4.23 and 4.24 are solved by an iterative scheme described in Appendix B for r_1, F_u and E_u to within a

tolerance of 10^{-6} starting with reasonable initial guesses. E_f can then be varied to maximise the increase of mean flow kinetic energy. For the convective flow the increase in the kinetic energy comes from the CAPE. For the forced flow however, the kinetic energy is increased by the work done by the pressure field.

4.4.2 Energy Conversion Within the Updraught, Downdraught and Combined Circulations.

In this section E_f was varied in the range $0 \leq E_f \leq 1$ and the case of zero inflow shear with $r_o = 0.2$ and $\sqrt{\frac{\gamma_u - \beta}{\beta - \gamma_f}} = 1.0$ was considered. For each value of E_f the following quantities were calculated for updraught, downdraught and total circulation.

The net production of vertically integrated kinetic energy:-

$$\int_{outflow} \frac{1}{2} \rho_1 u_1^2 dz_1 - \int_{inflow} \frac{1}{2} \rho_0 u_0^2 dz_0 \qquad (4.25)$$

The net flux of kinetic energy:-

$$\int_{outflow} \frac{1}{2} \rho_1 u_1^3 dz_1 - \int_{inflow} \frac{1}{2} \rho_0 u_0^3 dz_0 \qquad (4.26)$$

The vertically integrated net release of CAPE:-

$$\int_{outflow} \rho_1 \left\{ \int_{z_0}^{z_1} g \delta \phi_b \, dz \right\} dz_1 \qquad (4.27)$$

The net flux of CAPE:-

$$\int_{outflow} \rho_1 u_1 \left\{ \int_{z_0}^{z_1} g\delta\phi_p \, dz \right\} dz_1 \qquad (4.28)$$

The net production of kinetic energy and release of CAPE are normalised by the vertically integrated net inflow of kinetic energy.

ie $$\int_{inflow} \frac{1}{2} \rho_0 u_0^2 \, dz_0$$

The net flux of kinetic energy and net flux of CAPE are normalised by the inflow flux of kinetic energy.

ie $$\int_{inflow} \frac{1}{2} \rho_0 u_0^3 \, dz_0$$

This normalisation enables comparisons to be made between systems with different values of E_f and different propagation speeds. For the convective circulation it may be more logical to normalise the release of CAPE in the updraught by, for example, the value for the streamline of maximum displacement since this represents the CAPE of air originally at the surface. For the forced flow however, the choice of normalisation is not so obvious. For both forced and convective circulations the normalisation should incorporate the speed of propagation of the system - which has been achieved by normalisation by the inflow kinetic energy and inflow flux of kinetic energy.

The iterative scheme is not well conditioned near $E_f=0$ as F_f tends to infinity. An analytical treatment is necessary in this region. From 4.12:-

$$\left(1-\sqrt{1-E_f}\right) = \frac{1}{F_f \sin\frac{r_1}{F_f}}\left[r_o - (1-r_1)\cos\frac{r_1}{F_f}\right]$$

as E_f tends to zero, the left hand side of the equation tends to zero. $r_o-(1-r_1)\cos(r_1/F_f)\rightarrow 0$ since $1/F_f/(\sin(r_1/F_f))=0$ for any r_1/F_f where $r_1 \leq 1$. The numerical solution indicates that $1/F_f \rightarrow 0$ as $E_f \rightarrow 0$. From the equation for pressure continuity 4.19

$$E_u = E_f - \left(\frac{1-r_1}{F_f}\right)^2 - \left(\frac{r_1-r_o}{F_u}\right)^2$$

when $\sqrt{\frac{\gamma_u-\beta}{\beta-\gamma_f}} = 1.0$, $F_u = F_f \rightarrow \infty$, and E_u tends to zero. Within the convective updraught then 4.5

$$\left(1+\sqrt{1-E_u}\right) F_u \sinh\frac{1-r_1}{F_u} = 1 - (r_1-r_o)\cosh\frac{1-r_1}{F_u}$$

becomes $1-r_1 = r_o$ so that the depth of the outflow is equal to the depth of the inflow. The net displacement of a streamline in the updraught outflow when $1-r_1 = r_o$ becomes, from 4.4

$$1-\mathcal{J}_1 = \mathcal{J}_o \quad .$$

There is no relative moving together of streamlines. Outflow velocity, $-u_o dz_o/dz_1 = u_1$, so there is no change in velocity on outflow. Production of kinetic energy falls to zero as E_f tends to zero.

For the forced downdraught from 4.11

$$\mathcal{J}_1 - \mathcal{J}_o = -r_o$$

and $u_1=u_o dz_o/dz_1=u_o$. There is no net generation of kinetic energy and all streamlines are equally displaced. Curves from 4.25 and 4.26 tend to zero as E tends to zero. However since $\int_{z_o}^{z_1} g\,\delta\phi_p\,dz$ remains finite curves from 4.27 and 4.28 will attain a constant value. When normalised by the inflow kinetic energy or rate of inflow of kinetic energy they will tend to zero as E_f tends to zero because u_o is proportional to F_f which tends to infinity.

The continuation of the curves for $E_f<1$ at higher rates of kinetic energy generation correspond to solutions with relative inflow at the rear which are excluded from the permitted set of solutions.

For the convective updraught, figures 4.4.1 and 4.4.2 show an increase of CAPE release and kinetic energy production with E_f. Rate of CAPE release and rate of kinetic energy production (figures 4.4.3 and 4.4.4) are also a maximum for $E_f=1$.

In the forced circulation the CAPE of the flow increases since work must be done on it to make it descend. The curves in figures 4.4.1 and 4.4.3 are negative everywhere - with a maximum negative value at $E_f=1$. Net generation of kinetic energy only occurs for $E_f>0.8$ for the forced downdraught, figure 4.4.2. Since the outflow depth is always greater than the inflow depth (except for $E_f=0$ where it is equal) the mean outflow velocity is less than the mean inflow velocity and the outflow shear is small - there is a net decrease of kinetic energy for $E_f\leq 0.8$.

In calculating an "efficiency", $\mathcal{E}_K$, for the total circulation after the manner described in Moncrieff (1981) where

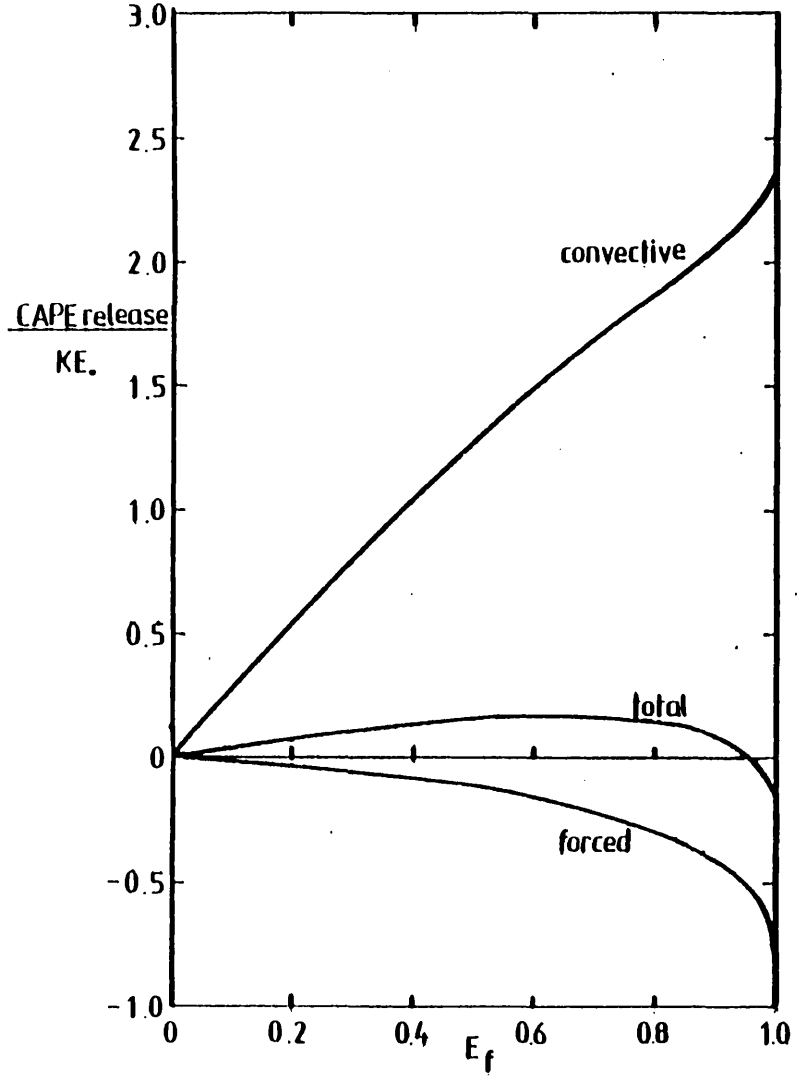


Figure 4.4.1.

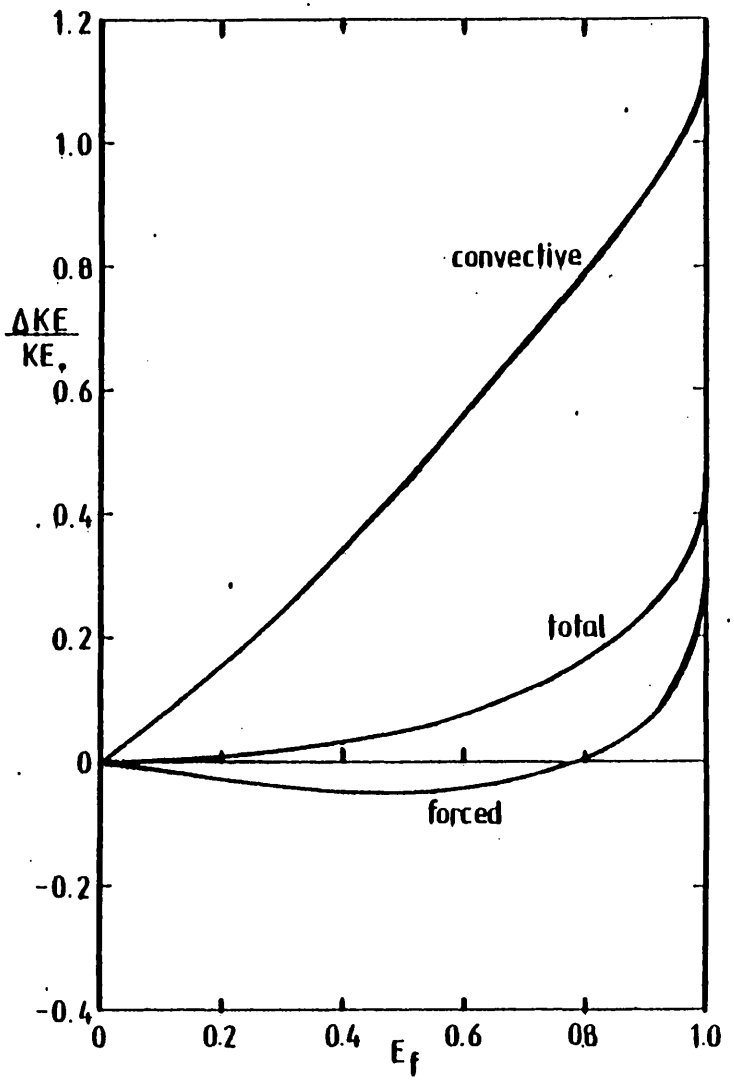


Figure 4.4.2.

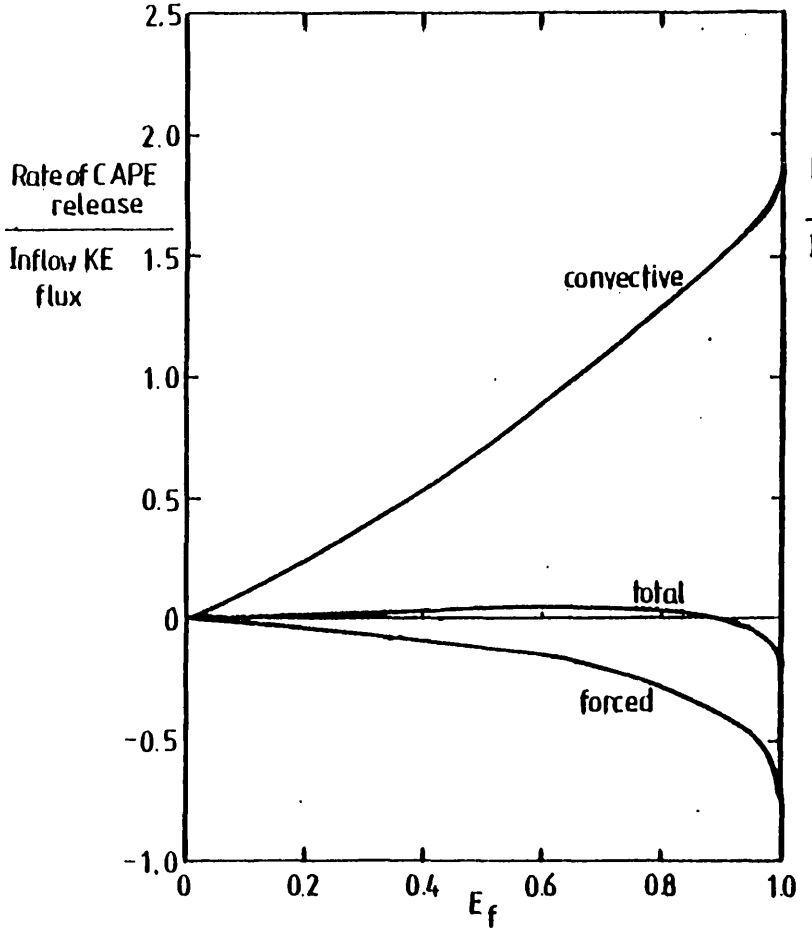


Figure 4.4.3.

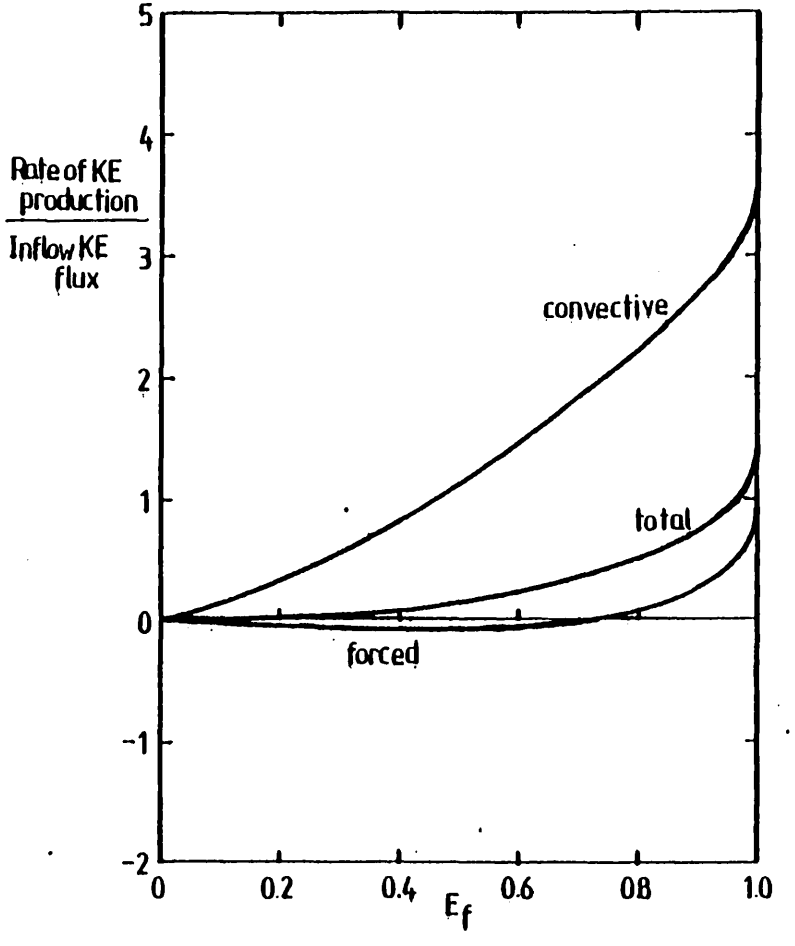


Figure 4.4.4.

$$\varepsilon_k = \frac{\int_{outflow} \frac{1}{2}\rho u_1^3 \, dz_1 - \int_{inflow} \frac{1}{2}\rho_0 u_0^3 \, dz_0}{\int_{outflow} \rho_1 u_1 \left[\int_{z_0}^{z_1} g\delta\phi_p dz \right] dz_1}$$

a problem becomes apparant. Since CAPE is released by the convective flow and generated by the forced flow the sum of the two terms may be zero for some E_f. From figure 4.4.3 we see this will occur for $E_f \sim 0.9$. Hence a maximum (infinite) efficiency occurs for this value of E_f. Thus this particular definition of efficiency cannot sensibly be applied to this complex circulation. (The same problem may arise for any circulation involving a forced flow.) This bulk treatment does show that work done by the pressure field in the forced flow is very important in generating kinetic energy. While kinetic energy is generated by the convective updraught, a large amount is in fact produced through work done by the pressure field in the forced circulation (for $E_f > 0.8$). The greatest increase in mean flow kinetic energy for both updraught and downdraught occurs for $E_f = 1$, which value will be used in all future calculations.

4.4.3 Alternative Closure Schemes.

Alternative closure schemes such as continuity of velocity on outflow at $\mathcal{J}_1 = r_1$ or a momentum constraint are not suitable, since there is no a priori requirement that this should be necessary. To prove this point, continuity of velocity at $\mathcal{J}_1 = r_1$ implies, from 4.8 and 4.15

$$c_u(1-E_u)^{1/2} = c_f(1-E_f)^{1/2}$$

In general this can only hold if $E_u = E_f = 1$. In this circumstance the

equation for pressure continuity cannot be satisfied unless the inflow shear is large and positive or large and negative. This can be seen from 4.18

$$\left(\frac{c_f}{c_u}\right)^2 - 1 = \left(\frac{r_1 - r_0}{F_u}\right)^2 + \left(\frac{c_f}{c_u}\right)^2 \left(\frac{1 - r_1}{F_f}\right) \geq 0$$

where all terms on the right hand side are greater than or equal to zero.

A momentum closure of the type employed for two-dimensional systems in TMM82 is not suitable, because the internal flow must be three-dimensional.

4.4.4 Variation of the Net Mass Flux and F with E .

Solutions corresponding to E_f=1.0 have a stagnation point in the outflow of the forced circulation at $\zeta_1 = r_1$. This is readily seen since from 4.12 and 4.15,

$$\frac{u_1(r_1)}{c_f} = \sqrt{1 - E_f}$$

Figure 4.4.5 shows that the shallowest updraught outflow occurs when E_f=1. The net mass flux out of the three layers $r_1 \leq \zeta \leq 1$, $r_0 \leq \zeta_1 \leq r_1$ and $0 \leq \zeta_1 \leq r_0$ as E_f varies were calculated in the following manner

$$M1 = \frac{\int_{r_1 H}^{H} \rho_1 u_1 dz_1 - \int_{r_1 H}^{H} \rho_0 u_0 dz_0}{\int_{r_1 H}^{H} \rho_0 u_0 dz_0}$$

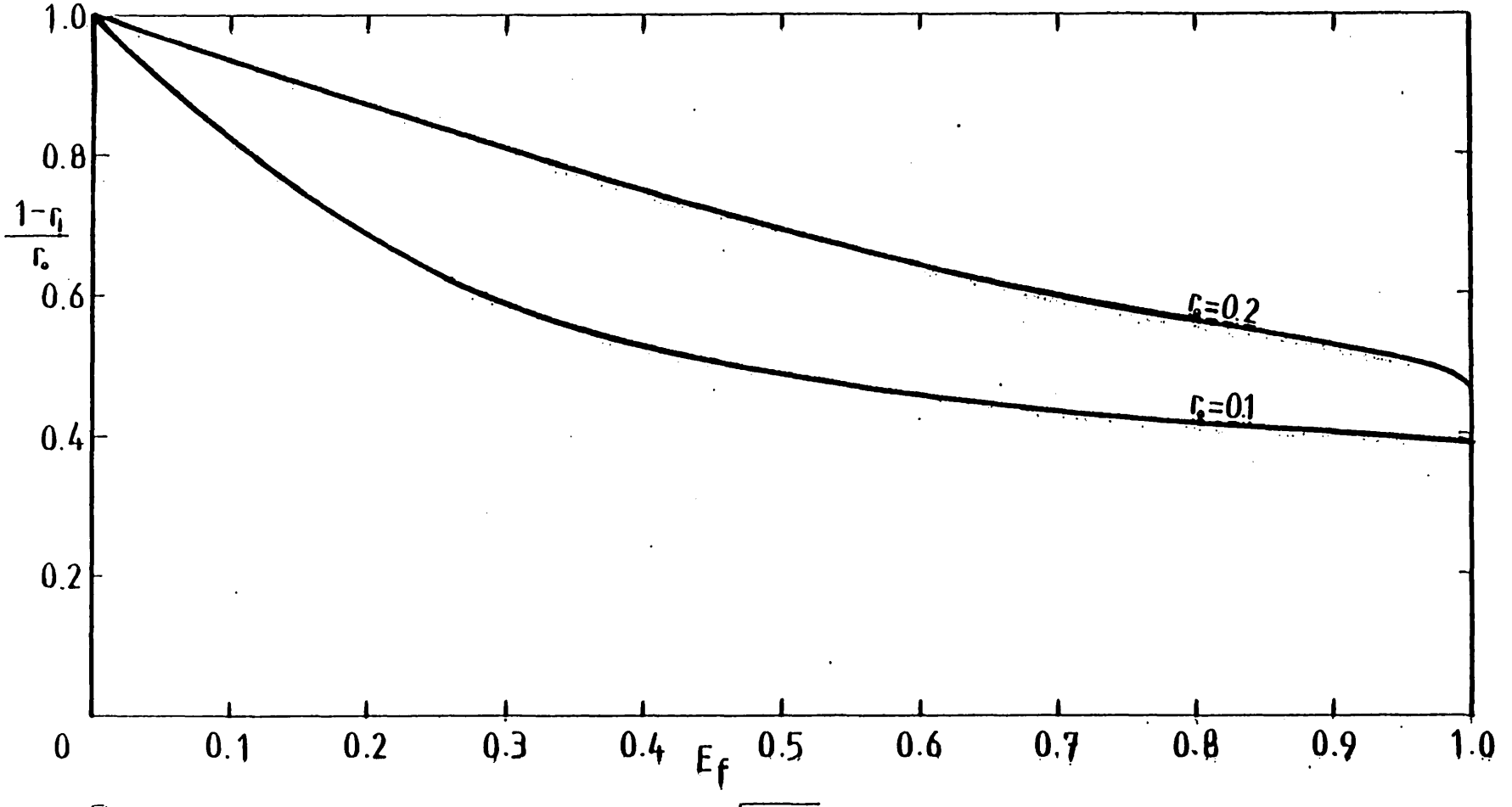
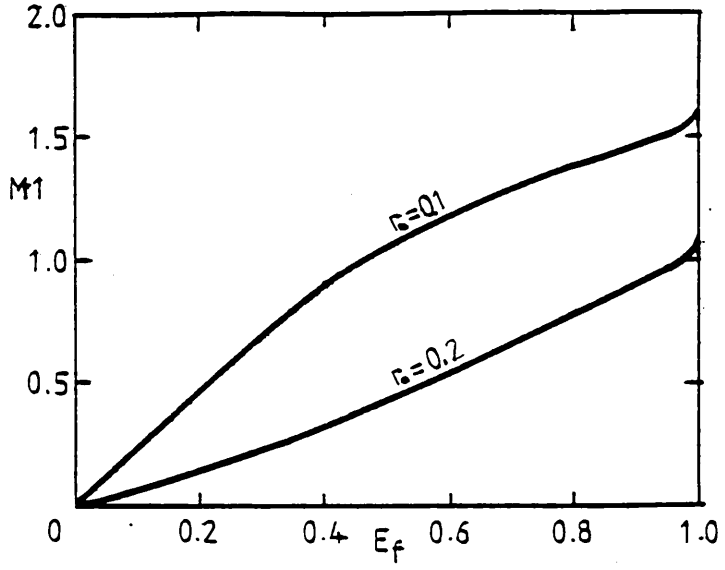
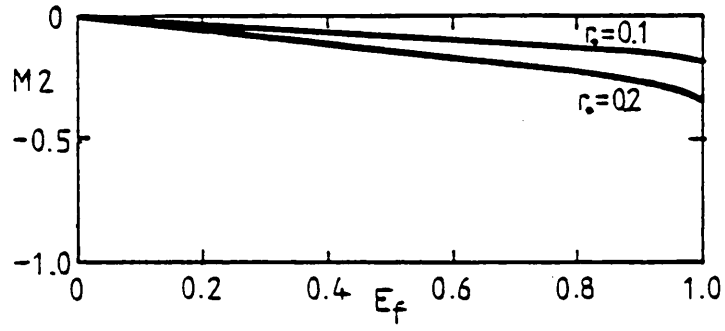


Figure 4.4.5. Variation of $(1-r_1)/r_0$ with E_f. $\Delta c=0$, $\sqrt{\frac{\gamma_u - B}{B - \gamma_f}} = 1$.





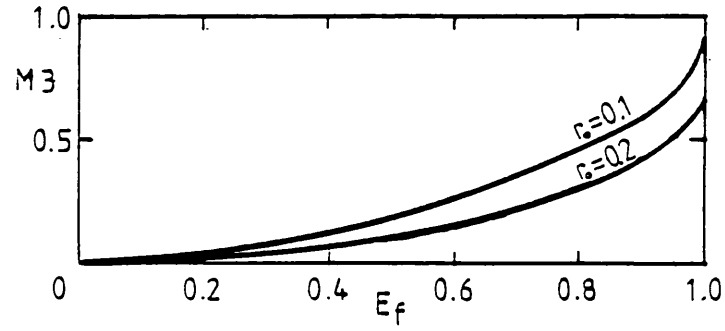


Figure 4.4.6. Variation of mass fluxes with E_f. $\Delta c=0$. $\sqrt{\frac{r_a-\beta}{\beta-r_f}}=1$.

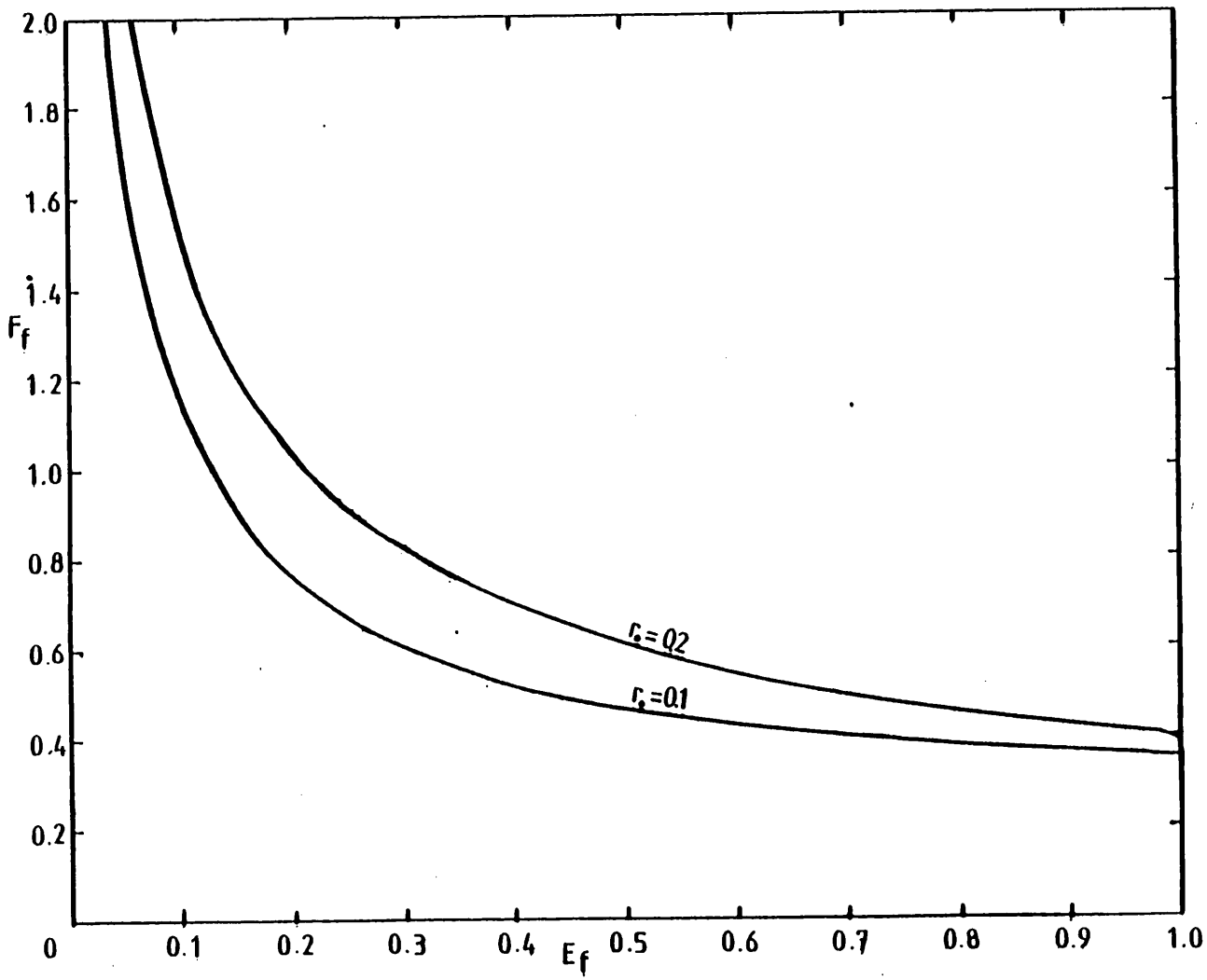


Figure 4.4.7. Variation of F_f with E_f. $\Delta c = 0$. $\sqrt{\frac{\gamma_w - B}{B - \gamma_f}} = 1$.

$$M2 = \frac{\int_{r_0 H}^{\eta H} \rho_1 u_1 dz_1 - \int_{r_0 H}^{H} \rho_0 u_0 dz_0}{\int_{r_0 H}^{\eta H} \rho_0 u_0 dz_0}$$

$$M3 = \frac{\int_{0}^{r_0 H} \rho_1 u_1 dz_1 - \int_{0}^{\delta H} \rho_0 u_0 dz_0}{\int_{0}^{r_0 H} \rho_0 u_0 dz_0}$$

for the three layers denoted by the limits of the integrals.

The net mass flux out of the upper and lower layers is a maximum for E_f=1.0, for which value the net mass flux into the middle layer is a maximum. These curves of M1, M2 and M3 are plotted in figure 4.4.6. They are consistent with the two-dimensional pattern of convergence and divergence found by Gamache and Houze (1982) for a squall line which passed through the GATE network on 12 September 1974.

The solution with greatest "mechanical efficiency" occurs for the lowest propagation speed (ie. lowest value of F_f which is equal to F_u for the unsheared case) as was found in MM. Variation of F_f with E_f is shown in figure 4.4.7 for r_o=0.1 and r_o=0.2. All cases examined will take the value E_f=1.0 corresponding to maximum "mechanical efficiency".

4.5 Dependence of the Propagation Speed of Updraught and Downdraught on Inflow Depth, Shear, and Differential Lapse Rate Ratio.

4.5.1 Inflow Depth.

In the absence of shear and with $\sqrt{\frac{\gamma_u - B}{B - \gamma_f}}$ =1.0, F_u and F_f are identical. F_u and F_f increase as the inflow depth to the updraught increases, figure 4.5.1. The relationship between F_u (or F_f) and r_o

is approximately linear for $0 \leq r_o \leq 0.3$ and may be simply expressed:-

$$F = 0.31900 + 0.31367 r_o \ (\pm 0.00001) \qquad (4.29)$$

There is the somewhat surprising result that as r_o tends to zero, F_u and F_f tend to 0.32. That F_f should be finite is not unexpected. In this limit the flow with $r_o = 0$ is that described by TMM80 where $F_f = 1/n\pi$ for $n = 1, 2, 3 \ldots$ The value of F_u for the convective updraught is related to F_f by 4.20 which in the unsheared case becomes:-

$$F_u = F_f \Big/ \sqrt{\frac{\gamma_u - B}{B - \gamma_f}} \ .$$

In the absence of shear then, the system should propagate more quickly when r_o is larger. The fractional increase in kinetic energy of the updraught is smaller - since compression of the outflow and consequent acceleration of the air is lower.

4.5.2 Shear.

The propagation speed for the forced circulation which is proportional to F_f does not vary significantly with the shear (Δc), figure 4.5.2, or the evaporation of water into the downdraught (γ_f), (figure 4.5.3).

$$F_f = F_u \left(\frac{\Delta c}{\sqrt{2UCAPE}} = 0, \sqrt{\frac{\gamma_u - B}{B - \gamma_f}} = 1, r_o, E_f \right) \qquad (4.30)$$

is a satisfactory approximation to make - better than 0.3% for $\sqrt{\frac{\gamma_u - B}{B - \gamma_f}} \gtrsim 0.4$.

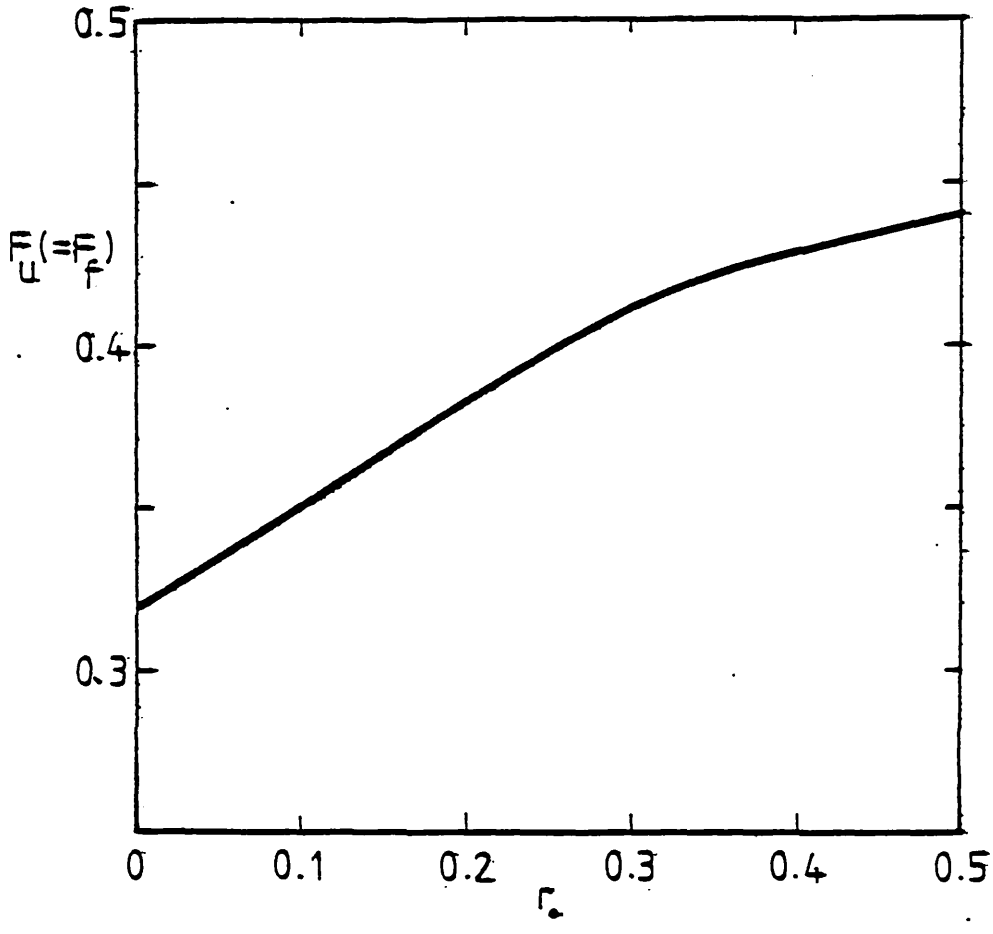


Figure 4.5.1. Variation of propagation speed ($= F_u\sqrt{2UCAPE}$) with inflow depth, r_e. $\Delta c=0$. $\sqrt{\frac{\gamma_u - B}{B - \gamma_f}} = 1$.

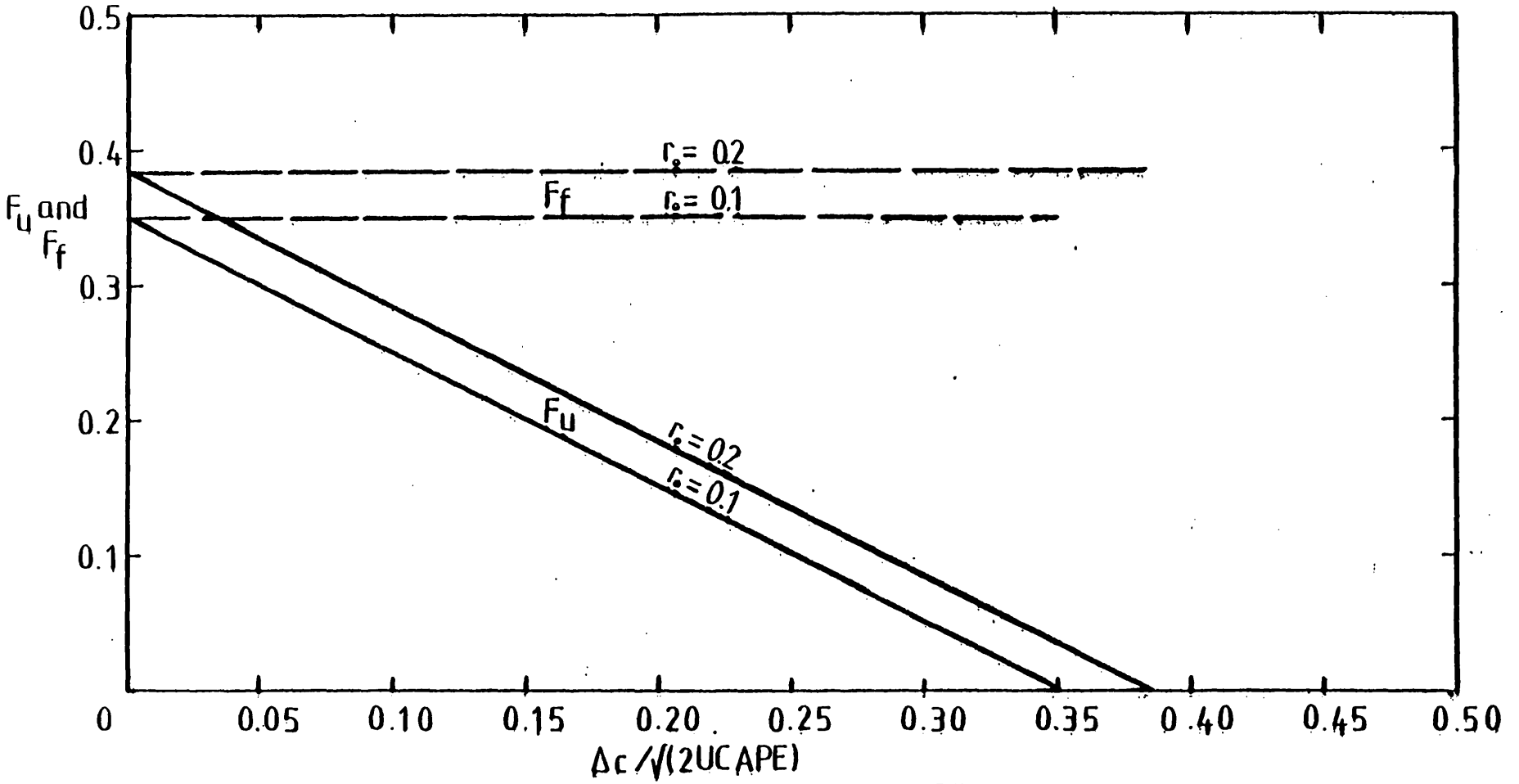


Figure 4.5.2. Variation of F_u and F_f with $\Delta c/\sqrt{2UCAPE}$. E_f=1. $\sqrt{\frac{\gamma_u - B}{B - \gamma_f}} = 1$.

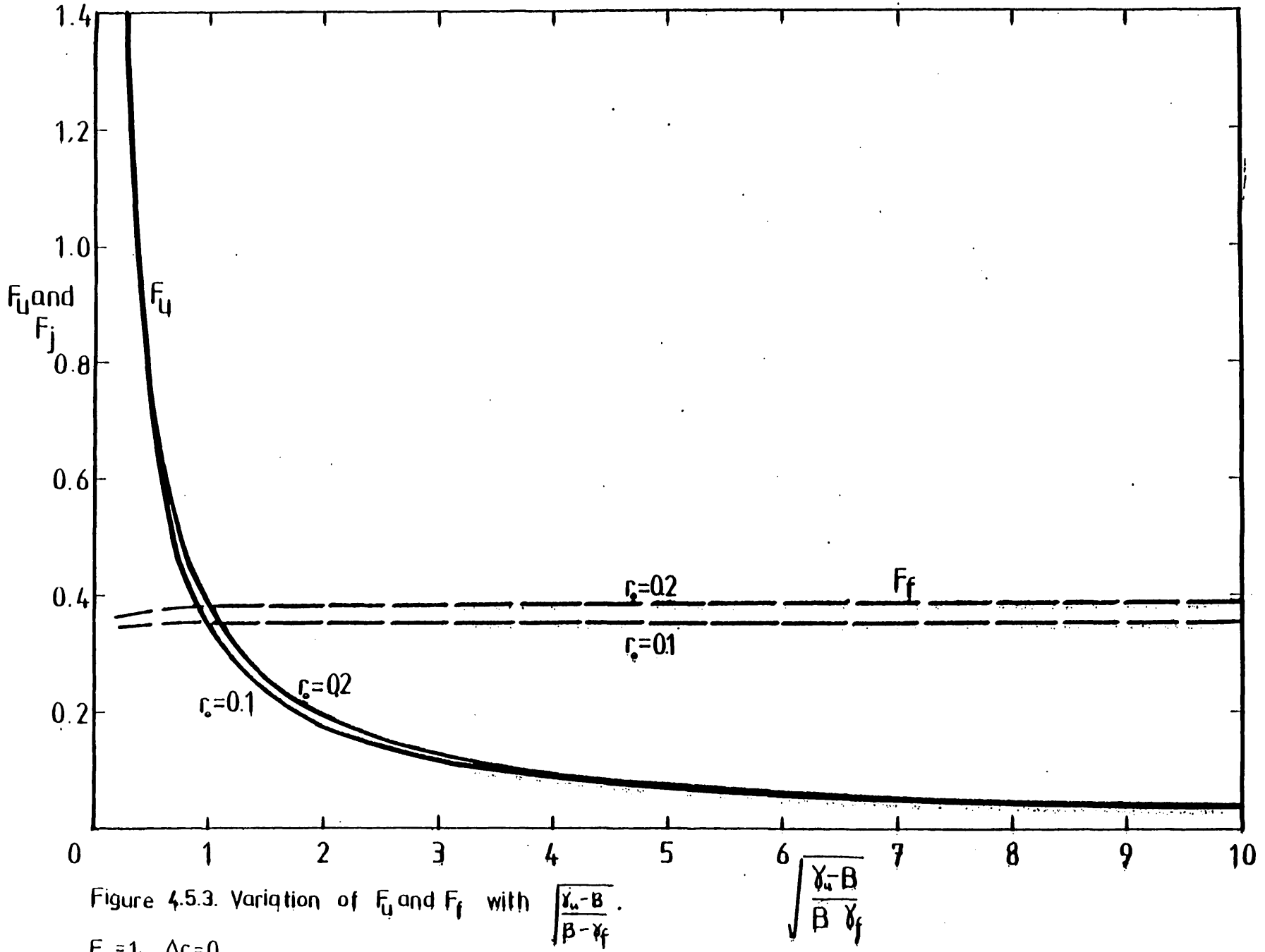
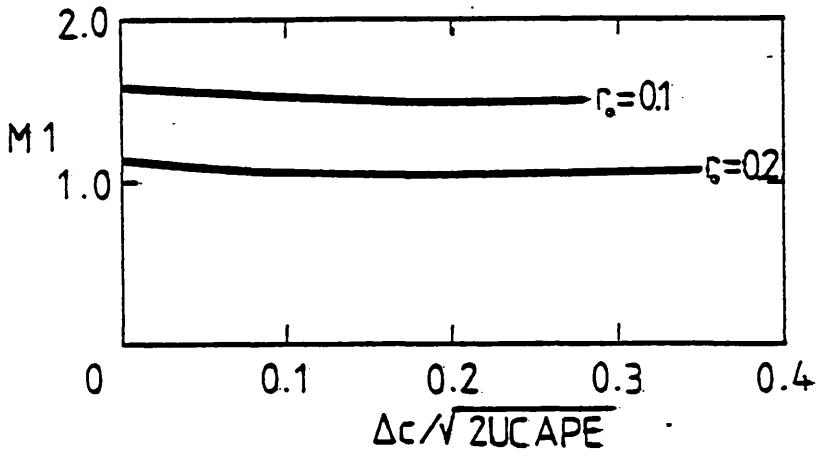
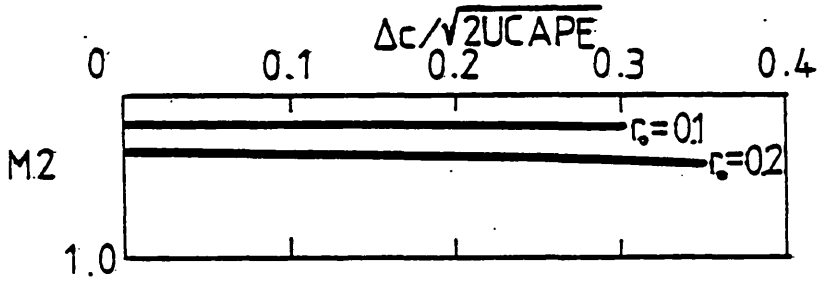


Figure 4.5.3. Variation of F_u and F_f with $\sqrt{\frac{\gamma_u - B}{\beta - \gamma_f}}$.

$E_f = 1$. $\Delta c = 0$.





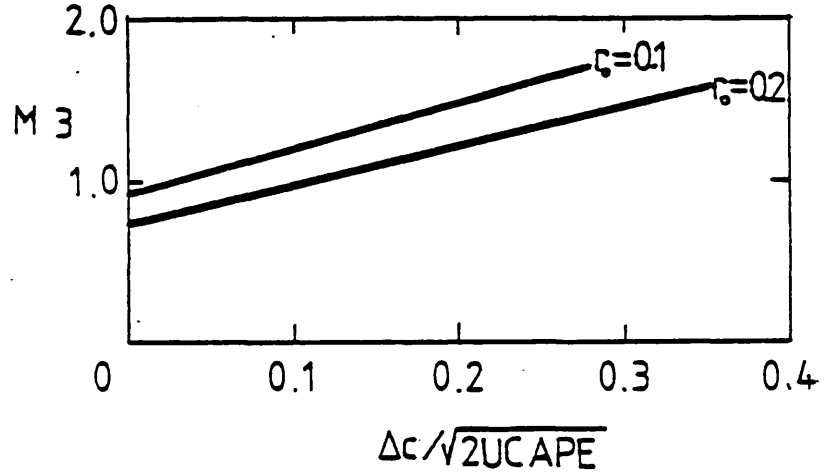


Figure 4.5.4. Variation of net mass fluxes with $\Delta c / \sqrt{2UCAPE}$. E_f=1. $\sqrt{\frac{\gamma_u - B}{B - \gamma_f}} = 1$.

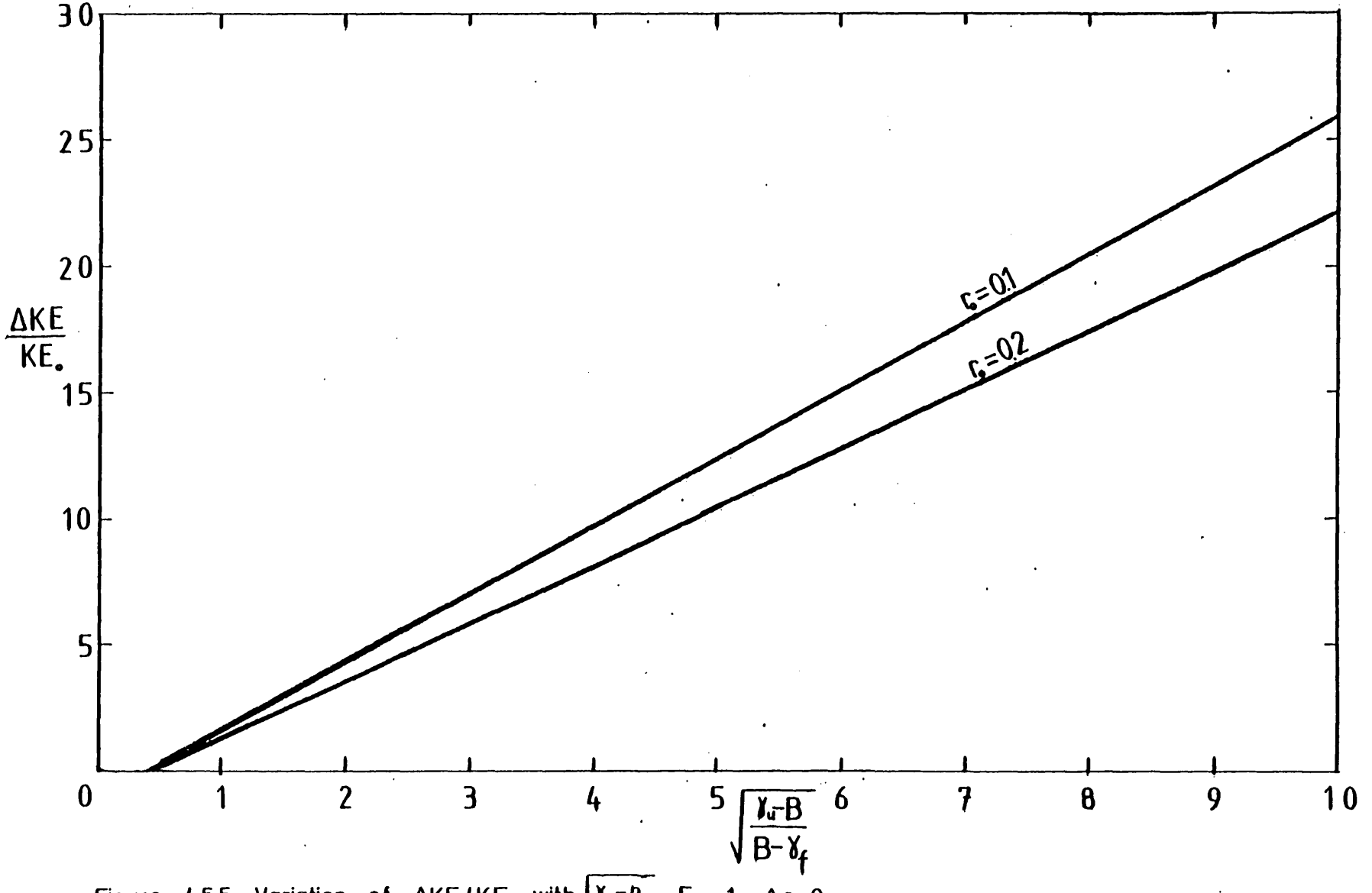


Figure 4.5.5. Variation of $\Delta KE/KE_.$ with $\sqrt{\frac{\gamma_u - \beta}{B - \gamma_f}}$. $E_f = 1$. $\Delta c = 0$.

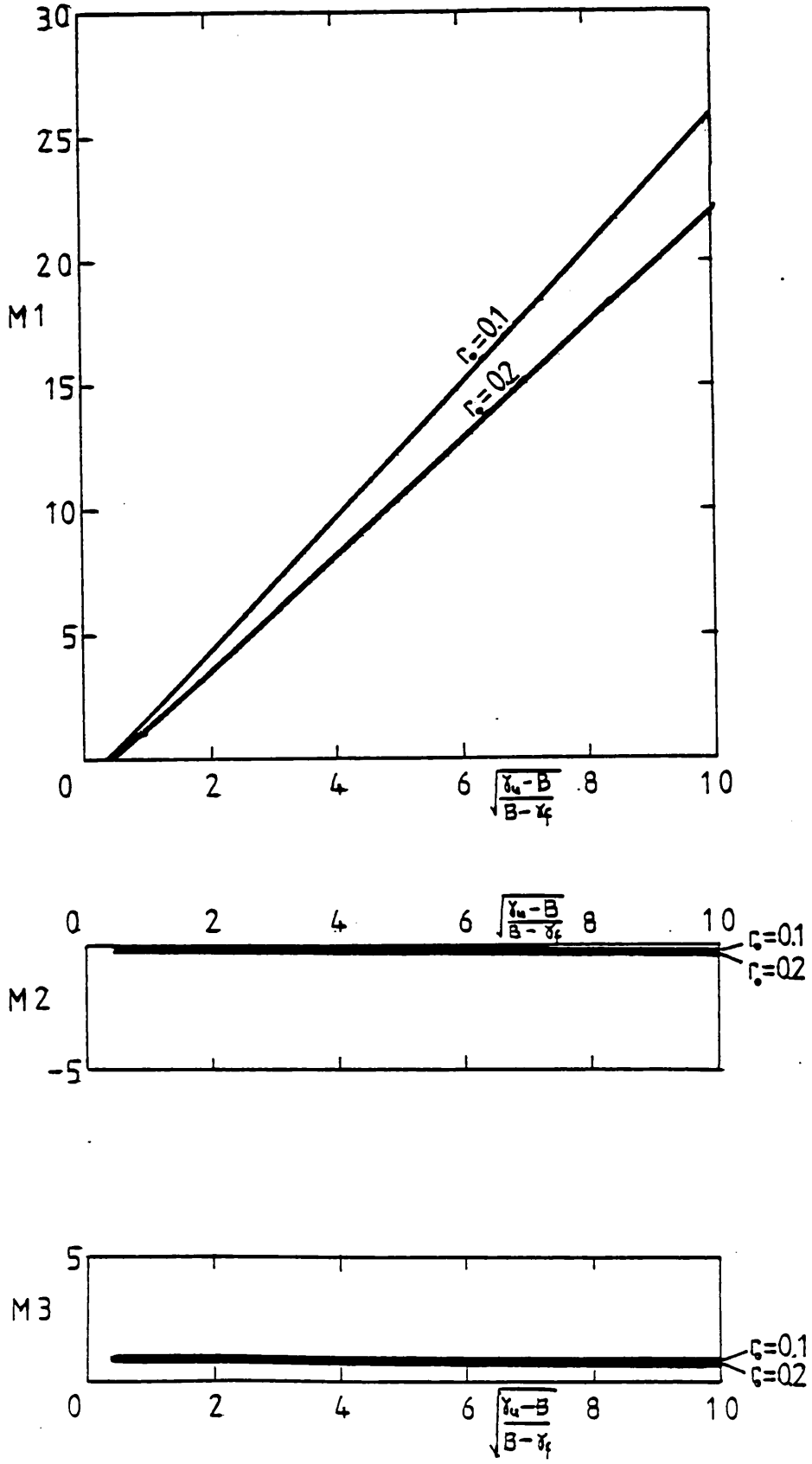


Figure 4.5.6. Variation of mass fluxes with $\sqrt{\frac{\gamma_u - B}{B - \gamma_f}}$.

$\Delta c = 0$. $E_f = 1$.

As the shear is increased F_u decreases approximately linearly, eventually becoming large enough to reduce F_u to zero. A larger shear is required to achieve this effect for a deeper convective inflow layer:-

$$\text{ie.} \qquad F_u = F_u\left(r_o,\ E_f = 1,\ \Delta c = 0,\ \sqrt{\frac{\gamma_u - B}{B - \gamma_f}} = 1\right) - \frac{\Delta c}{\sqrt{2UCAPE}} \,. \qquad (4.31)$$

F_f increases by less than 0.1% as F_u tends to zero for $r_o = 0.1$. For $r_o = 0.2$, F_f increases by only 1%. This change in F_f can be ignored when calculating storm speeds.

The limiting shear at which F_u tends to zero corresponds to r_1 tending to 1, ie. the convective outflow is being squeezed by the forced circulation which is expanding to occupy the entire depth of the atmosphere. Logically one might conclude that large shear inhibits a steadily propagating convective updraught.

The effect of introducing shear on net mass fluxes for the three layers is shown in figure 4.5.4. Upper and middle layers exhibit little change. However the lower level "divergence" is increased by nearly 50% when $\frac{\Delta c}{\sqrt{2UCAPE}} = 0.2$. This corresponds to an inflow velocity difference of $9 ms^{-1}$ for UCAPE $\sim 1000 Jkg^{-1}$. A minimum in the upper layer divergence occurs for $r_o = 0.2$ when $\frac{\Delta c}{\sqrt{2UCAPE}} = 0.2$. This may indicate why small shears are conducive to the maintenance of narrow, fast flowing updraught outflows - but large shears are not.

4.5.3 Differential Lapse Rate Ratio.

F_u is extremely sensitive to changes in $\sqrt{\frac{\gamma_u - B}{B - \gamma_f}}$, see figure 4.5.3. As moisture is evaporated into the forced downdraught, increasing γ_f,

F_u decreases. For small values of $\sqrt{\frac{\gamma_u - B}{B - \gamma_f}}$ a point is reached at which the mean kinetic energy of the convective updraught is lower on outflow than inflow, figure 4.5.5. These solutions have an expanding updraught which was not possible in the isentropic atmosphere case. These values of $\sqrt{\frac{\gamma_u - B}{B - \gamma_f}}$ however may be too low to correspond to a physically realisable situation - but it is very difficult making comparisons with "real" data - for reasons explained in chapter five.

Increasing the evaporation of water into the forced circulation leads to greatly increased kinetic energy production in the updraught air. Examining net horizontal mass fluxes out of the three layers previously detailed in section 4.4.6 the upper layer one-dimensional divergence increases linearly with $\sqrt{\frac{\gamma_u - B}{B - \gamma_f}}$ whilst middle and lower layer values are barely changed, figure 4.5.6.

4.6 Outflow Profiles of Relative Velocity, Pressure and Entropy Perturbation, and the Role of the Convective Downdraught.

Relative velocity, pressure and entropy perturbation outflow profiles are shown in figure 4.6.1 for a system consisting of convective updraught and forced downdraught. Note all variables are normalised in terms of the convective updraught properties:-

$$\frac{u_1}{\sqrt{g(\gamma_u - B)H^2}}, \quad \frac{\delta p_1 / \rho_s}{\frac{1}{2}g(\gamma_u - B)H^2}, \quad \frac{\delta \phi_1}{(\gamma_u - B)H}.$$

Velocity profiles show upper and lower level acceleration and mid-level deceleration. The pressure change is positive within the updraught air - decreasing to become negative at the surface. The magnitude of the surface pressure change decreases as evaporation into the downdraught increases. From 4.1C the pressure change within the

$\sqrt{(\gamma_u - B)/(B - \gamma_f)}$	0.6	1.0	1.4
r_1	0.84	0.91	0.93
F	0.628	0.383	0.274
F_F	0.377	0.383	0.384

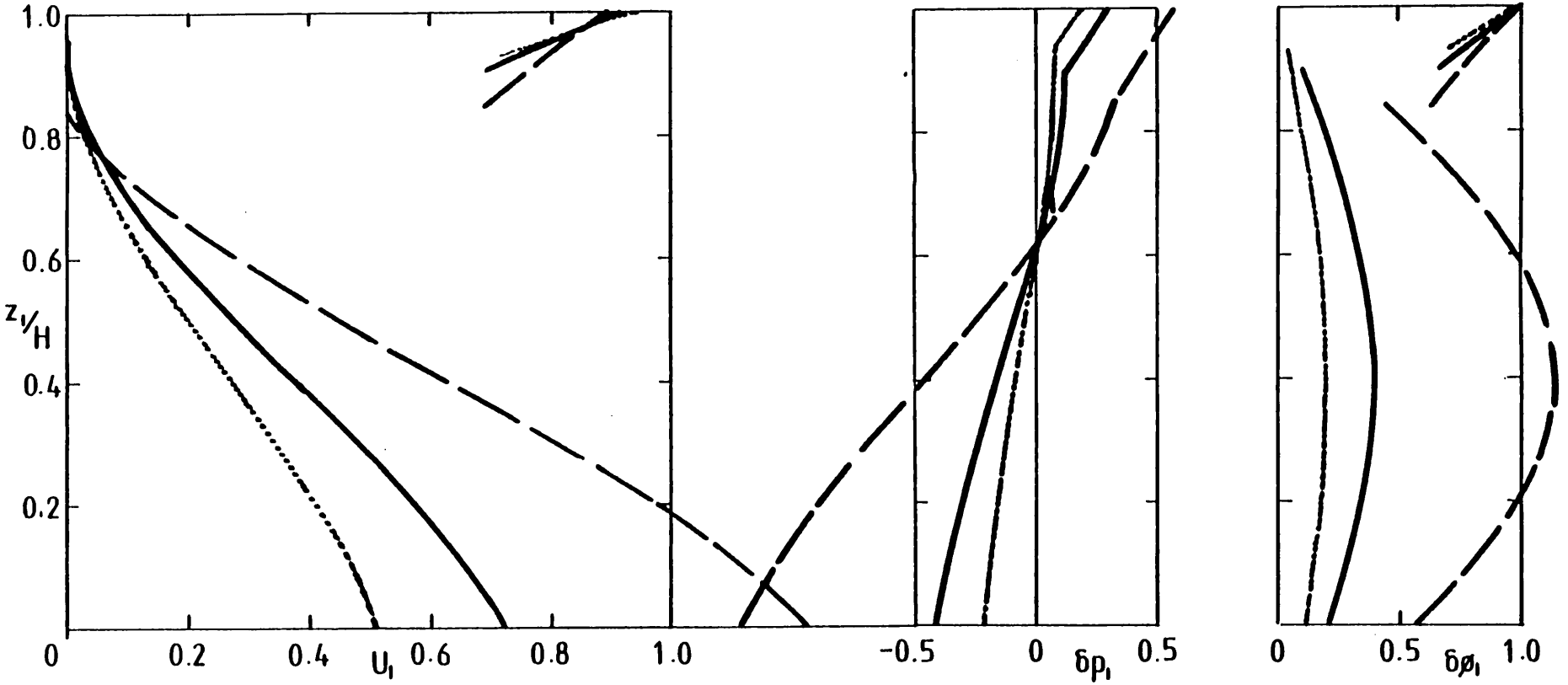


Figure 4.6.1. Outflow profiles of relative velocity, pressure and entropy perturbation. $r = 0.2$. $E_f = 1$. $\Delta c = 0$. $\sqrt{\frac{\gamma_u - B}{B - \gamma_f}} = 1$ (solid line), $\sqrt{\frac{\gamma_u - B}{B - \gamma_f}} = 0.6$ (broken lines), $\sqrt{\frac{\gamma_u - B}{B - \gamma_f}} = 1.4$ (dotted lines).

convective updraught is dominated by the term $\left(\frac{r-r_0}{r_u}\right)^2$. This is the contribution from heating resulting from the net displacement of the streamlines and is always larger than the dynamic pressure change.

Warming occurs at all levels in the outflow with maxima in the middle level of the forced downdraught corresponding to air which has descended furthest, and at the top of the convective outflow profile to air which has ascended the greatest distance.

In chapter two we saw that the pressure perturbation arising from a convective downdraught is always positive. A model incorporating a convective downdraught would then be required to have a net positive pressure deviation on outflow for the two limiting streamlines of the forced flow.

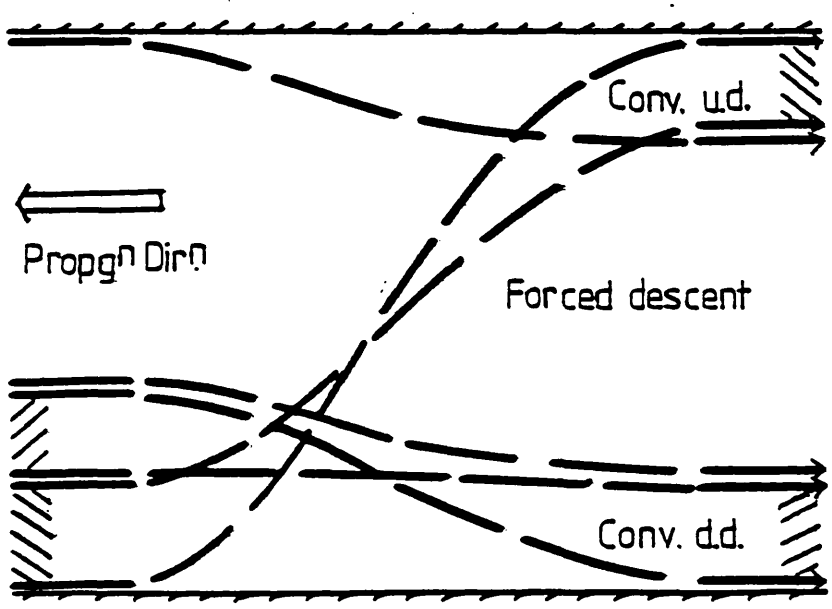


Figure 4.6.2

The outflow velocity profile for the forced flow must then be of the n=2 type in TMM8C (discussed in chapter three) with deceleration

along the top and bottom streamlines and middle level acceleration to satisfy mass continuity. Such an acceleration at middle levels has never been observed. In fact the flow is always decelerated at middle levels. For this reason the convective downdraught cannot play a role in the dynamical forcing in this model. A flow such as that shown in figure 4.6.2 does not produce velocity profile modifications consistent with observations.

4.7 Summary.

Maximising the increase of mean flow kinetic energy when the flow includes a forced response from the environment produces physically reasonable and self consistent results as will be illustrated in chapter five. As in MM this corresponds to the existence of a stagnation point in the outflow. The predicted pattern for convergence and divergence over the entire system resembles that described by Gamache and Houze (1982) for the net effect of squall line and mesoscale response. The most "efficient" conversion occurs at the lowest propagation speeds (smallest F_u, F_f); the convective updraught always becoming narrower after ascending.

F_f, and the propagation speed of the forced downdraught, are remarkably insensitive to shear and to the quantity of evaporation into the forced circulation. By contrast F_u and the propagation speed of the convective updraught are very sensitive to Δc and $\sqrt{\frac{\gamma_u - B}{B - \gamma_f}}$. A higher lifting condensation level produces a faster propagating system but a lower efficiency of energy conversion. Introducing a difference in inflow speed between forced and convective circulations has a similar effect as does increasing the amount of evaporation into the forced circulation. Large shear tends to suppress the propagation of

the convective updraught.

The model has a rather thinner updraught outflow than the anvil thicknesses commonly observed in the tropics, (see section 1.1). This may in large part be due to the absence of mixing in the model - which also makes comparison of predicted heating with observations rather difficult.

This model suggests that the convective updraught and the forced downdraught are the dynamically important components of the flow. The convective downdraught is a by-product of the convective updraught produced precipitation. Its generation and dynamics are probably governed by the dynamics of the convective updraught. This model suggests that it does not play a deterministic role in the mesoscale circulation, although it is thermodynamically important in that it stabilises the boundary layer in a very significant fashion.

CHAPTER FIVE

CONCLUDING REMARKS

5.1 Summary.

Widespread unsaturated forced descent has been identified as an important contributor to the energy, moisture and momentum budgets of tropical clusters and consequently to the larger scale circulations. Two different types of convective forcing and mesoscale response have been investigated.

Various convective circulations were examined in chapter two in order to produce a more realistic (shallower) downdraught with a less extremely sheared outflow profile of horizontal velocity. A shallow downdraught with a mid-level undeviated streamline of the type described in MM can only be developed if either the downdraught environmental lapse rate is an order of magnitude smaller than that of the updraught so that a masive amount of evaporation and cooling occurs in the downdraught or there is a vertical gradient of outflow perturbation pressure across the air between updraught and downdraught outflows. Neither of these conditions seems realistic particularly in the latter case since the type of pressure perturbation produced would require a middle-level acceleration of the outflow between updraught and downdraught which is not detected observationally.

When the updraught and downdraught retain an undeviated streamline but may become thicker or thinner on outflow a more promising outcome is produced. Updraught and downdraught can travel with the same speed

although the vertical profile of pressure perturbation with a larger upper level increase would tend to produce a greater upper level acceleration of the flow favouring the forced updraught.

Possible forced response modes with jet-type velocity profiles subject to a mean negative pressure change are examined in chapter three. n=2 type modes, with upper level ascent and lower level descent, are not possible for large jet amplitudes. However, the n=1 descent modes with lower level deceleration are possible. This would suggest, that if convective forcing and mesoscale response are of a "wake" type, the observed lower level descent and acceleration of the flow can be explained by this dynamical mechanism. However, upper level ascent would not be produced over such a large area, suggesting that observational results implying anvil ascent must be treated with some caution.

The second type of model does not make such a distinction between squall and wake regions. The generation of mean flow kinetic energy is maximised as in the "type A" model. It would seem that this "type B" model is to be preferred as a description of the dynamically important components of the squall and response. The one-dimensional pattern of divergence calculated for this model shows upper and lower level divergence and middle level convergence which is found observationally by Gamache and Houze (1982) for the combined squall and anvil system. The n=1 response mode of the "type A" circulation cannot produce such a pattern with upper level divergence since there is descent at all levels. (There is no n=2 mode solution for an easterly jet type inflow profile.)

The second type of model reproduces the surface pressure fall

seen in the "mesoscale" response region by Johnson and Nicholls (1983). The convective scale downdraught is discounted as a dynamically important feature regarding the forced response; it is a by-product of the convective updraught, although important locally in enhancing the convergence of boundary layer air to feed the convective updraught and generating new cells. It is not important as an organising mechanism to the mesoscale squall cluster circulation.

5.2 Calculation of Model Parameters from Data.

This section is concerned with assigning values to the important flow-governing parameters produced by the analyses of the forced circulations in chapters three and four. In chapter three the propagation speed of the simple circulation described in TMMEC and in section 3.2.1 when moving into still air is $F_f\sqrt{(g(B-\gamma_f)H^2)}$, where $F_f=1/n\pi$. B is the lapse rate of $\log\theta$ for the environment (or pre-disturbance atmosphere) and γ_f is the lapse rate of $\log\theta$ for a parcel suffering a forced displacement. H is the depth of the circulation (eg. surface to the level of neutral buoyancy (LNB)) and is not related to a particular parcel displacement. This is in marked contrast to the UCAPE of a convective updraught where the quantity $g(\gamma_u-B)H^2/2$ corresponds to the available potential energy of a parcel raised through a height H assuming γ_u-B represents a vertically averaged lapse rate difference of $\log\theta$. A second point of contrast lies in the value of γ for convective and forced flows. To a very good approximation a parcel ascending in a cumulonimbus circulation follows a saturated constant θ_w path. UCAPE may be taken to be the positive area on a tephigram. By contrast in the forced circulation, although the descending parcel conserves θ_w it is substantially

unsaturated and the process is in fact unspecified. Kamburova and Ludlam (1966) and Betts and Silva Dias (1979) have attempted to develop simple methods for specifying such forced descent. However, only post-disturbance diagnostic analysis seems possible.

The first objective of this section will be the calculation of a vertically averaged value of $B-\gamma_f$ for forced descent leading to an estimate of the propagation speed for the forced flow. The second part of this section concerns the calculation of $\sqrt{\frac{\gamma_u-B}{B-\gamma_f}}$ for the circulation described in chapter four. A consistent set of parameters for this circulation will be developed which suggest a value for the ratio of the differential lapse rates for convective and forced circulations ($\sqrt{\frac{\gamma_u-B}{B-\gamma_f}}$).

5.2.1 Calculation of $(B-\gamma_f)$ from Data.

The following criteria were developed in order to make a first estimate.

(i) Take successive vertical profiles of θ_e on occasions when squall clusters are passing an observing station and try to locate sections of the profiles where recognisable features have descended (eg. jet or vertically increasing or decreasing θ_e sections of profiles). Although this is an entirely subjective technique for observational data a more appropriate objective criterion cannot be devised at present. Profiles with a temporal separation of about an hour or less are required, eg. VIMHEX data; the sparser 3-6 hourly soundings from the GATE are not suitable for determining the origin of the descending air.

(ii) From successive profiles θ should increase at a given height (taken to be at constant pressure levels, which appears to introduce a

maximum error in θ of 0.05K which can be ignored for all practical purposes since VIMHEX θ data is only calculated to 0.1K).

(iii) A minimum final layer depth of 25mb is required (corresponding to the interpolation interval for the VIMHEX 1972 Rawinsonde Data, Betts and Miller (1975)). Descent from above 400mb, corresponding to anvil outflow, and to below 850mb, corrresponding to convective downdraught descent, should be avoided.

The squall line numbers are given in table 5.2.1 together with propagation speeds and directions. The soundings were those identified by Miller and Betts (1977) to be associated with squall lines. Although the VIMHEX data does have a better temporal resolution than the GATE data the Venezuelan squall lines are on the whole much smaller than the GATE squall lines (mean length was 100km for Venezuelan squall lines cf. 350km for Eastern Atlantic squall lines, Fernandez, 1982), and consequently showed more three-dimensional flow characteristics with considerable transverse flow modification, Fernandez (1980). Consequently identification of layers in which descent occurs is very difficult. Successive profiles may show that the sonde is rising through air with completely different characteristics. The profiles of θ_e were taken from Betts and Miller (1975) which are given at 25mb intervals, between the surface and 150mb.

The profiles used are shown in figures 5.2.1-5.2.7 and are for squall line numbers 14, 27, 35, 53, 56, 60 and 64. Perhaps the most convincing example of descent is shown in figure 5.2.2 corresponding to squall line 27 in which a shallow, low θ_e minimum, feature descends. Where more than one possible level of origin of air occurs the two extreme levels are chosen and the following calculation

VIMHEX Squall-line Data.

Date	Storm no.	Storm vel. (deg/ms^{-1})	"Before" sounding	Local time.	"After" sounding	Local time.
27 June	14	104/11.7	81	1806	82 83	2001 2126
3 July	27	079/15.0	100	1956	101 102	2113 2222
9 July	35	085/10.7	120	1523	121 122	1648 1807
28 July	53	110/9.9	192	1843	193 194	2002 2125
31 July	56	092/14.7	203	1503	204	1845
7 August	60	095/13.8	226	1759	227 228 229	1907 2028 2150
11 August	64	079/15.5	241	1446	242 243	1604 1713
Mean speed		13.0ms^{-1}				
Standard deviation		2.1ms^{-1}				

Table 5.2.1

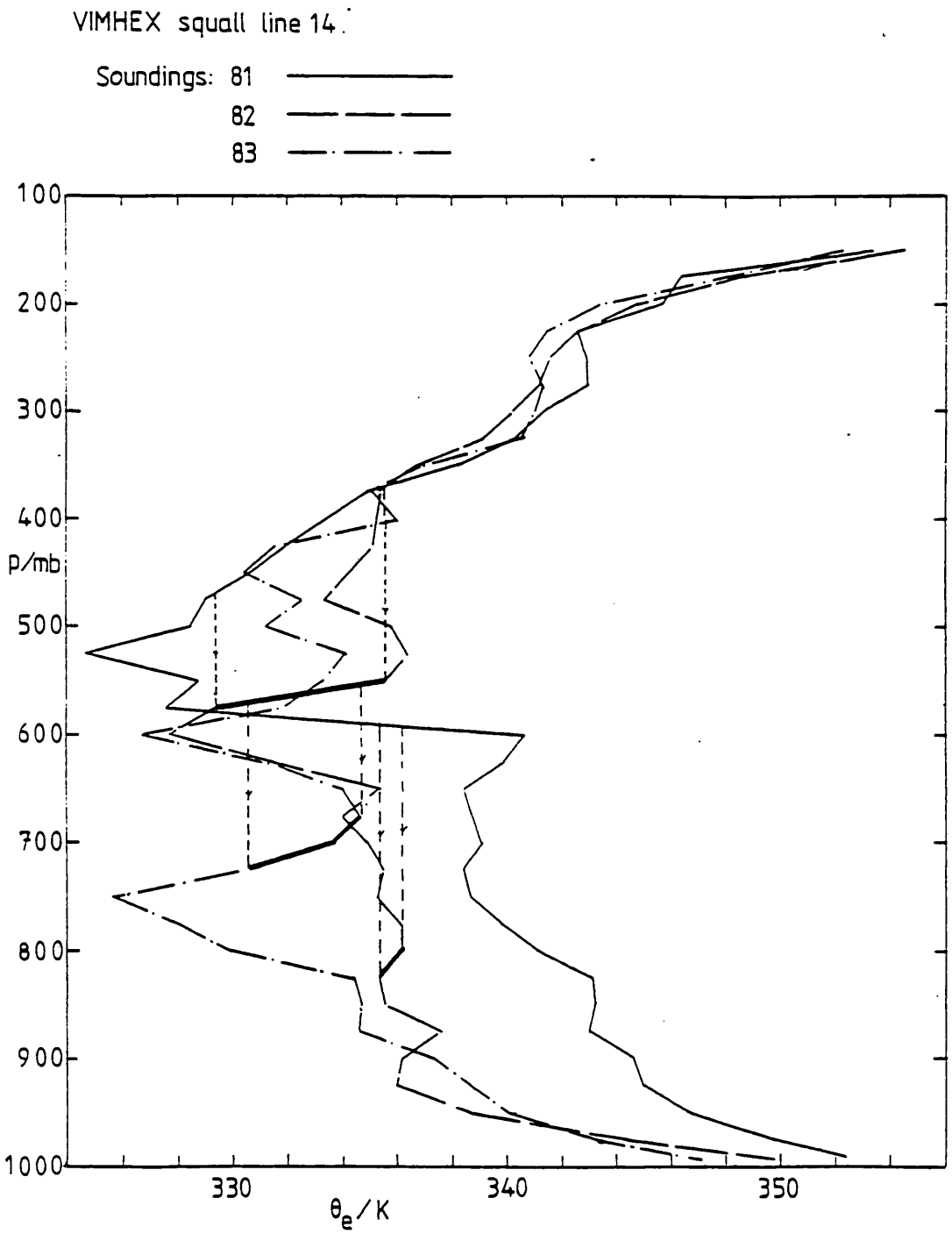


Figure 5.2.1. θ_e profiles at approximately hourly intervals (see table 5.2.1). Broad lines indicate final level of descending air. Distance of descent is shown by vertical broken lines.

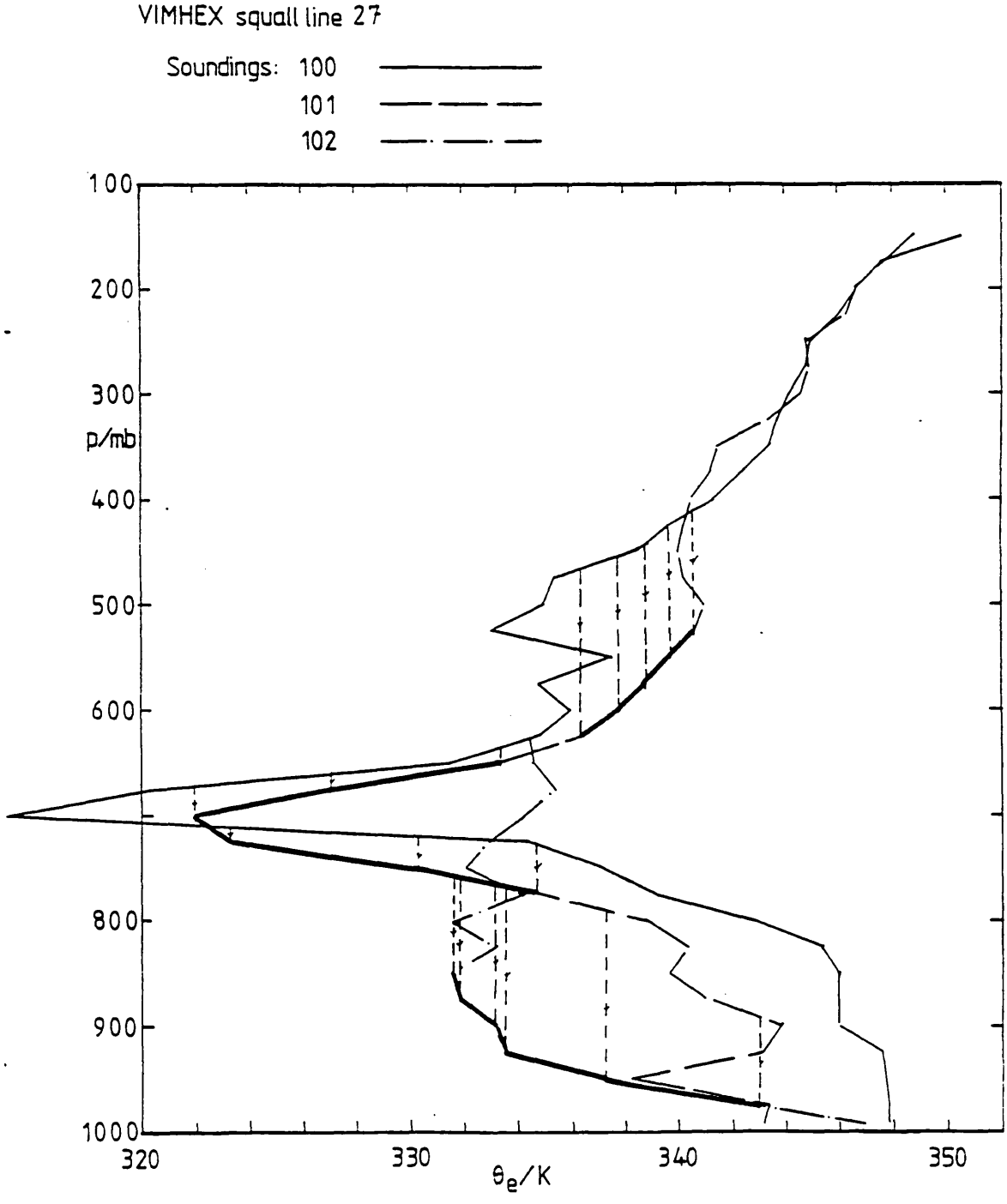


Figure 5.2.2. See figure 5.2.1.

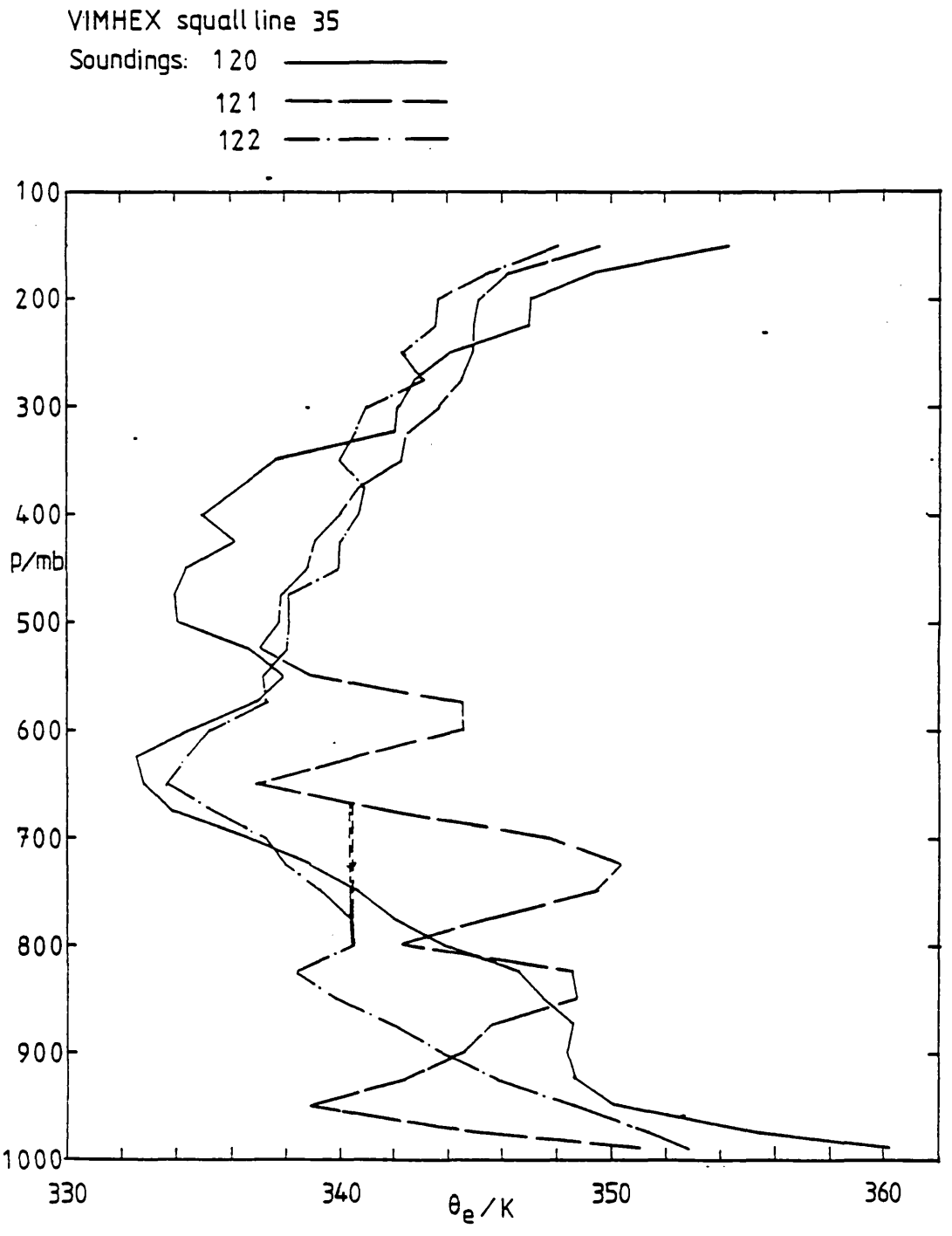


Figure 5.2.3. See figure 5.2.1.

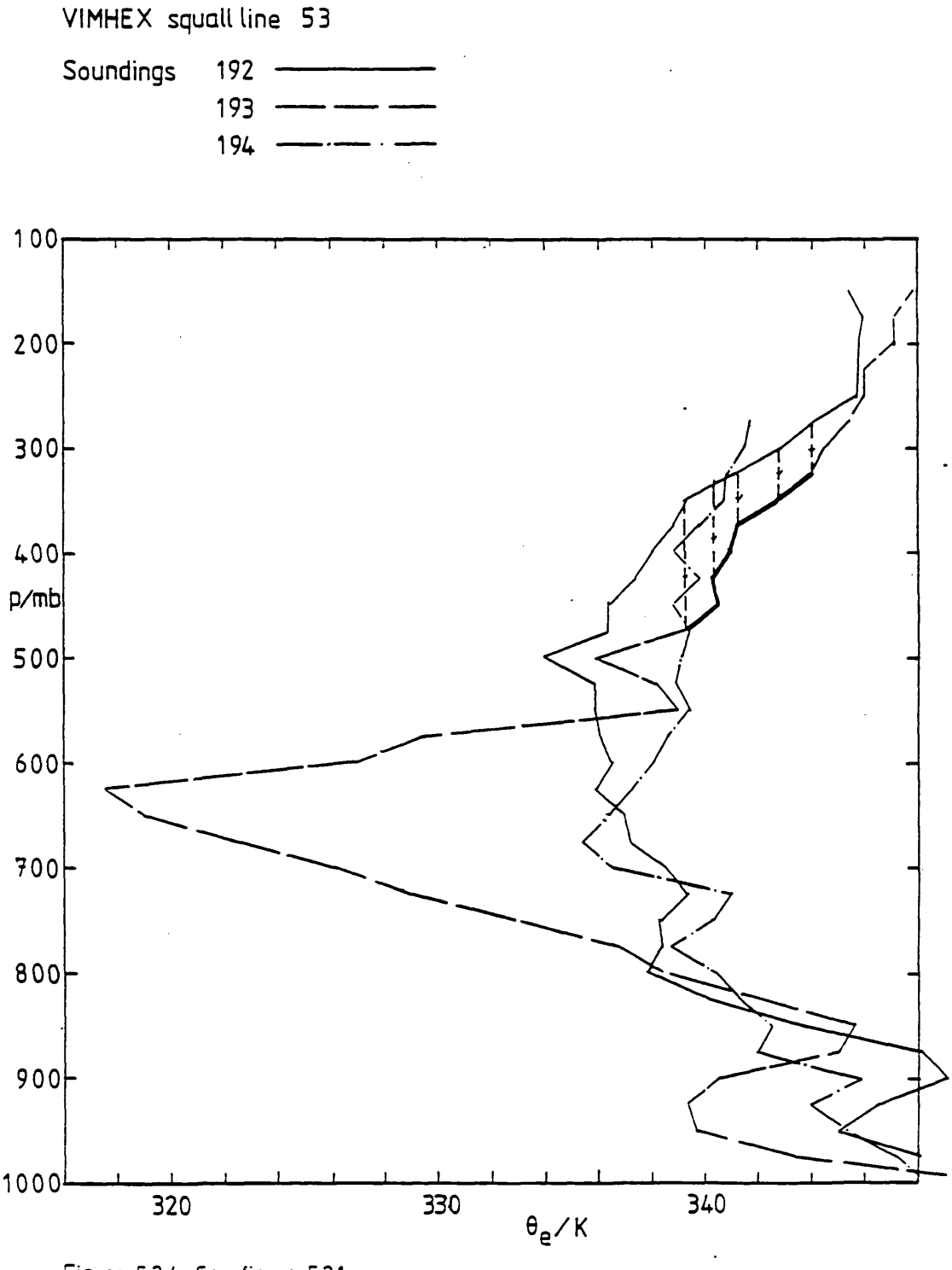


Figure 5.2.4. See figure 5.2.1.

VIMHEX squall line 56

Soundings: 203 ——————

204 — — — —

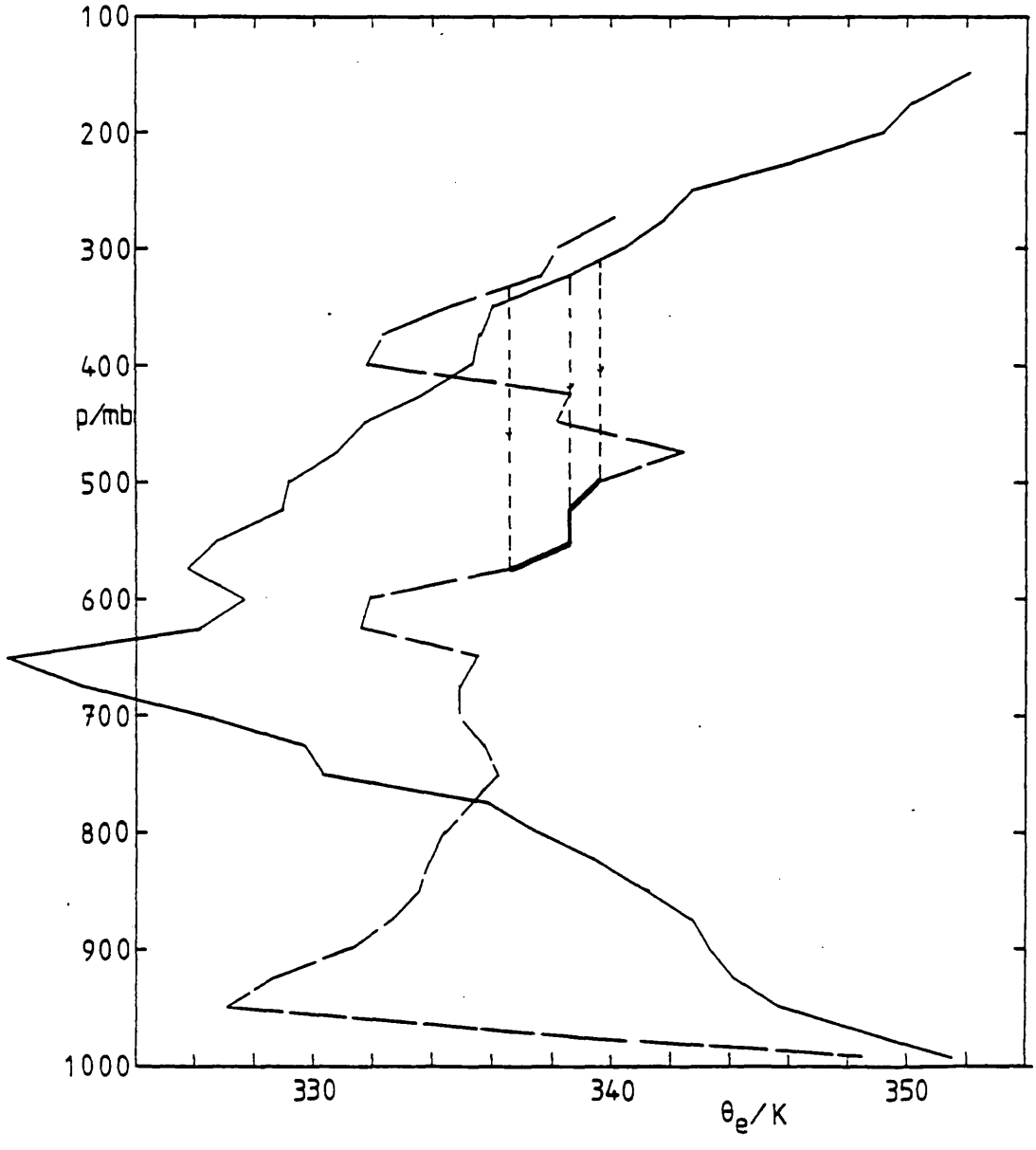


Figure 5.2.5. See figure 5.2.1.

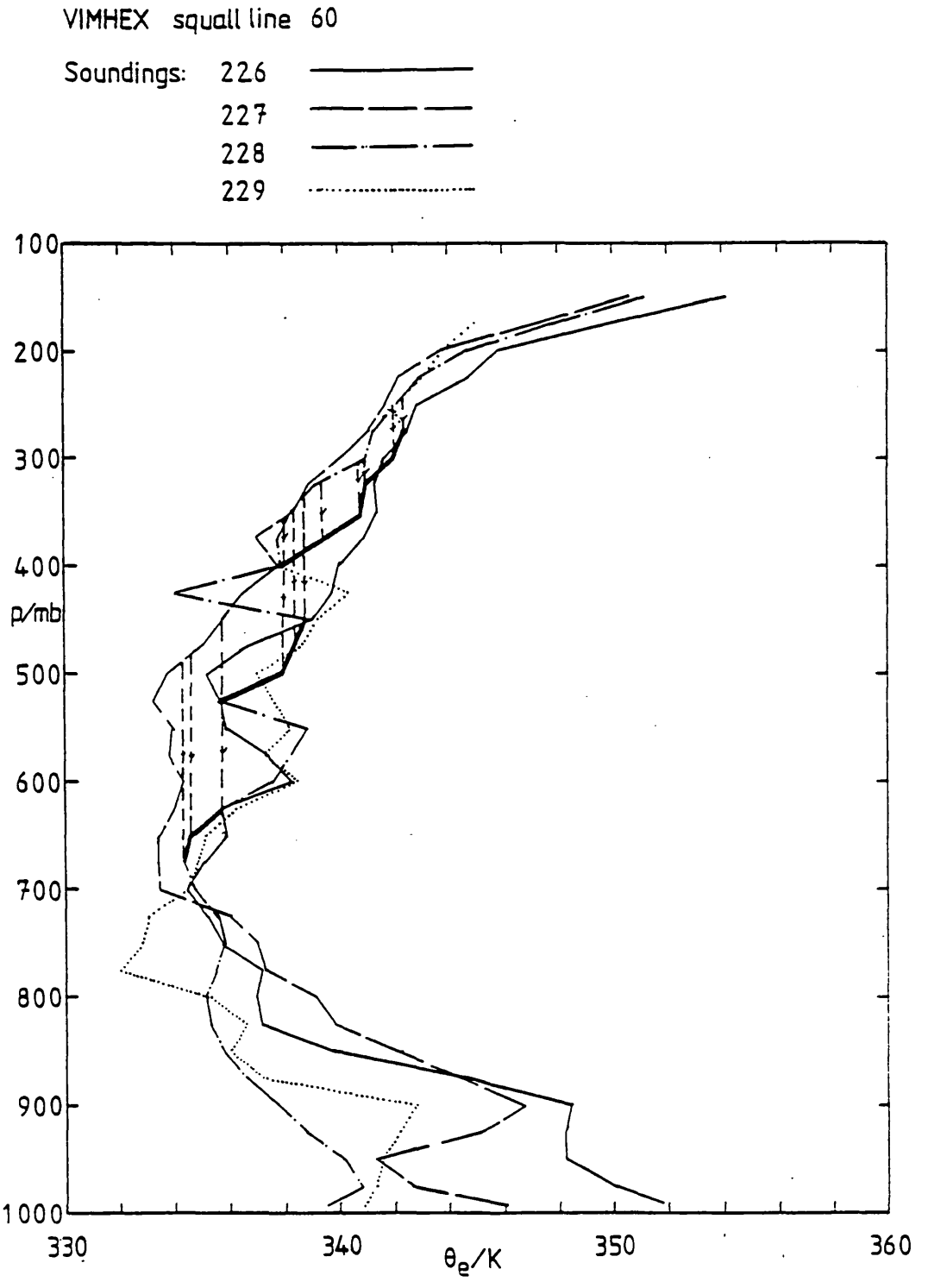


Figure 5.2.6. See figure 5.2.1.

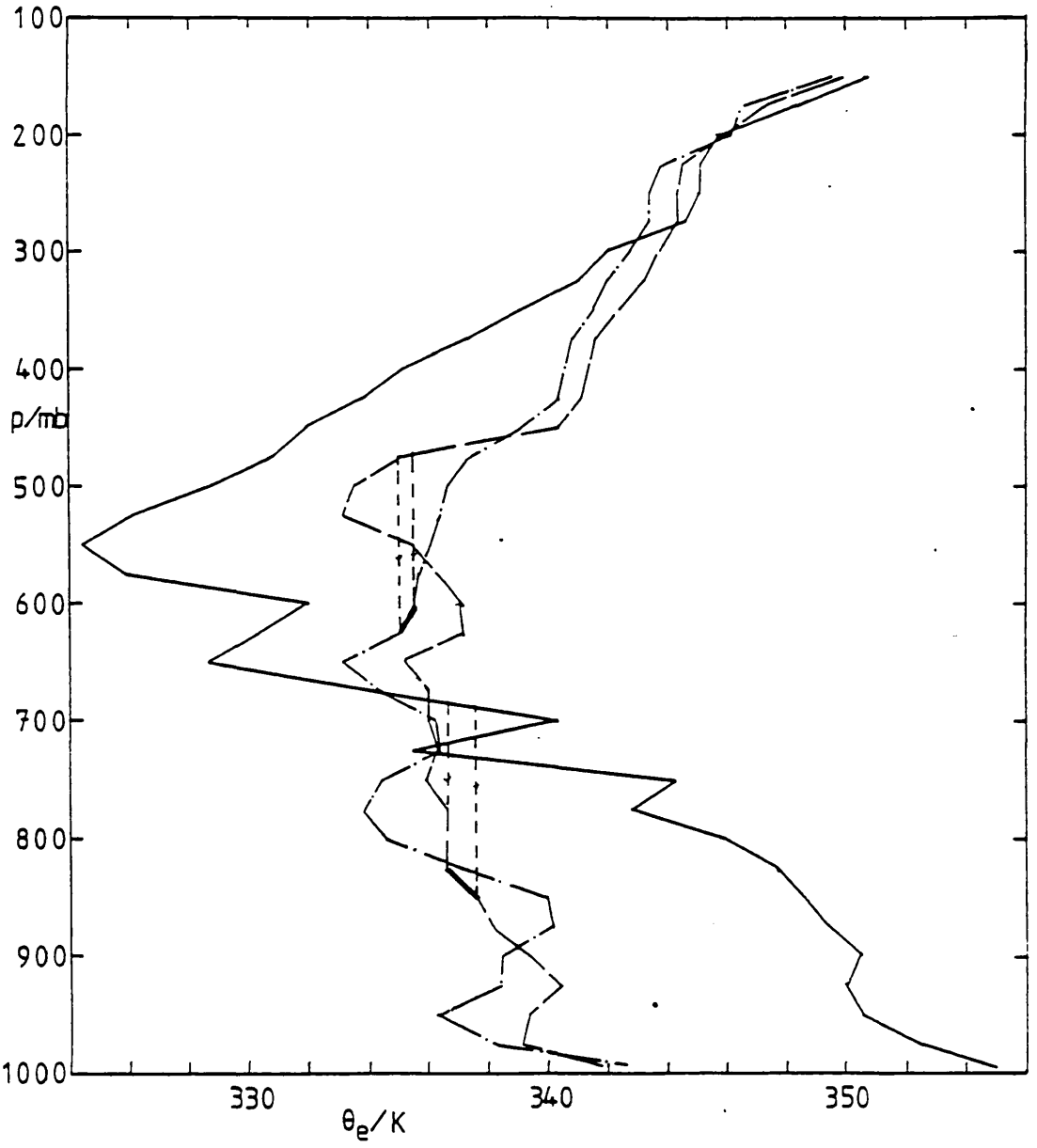


Figure 5.2.7. See figure 5.2.1.

performed for both values and the mean taken.

$B=\partial \ln\theta/\partial z$ and $\gamma=D\ln\theta/Dz$ can be written in discrete form in the following way.

$$B = \frac{1}{\bar{\theta}_{env}} \frac{\Delta\theta_{env}}{\Delta z} , \qquad \gamma = \frac{1}{\bar{\theta}_{parcel}} \frac{\Delta\theta_{parcel}}{\Delta z} .$$

When descent occurs from p_1 to p_2, the parcel potential temperature changes from θ_1 to θ_2(parcel) and the environmental temperature (undisturbed) is θ_1 at p_1 and θ_2(environment) at p_2. Hence $\Delta\theta$(environment)= θ_2(environment)-θ_1 and $\Delta\theta$(parcel)= θ_2(parcel)-θ_1, (see figure 5.2.8).

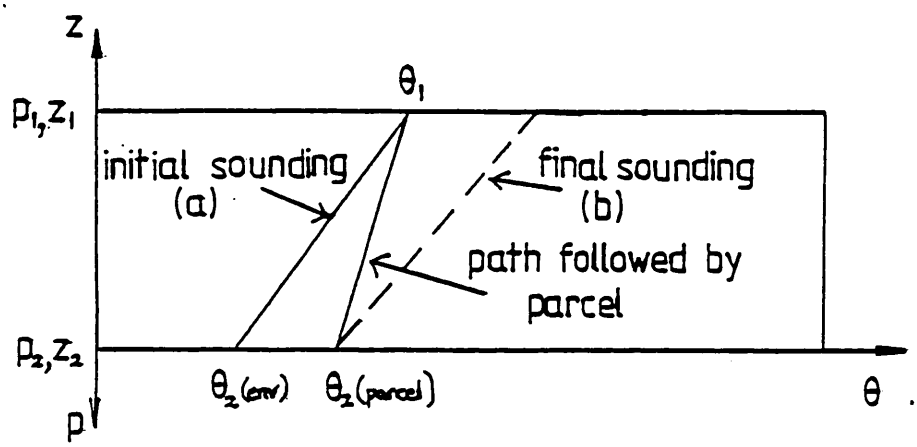


Figure 5.2.8

$\bar{\theta}$(environment) and $\bar{\theta}$(parcel) are both approximated to the mean value of θ for the layer which descends ($\bar{\theta}$). Hence

$$B-\gamma_f \simeq \frac{1}{\bar{\theta}} \frac{\left(\Delta\theta_{env} - \Delta\theta_{parcel}\right)}{z(p_2)-z(p_1)}$$

$$= \frac{1}{\bar{\theta}} \frac{\left(\theta_{2\,env} - \theta_{2\,parcel}\right)}{z(p_2)-z(p_1)}$$

ie. the numerator is the difference in potential temperature at the

final pressure level (p_2) and can be simply calculated by subtracting initial from final θ values at the same level (figure 5.2.8).

Δz is more complicated to calculate. The final θ for the parcel descent is chosen to be a level in the tabulated data set so that θ_2(parcel) is simply the tabulated value at p_2 for sounding b. By interpolating with respect to log(p) the value of θ at level p_1 of sounding a can be found (ie. θ_1).

From p_1, θ_1, p_2 and θ_2(parcel), T_1 and T_2 may be calculated using $T = \theta(p/p_0)^{R/c_p}$. Taking $\bar{T}=(T_1+T_2)/2$ the perfect gas formula can then be used to calculate

$$\Delta z = z_2 - z_1 = -\frac{R\bar{T}}{g} \ln(p_2/p_1) .$$

This procedure produces a set of $\Delta\theta$(= θ_2(parcel)- θ_2(environment)) and Δz at each final tabulated pressure level at which forced descent is assumed to occur at 25mb intervals. The mean values $\bar{\Delta\theta}$ and $\bar{\Delta z}$ are then calculated for each 25mb interval. The mean value for each vertical layer which descends can then be calculated:-

$$B-\gamma_f = -\frac{1}{\bar{\theta}} \frac{1}{n} \sum_{i=1}^{n} \frac{\bar{\Delta\theta_i}}{\bar{\Delta z_i}}$$

The stages in the calculation for each profile are shown in table 5.2.2. Estimates of errors in $B-\gamma_f$ were made as follows. Tabulated values of θ are given to 0.1K. The maximum error in $\Delta\theta$ is then 0.2K. This produces a maximum error in $1/n \sum_i \frac{\bar{\Delta\theta_i}}{\bar{\Delta z_i}}$ of $1/\sqrt{n}$ $\frac{\text{Error}(\Delta\theta)}{\Delta\theta}$ which varies between about 5 and 40% (see individual calculations). By contrast the error in Δz arises by at most an error of 10mb in p_1 which for a mean descent of 1km corresponds to a 10% error in any one

Calculation details.

Calculation	SL	Sounding pair	Layer (mb)	θ_i(env) /K	p_2 /mb	θ_i(parcel) /K	p_1 /mb	θ_1/K	Δz/m	$\Delta\theta$/K $=\theta_{ipar}-\theta_{env}$	$\bar{\Delta\theta}$ /K	$\bar{\Delta z}$ /m
(a)	14	81/82	575-550	315.9	575	318.2	470	327.9	-1576	+2.3	+2.7	-2324
				317.3	550	320.4	367	334.9	-3072	+3.1		
(b)	14	81/82	825-775	305.3	825	305.9	591	317.5	-2752	+0.6	+0.65	-2604.5
				306.0	800	306.7	593	317.7	-2457	+0.7	+0.55	-2323.5
				307.0	775	307.4	593	317.7	-2190	+0.4		
(c)	14	82/83	725-675	308.8	725	309.9	570	318.6	-1946	+1.1	+0.65	-1886
				309.9	700	310.1	558	319.7	-1826	+0.2	+0.2	-1701.5
				311.1	675	311.3	554	320.0	-1577	+0.2		
(d)	27	100/101	775-525	306.5	775	307.1	728	308.3	-1038	+0.6	+0.95	-687.5
				307.2	750	308.5	720	309.1	-337	+1.3	+1.85	-255
				308.5	725	310.9	710	310.3	-173	+2.4	+1.85	-254
				311.5	700	312.8	672	313.8	-335	+1.3	+0.7	-257
				313.7	675	313.8	660	314.4	-184	+0.1	+0.05	-187
				314.8	650	314.8	635	315.5	-190	0	+0.15	-535/ -1246.5
				315.9	625	316.2	560/ 467	320.0/ 327.9	-880/ -2303	+0.3	+0.55	-1508.5/ -2220
				317.1	600	317.9	455	329.0	-2137	+0.8	+0.8	-2095.5
				318.8	575	319.6	442	330.2	-2054	+0.8	+0.7	-2036.5
				320.9	550	321.5	424	331.9	-2019	+0.6	+0.65	-1963
				323.0	525	323.7	410	333.2	-1907	+0.7		

Table 5.2.2(i)

Calculation details.

Calculation	SL	Sounding pair	Layer (mb)	θ_2(env) /K	p_2 /mb	θ_2(parcel) /K	p_1 /mb	θ_1/K	Δz/m	$\Delta\theta$/K $=\theta_{par}-\theta_{env}$	$\bar{\Delta\theta}$ /K	$\bar{\Delta z}$ /m
(e)	27	101/102	975-850	297.2	975	298.1	791	306.4	-1793	+0.9	+1.25	-1797
				298.0	950	299.6	768	307.5	-1801	+1.6	+0.85	-1700
				301.0	925	301.1	766	307.6	-1599	+0.1	+0.4	-1520
				301.5	900	302.2	759	308.0	-1441	+0.7	+0.95	-1319
				301.9	875	303.1	759	308.0	-1197	+1.2	+1.35	-1084.5
				302.8	850	304.3	757	308.1	-972	+1.5		
(f)	35	121/122	800-775	306.5	800	307.9	669	313.9	-1485	+1.4	+1.1	-1358
				308.8	775	309.6	668	313.5	-1231	+0.8		
(g)	53	192/193	475-450	325.8	475	326.9	350	336.9	-2292	+1.1	+0.75	-2244.5
				329.1	450	329.5	335	337.1	-2197	+0.4		
(h)	53	192/193	375-325	333.5	375	335.4	325	339.8	-1044	+1.9	+1.5	-1018.5
				336.9	350	338.0	305	341.9	-993	+1.1	+0.85	-1035
				339.8	325	340.4	280	355.9	-1077	+0.6		
(i)	56	203/204	575-525	319.2	575	319.6	345	335.7	-3889	+0.4	+0.4	-3955
				322.0	550	322.4	323	338.0	-4021	+0.4	+0.4	-3839
				324.3	525	324.7	323	338.0	-3657	+0.4		
(j)	60	227/228	675-625	312.2	675	313.5	600/ 489	317.3/ 324.3	-953/ -2563	+1.3	+1.2	-1652/ -2457
				313.8	650	314.9	483	324.6	-2351	+1.1	+0.6	-2462.5
				315.5	625	315.6	450	326.2	-2574	+0.1		
(k)	60	227/228	525-450	322.4	525	324.1	450	326.2	-1191	+1.7	+1.95	-1883.5
				323.6	500	325.8	355	334.1	-2576	+2.2	+2.1	-2431
				325.1	475	327.1	350	335.7	-2286	+2.0	+2.55	-2289
				326.2	450	329.3	330	336.8	-2292	+3.1		

Table 5.2.2(ii)

Calculation details.

Calculation	SL	Sounding pair	Layer /mb	$\theta_{(env)}$ /K	p_2 /mb	$\theta_{(parcel)}$ /K	p_1 /mb	θ_1/K	Δz/m	$\Delta\theta$ /K $=\theta_{par}-\theta_{env}$	$\overline{\Delta\theta}$/K	$\overline{\Delta z}$ /m
(l)	60	228/229	400-275	332.1	400	332.6	400	332.1	0	+0.5	+0.8	-564
				333.5	375	334.6	321	337.2	-1128	+1.1	+1.3	-1092.5
				335.6	350	337.1	302	339.4	-1057	+1.5	+1.45	-812.5
				336.8	325	338.2	300	339.6	-568	+1.4	+0.95	-845.5
				339.6	300	340.1	255	341.9	-1123	+0.5	+0.4	-1009.5
				340.9	275	341.2	241	342.4	-896	+0.3		
(m)	64	241/242	850-775	306.3	850	306.8	689/ 732	311.7/ 311.2	-1759/ -1262	+0.5	+0.6	-1655.5/ -1151
				306.8	825	307.5	685/ 729	311.8/ 311.3	-1552/ -1040	+0.7	+0.8	-1421/ -909.5
				307.3	800	308.2	685/ 729	311.8/ 311.3	-1290/ -779	+0.9	+0.9	-1156/ -645
				307.7	775	308.6	685/ 729	311.8/ 311.3	-1022/ -511	+0.9		
(n)	64	242/243	625-600	315.1	625	315.9	479	326.6	-2103	+0.8	+0.55	-1979.5
				317.0	600	317.3	474	326.9	-1856	+0.3		

Table 5.2.2(iii)

measurement and an error in $B-\gamma_f$ of less than 5%. It is probable that mixing may lead to a mis-identification of the layer of origin which may prove far more important a source of error. This can only be minimised by chosing soundings of high temporal resolution.

The values of $P-\gamma_f$ calculated for each descending layer together with error estimates are given in table 5.2.3. UCAPE was also calculated for all seven squall lines so that an estimate of (γ_u-B) could be made. The mean value of θ_w was calculated for the layer 975-900mb. Parcel ascent was then assumed with this value of θ_w. UCAPE was taken to be the positive area on the tephigram. (This may be an overestimate since cloud top height should be used for the upper limit of integration and not the level of neutral buoyancy.)

H was calculated to be the distance from the surface to the LNB. From H and UCAPE, (γ_u-B) and $\sqrt{\frac{\gamma_u-B}{B-\gamma_f}}$ were calculated. The results are summarised in table 5.2.3.

The variation in $(B-\gamma_f)$ and consequently in FCAPE are averaged for each squall line. In addition the mean difference in inflow speed to convective and forced circulations for a model flow of the type developed in chapter four must be calculated. The mean inflow speed parallel to the squall line propagation direction into the convective flow is taken to be the mean inflow speed between the surface and a pressure level corresponding to twice the depth of the LCL defined by the UCAPE calculation. The forced flow inflow is defined to be above this layer and below the LNB.

For both types of model ("A" in chapter three and "B" in chapter four) the predicted propagation speed from theory is for a disturbance moving into still air. This speed must be added onto the air speed

Parameters Calculated from VIMHEX Squall Line Data.

Calc.^{n}	SL	$(B-\gamma_f)$ /$10^{-6}m^{-1}$	$\varepsilon(B-\gamma_f)$ /$10^{-6}m^{-1}$	H/km	UCAPE /Jkg^{-1}	(γ_u-B) /$10^{-6}m^{-1}$	FCAPE /Jkg^{-1}	$\sqrt{\frac{\gamma_u-B}{B-\gamma_f}}$	Δc /$\sqrt{2UCAPE}$	Mean wind speed/ms^{-1} (parallel to ppgn. dirn.)	$\langle\Delta z\rangle$ /60mins^{-1} m
(a)	14	3.6	0.3	12	700	1.0	2600	0.53	-0.11	10.45	1203
(b)	14	0.8	0.2				600	1.12			
(c)	14	0.4	0.1				300	1.58			
(d)	27	6.5	0.5	12	600	1.0	4300	0.39	+0.14	5.47	975
(e)	27	2.3	0.2				1500	0.66			
(f)	35	2.6	0.5	13	1000	1.2	2200	0.68	+0.11	2.96	1031
(g)	53	1.0	0.3	11	700	1.2	600	1.10	-0.00	6.21	1089
(h)	53	3.4	0.4				2100	0.59			
(i)	56	0.3	0.1	11	600	1.0	200	1.83	+0.23	7.20	1053
(j)	60	1.3	0.2	13	900	1.1	1100	0.92	+0.16	4.68	1256
(k)	60	3.0	0.2				2500	0.61			
(l)	60	9.8	0.3				8200	0.34			
(m)	64	2.4	0.3	15	1300	1.2	2500	0.71	+0.07	4.37	1097
(n)	64	0.9	0.3				900	1.15			
Mean		2.5		12.4	830	1.1	1900	0.9	+0.1	5.9	1100
σ		1.5		1.3	240	0.1	1100	0.4	0.1	2.2	90

Table 5.2.3

relative to the ground to obtain a propagation speed relative to the ground. This air speed was taken to be the mean of the velocity component parallel to the direction of propagation in the surface to the LNB layer. These results are summarised in table 5.2.3. Mean and standard deviation are calculated for each quantity.

Mean values are now used in the following calculations since errors in individual (B-γ_f) calculations may be as large as 25%. In reality one would expect variation in this parameter depending on the rainfall rate and the pre-forced circulation relative humidity.

5.2.2 Results of the Comparison.

(i) Comparison of propagation speed with that predicted by the simple TMM80 model of chapter three.

(a) incompressible case:-

$$F = 1/n\pi$$

$$c = [1/(n\pi)]\sqrt{2FCAPE}$$

$$= [1/(n\pi)]\sqrt{2x2000}$$

$$= 20.1/n \text{ ms}^{-1}$$

(b) compressible case:-

n=1 downdraught, $F = 1.19/\pi$.

n=2 (upper level ascent, lower level descent), $F = 1/(2\pi)$.

n=1, c(predicted)=5.9+24.0=29.9ms^{-1}

n=2, c(predicted)=5.9+10.1=16.0ms^{-1}

Note $\langle c(\text{propagation})\rangle = 13 \pm 2 \text{ms}^{-1}$ so that only the n=2 mode (incompressible or compressible case) lies within two standard deviations of the mean value.

Comparison of the calculated value of $\sqrt{\frac{\gamma_u - B}{B - \gamma_f}}$ with that predicted in

chapter four.

This calculation operates "in reverse".

$$\langle c(\text{relative})\rangle = \langle c(\text{propagation})\rangle - \langle c(\text{mean})\rangle = 13.0 - 5.9 = 7.1 \text{ms}^{-1}.$$

$$\langle c(\text{relative})\rangle / \sqrt{2\text{UCAPE}} = 7.1/\sqrt{2\text{x}830} = 0.174.$$

We now want to calculate F_u for the updraught circulation from the relationship:- $c(\text{relative}) = (c_u + c_f)/2$ and $\Delta c = c_f - c_u$.

$$F_u = c_u/\sqrt{2\text{UCAPE}} = c(\text{relative})/\sqrt{2\text{UCAPE}} - 0.5\text{x}\Delta c/\sqrt{2\text{UCAPF}}$$

$$= 0.174 - 0.5\text{x}0.1$$

$$= 0.124.$$

The effect of shear on F_u is removed by using the equation

$$F_u(\Delta c = 0) = F_u(\Delta c) + \Delta c/\sqrt{2\text{UCAPE}}.$$

$$\text{Thus } F_u(\Delta c = 0) = 0.124 + 0.1 = 0.224.$$

From figure 4.5.3, the value of $\sqrt{\frac{\chi_u - \bar{\chi}}{\bar{\chi} - \chi_f}}$ corresponding to this value of F_u (for $r_o = 0.1$) is 1.5. This compares with a mean value of 0.9 ± 0.4 from the VIMHEX squall lines and lies within two standard deviations of the mean value.

An estimate of the mean mesoscale descent rate may be made from these as a further guide to the validity of the data processing method. A mean descent distance ($|\Delta z|$) may be calculated for 60 minutes for each squall line assuming uniform descent. As can be seen from table 5.2.3 the mean for all squall lines is 1100m with a standard deviation of 90m. This gives a descent rate of 30cms^{-1}. This descent rate seems rather large cf. Gamache and Houze (1982) who suggested a maximum descent rate of 6cms^{-1}, but Zipser (1977) suggests

5-25cms^{-1} at about 500m above the surface and just above the mixed layer.

The mean descent rate calculated from VIMHEX data would produce a heating rate of 0.8Kh^{-1} assuming $(\Gamma_d - \Gamma_s) \sim 2.5 \times 10^{-6} m^{-1}$. This heating rate may not be steady over the period of the mature stage of a squall line. Ideally we would like to know the horizontal temperature change across the forced flow which requires data for a longer period (several hours after rainfall has ceased). A recent study of boundary layer and surface changes by Johnson and Nicholls (1983) suggests warming continues to occur for several hours after rain has stopped falling from the anvil.

These calculations can only provide order of magnitude guides. It is inherently difficult to calculate a forced descent lapse rate because it requires consecutive soundings unlike the UCAPE calculation in which the quantity calculated corresponds simply to the positive area on a tephigram from a single sounding.

Single station data can be used providing the squall lines studied are sufficiently "two-dimensional". In this respect the Venezuelan squall lines (notably numbers 14 and 56) experience relative inflow at the rear. Ideally West African squall lines probably provide a better choice for study since they are of much greater transverse length (Fernandez, 1982) if a sufficiently small time resolution could be obtained (ie. hourly soundings).

5.3 Suggestions for Further Research.

The various models of convective circulations developed in chapter two have suggested a form for the pressure perturbation field produced

but reliable observations do not exist to test these predictions. Consequently it would be valuable to look at the pressure perturbation fields produced in numerical simulations of tropical squall line elements. Calculation of the ratio $\langle \delta p \rangle / KE_o$ for forced flows in numerical simulations would also make an interesting comparison with the type of values predicted in chapter three for uniformly sheared and jet profile inflows to circulations. The horizontal scale of the MM simulation however was not sufficiently large to accommodate a reasonable dynamical representation of the processes considered here. Ideally, a combination of numerical simulation and observations of West African squall lines would be most useful for a comparison with the dynamical models explored in this thesis. Presumably, the observations of the COPT 1981 experiment would be of great use in this context when the data has been processed.

The model developed in chapter four (the intertwined flow) should be extended to include compressibility since, as previous results in chapters two and three indicate, the consequences are unpredictable and may produce a deeper outflow layer from the convective circulation.

The many component flows studied can be used to look at the consequences of relative inflow at the rear as is found in the Venezuelan squall lines although the Eastern Tropical Atlantic and West African squall lines suggest this effect is not important to the larger, more two-dimensional squall lines. This is a possible direct extension of the models considered here, although at the expense of forming a much more complicated model.

There is a clear need for more detailed and temporally frequent

observations of squall clusters, particularly to produce three dimensional wind and thermodynamic fields. Single station radiosonde data combined with radar to locate the relative position and direction of a squall line would probably provide one of the most cost-effective ways of producing composited fields for a particular geographical location. The calculations performed in section 5.2 illustrate the need for better temporal resolution of thermodynamic fields.

Mixing of updraught air with environmental air occurs to some extent and may be responsible for producing the much thinner anvils than are predicted by the model developed in chapter four. The consequences of mixing probably cannot be tackled by these simple analytic models. Further dynamical progress can probably only be made using numerical models.

A means of specifying foced descent from initial thermodynamic profiles does not presently exist. It may not be possible to make any progress in this matter since it involves the interaction between convective and meso-scales; however it may be possible to asign a value to $\sqrt{\frac{\gamma_u - \beta}{\beta - \gamma_4}}$ typical of squall clusters occurring in a particular geographical area and relate this parameter to the net rainfall or rainfall rates in the cell and mesoscale descent regions.

Appendix A

In chapter two the displacement equation 2.14 with boundary conditions 2.15 and 2.16 is solved for sheared compressible flows as follows. 2.14 is rearranged:-

$$\left(\frac{d\mathcal{J}_0}{d\mathcal{J}_1}\right)^2 \exp\left[2(\mathcal{J}_1-\mathcal{J}_0)D-1\right]\left(\frac{u_0}{c}\right)^2 = -\left[E+\frac{2}{F^2}\int_{\mathcal{J}_0^*}^{\mathcal{J}_1^*}(\mathcal{J}_1-\mathcal{J}_0)\,d\mathcal{J}_0\right]$$

and differentiated with respect to $\mathcal{J}_1$ writing $d\mathcal{J}_0/d\mathcal{J}_1=\mathcal{J}_0'$ to give

$$\frac{d^2\mathcal{J}_0}{d\mathcal{J}_1^2} = -\left(\frac{c}{u_0}\right)^2\frac{1}{F^2}(\mathcal{J}_1-\mathcal{J}_0)\exp\left[-2(\mathcal{J}_1-\mathcal{J}_0)D\right] \qquad (A.1)$$

$$-\left(\frac{c}{u_0}\right)\frac{d}{d\mathcal{J}_0}\left(\frac{u_0}{c}\right)\left[\mathcal{J}_0'^2-\exp\left[-2(\mathcal{J}_1-\mathcal{J}_0)D\right]\right]-\mathcal{J}_0'(1-\mathcal{J}_0').$$

Writing $$F_2 = \frac{d^2\mathcal{J}_0}{d\mathcal{J}_1^2} = F_2(\mathcal{J}_0,\mathcal{J}_0',\mathcal{J}_1) \qquad (A.2)$$

$$F_1 = \frac{d\mathcal{J}_0}{d\mathcal{J}_1} = F_1(\mathcal{J}_0,\mathcal{J}_1) \qquad (A.3)$$

a NAG library routine D02EBF is used to integrate the system of first order ordinary differential equations, F_1 and F_2, from the point $\mathcal{J}_0=r_0$, $\mathcal{J}_1=r_1$, where $d\mathcal{J}_0/d\mathcal{J}_1=\sqrt{1-E}\exp(-2(r_1-r_0)D)$ to the point $\mathcal{J}_0=0$. The value of F is varied until the difference between $\mathcal{J}_0(\mathcal{J}_1=1)$ and 0, the endpoint value, is reduced to the tolerance (10^{-7}). The routine generates intermediate values of $\mathcal{J}_1$, $\mathcal{J}_0$ and $\mathcal{J}_0'$ from which u_1, δp_1 and $\delta\phi_1$ are calculated in the following manner. From the continuity

equation 2.12

$$u_1 = -u_0 \frac{\rho_0}{\rho_1} \frac{d\rho_0}{d\rho_1}$$

$$= -u_0 \exp\left[(\rho_1-\rho_0)D\right] \rho_0' \qquad (A.4)$$

and $$\delta\phi_1 = (\gamma-B) H (\rho_1-\rho_0). \qquad (A.5)$$

δp_1 is given at any height z_1 in the outflow by:-

$$\frac{\delta p_1}{\rho_1} = \frac{1}{2}c^2 E + \int_{z_0^*}^{z_1^*} g\delta\phi_1 dz + \int_{z_1^*}^{z_1} g\delta\phi_1 dz_1$$

$$\frac{\delta p_1}{\frac{1}{2}c^2\rho_s} = \exp(-\rho_1 D)\left[E + \left(\frac{\rho_1^* - \rho_0^*}{F}\right)^2 + \frac{2}{F^2}\int_{z_1^*}^{z_1} (\rho_1-\rho_0) d\rho_1\right].$$

In discrete form when $\rho_1 = nh_0$ this becomes

$$\frac{\delta p_1}{\frac{1}{2}\rho_s c^2} = \exp(-nh_0 D)\left[E_u + \left(\frac{\rho_1^* - \rho_0^*}{F}\right)^2 + \frac{2}{F^2} h_0 \sum_{\ell=\frac{r_1}{h_0}+1}^{\ell=n} \exp(-\ell h_0)(\ell h_0 - \rho_0(\ell h_0)\right].$$

where h_0 is the summation interval and r_1 and h_0 are chosen such that r_1/h_0 and ρ_1/h_0 are integers.

In chapter three the same displacement equation, A.1, is solved where $F^2 = -F_f^2$. Integration procedes from $\rho_0 = 1$, $\rho_1 = r_1$ to $\rho_1 = 0$. The

value of F_f is varied until the difference between $f_0(f_1=0)$ and r_0 is reduced to the required tolerance (10^{-7}). u_1 and $\delta\phi_1$ are calculated as before. A.6 becomes

$$\frac{\delta p_1}{\frac{1}{2}\rho_s c^2} = \exp(-nh_0 D)\left[E_f - \left(\frac{f_1^* - f_0^*}{F_f}\right)^2 + \frac{2}{F_f^2} h_0 \sum_{\ell=\frac{r_1}{h_0}-1}^{\ell=n} \exp(-\ell h_0)\left(\ell h_0 - f_0(f_1=\ell h_0)\right)\right].$$

Appendix B

A general method for solving simultaneous transcendental equations developed by P. Burrow (paper in preparation) was employed. Let $x=F(x,y,z)$. Consider the expression $x=(x^{n-1}F)^{1/n}=F_1(x,y,z)$

$$\frac{\partial F_1}{\partial x} = \frac{1}{n}\left[x^{n-1}F\right]^{1/n-1}\left\{(n-1)x^{n-2}F + x^{n-1}\frac{\partial F}{\partial x}\right\}$$

$$= \frac{1}{n}\left(x^{n-1}F\right)^{1/n} x^{-n+1}F^{-1}\left\{(n-1)x^{n-2}F + x^{n-1}\frac{\partial F}{\partial x}\right\}$$

$$\approx \frac{1}{n}\left\{(n-1) + \frac{\partial F}{\partial x}\right\}$$

$$\frac{\partial F_1}{\partial y} = \frac{1}{n}\left[x^{n-1}F\right]^{1/n-1} x^{1-n}F^{-1}x^{n-1}\frac{\partial F}{\partial y}$$

$$\approx \frac{1}{n}\frac{\partial F}{\partial y}$$

F_1 is required to vary slowly with all independent variables x, y, z.... This is achieved most efficiently when $n=1-\partial F/\partial x$ and $n>1$. Expressions used for r_1, E_u and F_u from 4.5, 4.12, 4.19 and 4.20 were

$$r_1 = r_0 + \frac{1}{\cosh \frac{1-r_1}{F_u}} \left[1 - (1+\sqrt{1-E_u})\, F_u \sinh \frac{1-r_1}{F_u} \right] \qquad (B.1)$$

$$E_u = \left(\frac{F_f}{F_u}\right)^2 \left[E_f - \left(\frac{1-r_1}{F_f}\right)^2 \right] \Big/ \left(\frac{\gamma_u - B}{B-\gamma_f}\right) - \left(\frac{r_1 - r_0}{F_u}\right)^2 \qquad (B.2)$$

$$F_u = \left(r_0 - (1-r_1)\cos\frac{r_1}{F_f}\right) \Big/ \left[(1-\sqrt{1-E_f}) \sin\frac{r_1}{F_f} \sqrt{\frac{\gamma_u - B}{B-\gamma_f}} \right] - \frac{\Delta c}{\sqrt{2UCAPE}}. \qquad (B.2)$$

F_f is eliminated from B.2 and B.3 using 4.12 ie.

$$F_f = \left(F_u + \frac{\Delta c}{\sqrt{2UCAPE}} \right) \sqrt{\frac{\gamma_u - B}{B-\gamma_f}}.$$

From trial solutions x and $x+\delta x$, producing F_f and $F_f+\delta F_f$, n may be calculated, and similarly for the other variables, the procedure continuing until F_f is within a desired tolerance of x.

Acknowledgement

I would like to thank my supervisor Dr M.W.Moncrieff for his guidance and encouragement over the last three years. Dr.J.S.A.Green, Dr.V.H.Y.Tam and Dr.A.J.Thorpe provided useful discussion and criticism which are gratefully acknowledged. This work was undertaken while in receipt of an NERC studentship.

References

Aspliden, C.I., Tourre, Y. and Sabine, J.B. Some climatological aspects of West African disturbance lines during GATE. Mon.Wea.Rev. 104 pp1029-1035, 1976.

Barnes, G.M. and Garstang, M. Subcloud layer energetics of precipitating convection. Mon.Wea.Rev. 110 pp102-117, 1982.

Betts, A.K. The scientific basis and objectives of the U.S. convection subprogram for the GATE.
Bull.Amer.Met.Soc. 55 pp304-313, 1974.

Betts, A.K. The thermodynamic transformation of the tropical subcloud layer by precipitation. J.Atmos.Sci. 33 pp1008-1020, 1976.

Betts, A.K., Grover, R.W. and Moncrieff, M.W. Structure and motion of tropical squall lines over Venezuela. Quart.J.R.Met.Soc. 102 pp395-404, 1976.

Betts, A.K. and Miller, R.D. Vimhex 1972 rawinsonde data . Research report, Dept.Atmos.Sci., Colorado State University, Fort Collins, 1975.

Betts, A.K. and Silva Dias, M.F. Unsaturated downdraught thermodynamics in cumulonimbus. J.Atmos.Sci. 36 pp1061-1071, 1979.

Brown, J.M. Mesoscale unsaturated downdraughts driven by rainfall evaporation: A numerical study. Mon.Wea.Rev. 36 pp313-338, 1979.

Charba, J. Application of gravity current model to analysis of squall-line gust front. Mon.Wea.Rev. 102 pp140-156, 1974.

Cheng, C.P. and Houze, R.A. Distribution of convective and mesoscale precipitation in GATE radar echo patterns. Mon.Wea.Rev. 107 pp1370-1381, 1979.

Chong, M., Testud, J. and Roux, F. Three-dimensional wind field analysis from dual-doppler radar data. Part II. Minimising the error due to temporal variation. Submitted to J.Appl.Met. 1983.

Echternacht, K.L., Garstang, M. Changes in the structure of the tropical subcloud layer from the undisturbed to disturbed states. Mon.Wea.Rev. 104 pp407-417, 1976.

Emmitt, G.D. Tropical cumulus interaction with and modification of the subclouud region. J.Atmos.Sci. 35 pp1485-1502, 1978.

Fernandez, W. Environmental conditions and structure of some types of convective mesosystems observed over Venezuela. Arch.Meteor.Geoph.Biokl.Ser.A. 29 pp249-267, 1980.

Fernandez, W. Environmental conditions and structure of the West African and Eastern Tropical Atlantic squall lines. Arch.Meteor.Geoph.Biokl.Ser.A. 31 pp71-89, 1982.

Fortune, M. Properties of African squall lines inferred from time-lapse satellite imagery. Mon.Wea.Rev. 108 pp153-168, 1980.

Frank, N.L. Atlantic tropical systems of 1969. Mon.Wea.Rev. 98 pp307-314, 1970.

Fritsch, J.M. and Chappell, C.F. Numberical prediction of convectively driven mesoscale pressure systems. Part I: convective parameterisation. J.Atmos.Sci. 37 pp1722-1733, 1980a.

Fritsch, J.M. and Chappell, C.F. Numerical prediction of convectively driven mesoscale pressure systems. Part II: mesoscale model. J.Atmos.Sci. 37 pp1734-1762, 1980b.

Gamache, J.F. and Houze, R.A. Mesoscale air motions associated with a tropical squall line. Mon.Wea.Rev. 110 pp118-135, 1982.

Gray, W.M. Cumulus convection and larger scale circulations. Part I. Broadscale and mesoscale considerations. Mon.Wea.Rev. 101 pp839-855, 1973.

Gray, W.M., Ruprecht, R. and Phelps, R. Relative humidity in tropical weather systems. Mon.Wea.Rev. 103 pp685-690, 1975.

Green, J.S.A. and Pearce, R.P. Cumulonimbus convection in shear. Tech.Note 12, Dept.Met., Imperial College, London, 1962.

Houze, R.A. A climatological study of vertical transports by cumulus-scale convection. J.Atmos.Sci. 30 pp1112-1123, 1973.

Houze, R.A. Structure and dynamics of a tropical squall line system. Mon.Wea.Rev. 105 pp1540-1567. 1977.

Houze, R.A. and Cheng, C.P. Radar characteristics of tropical convection observed during GATE: mean properties and trends over the summer season. Mon.Wea.Rev. 105 pp964-980, 1977.

Hoxit, L.R., Chappell, C.F. and Fritsch, J.M. Formation of mesolows/pressure troughs in advance of cumulonimbus clouds. Mon.Wea.Rev. 104 pp1419-1428, 1976.

ICSU/WMO. International Council of Scientific Unions/World Meteorological Organisation. The planning of GARP tropical

experiments, GATE Rep.1, 188pp, Geneva, 1972.

Johnson, R.H. and Nicholls, M.E. A composite analysis of the boundary layer accompanying a tropical squall line. Mon.Wea.Rev. 111 pp308-319, 1983.

Kamburova, P.L. and Ludlam, F.H. Rainfall evaporation in thunderstorm downdraughts. Quart.J.R.Met.Soc. 92 pp510-518, 1966.

Leary, C.A. and Houze, R.A. The structure and evolution of convection in a tropical cloud cluster. J.Atmos.Sci. 37 pp437-457, 1979a.

Leary, C.A. and Houze, R.A. Melting and evaporation of hydrometeors in precipitation from anvil clouds of deep tropical convection. J.Atmos.Sci. 36 pp669-679, 1979b.

Mansfield, D.A. Squall lines observed in GATE. Quart.J.R.Met.Soc. 103 pp569-574, 1977.

Martin, D.W. and Sikdar, D.N. A case study of W.Atlantic cloud clusters: Part II. Dynamic structure and environment. Mon.Wea.Rev. 107 pp1343-1369, 1979.

Martin, D.W. and Suomi, V.E. A satellite study of cloud clusters over the tropical North Atlantic Ocean. Bull.Amer.Met.Soc. 53 pp135-156, 1972.

Miller, M.J. and Betts, A.K. Travelling convective storms over Venezuela. Mon.Wea.Rev. 105 pp833-848, 1977.

Moncrieff, M.W. A theory of organised steady convection and its transport properties. Quart.J.R.Met.Soc. 107 pp29-50, 1981.

Moncrieff, M.W. and Green, J.S.A. The propagation and transfer properties of steady convective overturning. Quart.J.R.Met.Soc. 98 pp336-352, 1972.

Moncrieff, M.W. and Miller, M.J. The dynamics and simulation of tropical cumulonimbus and squall lines. Quart.J.R.Met.Soc. 102 pp373-394, 1976.

Nitta, T. Response of cumulus updraught and downdraught to GATE A/B-scale motion systems. J.Atmos.Sci. 34 pp1163-1186, 1977.

Riehl,H. Some aspects of cumulonimbus convection in relation to tropical weather systems. Bull.Amer.Met.Soc. 50 pp587-595, 1969.

Riehl, H. and Malkus, J.S. On the heat balance of the equatorial trough zone. Geophysica, 6 pp503-538, 1958.

Ryan, B.F. and Carstens, J.C. A comparison between a steady-state downdraught model and observations behind squall lines. J.Appl.Met. 17 pp395-400, 1978.

Schlesinger, R.E. A numerical model of deep moist convection: Part II. A prototype experiment and variations upon it. J.Atmos.Sci. 30 pp1374-1391, 1973.

Tam, H.Y. Cumulonimbus convection and parameterisation . PhD thesis, Imperial College, London, 1979.

Thorpe, A.J., Miller, M.J. and Moncrieff, M.W. Dynamical models of two-dimensional downdraughts. Quart.J.R.Met.Soc. 106 pp463-484, 1980.

Thorpe, A.J., Miller, M.J. and Moncrieff, M.W. Two-dimensional

convection in non-constant shear: a model of mid-latitude squall lines. Quart.J.R.Met.Soc. 108 pp739-762, 1982.

Williams, K.T. and Gray, W.M. Statistical analysis of satellite-observed trade wind cloud clusters in the Western North Pacific. Tellus, 25 pp313-336, 1973.

Yanai, M., Esbensen, S. and Chu, J.H. Determination of bulk properties of tropical cloud clusters from large-scale heat and moisture budgets. J.Atmos.Sci. 30 pp611-627, 1973.

Zipser, E.J. Role of organised unsaturated convective downdraughts in the structure and rapid decay of an equatorial disturbance. J.Appl.Met. 8 pp799-814, 1969.

Zipser, E.J. Mesoscale and convective-scale downdraughts as distinct components of squall line structure. Mon.Wea.Rev. 105 pp1568-1589, 1977.